THEORETICAL CHEMICAL KINETICS OF ATMOSPHERIC REACTIONS WITH NEAR-ZERO AND NEGATIVE BARRIERS

CHOW KA CHUN RONALD

M.Phil

The Hong Kong Polytechnic University

2018

The Hong Kong Polytechnic University

Department of Applied Biology and Chemical Technology

Theoretical Chemical Kinetics of Atmospheric Reactions with Near-zero and Negative Barriers

CHOW Ka Chun Ronald

A thesis submitted in partial fulfilment of the requirements for the degree of Master of Philosophy

June 2017

CERTIFICATE OF ORIGINALITY

I hereby declare that this thesis is my own work and that, to the best of my knowledge and belief, it reproduces no material previously published or written, nor material that has been accepted for the award of any other degree or diploma, except where due acknowledgement has been made in the text.

_____

CHOW Ka Chun Ronald

Abstract

Abstract of the thesis entitled

“Theoretical Chemical Kinetics of Atmospheric Reactions with Near-zero and Negative Barriers”

submitted by CHOW Ka Chun Ronald

for the degree of Master of Philosophy in Chemistry

at The Hong Kong Polytechnic University

The atmosphere consists of many gases and radicals and many reactions could occur, thereby forming a very dynamic system. Due to the unstable nature of radicals, they are short-lived which make experimental studies difficult. Moreover, reactions involving radicals (such as radical-radical reactions) have low or negative barriers. The life time of these radicals short, which make them and their reactions difficult to observe. Furthermore, some conditions can be challenging to achieve in laboratory, such as very high or very low temperature and/or pressure, or the complete desirable ranges. In view of these experimental challenges of gas phase studies, theoretical methods (*ab initio* (wavefunction-based) methods, density functional theory (DFT), and the transition state theory (TST)) provide alternative ways to study gas phase reactions without subject to the aforementioned difficulties, especially for reactions involving radicals.

This work aims to establish reliable and practical methods to calculate rate coefficients for chemical reactions with low or negative barriers, which involves the investigation of the interrelationships between the rate coefficients, the reaction surface and the computed barrier heights. In particular, two atmospherically important reactions were studied computationally, namely the $CH_3C(O)OCH_3$ + Cl reaction and the BrO + HO_2 reaction. The former is a reaction with a low barrier while the major channel of the latter is a reaction with a negative barrier.

Rate coefficient calculations showed that one vibrational mode changed dramatically along the reaction coordinate, leading to a dramatic change of the zero-point energy (ΔZPE) along the reaction coordinate. Consequently, large variational effects resulted for reactions with flat and very flat reaction surfaces, which were characterized by small classical adiabatic ground-state transmission factors (CAG factors). This approach is effective in compensating for the deficiency of the TST method. The results also showed that the locations of the maxima of the ΔG curves at certain temperatures were a bit away from the saddle point at a negative reaction coordinate (i.e. in the reactant side), especially for reactions with low and negative barriers. This indicated that the choice of the intrinsic reaction coordinate in rate coefficient calculations had to cover the maximum of a ΔG curve in order to obtain accurate rate coefficients. It was also found that the pre-exponential entropic terms, which were computed using the vibrational frequencies and geometrical parameters, had significant effects on the computed rate coefficients, especially for chemical reactions with low and negative barriers. Thus, in addition to the accuracies of the computed barrier heights, the accuracies of the computed harmonic frequencies and geometries along the reaction coordinate also play crucial roles as they in part determined the accuracies of rate coefficients.

This work has also provided the computed barrier heights, reaction mechanisms, reaction enthalpies and rate coefficients of the two reactions, so that they can be used for further kinetic modeling.

Publications

1. Chow, R.; Mok, D. K. W.; Lee, E. P. F.; Dyke, J. M. A theoretical study of the atmospherically important radical–radical reaction BrO + HO_2; the product channel $O_2(a^1\Delta_g)$ + HOBr is formed with the highest rate. *Phys. Chem. Chem. Phys*. **2016**, 18, 30554-30569.
2. Chow, R.; Ng, M.; Mok, D. K. W.; Lee, E. P. F.; Dyke, J. M. Rate Coefficients of the Cl + $CH_3C(O)OCH_3$ → HCl + $CH_3C(O)OCH_2$ Reaction at Different Temperatures Calculated by Transition-State Theory with ab Initio and Density Functional Theory Reaction Paths. *J. Phys. Chem. A* **2014**, 118, 2040-2055.

Acknowledgement

This thesis would not have been possible without the guidance, help and support from the following individuals, so I must convey my gratitude to all of them in the acknowledgement.

I would like to express my deepest gratitude to my supervisor, Dr. Daniel Kam Wah Mok, for his continuous guidance and patience throughout my study. I would also like to thank him for giving me an opportunity to pursue further studies in the field of computational chemistry as a graduate student. I appreciate his immense knowledge in physical chemistry, quantum mechanics, computational chemistry, classical physics and computer programming. I am also very deeply grateful to him for spending a lot of time to have in-depth discussions with me. In addition, I would like to thank him for giving me some opportunities to build a computer cluster.

I would like to express my sincere gratitude to Dr. Edmond P. F. Lee and Prof. John M. Dyke for their generous help and fruitful discussions during my study period. During the preparation of this thesis, they spent tremendous efforts in giving me valuable comments on my thesis and presentation. In particular, I would like to thank Dr. Edmond P. F. Lee for running all the computationally expensive quantum chemical calculations which are essential to the completion of the research projects.

I am also indebted to Dr. Peng Zhang (Department of Mechanical Engineering, HK PolyU) for his instructions on using the software, VARIFLEX.

Special thanks go to Dr. Maggie Ng. I would like to thank her for teaching me to use Gaussian 09 and PolyRate software packages and sharing her experience in performing electronic structure and rate coefficient calculations with me.

Finally, I would like to thank my parents and all of my friends for their endless encouragement, full support and patience throughout my study. In particular, I would like to thank Mr. Harold M. C. Chan, Mr. Angelos Ching and Mr. Chris Wong for having discussions with me on various types of computer-related issues.

Table of Contents

List of Figures

List of Tables

List of Abbreviations

2-TST	Two Transition State Theory
μVT	Microcanonical Variational Transition State Theory
AO	Atomic Orbital
BD	Brueckner Doubles
BD(T)	Brueckner Doubles with Perturbative Triples
BD(TQ)	Brueckner Doubles with Perturbative Triples and Quadruples
BFGS	Broyden-Fletcher-Goldfarb-Shanno
BO	Brueckner Orbital
CAG	Classical Adiabatic Ground-state
CBS	Complete Basis Set
CC	Couple Cluster
CCSD	Coupled Cluster Singles and Doubles
CCSD(T)	Coupled Cluster Singles and Doubles with Perturbative Triples
CI	Configuration Interaction
CIS	Configuration Interaction Singles
CISD	Configuration Interaction Singles and Doubles
CPU	Central Processing Unit
CVT	Canonical Variational Transition State Theory
CUS	Canonical Unified Statistical Theory
DF	Density Fitting
DFP	Davidon–Fletcher–Powell
DFT	Density Functional Theory

DWI	Distance Weighted Interpolants
E,*J*-TST	Transition State Theory at Energy and Angular Momentum Resolved Levels
GGA	Generalized Gradient Approximation
GTO	Gaussian Type Orbital
GTS	Generalized Transition State
HF	Hartree-Fock
HK	Hohenberg-Kohn
HPC	Hessian-based Predictor-Corrector
ICVT	Improved Canonical Variational Transition State Theory
IRC	Intrinsic Reaction Coordinate
KS	Kohn-Sham
LCAO	Linear Combination of Atomic Orbitals
LSDA	Local Spin Density Approximation
LQA	Local Quadratic Approximation
MEP	Minimum Energy Path
Meta-GGA	Meta-Generalized Gradient Approximation
MO	Molecular Orbital
MP	Møller-Plesset Perturbation Theory
MP1	First-Order Møller-Plesset Perturbation Theory
MP2	Second-Order Møller-Plesset Perturbation Theory
MT	Multidimensional Tunneling
OVOC	Oxygenated Volatile Organic Compound
PC	Product Complex

PES	Potential Energy Surface
PST	Phase Space Theory
QST	Quadratic Synchronous Transit
RC	Reactant Complex
RHF	Restricted Hartree-Fock
RI	Resolution Identity
ROHF	Restricted Open-shell Hartree-Fock
RRKM	Rice–Ramsperger–Kassel–Marcus
SCF	Self-Consistent Field
SCT	Small Curvature Tunneling
SD	Slater Determinant
SIE	Self-Interaction Error
SO	Spin Orbit
SP	Separate Products
STO	Slater Type Orbital
STQN	Synchronous Transit-Guided Quasi-Newton
TS	Transition State
TST	Transition State Theory
UHF	Unrestricted Hartree-Fock
VOC	Volatile Organic Compound
VTST	Variational Transition State Theory
ZCT	Zero Curvature Tunneling
ZPE	Zero Point Energy

Chapter 1.

Introduction

1.1 Background

The science of studying chemical and physical processes in the upper atmosphere is known as aeronomy, which is an interdisciplinary field [1]. It comprises of atmospheric physics, chemical kinetics and the study of reaction mechanisms. The proposal of the photochemical mechanism in the formation of ozone in the stratosphere by Chapman in 1930 marked the start of aeronomy [2]. Later on, when the stratospheric ozone depletion by chlorofluorocarbons (CFCs) due to their long life time was realized in 1970s, there was a need in mathematical models for predicting the current and future amounts of ozone in the atmosphere with the consideration of the involvement of the pollutants [1]. Thus, tremendous efforts have been dedicated to research in these mathematical models for the past 30 years, in which the chemical databases play an important role in atmospheric modeling [1], which helps unravel the fate and transport of pollutants [3,4].

However, some atmospheric reactions present challenges to experimental studies, such as radical-radical reactions and, hydrogen-transfer reactions. In radical-radical reactions, the lifetime of radicals is short which makes detection difficult in experimental investigations [6]. In addition, some experimental conditions can be challenging to achieve in laboratories, such as extreme ranges of temperature and pressure. Hence, theoretical chemical kinetics can serve to obtain the rate coefficients and thermodynamic parameters at consistent and high level of accuracy by using potential energy surface which is produced by quantum chemical methods (*ab initio* and density functional theory) [7]. These theoretical thermodynamic quantities and rate coefficients are calculated from the first principles without the use of empirical parameters and experimental data. Thus, experimental limitations and the challenges (short lifetime of radicals) will be a problem for theoretical investigations. Moreover, detailed reaction mechanisms which are usually

difficult to work out in experimental investigations of chemical reactions, can be elucidated.

There have been ongoing efforts devoted in development of in quantum chemical methods, including *ab initio* methods and density functional theory (DFT) [7], to obtain reliable barrier height, optimized geometry and harmonic vibrational frequencies of compounds, potential energy surface and reaction path (intrinsic reaction coordinate). In terms of theoretical chemical kinetic, the transition state theory (TST) [8] and its variant, the variational transition state theory (VTST) [8] have been developed to predict rate coefficients with and without tunneling at various levels by using the aforementioned results obtained from quantum chemical methods.

Both quantum chemical methods and the transition state theory family come in different levels of approximation. Two major classes of quantum chemical methods are employed in this study, namely *ab initio* methods and density functional theory. *Ab initio* methods are wavefunction-based methods [9] while DFT is based on electron density [10]. The differences in various *ab initio* methods lie in the treatment of electron correlation. Some examples of *ab initio* method developed to treat electron correlation include the second-order Moller-Plesset perturbation theory (MP2) [7], the coupled-cluster single and doubles (CCSD) [7], the coupled-cluster single, doubles and perturbative triples (CCSD(T)) [7], the Brueckner doubles (BD) [9, 10], the Brueckner doubles with perturbative triples (BD(T)) [9, 11] and the Brueckner doubles with perturbative triples and quadruples (BD(TQ)) [9, 11]. Electron correlation is also treated in the density functional theory by using different exchange-correlation functional [7], which will be discussed in Chapter 2. Another important element in computing electronic energies and molecular properties is the basis set. Correlation-consistent basis sets are used and various extrapolation schemes [12] are available to extrapolate the computed electronic energies to the complete basis set (CBS) limit.

For theoretical chemical kinetics, the TST has been the cornerstone in this field. Later, the refinement on the TST leads to the VTST [7] which comes with three forms, the canonical VTST (CVT) [7], the microcanonical VTST (μVT) [7] and the improved canonical VTST (ICVT) [7]. Both the TST and the VTST allow to account for multi-dimensional tunneling corrections, namely, zero curvature tunneling (ZCT) [7] and small curvature tunneling (SCT) [7] schemes. The major difference between the TST and the

VTST lies in the consideration of the location of the dividing surface of a reaction, which is the surface that separates the reactant region from the product region in the potential energy surface. The dividing surface of a chemical reaction in the TST approach is defined to be located at the saddle point while that in the VTST approach is defined as where the the number of trajectories crossing the dividing surface is minimum, which can be different from the saddle point. The detailed discussions of the TST and the VTST approaches are covered in chapter 3. Thus, the VTST gives more accurate rate coefficients than the TST because a better position of the transition state in a chemical reaction is considered in the VTST, as evidenced in the work described in this thesis.

Different levels of theories in *ab initio*/DFT can yield very different results of barrier heights, reaction enthalpies, and imaginary vibrational frequency of the transition state, which in turn yield different rate coefficients at various TST levels. This enables an investigation on the interrelationship between different levels of *ab initio*/DFT and different levels of TST and their impacts on computed rate coefficients, which is one of the major themes of this thesis.

Two theoretical studies form substantial parts of this thesis and the major channels of both reactions are hydrogen abstraction reactions, where quantum tunneling may be important. The first theoretical study is the $CH_3C(O)OCH_3 + Cl \rightarrow CH_3C(O)OCH_2 + HCl$ reaction. It is atmospherically significant because methyl acetate is widely used in industry [13] and it is volatile. Chlorine atom is known to react with VOCs rapidly, faster than those with OH radical [14]. Literatures show that this reaction has a very low experimentally derived activation energy (0.71 $kcal.mol^{-1}$) [15]. Laider and coworker point out that the TST may have problems when the reaction barrier is low [16]. The second theoretical study is a radical-radical reaction, the reaction between BrO radical and HO_2 radical, which is involved in stratospheric ozone depletion. There have been some experimental studies [17] on this reaction and they suggest that the major channel is the $BrO + HO_2 \rightarrow HOBr + O_2$ channel and it has a negative activation energy whereas the minor channel is $BrO + HO_2 \rightarrow HBr + O_3$ [18]. Various experimental measurements on the rate coefficients of the $BrO + HO_2 \rightarrow HOBr + O_2$ channel have been made and they show negative temperature dependence behavior [17], which means that the rate coefficients decrease with increasing temperature. The negative temperature behavior of rate coefficients suggests that a pre-reactive complex may form and the reaction may proceed through this pre-reactive complex [18]. For the two atmospherically important

reactions, there were no previous computational studies on these reactions but there have been some experimental studies on them. Moreover, the TST may not give reliable rate coefficients for reactions with low [7] or even negative barriers [19]. Therefore, both reactions provide opportunities to establish reliable and practical methods to compute rate coefficients for such type of gas-phase reactions because computed rate coefficients can then be compared with the experimental rate coefficients in literatures. This thesis reports the first theoretical studies on the $CH_3C(O)CH_3$ + Cl reaction and the BrO + HO_2 reaction. Computational studies have been carried out to determine the energetics and the reaction mechanisms of all the possible channels of these two reactions using state-of-the-art *ab initio* and DFT methods. The interrelationship between different levels of *ab initio*/DFT and different levels of TST theories and their impacts on computed rate coefficients have been investigated. Finally, rate coefficient calculations have been performed for the major channels of these two reactions at various TST levels. The rate coefficients and reaction enthalpies obtained may contribute to thermochemical and kinetic database, which can then be used for atmospheric modeling.

1.2 Objectives

The objectives of this thesis are threefold.

1. To use state-of-the-art *ab initio* and DFT methods to study the energetics and the reaction mechanisms of atmospherically important reactions.
2. To investigate the effects of computed barrier heights, imaginary vibrational frequencies on computed tunneling contributions and shapes of ΔG curves obtained at different levels of theory on the computed rate coefficients.
3. To establish a reliable and practical method to obtain reliable rate coefficients of gas phase reactions with small or negative barrier in an *ab initio* manner.

1.3 Thesis Outline

This thesis is organized as follows. Quantum chemical methods and basis sets employed in this thesis and the algorithm of reaction path are reviewed in chapter 2. Chapter 3 is devoted to discussing theoretical chemical kinetics, in which various levels of the TST and the VTST are reviewed in the perspective of dynamical systems. In

chapter 4, a theoretical study in the reaction kinetic and energetics of the $CH_3C(O)OCH_3$ + Cl $\rightarrow$ $CH_3C(O)OCH_2$ + HCl reaction is presented. In chapter 5, another theoretical study in the reaction kinetics and energetics of the BrO + HO_2 reaction is presented. Finally, the conclusions of main findings in this thesis are summarized in chapter 6.

1.4 References

1. Cox, R. A. *Chem. Rev.* **2003**, 103, 4533-4548.
2. Chapman, S. *Mem. R. Meteorol. Soc.* **1930**, 3, 103.
3. Wiersma, G. B.; Frank, C. W.; Case, M. J.; Crockett, A. *B. Environmental Monitoring and Assessment* **1984**, 4, 233-255.
4. Finlayson-Pitts, B. J.; Pitts, J. N., Jr. Chemistry of the upper and lower atmosphere; Academic press, 2000.
5. Friesner, R. A. *PNAS* **2005**, 102, 6648-6653.
6. Franciso, J. S.; Muckerman, J. T.; Yu, H-G. *Acc. Chem. Res.* **2010**, 43, 1519-1526.
7. Miller, J. A.; Klippenstein, S. J.; Truhlar, D. G. *Chem. Rev.* **2006**, 106, 4518-4584.
8. Bartlett, R. J.; Grabowski, I.; Hirata, S.; Ivanov, S. *J. Chem. Phys.* **2005**, 122, 034104.
9. Raghavachari, K.; Pople, J. A.; Replogle, E. S.; Head-Gordon, M. *J. Phys. Chem.* **1990**, 94, 5579.
10. Cohen, A. J.; Mori-Sanchez, P.; Yang, W. *Chem. Rev.* **2012**, 112, 289-320.
11. Lee, T. J.; Kobayashi, R.; Handy, N. C.; Amos, R. D. *J. Chem. Phys.* **1992**, 96, 8931.
12. Klopper, W.; Bak, K. L.; Jorgensen, P.; Olsen, J.; Helgaker, T. *J. Phys. B: At. Mol. Opt. Phys.* **1999**, 32, R103-R130.
13. Christensen, L. K.; Ball, J. C.; Wallington, T. J. Atmospheric Oxidation Mechanism of Methyl Acetate *J. Phys. Chem. A* **2000**, 104, 345– 351.
14. De Haan, D. O.; Brauers, T.; Oum, K.; Stutz, J.; Nordmeyer, T.; Finlayson-Pitts, B. Heterogeneous Chemistry in the Troposphere: Experimental Approaches and Applications to the Chemistry of Sea Salt Particles *J Int. Rev. Phys. Chem*. **1999**, 18, 343– 385.
15. Cuevas, C. A.; Notariob, A.; Martineza, E.; Albaladejo, J. Influence of Temperature in the Kinetics of the Gas-phase Reactions of a series of Acetates with Cl atoms *Atmospheric Environment* **2005**, *39*, 5091-5099.
16. Laider, K. J.; King, M. C. *J. Phys. Chem.* **1983**, 87, 2657-2664.
17. Atkinson, R; Baulch, D . L.; Cox, R. A.; Crowley, J.N.; Hampson, J.N. et al. Evaluated kinetic and photochemical data for atmospheric chemistry Vol III Gas-phase reactions of inorganic halogens. *Atmos. Chem. Phys.* **2007**, 7, 981-1191.
18. Larichev, M.; Maguin, F.; Le Bras, G.; Poulet, G. *J. Phys. Chem*. **1995**, 99, 15911–15918.

19. Miller, W. H. Unified statistical model for "complex" and "direct" reaction mechanisms. *J. Chem. Phys* **1976**, 65, 2216-2223.

Chapter 2.

Quantum Chemistry

The major theme of this thesis revolves around the calculations of rate coefficients of gas phase reactions. The knowledge of the potential energy surface (PES) of the reaction system is required for the subsequent rate coefficient calculations. The PES can be obtained by solving the Schrodinger equation to obtain the electronic energy by repeating that at a number of nuclear coordinates. Several approximations are required to obtain an approximate solution to the Schrodinger equation, which are discussed in detail in this chapter. In the following, the state-of-the-art quantum chemical methods for computing electronic energy, and hence, the potential energy surface are reviewed in this chapter.

2.1 Many-body Schrodinger Equation

The above properties of molecules can be obtained by solving the time independent Schrodinger equation:

$$\hat{H}\,\Psi = E\,\Psi \tag{2.1}$$

where Ψ is the many-body wavefunction, E is the energy and $\hat{H}$ is the Hamiltonian operator which is for a system containing M nuclei and N electrons:

$$\hat{H} = -\sum_{i=1}^{M}\frac{\hbar^2}{2M_A}\nabla_A^2 - \sum_{i=1}^{N}\frac{\hbar^2}{2m_e}\nabla_i^2 - \sum_{i=1}^{N}\sum_{A=1}^{M}\frac{k_e e^2 Z_A}{r_{iA}} + \sum_{i=1}^{N}\sum_{j>i}^{N}\frac{k_e e^2}{r_{ij}} + \sum_{A=1}^{M}\sum_{B>A}^{M}\frac{k_e e^2 Z_A Z_B}{R_{AB}} \tag{2.2}$$

where $\hbar$ is the Planck constant (h) divided by 2π, m_e is the mass of an electron, M_A is the mass of the nucleus, k_e is the Coulomb's constant, e is the elementary charge, Z_A is an atomic number, r_{ij} is the distance between electrons i and j and ∇_i^2 is the Laplacian

operator which is the second partial derivative with respective to the position when the positions of the atoms are in Cartesian coordinate, in this case the Laplacian operator is expressed as:

$$\nabla_i^2 = \frac{\partial^2}{\partial x_i^2} + \frac{\partial^2}{\partial y_i^2} + \frac{\partial^2}{\partial z_i^2} \tag{2.3}$$

In equation (2.2), the first two terms are the kinetic energy operators of the nuclei and the electron respectively; the third term is the electrostatic attraction between the electron and the nuclei; the last two terms are the repulsion between electrons and the nuclei, respectively. The energy of a system with the given orthonormal many-body wavefunction (Ψ) in space (τ) is given by:

$$E = \int \Psi^* \hat{H} \Psi \, d\tau = \langle \Psi | \hat{H} | \Psi \rangle \tag{2.4}$$

where $\hat{H}$ is the Hamiltonian operator, $|\Psi\rangle$ and $\langle \Psi^* |$ are the wavefunction and its complex conjugate in Dirac's bra-ket notation, respectively. Basically, there is no analytical solution for the many-body Schrodinger equation unless there are only two or three particles in the molecular system (such as H_2^+). In order to obtain the energy of the many-body system, approximations must be made, and the first simplification is the Born-Oppenheimer approximation [1]. It assumes that the nuclei are stationary since they are much heavier than electrons. With this approximation, the motions of electrons and the nuclei are decoupled and the total Schrodinger equation becomes two equations, one for the nuclei and another one for the electrons with the position of nuclei kept fixed in the electronic Schrodinger equation. The kinetic energy operator of the nuclei is excluded and the nuclear-nuclear Coulomb repulsion is a constant at a particular location of the nuclei. The eigenvalue of the electronic Schrodinger equation is the energy (E_e) of the system without the kinetic energy of the nuclei. Upon solving the electronic Schrodinger equation with a number of nuclear positions, the potential energy surface of the molecular system can be obtained. The nuclear Schrodinger equation is describing the motions of the nuclei in the potential energy function.

2.2 Hartree-Fock Theory

Electrons are fermions which mean that the wavefunctions would be anti-symmetric upon exchange of particles. Because of this, electrons in the system cannot have the same set of quantum numbers, as described in the Pauli Exclusion Principle. In order to solve the Schrodinger equation, the dynamical correlation between electrons in a molecule is ignored. Thus, the independent-particle model is employed which assumes the motion of an electron is independent of the motion of the rest of the electrons.

The simplest many-body wavefunction under the above constraints and the method for obtaining the ground-state wavefunction and corresponding energy is the Hartree-Fock theory [2]. The Hartree-Fock theory can be considered as an approximation of the many-body Schrodinger wavefunction. It assumes that each particle moves in a mean field which is created by other particles and it also neglects electron correlation.

Thus, the one-particle wavefuntion ($\chi(x, y, z, \omega)$) for an electron is known as a spin orbital, which is a product of a molecular orbital ($\psi(x, y, z)$) and a spin function, $\alpha(\omega)$ or $\beta(\omega)$. The molecular orbital is a one-electron spatial function and is known as the spatial part of the spin orbital. In the spin function, ω is the spin coordinate, $\alpha(\omega)$ represents the spin-up state while $\beta(\omega)$ represents the spin-down state of an electron.

Since the electrons only interact with a mean field, the total wavefunction for a *n*-electron system can be expressed as products of *n* spin orbitals:

$$\Psi_{n-particle} = \chi_1(1)\chi_2(2)\cdots\chi_n(n) \tag{2.5}$$

where $\chi_j(j)$ represents $\chi(x_j, y_j, z_j, \omega_j)$ which denotes the spin orbital of electron *j*. In order to satisfy the anti-symmetric requirements of the wavefunctions of electrons, the wavefunctions used in Hartree-Fock theory are formulated in determinants, which are known as Slater determinants [3]. For a Slater determinant which describes *n* electrons, it is expressed as:

$$\Phi_{SD} = \frac{1}{\sqrt{n!}}\begin{vmatrix} \chi_1(\mathbf{1}) & \chi_2(\mathbf{1}) & \dots & \chi_n(\mathbf{n}) \\ \chi_1(\mathbf{2}) & \chi_2(\mathbf{2}) & \dots & \chi_n(\mathbf{n}) \\ \vdots & \vdots & \ddots & \vdots \\ \chi_1(\mathbf{n}) & \chi_2(\mathbf{n}) & \cdots & \chi_n(\mathbf{n}) \end{vmatrix} \tag{2.6}$$

where Φ_{SD} is Slater determinant. In general, the molecular orbitals are orthonormal. Then the energy of Slater determinant is calculated with the electronic Hamiltonian operator (H_{el}) as

$$E_{SD} = \int \Phi_{SD} \hat{H}_{el} \Phi_{SD} \, d\tau = \langle \Phi_{SD} | \hat{H}_{el} | \Phi_{SD} \rangle \tag{2.7}$$

Since electron repulsion is replaced by electron interactions with a mean field in Hartree-Fock theory, the electronic Hamiltonian operator can then be reduced to *n* one-electron operators known as Fock operator which is defined as:

$$\hat{F}_i = \hat{h}_i + \sum_{\mu} \sum_{\nu} P_{\lambda\sigma} \left(\hat{J}_{\mu\nu} - \frac{1}{2} \hat{K}_{\mu\nu} \right) \tag{2.8}$$

where

$$\hat{h}_i = -\frac{1}{2} \nabla_i^2 - \sum_A \frac{Z_A}{r_{iA}} \tag{2.9}$$

$$\hat{J}_{\mu\nu} = \int \int \psi_\mu(r_1) \, \psi_\nu(r_1) \frac{1}{r_{12}} \psi_\lambda(r_2) \psi_\sigma(r_2) \, dr_1 \, dr_2 \tag{2.10}$$

$$\hat{K}_{\mu\nu} = \int \int \psi_\mu(r_1) \; \psi_\lambda(r_1) \frac{1}{r_{12}} \psi_v(r_2) \psi_\sigma(r_2) \, dr_1 \, dr_2 \tag{2.11}$$

$$P_{\lambda\sigma} = 2 \sum_i c_{i\lambda}{}^* c_{i\sigma} \tag{2.12}$$

where $\hat{F}_i$ is the Fock operator, $P_{\lambda\sigma}$ is the density matrix and its diagonal elements give the probability of an electron in a certain orbital, $\hat{h}_i$ is the exact one-electron operator which contains the kinetic energy operator and the electron-nucleus potential energy operator. $\hat{J}_{\mu\nu}$ is the Coulomb operator in which represents the electron-electron repulsion term. $\hat{K}_{\mu\nu}$ is the exchange operator which is the electron exchange energy arises from the anti-symmetry of the wavefunction and it is essentially a consequence of using Slater determinants as the trial wavefunction in Hartree-Fock theory.

A drawback of using the mean-field approximation is that unphysical self-interaction of electron may arise. Fortunately, this unphysical result is cancelled with $\widehat{K}_{\mu\nu}$ [5] where $\widehat{K}_{\mu\nu}$ is the exchange operator. Then the Hartree-Fock energy is calculated as equation (2.7) with the Fock operator instead of the electronic Hamiltonian operator.

The Schrodinger equation can be solved by the Lagrange's multiplier method where λ_i is the Lagrange multiplier with the constraint of orthonormal molecular-orbitals as:

$$\frac{\delta E}{\delta \phi_i} = \frac{\delta}{\delta \phi_i}\left(\langle \Psi | \hat{F} | \Psi \rangle - \sum_i \lambda_i \langle \phi_i | \phi_i \rangle \right) = 0 \tag{2.13}$$

The results would be a set of the Hartree-Fock equations

$$\widehat{F}_i \Phi_{\mathrm{SD}} = \varepsilon_i \Phi_{\mathrm{SD}} \tag{2.14}$$

where ε_i has the physical meaning of orbital energy. Due to its high dimensionality, the best way of solving it involves the expansion of molecular orbitals as the linear combination of atomic orbitals [6]. Variational principle makes solving the Hartree-Fock equations possible, so it is briefly introduced in the next section.

2.2.1 Variational Principle

In order to obtain the approximate ground state of systems, the variational principle is employed, which gives the upper bound for the true ground state energy. Given the Slater determinants (Φ_{SD}), the expectation value (E) is evaluated by using the Hamiltonian operator ($\widehat{H}$) and integrating over space in the spherical coordinates (τ):

$$E = \int \Phi^* \widehat{H} \Phi \, d\tau \tag{2.15}$$

Φ would give the exact ground-state energy if it was the exact wavefunction (Ψ). In this scenario, Φ is a trial wavefunction. Upon the evaluation of equation (2.15), the resulting energy is always greater than the exact energy.

$$E > E_{exact} = \int \Psi^* \widehat{H} \Psi \, d\tau \tag{2.16}$$

The molecular orbital (ψ_i) plays the role of Φ in equation (2.15) and it may be expressed as the linear combination of any basis functions (ϕ_μ), in mathematical form:

$$\psi_i = \sum_i c_{i\mu}\phi_\mu \tag{2.17}$$

where c_i are the expansion coefficients. Then the energy computed with the molecular orbital (denoted as $E_{trial}[c_i]$) is given by:

$$E_{trial}[c_i] = \langle \Psi_i | \hat{H} | \Psi_i \rangle > E_{true} \tag{2.18}$$

$E_{trial}[c_i]$ is higher than the true ground state energy. Thus, the lower the $E_{trial}[c_i]$ value, the closer it is to the true energy. Therefore, the best choice of the wavefunction and correspond ground-state energy are obtained by minimizing energy with respect to the molecular orbital coefficients ($c_{i\mu}$). Mathematically, this is done by:

$$\frac{\partial E_{trial}}{\partial c_{i\mu}} = 0 \tag{2.19}$$

The variational principle is also employed in configuration interaction and density functional theory, which will be discussed in sections 2.4.1 and 2.5, respectively.

2.2.2 Hartree-Roothaan-Hall equation

Using the variational principle, the integro-differential equations for molecular orbitals can be reduced to a matrix eigenvalue problem of calculating the expansion coefficients known as the Hartree-Roothaan-Hall equation [7]:

$$\boldsymbol{FC} = \boldsymbol{SC}\varepsilon \tag{2.20}$$

where $\boldsymbol{F}$ is the Fock operator, $\boldsymbol{C}$ is the coefficients matrix, ε is the orbital energy and $\boldsymbol{S}$ is the overlapped integral calculated as:

$$\boldsymbol{S} = \int \phi_\mu^* \phi_\nu \, dx \, dy \, dz \tag{2.21}$$

Since the Fock operator depends on the coefficient in the density matrix non-linearly in Roothaan-Hall equation, the most effective way is to solve it by an iterative method known as self-consistent field (SCF) theory [8]. It involves the calculation of the charge density as:

$$\rho(r) = \sum_{\mu}^{n} \sum_{v}^{n} P_{\mu\nu}\, \phi_{\mu} \phi_{v} \tag{2.22}$$

where n is the total number of electrons.

Equation (2.20) is solved in order to obtain the Hartree-Fock wavefunction and the corresponding ground-state energy.

2.2.3 Restricted Hartree-Fock and Unrestricted Hartree-Fock

The previous discussion on the Fock operator is applicable to closed-shell systems only, which are systems of doubly occupied spatial orbitals (i.e. each orbital is occupied by an α (spin-up) electron and a β (spin-down) electron), as shown in Figure 2.1. For such arrangement of electrons, it is known as restricted Hartree-Fock method, abbreviated as the RHF method, and it works very well for closed-shell systems. Their spin-multiplicity of the electronic wavefunctions is 1. In the RHF method, its wavefunction is an eigenfunction of the total spin operator S^2. Moreover, the spin orbitals of paired electrons in a spatial orbital in the RHF method have the same spatial parts.

However, for molecules or atoms with open-shell states, the RHF method is not applicable but there are two different formalisms to cope with the open-shell situations, namely the restricted open-shell Hartree-Fock (ROHF) formalism and the unrestricted Hartree-Fock (UHF) formalism.

The ROHF formalism, as an extension of the RHF formalism, restricts that the spatial parts to be the same for the α and β spin functions but it also uses half-filled orbitals for the unpaired electrons, as shown in Figure 2.1. Similar to the RHF wavefunction, the ROHF wavenfunction remains as an eigenfunction of the total spin operator S^2, as in the RHF method. The ROHF wavefunction is constructed by using Slater determinants composing of closed-shell subsets (doubly occupied spatial orbitals) and open-shell subsets (singly filled orbitals). However, there are some open-shell states which can only be described by using multi-determinants in the ROHF wavefunction.

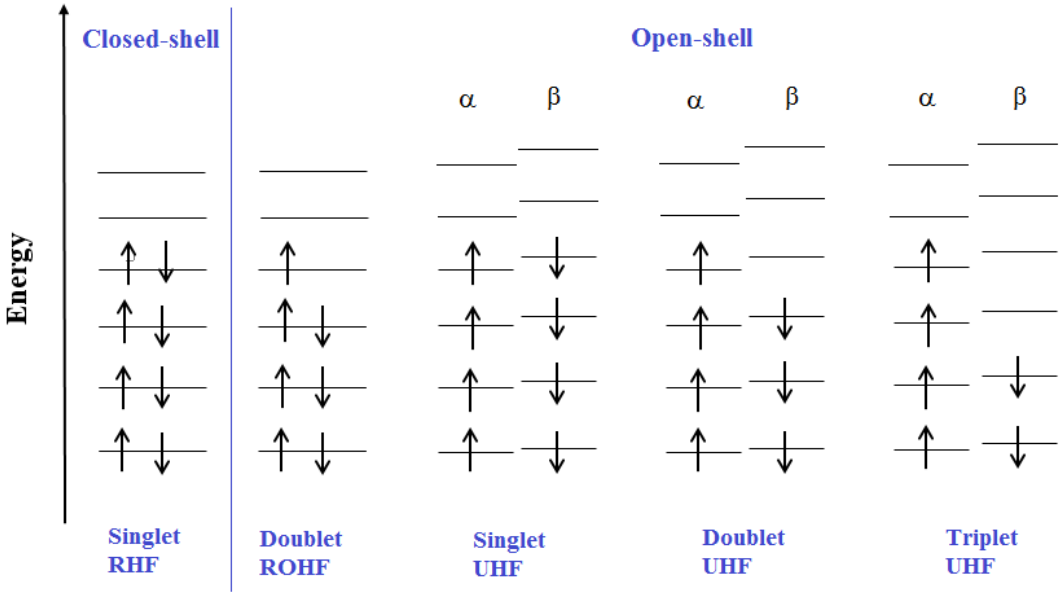

Figure 2.1 Illustrating the RHF and the UHF singlet states, and the ROHF and the UHF doublet states and the UHF triplet state.

The UHF formalism, on the other hand, does not restrict the spatial wavefunction of α and β electrons to be the same. In the UHF formalism, the spatial part of the α electrons can be different from that of the β electrons, leading to two sets of spatial orbitals equations which results in different molecular orbital coefficients as number of electrons in the two equations may not be the same:

$$\psi_i^{\alpha} = \sum_i c_{i\mu}^{\alpha}\phi_{\mu}\,;\ \psi_i^{\beta} = \sum_i c_{i\mu}^{\beta}\phi_{\mu} \tag{2.23}$$

Two Fock matrices can then be set up in order to produce two sets of orbitals with the Fock operators defined as:

$$\hat{F}_i^{\alpha} = h_i + \sum_{\lambda\sigma}\left[\left(P_{\lambda\sigma}^{\alpha} + P_{\lambda\sigma}^{\beta}\right)\left\langle\psi_{\mu}\psi_{\nu}\middle|\psi_{\lambda}\psi_{\sigma}\right\rangle - P_{\lambda\sigma}^{\alpha}\left\langle\psi_{\mu}\psi_{\lambda}\middle|\psi_{\nu}\psi_{\sigma}\right\rangle\right] \tag{2.24}$$

$$\hat{F}_i^{\beta} = h_i + \sum_{\lambda\sigma}\left[\left(P_{\lambda\sigma}^{\alpha} + P_{\lambda\sigma}^{\beta}\right)\left\langle\psi_{\mu}\psi_{\nu}\middle|\psi_{\lambda}\psi_{\sigma}\right\rangle - P_{\lambda\sigma}^{\beta}\left\langle\psi_{\mu}\psi_{\lambda}\middle|\psi_{\nu}\psi_{\sigma}\right\rangle\right] \tag{2.25}$$

By substituting the two spin-specific Fock operators into the unrestricted version of Roothaan-Hall equations, Pople-Nesbet equations [9] are obtained as

$$\boldsymbol{F}^{\alpha}\boldsymbol{C}^{\alpha} = \boldsymbol{S}\boldsymbol{C}^{\alpha}\varepsilon^{\alpha};\ \boldsymbol{F}^{\beta}\boldsymbol{C}^{\beta} = \boldsymbol{S}\boldsymbol{C}^{\beta}\varepsilon^{\beta} \tag{2.26}$$

The two Pople-Nesbet equations are coupled together because the Coulomb operator in the two spin-specific operators are the same while the exchange operator is different (spin-specific). Finally, by solving the Pople-Nesbet equations, two different sets of molecular orbitals with corresponding energies are obtained. Since the spatial parts of the UHF wavefunctions are different, the resulting wavefunction does not only describe the ground state but it also contains some contributions from high spin states which is known as spin contamination. The UHF wavefunctions are not eigenfunctions of the square of the spin operators (S^2), which means that $\langle S^2 \rangle \neq S(S+1)$. If the spin contamination is severe (the difference between $\langle S^2 \rangle$ and $S(S+1)$ is larger than 10% [10]), the resulting energy is not accurate.

For closed-shell singlet molecules at equilibrium geometries, both the RHF and the UHF wavefunctions are nearly identical and they give the same electronic energy. For such cases, the RHF wavefunction is used because the RHF wavefunction gives an accurate description of the orbitals (two electrons in a spatial orbital) and its calculation requires less CPU time than that of the UHF wavefunction. The paired electrons constraint in the RHF formalism does not permit RHF wavefunction to describe the dissociation process correctly. In the dissociation of H_2, as the bond length between two hydrogen atoms increases, the RHF wavefunction remains as a closed-shell description, so it will yield H^+ and H^- instead of two hydrogen atoms. However, the UHF wavefunction can give a qualitatively accurate description of the dissociation of H_2 to form two hydrogen atoms because it allows electrons of different spin to have their own spatial orbitals. Although the ROHF formalism can yield a realistic description of open-shell molecules (two electrons in a spatial orbital) and accurate total spin of the molecules of open-shell states, its implementation is much more complicated than that of the UHF formalism because it actually requires multi-determinants (therefore multi-reference) in order to achieve the correct description. The UHF formalism, on the other hand, contains actually two sets of spatial orbitals, which are like providing two sets of determinants for the description of the open-shell states. Therefore, the UHF formalism is an approximation to the ROHF formalism for open-shell molecules. Given the advantages

of UHF formalism, it will be used in the optimization of open-shell singlet species in Chapter 5.

2.3 Electron Correlation

The Hartree-Fock method accounts for about 99% of total electronic energy (E_{exact}) when a sufficiently large basis set is employed [11]. The remaining 1% is known as correlation energy (E_{corr}). It can be defined as:

$$E_{corr} = E_{exact} - E_{HF} \tag{2.27}$$

The total electronic energy is a large number and it increases as the number of electrons in an atom increases, so the remaining 1% of energy would still be very significant. Thus, the correlation energy needs to be properly accounted in order to obtain reliable electronic energy. There are two types of electron correlation, namely dynamical correlation and non-dynamical correlation. Dynamical correlation refers to the instantaneous correlation of electron movements due to Coulombic repulsion, which is ignored in the Hartree-Fock theory. On the other hand, static correlation refers to systems which actually require two or more determinants to represent the total wavefunctions, such scenarios include bond dissociation, excited states and molecules of near-degenerate effect. For bond dissociation processes, as discussed in the section 2.2.3, the RHF wavefunction assumes single determinant so it cannot yield correct description. The ROHF and the UHF wavefunctions can correctly describe the bond dissociation processes because they make use of two or more references (i.e. determinants). For some excited state species, such as open-shell singlet O_2 ($\tilde{a}^1\Delta_g$), which require more than 1 determinant in order to obtain a correct description of the electronic structures. Near-degenerate effect arises when some of the valence molecular orbitals are near degenerate. Therefore, more than one determinants are required to describe the electron configurations accurately because none of the determinants is dominant in the total wavefunction. For such cases, multi-reference *ab initio* methods are required to obtain reliable electronic energies.

2.4 Post-Hartree-Fock Methods

Up to this point, only the occupied molecular orbitals are introduced as they are optimized in Hartree-Fock theory as the Fock operator only depends on the occupied orbitals but not the virtual orbitals. Improvements on Hartree-Fock theory are known as post-Hartree-Fock methods and they include configuration interaction [12], Møller-Plesset perturbation theory [13] and coupled-cluster theory [14]. All of them make use of virtual orbitals for improving the Hartree-Fock energy.

2.4.1 Configuration Interaction (CI)

One way to improve the Hartree-Fock energy is to include more Slater determinants. The variation principle states that the wavefunction that gives the lowest energy is the best estimate of the exact wavefunction. Including more determinants will make the wavefunction more flexible and able to capture some of the correlation energy. Consequently, Slater determinants describing the electronic configuration of excited states can be included into the Hartree-Fock wavefunction to form the configuration interaction [12] wavefunction. Theoretically, all possible configurations of a molecular system can be included and this leads to the full configuration interaction wavefunction. Technically, the full CI (FCI) wavefunction can be expressed as:

$$\Psi_{FCI} = a_0 \Phi_{HF} + \sum_S a_S \Phi_S + \sum_D a_D \Phi_D + \sum_T a_T \Phi_T + \cdots \tag{2.28}$$

$$= a_0 \Phi_{HF} + \sum_{i=1} a_i \Phi_i$$

where a_i is the CI coefficients and the subscripts, *S*, *D*, *T* are denoted as single excitation, double excitation and triple excitation respectively. In reality, full CI is rarely used to compute the electronic energies of large molecular systems. A more feasible way is to compute the electronic energy of a molecular system with truncated configuration interaction. For example, if equation (2.28) is truncated after the second term, configuration interaction single excitation (CIS) wavefunction is obtained. A more commonly used truncated CI is configuration interaction single double (CISD), in which equation (2.28) is truncated after the third term. The CI coefficients (i.e. a_S, a_D, a_T in equation (2.28) are then varied to give lowest CI energy. In the CI method, the Fock

matrix is then replaced by CI matrix in which the CI energies are obtained from the diagonalization of the CI matrix.

2.4.2 Coupled-Cluster Theory

Another prevalent post-Hartree-Fock method is coupled-cluster (CC) theory [16]. CC is analogous to the CI method in which the excitation of electrons from occupied orbitals to virtual orbitals and it is used to account for electron correlation. It is closely related to the CI theory by the fact that full coupled-cluster and full CI both lead to the exact energy of a reaction system in a given basis set with finite size. The exponential ansatz is used in coupled-cluster theory to describe the wavefunction of the ground state ($|\Psi_{CC}\rangle$). Mathematically, it is expressed as:

$$|\Psi_{CC}\rangle = e^{\hat{T}}|\Phi_{HF}\rangle \tag{2.29}$$

where $\hat{T}$ is the cluster operator which excites electron to virtual orbitals. The exponential operator can then be expanded as power series:

$$e^{\hat{T}} = 1 + \hat{T} + \frac{\hat{T}^2}{2!} + \frac{\hat{T}^3}{3!} + \frac{\hat{T}^4}{4!} + \cdots \tag{2.30}$$

Furthermore, the cluster operator, $\hat{T}$, can also be expanded:

$$\hat{T} = \hat{T}_1 + \hat{T}_2 + \hat{T}_3 + \hat{T}_4 + \cdots \tag{2.31}$$

where $\hat{T}_1$ is the single excitation operator, $\hat{T}_2$ is the double excitation operator, and so on and so forth. If we truncate equation (2.31) to the first two terms, the following equation results:

$$e^{\hat{T}} = 1 + \hat{T}_1 + \hat{T}_2 + \frac{\hat{T}_1^{\,2}}{2} + \hat{T}_1\hat{T}_2 + \frac{\hat{T}_2^{\,2}}{2} \ldots \tag{2.32}$$

Through the power series expansion of the exponential of the cluster operator, many excitations of Slater determinants can be generated. Similar to the CI method, the power series can also be truncated as well. In equation (2.31), if only single and double excitations are considered and this implementation is known as coupled-cluster single

double, abbreviated as CCSD [17]. A popular approach for obtaining reliable electronic energy is CCSD(T) [18], which means that the single and double excitations are treated by CC methods while triple excitation is treated by perturbation theory. For CCSD, 95% of correlation energy for molecules at their equilibrium geometries can be recovered [19]. With CCSD(T), 99% of the correlation energy can be recovered [19], so CCSD(T) very often serves as a golden standard in the field of computational chemistry [20]. Although coupled-cluster theory brings high accuracy, their computational costs are also high.

2.4.3 Explicitly Correlated Methods

Due to the use of Slater determinants in the Hartree-Fock wavefunctions, slow convergence of correlation energy with respect to the size of basis sets results. Slater determinants are built from one-electron orbital, consequently electron correlation due to Coulomb repulsion between two electrons (Coulomb hole) cannot be described properly. Therefore, the electron-electron cusp condition of the actual wavefunction (a point of discontinuity given by the first derivative of the wavefunction at $r_{12} = 0$ where r_{12} is the inter-electronic distance), which is significant when the r_{12} is very small (i.e. $r_{12} \rightarrow 0$), cannot be described by the Hartree-Fock wavefunction. For a very small value of r_{12}, the wavefunction is proportional to r_{12} linearly. By incorporating the r_{12} term in the wavefunction, the cusp condition can be met and the convergence can be accelerated [21, 22]. This technique is known as R12 method [23]. More generally, for methods including the r_{12} term in the wavefunction, they are known as explicitly correlated methods. In 2009, an improved implementation of R12 method is devised and it is known as F12 method. In F12 method [24], the r_{12} term is incorporated in a wavefunction in form of a Slater function (i.e. $\exp(-\alpha r_{12})$) which resembles a Slater orbital and it can speed up basis set convergence and improves numerical stability. It is now implemented along with CCSD(T) as CCSD(T)-F12 theory [25].

There are two available approximations to CCSD(T)-F12 to reduce the computational costs, which are CCSD(T)-F12a and CCSD(T)-F12b [26]. CCSD(T)-F12a tends to overestimate the correlation energies whereas CCSD(T)-F12b tends to underestimate them [27]. Moreover, CCSD(T)-F12a is found to yield good results for small basis sets (AVDZ and AVTZ) but the quality of CCSD(T)-F12a results deteriorates the size of the basis sets expand. On the contrary, CCSD(T)-F12b has a good performance for large basis sets [27].

2.4.4 Brueckner's Theory

The Hartree-Fock orbital is a good starting point but they are not necessary to be the best choice of orbitals since the correlation effect is not considered in the Hartree-Fock orbital. Brueckner orbital [28] is another type of orbital which is better than the Hartree-Fock orbital because it obeys Brillouin's theorem. Brillouin's theorem states the wavefunction obtained by single excitation is orthonormal to the exact reference wavefunction, i.e.

$$\langle \Phi_S | \hat{H} | \Psi_{exact} \rangle = 0 \tag{2.33}$$

Brueckner orbitals (BO) are obtained at Brueckner's condition:

$$\langle \Phi_B | \Psi_{exact} \rangle = max \tag{2.34}$$

The overlap between the Brueckner determinant (Φ_B) and the exact wavefunction (Ψ_{exact}) is maximum. As a result of the Brueckner condition, the singly excitation coefficient is 0 ($a_s = 0$).

In order to construct the BO, the easiest way is to start with the full CI wavefunction because it is the exact wavefunction. However, obtaining the full CI wavefunction is not feasible practically so only approximate BO can be constructed and the process starts with truncated CI wavefunction or truncated CC wavefunction. The single excitation determinant is then optimized by rotating the single excitation determinant until it is orthonormal to the ground state wavefunction in order to satisfy equation (2.34) [27], so this is an iterative process.

For molecules with moderate non-dynamical correlation where CCSD(T) may not be applicable due to large T_1 value, the Brueckner double with perturbative triple excitations (BD(T)) serves as a remedy because its single excitation coefficient is exactly 0.

2.4.5 Møller-Plesset Perturbation Theory

Møller-Plesset perturbation theory (MP*n*) [13] is a post-Hartree-Fock method to account for electron correlation by using perturbation theory [29]. Perturbation theory was originally developed as a technique to solve the Schrodinger equation with complicated potential, which can be considered as a sum of simple potential functions. Then the complicated potential can be solved by adding an additional term (which is usually to be small). For an unperturbed system, its Schrodinger equation is:

$$\hat{H}^{(0)}\,\Psi^{(0)} = E^{(0)}\,\Psi^{(0)} \tag{2.35}$$

where $E^{(0)}$, $\hat{H}^{(0)}$, $\Psi_i^{(0)}$ are the energy, Hamiltonian and wavefunction of the unperturbed system respectively. If the perturbation (λ) is small, the perturbed Hamiltonian operator ($\hat{H}$) can be split into two parts:

$$\hat{H} = \hat{H}^{(0)} + \lambda\hat{H}' \tag{2.36}$$

where $\hat{H}^{(0)}$ is the unperturbed Hamiltonian operator, and $\hat{H}'$ is perturbing operator.

Møller and Plesset considered the interactions between electrons in the many-body Schrodinger equation as a perturbation problem in which the Hamiltonian is perturbed by the correlation potential, and this approach is known as Møller-Plesset perturbation theory. In MP*n*, the unperturbed Hamiltonian, perturbing operator, and the wavefunction in Schrodinger equation are replaced by the sum of all Fock operators, correlation potential, Hartree-Fock wavefunction, respectively [14].

For small λ, both the ground-state energy and the Hatree-Fock wavefunction can be expanded in power series:

$$E = E^0 + \lambda E^{(1)} + \lambda^2 E^{(2)} + \cdots \tag{2.37}$$

$$|\Psi\rangle = |\Psi^{(0)}\rangle + \lambda|\Psi^{(1)}\rangle + \lambda^2|\Psi^{(2)}\rangle + \cdots \tag{2.38}$$

where the numbers in the superscript of energy and wavefunction represents the *n-th* order of perturbation. By substituting the equations (2.37) and (2.38) into the Schrodinger Equation, and sorting the terms of the power of λ, one can arrive at the infinite series of equations:

$$\hat{H}^{(0)}\left|\Psi^{(0)}\right\rangle = E_i{}^{(0)}\left|\Psi^{(0)}\right\rangle \tag{2.39}$$

$$\hat{H}^{(0)}\left|\Psi^{(1)}\right\rangle + \hat{H'}\left|\Psi^{(0)}\right\rangle = E_i{}^{(0)}\left|\Psi^{(1)}\right\rangle + E_i{}^{(1)}\left|\Psi^{(0)}\right\rangle \tag{2.40}$$

$$\hat{H}^{(0)}\left|\Psi^{(2)}\right\rangle + \hat{H'}\left|\Psi^{(1)}\right\rangle = E_i{}^{(0)}\left|\Psi^{(2)} + E_i{}^{(1)}\right|\Psi^{(1)}\rangle + E_i{}^{(2)}\left|\Psi^{(0)}\right\rangle \tag{2.41}$$

...

The zeroth order wavefunction is just the Hartree-Fock wavefunction:

$$E^{(0)} = \left\langle \Psi^{(0)}\middle|\hat{H}^{(0)}\middle|\Psi^{(0)}\right\rangle \tag{2.42}$$

where $\hat{H}^{(0)}$ is the Fock operator. The energy expressions at the various levels of perturbations are expressed as:

$$E^{(1)} = \left\langle \Psi^{(0)}\middle|\hat{V}\middle|\Psi^{(0)}\right\rangle \tag{2.43}$$

$$E^{(2)} = \left\langle \Psi^{(0)}\middle|\hat{V}\middle|\Psi^{(1)}\right\rangle \tag{2.44}$$

...

where $\Psi^{(n)}$ is the *n*-order perturbed wavefunction and $\hat{V}$ is the correlation potential. Equations (2.42) – (2.44) can then be used to rewrite the Hartree-Fock energy as:

$$\begin{aligned} E^{HF} &= \left\langle \Psi^{(0)}\middle|\hat{H}\middle|\Psi^{(0)}\right\rangle \\ &= \left\langle \Psi_i^{(0)}\middle|\hat{H}^{(0)} + \hat{V}\middle|\Psi_i^{(0)}\right\rangle \\ &= \left\langle \Psi^{(0)}\middle|\hat{H}^{(0)}\middle|\Psi^{(0)}\right\rangle + \left\langle \Psi^{(0)}\middle|\hat{V}\middle|\Psi^{(0)}\right\rangle \\ &= E^{(0)} + E^{(1)} \end{aligned} \tag{2.45}$$

According to equation (2.45), the Hartree-Fock energy can actually be obtained from the first-order of Moller-Plesset perturbation theory (MP1). Therefore, the second-order of Moller-Plesset perturbation theory (MP2) is necessary for accounting for the electron-electron correlation where the second-order correction of energy is given by:

$$E^{(2)} = \sum_{i}^{occ}\sum_{j>i}^{occ}\sum_{a}^{vir}\sum_{b>a}^{vir}\frac{(\langle ij|ab\rangle - \langle ia|jb\rangle)^2}{\varepsilon_i + \varepsilon_j - \varepsilon_a - \varepsilon_b} \quad (2.46)$$

where *i* and *j* are the occupied orbitals, *a* and *b* are unoccupied (virtual) orbitals, and ε_x (where *x*= *a, b, i* and *j*) are the corresponding orbital energies. Therefore, the electronic energy with MP2 correction is then given by:

$$E^{HF+MP2} = E^{(0)} + E^{(1)} + E^{(2)} \quad (2.47)$$

Ideally one could use higher order of perturbation theory (e.g. MP3 and MP4) to account for the electron correlation effect but this is not practical due to high computational costs. Thus, MP2 is commonly used for small systems. It approximately includes 80% - 90% of the correlation energy [30] and its computational cost is less than coupled-cluster theory and CI. A major disadvantage of perturbation theory is that it is not variational so the computed MP*n* energies may exhibit oscillating behavior [31] as shown in Figure 2.2.

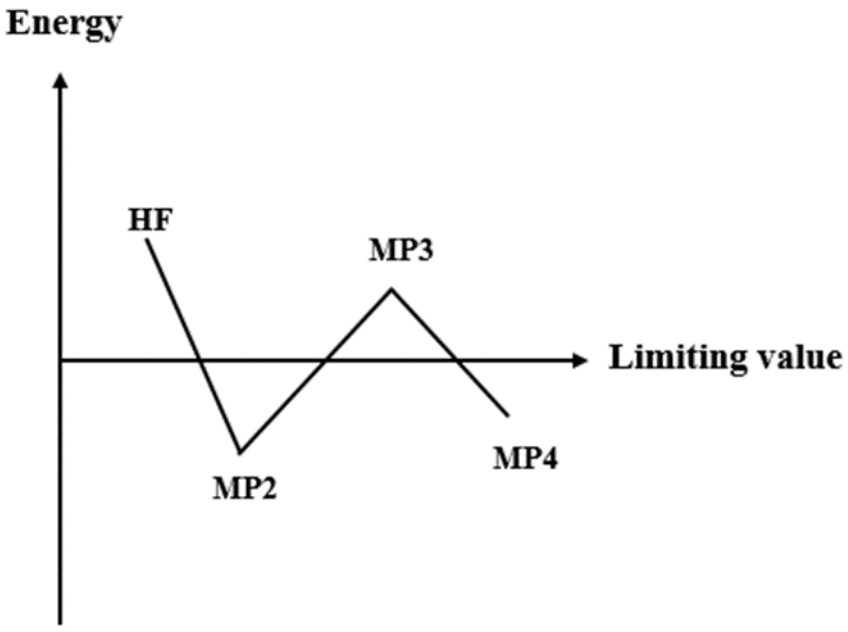

Figure 2.2 Oscillating behavior of electronic energies computed with Moller-Plesset perturbation theory

The performance of MP*n* depends on the quality of the reference wavefunction and the degree of the perturbation. MP*n* works best for small perturbation and good reference wavefunction.

2.5 Density Functional Theory

Density functional theory is not a wavefunction based method so it is not built on top of Hartree-Fock theory. It considers the electronic density as a fundamental property rather than the wavefunction. Hohenberg and Kohn prove that the electron density, $\rho(r)$, determines the ground state electronic energy, and it also uniquely determines the external potential (Columbic interaction between the electrons and the nuclei), this is known as the first Hohenberg-Kohn theorem [32]. The mathematical relationship between the electronic density and the wavefunction is:

$$\rho(r) = \int |\Psi(r, r_2, \dots, r_n)|^2 \, dr_2 \dots dr_n \tag{2.48}$$

and

$$\Psi_\rho = F[\rho(r)] \tag{2.49}$$

where the notation, $F[\dots]$, means functional.

The second Hohenberg-Kohn theorem [32] states that the electron density obeys variational principle such that the energy determined by a trial electron density ($E[\rho_{trial}(r)]$) must be greater than the exact ground state energy, which was defined by the exact ground state electron density ($E[\rho_{exact}(r)]$. Thus, one arrives at the following inequality:

$$E\left[\rho_{trial}(r)\right] > E\left[\rho_{\text{exact}}(r)\right] \tag{2.50}$$

The electronic Hamiltonian operator under the Hohenberg-Kohn formulation of DFT is:

$$\hat{H} = -\sum_{\alpha_i} \frac{\hbar^2}{2m_e} \frac{\partial^2}{\partial r_{\alpha_i}^2} - \sum_i \frac{k_e Z_i}{|R_i - r|} + \sum_{i<j} \frac{k_e e^2}{|r_i - r_j|} \tag{2.51}$$

where the second term is known as external potential, $\hat{V}_{ext}$. Therefore, the terms in equation can now be recollected as:

$$\hat{H} = \hat{F} + \hat{V}_{ext} \tag{2.52}$$

where $\hat{F}$ is the sum of the first and the second terms in equation (2.51). Then the energy functional given by the second Hohenberg-Kohn theorem is expressed as:

$$E[\rho(r)] = \hat{F}[\rho(r)] + \int V_{ext}(r)\rho(r)dr \tag{2.53}$$

The ground state energy may be determined minimizing equation with respect to the electron density. Although the Hohenberg-Kohn theorem is conceptually powerful, it is not practical in terms of implementation. More importantly, the exact electron density is not known.

Kohn and Sham introduced a practical method to implement density functional theory, known as Kohn-Sham Density Functional Theory (KS-DFT) [33, 34]. They transformed an interacting electrons problem to a problem of many-body non-interacting electrons with the same electron density as in the real system where the electrons are interacting. Then the electrons are described by one-dimension function called Kohn-Sham orbitals. The Hamiltonian given by KS-DFT is expressed as:

$$\hat{H}_{KS} = -\frac{1}{2}\nabla_i^2 + \hat{V}_{KS} \tag{2.54}$$

where $\hat{V}_{KS}$ is the Kohn-Sham effective potential and it is defined by:

$$\hat{V}_{KS} = V_{ext} + \frac{1}{2}\int \frac{\rho(r')}{|r-r'|}dr' + V_{XC} \tag{2.55}$$

where V_{ext} is the external potential, the second term is the Hartree potential, and the third term is the exchange-correlation potential, which is defined as:

$$\hat{V}_{XC} = \frac{\delta E_{XC}[\rho(r)]}{\delta\rho(r)} \tag{2.56}$$

In the spirit of the Hartree-Fock self-consistent field theory, a similar approach to KS-DFT can also be adopted. A set of Kohn-Sham equations can be obtained by solving the following equation:

$$\hat{H}_{KS}\phi_{KS} = \varepsilon\phi_{KS} \tag{2.57}$$

where ϕ_{KS} is the Kohn-Sham orbital and the Kohn-Sham kinetic energy is the energy of ϕ_{KS}, which is the kinetic energy of the non-interacting particles. The technique to solve equation is very much the same as the self-consistent field theory. First of all, an initial guess of electron density is required. Then the effective potential is constructed from the

guessed electron density. Then the Kohn-Sham orbitals are computed and hence a new electron density is then obtained. The procedure repeats until convergence is achieved. Finally, the total energy is obtained from the following expression:

$$E_{KS}[\rho] = \sum_i \varepsilon_i + \frac{1}{2}\int\int \frac{\rho(r)\rho(r')}{|r-r'|}\, drdr' + E_{XC}[\rho] + \int V_{ext}(r)\rho(r)dr \tag{2.58}$$

Equation (2.58) can be written into a more compact form:

$$E_{KS}[\rho] = T_s[\rho] + E_J[\rho] + E_{XC}[\rho] + E_{ne}[\rho] \tag{2.59}$$

where the first term is the kinetic energy of the non-interacting electrons, the second term is the Coulomb functional, the third term is the exchange-correlation functional and the last term is the nuclear-electron energy functional.

There is a problem with Equation (2.59), in which the term, $E_{XC}[\rho]$ is unknown. It encompasses all the non-classical effects of electronic interactions and the kinetic energy difference between the real system and the fictitious non-interacting system. The E_{XC} term can actually be further separated into two parts:

$$E_{XC}[\rho] = E_X[\rho] + E_C[\rho] \tag{2.60}$$

The $E_X[\rho]$ and $E_C[\rho]$ are the exchange term and the correlation term in DFT respectively. The exact form of $E_{XC}[\rho]$ is unknown at all and only approximations can be made. Consequently, using approximations for $E_{XC}[\rho]$ induces an error called self-interaction error (SIE) [35], which should not exist. By definition, SIE refers to the situation where an electron would interact with itself. In DFT, SIE arises from the fact that SIE in the Coulomb term does not cancel with SIE in the exchange term, whereas the two terms cancel exactly in the Hartree-Fock theory. Hence, there is no SIE within the Hartree-Fock theory. SIE in DFT functionals can lead to wrong potential energy curves for some open-shell species, such as very low barrier heights [38-43].

Since the exact functional of $E_{XC}[\rho]$ is not known, approximations are made at different levels, resulting in various types of functionals which correspond to different levels of chemical accuracy. Perdew introduced the term, "Jacob's Ladder" [44], to represent the set of different types of exchange-correlation functional with respective

chemical accuracy as shown in Figure 2.3. The categories of exchange-correlation functionals include LSDA (local spin density approximation) [34], GGA (generalized gradient approximation) [45], meta-GGA [46], hybrid-GGA [47-49] and double hybrid [50-51]. Due to their different formulations, they have different ability to mimic the actual exchange-correlation functional.

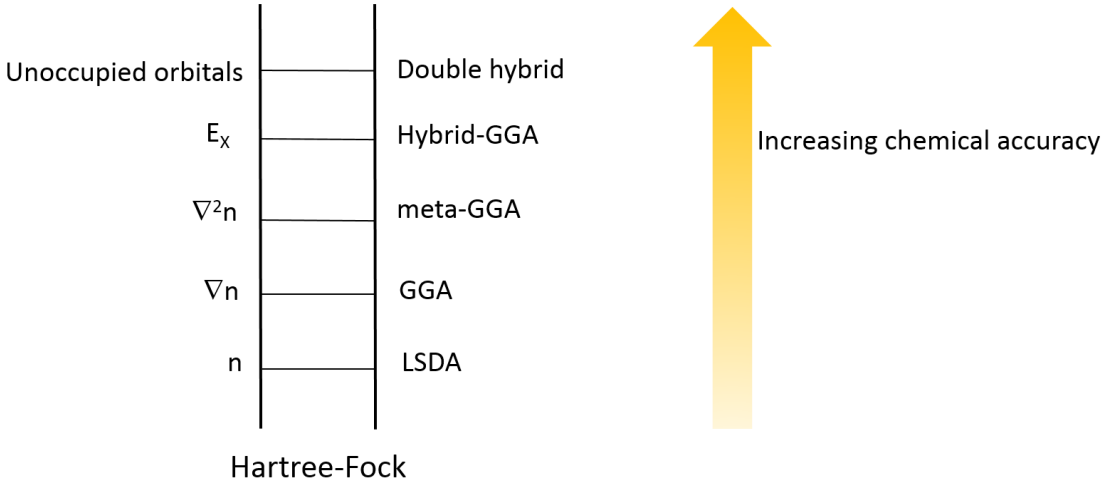

Figure 2.3 Jacob's Ladder

The oldest form of exchange-correlation functional is LSDA shown in Figure 2.3. In LSDA, the exchange energy is approximated by considering only local spin densities of a uniform electron gas, so it is the crudest approximation of exchange-correlation function. Consequently, it is at the lowest rung of the Jacob's ladder and it serves as the starting point for further improvement. The second rung of approximation in the Jacob's ladder is semi-local GGA which incorporates the unitless spin density gradient, which is the first derivative of the spin density. Since both LSDA and semi-local GGA do not consider non-locality, they often yield unphysical results. Therefore, the third rung of the Jacob's ladder considers the second derivative of the spin density to improve chemical accuracy, and it is known as meta-GGA. The self-interaction error is very severe in LSDA and severe in both semi-local GGA and meta-GGA [35]. In order to minimize the self-interaction error, Hartree-Fock exchange character is incorporated into the GGA functionals [35] which are known as hybrid functionals and they are on the fourth rung on the Jacob's ladder. The self-interaction error decreases as the Hartree-Fock exchange character in the hybrid functionals increases. The fifth (highest) rung on the Jacob's ladder is the double hybrid functional which takes Kohn-Sham unoccupied orbitals into

consideration as well, so it allows for better description of the correlation effect. This class of functional is gaining popularity in the community of quantum chemistry.

In this thesis, 5 hybrid functionals are employed to study chemical reactions, and they are B3LYP [52, 53], BH&HLYP [53,54], M05 [55], M06 [56] and M06-2X [56] in which the latter three are known as the Minnesota functionals. The proportional of the Hartree-Fock exchange character (%HF Exchange) present in different hybrid functionals employed in the calculations in this thesis are shown in Table 2.1.

Hybrid Functional	%HF Exchange	Ref(s)
B3LYP	20%	52. 53
M05	28%	55
M06	27%	56
BH&HLYP	50%	53. 54
M06-2X	54%	56

Table 2.1 Hartree-Fock exchange of different hybrid functionals

B3LYP functional performs very well in geometry optimization but it tends to underestimate the barrier height [58]. BH&HLYP functional contains a larger proportion of Hartree-Fock exchange so it can partially eliminate the self-interaction error [35]. M05 functional is one of the first family of Minnesota functional developed in 2005 and it aims to be widely used in thermochemistry, thermochemical kinetics, organometallic, and nonmetallic bonding. M06 functional is an improved version of the M05 functional and it is a general purpose functional. M06-2X functional contains double Hartree-Fock exchange of that in the M06 functional and it is recommended to be useful in main group thermochemistry, kinetics and non-covalent interactions. However, it is not recommended to be used for multi-reference species, such as transition metals and organometallic compounds.

DFT offers a more accurate description of many-body systems than Hartree-Fock but their computational costs are roughly the same, so DFT has gained popularity in the quantum chemistry community. However, there are also some disadvantages of DFT. Since the exchange-correlation functional used in DFT is not exact, approximation can lead to self-interaction error (as discussed before) which in-turn leads to wrong asymptotic $-1/r$ behavior of the exchange-correlation potential of LSDA, GGA and meta-

GGA functionals [58, 59]. Accurate descriptions of asymptotic *-1/r* behavior are required in charge-transfer reactions and Rydberg excitations [58], which can be circumvented by using long-range corrected functionals [59]. Since the works in this thesis do not require the use of long-range corrected functionals, they are not reviewed in this section.

Besides, there is no systematic way to improve DFT functionals, unlike the *ab initio* methods. Since the exact $E_{XC}[\rho]$ term remains unknown, a more feasible approach is to fit the functional form to a set of available experimental data with different numbers of parameters [51]. For example, atomization energies, ionization potentials, proton affinities and total atomic energies of the first and second row systems are used in parametrizing the $E_{XC}[\rho]$ term in the B3LYP functional [52]. Therefore, there is no way to systematically improve the approximations made in the $E_{XC}[\rho]$ term in DFT.

2.6 Basis Sets

Basis set is a set of basis functions (one-electron orbitals) which mimic the atomic orbitals of different atoms. Then molecular orbitals are constructed by taking linear combination of basis functions. There are mainly two types of basis functions, namely Slater Type Orbitals (STOs) [60] and Gaussian Type Orbitals (GTOs) [61], which are defined in spherical polar coordinate as:

$$\phi^{STO}(r,\theta,\varphi) = NY_{l,m}(\theta,\varphi)r^{n-1}e^{-\zeta r} \tag{2.61}$$

$$\phi^{GTO}(r,\theta,\varphi) = NY_{l,m}(\theta,\varphi)r^{2n-2-l}e^{-\zeta r^2} \tag{2.62}$$

where N is the normalization constant, $Y_{l,m}$ is the spherical harmonic function, r is the distance between the nucleus and electron, l is the angular momentum quantum number of the orbital, ζ controls the width and the diffuseness of the orbital. ζ also serves as a measure on how far the region away from the nucleus is covered by the basis function. A basis function with large ζ value covers the region closer to the nucleus (i.e. tight functions) whereas a basis function with small ζ covers the region distant from the nucleus (i.e. diffuse functions). STOs can mimic the real atomic orbital precisely because both of them have dependence on exp(-r), but the two-electron integral in the SCF cycle cannot be evaluated analytically with STOs. Therefore, GTOs (also known as primitive Gaussian functions) are introduced which can be used for analytical integration because

they have dependence on exp(-r^2). Atomic orbitals have an electron-nuclear cusp (a point of discontinuity given by the first derivative of the wavefunction at $r = 0$) at the nuclei, which is known as the cusp condition. STOs retain the cusp condition while GTOs cannot reproduce the cusp condition. Hence, a linear combination of GTOs is used to overcome their disadvantages [62]. If a fixed linear combination of GTOs is used, such set of GTOs is known as contracted basis set:

$$\phi^{cGTO} = \sum_{i}^{k} a_i \phi_i^{GTO} \tag{2.63}$$

they are good for reducing the computational costs. Thus, GTOs are more popular than STOs in molecular orbital calculations.

There are a few levels of basis set. At the lowest level, there is minimal basis set, which refers to the minimum number of basis functions which are barely to describe the electrons of an atom. An improved choice of basis set is the double zeta (DZ) in which it doubles the basis functions in the minimal basis set. Similarly, one can employ the triple zeta (TZ) and the triple of the number of minimal basis set are used in the calculations. However, the computational cost increases dramatically with the increasing number of basis sets. Therefore, one can choose to double or triple only the valence orbitals which leads to valence double zeta (VDZ) and valence triple zeta (VTZ) respectively in order to reduce the computational cost and these are known as split valence basis sets. Examples will be given to illustrate the idea of split valence basis sets in the discussion of Pople basis sets [63]. In split valence basis sets, the key idea is that the contracted basis functions, which are employed to describe valence orbitals, are split into contracted and uncontracted functions for adding more flexibility in bonding.

Basis sets only consider the occupied atomic orbitals of an atom in its ground state but not the polarization effect in its molecular configuration. Polarization effect refers to the shift of the electron cloud of one atom by the presence of a neighboring atom. An effective solution is to include basis functions which are of one higher angular momentum quantum number than the valence orbitals. These extra basis functions are known as polarization functions. Moreover, the electron density in the basis functions are centered on atoms which cannot provide accurate descriptions for ions, electronegative atoms, electron affinities and gas phase acidities. A way to circumvent this problem is to include diffuse functions which are functions with small exponents.

There are two types of widely used contracted basis sets, namely Pople basis set [63] and Dunning correlation-consistent basis set [64-66], in which the latter one focuses on recovering electron correlation by adding extra basis functions to an atom with similar contributions to correlation energy. Pople basis sets are split valence basis sets which mean that the core electrons and the valence electrons are treated differently. The notation of Pople style basis set is k-nlmG where k is the number of primitive GTOs for the contracted basis function, which describes the core electrons (i.e. electrons in $1s^2$ configuration for the first row elements from Li to Ne). n is the number of GTOs for the inner part of valence orbitals, and l is number of GTOs for the outer part of valence orbitals. The numbers after the hyphen show the numbers of GTOs used for describing the valence functions. Two numbers after the hyphen (i.e. k-nlG) indicates a split valence basis of double-zeta quality while three numbers after the hyphen (i.e. k-nlmG) indicates a triple split valence basis. Finally, G in the notation indicates that GTOs are used. For example, in 6-31G basis set, a contracted GTO with 6 primitives serve as the individual core orbitals and the contracted valence GTO is split into two sets of functions, namely 3 contracted GTO primitive and 1 uncontracted GTO primitive for valence orbitals [67]. In the case of 6-311G basis set, there is one extra GTOs to the 6-31G basis set, that is, the valence orbitals are split into 3 parts and the numbers of GTOs primitive used to represent the inner, middle and outer parts of the valence orbitals are 3, 1, and 1 respectively [68, 69]. Diffuse functions are usually used in describing the valence orbitals and denoted by "+". They are mainly employed to describe anion and/or electronegative atoms, where electron clouds are expected to expand. In the notation of Pople basis set, an asterisk (*) is used to denote polarization functions for heavy atoms or all atoms, except H whereas two asterisks (**) are used to denote the inclusion of polarization functions for both hydrogen and non-hydrogen atoms. The same practice is adopted for +/++ notation as well. In the notation of Pople basis set, a plus sign (+) is used to indicate the use of a diffuse function.

Another type of contracted basis set is Dunning correlation consistent (often abbreviated as cc) basis sets which are designed specifically for recovering correlation energy from valence electrons in the electronic energy calculations. The notation of a Dunning correlation consistent basis set is cc-pVXZ where cc indicates that the basis set is correlation consistent, p indicates the inclusion of polarization functions in the basis set, and VXZ stands for valence X-tuple zeta basis set in which X can be D (double), T

(triple), so on and so forth. In terms of the consideration of the diffuse function, the abbreviation 'aug' which stands for augmented [70, 71], is used to indicate the inclusion of the diffuse functions in the Dunning correlation consistent basis set.

2.6.1 Basis Sets for Resolution of Identity and Density Fitting

Resolution of identity (RI) [72], also known as density fitting [73-79], is an approach to reduce the high computational cost of the Coulomb integral in Hartree-Fock and post-Hartree-Fock methods. Its goal is to approximate the $\frac{1}{r_{12}}$ operator in Coulomb integral (equation (2.10)) using one-electron auxiliary basis functions so that the electron density can be approximated by the linear combinations of density fitting basis sets. This method will be very important to shorten the calculation time required for post-Hartree-Fock methods, such as MP2 and CCSD(T)-F12.

In RI, the $\frac{1}{r_{12}}$ operator is expanded in one-electron auxiliary basis functions (ϕ_p):

$$\frac{1}{r_{12}} = \sum_{p}^{\infty} \phi_p(r_1)\phi_p(r_2) \tag{2.64}$$

where p is the index of the one-electron auxiliary basis function and r_i is the coordinate of electron i. As discussed in the Hartree-Fock theory, the Coulomb integral is evaluated as:

$$\hat{J}_{\mu\nu} = \int\int \psi_\mu(r_1)\,\psi_\nu(r_1)\frac{1}{r_{12}}\psi_\lambda(r_2)\psi_\sigma(r_2)\,dr_1\,dr_2 \tag{2.65}$$

it can then be rewritten in the notation of electron densities (ρ) as:

$$\hat{J}_{\mu\nu} = \int\int \rho_{\mu\nu}(r_1)\,\frac{1}{r_{12}}\rho_{\lambda\sigma}(r_2)\,dr_1 dr_2 \tag{2.66}$$

where $\rho_{\mu\nu} = \psi_\mu(r_1)\psi_\nu(r_1)$ and $\rho_{\lambda\sigma} = \psi_\lambda(r_2)\psi_\sigma(r_2)$. Then the calculations of electron densities can be approximated by applying the RI approximation [84]:

$$\rho_{\mu\nu}(r) = \sum_{P} d_P^{\mu\nu}\phi_P \tag{2.67}$$

where $d_P^{\mu\nu}$ are the fitting coefficients and ϕ_p is an auxiliary basis set with an index of P.

Then the Coulomb integral (involving four basis functions) can be reduced to some integrals involving two and three basis functions, which are less computationally expensive, by the following approximation [85]:

$$\left\langle \psi_\mu \psi_\nu \middle| \psi_\lambda \psi_\sigma \right\rangle \approx \sum_P \left\langle \psi_\mu \psi_\nu \middle| \phi_P \right\rangle d_P^{\lambda\sigma} + \sum_P d_P^{\mu\nu} \langle \phi_P | \psi_\lambda \psi_\sigma \rangle - \sum_{PQ} d_P^{\mu\nu} \left\langle \phi_P \middle| \phi_Q \right\rangle d_Q^{\lambda\sigma} \tag{2.68}$$

where Q is the index of another auxiliary basis set, $\left\langle \psi_\mu \psi_\nu \middle| \phi_P \right\rangle$ and $\langle \phi_P | \psi_\lambda \psi_\sigma \rangle$ involve three basis functions and $\left\langle \phi_P \middle| \phi_Q \right\rangle$ involves two basis functions. The approximation made in equation (2.68) reduce the complexity of the Coulomb integral by decomposing it to some integrals involving fewer basis functions, which require less computer memory for numerical evaluations, thereby speeding up the electronic structure calculations [86]. It has been shown that density fitting can speed up MP2 calculations by 10 times or more [87]. In density fitting, atoms-centered Gaussian functions are used as auxiliary basis sets. There are different types of auxiliary basis sets, including Coulomb fitting basis sets for evaluating Coulomb integrals in Hartree-Fock theory and DFT [84, 85, 88] and JK-Fit basis sets [89] for evaluating Coulomb and exchange integrals (which also involve four basis functions according to equation (2.11)). They have also been further developed for MP2 calculations, known as density fitted MP2 basis sets, which can be used in conjunction with the correlation-consistent basis sets [90, 91]. Besides, the Dunning correlation consistent basis set for atomic orbitals is also extended to accommodate for the need of calculations with F12 theory, so aug-cc-pVXZ-F12 (X = D, T and Q) basis sets [92] designed by Peterson et al. to meet the demands.

2.6.2 Complete Basis Set Extrapolation

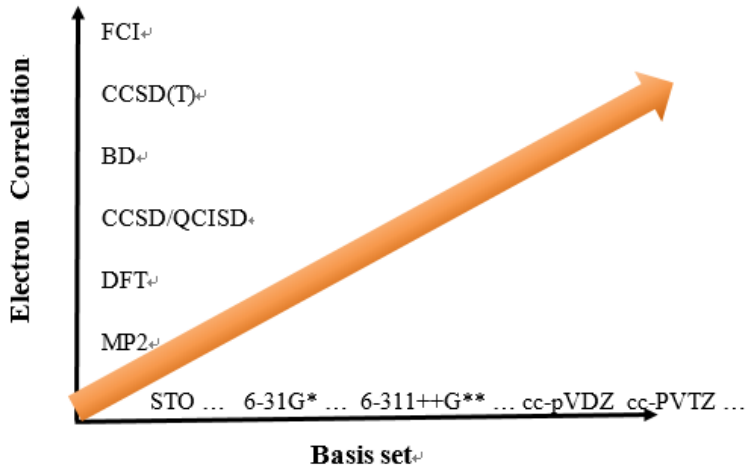

Figure 2.4 Convergence of computational results with increasing level of basis sets and electronic structure theory

Figure 2.4 shows that in order to obtain very accurate electronic structures of different compounds, the electronic structure theory used should approach FCI while the basis set used should approach the complete basis set (CBS) limit. By using Dunning correlation consistent basis set, one can obtain the electronic energy at the CBS limit by extrapolation. In this work, the extrapolation scheme employed is the two-point $1/X^3$ extrapolation scheme [93] which is given by:

$$E_X = E_{CBS} + AX^{-3} \tag{2.69}$$

where E_X is the relative energy obtained with augmented Dunning correlation consistent basis sets with cardinal number X (where D=2, T=3, Q=4), E_{CBS} is the relative energy at CBS limit and A is the unknown parameter. Since equation (2.69) is a two-point formulation, two equations are required to solve for the two unknown parameters, A and E_{CBS}.

2.7 Geometry Optimization

To obtain molecular properties, the first step is to carry out geometry optimization in order to look for the most stable configuration of a molecule known as a stationary point. There are some stationary points on the potential energy surface, including both energy minima (reactants, products, reactant and product complexes) and energy maximum (transition state) in the direction of reaction coordinate.

There are many available algorithms to carry out geometry optimization but the most efficient class of algorithm for such purpose is the Newton-Raphson method [94]. It assumes a parabolic potential energy surface (denoted as $E(\boldsymbol{r})$), which can be expanded according to Taylor series around a minimum ($\boldsymbol{r}_0$):

$$E(\boldsymbol{r}) = E(\boldsymbol{r_0}) + \frac{\boldsymbol{dE}}{\boldsymbol{dr}}(\boldsymbol{r} - \boldsymbol{r}_0) + \frac{1}{2}\frac{\boldsymbol{d^2E}}{\boldsymbol{dr^2}}(\boldsymbol{r} - \boldsymbol{r}_0)^2 \tag{2.70}$$

The first derivative and the second derivative of the energy function are known as gradient ($\boldsymbol{g} = \boldsymbol{dE/dr}$) and Hessian ($\boldsymbol{H} = \boldsymbol{d^2E/dr^2}$), respectively. Mathematically, gradient gives the direction of the steepest descent and Hessian gives the concavity of the potential energy surface at a point. Then the gradient and displacements are updated according to:

$$\boldsymbol{g}_{i+1} = \boldsymbol{g}_i + \boldsymbol{H}(\boldsymbol{r}_{i+1} - \boldsymbol{r}_i) \tag{2.71}$$

$$\boldsymbol{r}_{i+1} = \boldsymbol{r_i} - \boldsymbol{H}^{-1}\boldsymbol{g}_i \tag{2.72}$$

until the convergence criteria are achieved. As computation of the Hessian terms is computational costly, which leads to the development of the quasi-Newton method [87], in which Hessian is only computed once or estimated empirically in the beginning and then it is approximated according to the Broyden-Fletcher-Goldfarb-Shanno (BFGS) scheme [95-98] or the Davidon–Fletcher–Powell (DFP) scheme [99]. The algorithm used in optimizing all energy minima is the Berny algorithm [100] in the Gaussian 09 software [101], which is one of the quasi-Newton methods and the BFGS scheme is used to update the Hessian term. In the optimization process, the gradients and the displacements are updated until the convergence criteria (maximum force, maximum displacement, root-mean-square (RMS) force, RMS displacement) are met. As a result, the geometry optimization is completed.

For transition state search, Synchronous Transit-Guided Quasi-Newton method (STQN) [102, 103] method is employed, which is a combination of quasi-Newton method and interpolation between reactants and products. The interpolation method used is the quadratic synchronous transit (QST) method [104] and it helps obtain a good initial guess for the transition state in order for the quasi-new method to finish the geometry optimization. In QST method, an arc is employed to connect the reactants to the products. Then the algorithm will search for the transition state which is defined as the point where it is maximum along the arc but minimum in all directions perpendicular to the arc. In Gaussian, there are two available options for QST method, namely QST2 and QST3. In QST2, only optimized structures of reactants and products are required in the input file. In QST3, the initial guess of transition state is required in addition to the requirements of QST2 method. QST3 method is employed in all transition state searches in this thesis.

2.8 Vibrational Frequency Calculations

In the previous section, the Taylor series expansion of potential energy surface is briefly reviewed, leading to the gradient and Hessian terms in equation (2.70). The dimension of a Hessian matrix is 3N by 3N where N is the number of atoms in a molecule. The Hessian matrix with its elements in mass-weighted Cartesian coordinate is then diagonalized to yield 3N eigenvalues and 3N eigenvectors. Then the rotational modes and translation modes are projected out by using a matrix technique known as similarity transformation, leaving with 3N-6 vibrational modes for non-linear molecules or 3N-5 vibrational modes for linear molecules in the calculation. Finally, the vibrational frequencies are calculated from the eigenvalues by:

$$\tilde{\nu}_i = \sqrt{\frac{\lambda_i}{4\pi^2 c^2}} \tag{2.73}$$

where $\tilde{\nu}_i$ is the vibrational frequency in wavenumber, λ_i is the eigenvalue, and c is the speed of light. For energy minima, all eigenvalues in their Hessian matrices are positive. For transition state, one of the eigenvalue in its Hessian matrix is negative while the rest are positive.

2.9 Intrinsic Reaction Coordinate

Intrinsic reaction coordinate (IRC) is defined as the steepest descent path in the mass-weighted Cartesian coordinate which connects from the transition state to the products and reactants respectively. IRC calculation is used to confirm whether a transition state connects to the desirable products and reactants, respectively.

The default IRC algorithm used in Gaussian 09 is known as the Hessian-based Predictor-Corrector integrator [105, 106] in which local quadratic approximation (LQA) is used for the predictor steps (i.e. IRC points) whereas a modified Bulirsch-Stoer integrator is used for the corrector steps (i.e. optimization steps within each IRC point). A lot of energy and gradient evaluations are necessary in the modified Bulirsch-Stoer integrator, so it is a computationally expensive method. In order to decrease the computational cost, Bulirsch-Stoer integration is performed on a distance weighted interpolants (DWI) [107] surface which is fitted to the energies, the gradients and the Hessians (i.e. results of LQA calculations) at the beginning points and the endpoints of the predictor step.

2.10 Summary

Both wavefunction methods (ranging from Hartree-Fock theory to coupled-cluster theory) and density functional theory are reviewed in this chapter. Both advantages and limitations of the individual electronic structure theories are briefly discussed. The computational algorithms for carrying out geometry optimization, vibrational frequency calculation and IRC calculation are also briefly reviewed. The IRC plays an important role in the next chapter in rate coefficient calculations.

2.11 References

1. Born, M.; Oppenheimer, J. R. *Annalen der Physik* **1927**, *84*, 457.
2. Fock, V. *Z. Phys*. **1930**, *61*, 126–148.
3. Slater, J.C. *Phys. Rev*. **1929**, *34*, 1293–1322.)
4. Griffiths, D. J. The Variational Principle. In Introduction to quantum mechanics. Pearson Prentice Hall: Upper Saddle River, NJ, 1995; pp 256.
5. Perdew, J.P.; Zunger, A. *Phys. Rev. B* **1981**, *23*, 5048-5079.
6. Cances, E.; Le Bris, C. ESAIM: Mathematical Modelling and Numerical Analysis **2000**, 34, 749-774.
7. C. C. J. Roothaan, *Rev. Mod. Phys*. **1951**, *23*, 69, G. G. Hall, Proc. R. Soc. (London) **1951** *A205*, 541.
8. Cances, E.; Le Bris, C. ESAIM: Mathematical Modelling and Numerical Analysis **2000**, 34, 749-774.
9. Jensen, F. In Introduction to Computational Chemistry, 2nd ed. Wiley: West Sussex, 2007; pp 98
10. Young, D. Spin Contamination. In Computational Chemistry: A Practical Guide for Applying Techniques to Real World Problems; Wiley: New York, 2001; pp 227.
11. Jensen, F. Electron Correlation Methods. In An Introduction to Computational Chemistry; Wiley: Chichester, New York, 1999; pp 98.
12. Sherrill, C.D.; Schaefer, H.F. *Adv. Quant. Chem*. **1999**, *34*, 143.
13. Møller, C; Plesset, M. S. *Phys. Rev*. **1934**, *46*, 618.
14. Bartlett, R.J. *J. Phys. Chem*. **1989**, *93*, 1697-1708.
15. Harrison, R.J.; Handy, N.C. *Chem. Phys. Lett*. **1983**, *95*, 386
16. Cizek, J. J. Chem. Phys. **1966**, *45*, 4256.
17. Purvis, G. D.; Bartlett, R. J. *J. Chem. Phys*. **1982**, *76*, 1910.
18. Raghavachari, K.; Trucks, G. W.; Pople, J. A.; Headgordon, M. *Chem. Phys. Lett*. **1989**, *157*, 479.
19. Head-Gordon, M. *J. Chem. Phys*. **1996**, *100*, 13212-13225.
20. Cramer, C. J. Essentials of Computational Chemistry; John Wiley & Sons, Ltd, 2004.
21. Hylleraas, E. A. *Z. Phys*. **1929**, *48*, 469.
22. Hylleraas, E. A. *Z. Phys*. **1929**, *54*, 347.
23. Kutzelnigg, W; Klopper, W. *J. Chem. Phys*. **1991**, *94*, 1985.
24. Ten-no, S. *Chem. Phys. Lett*. **2004**, *398*, 56-61.
25. Knizia, G.; Adler, T.B.; Werner, H-J. *J. Chem. Phys*. **2009**, *130*, 054104
26. Adler, T. B.; Knizia, G.; Werner, H. J. *J. Chem. Phys*. **2007**, *127*, 221106.

27. Werner, H.-J.; Knowles, P. J. MOLPRO User Manual version 2012.1.
28. Handy, N.C.; Pople, J.A.; Head-Gordon, M.; Raghavachari, K.; Trucks, G.W. *Chem. Phys. Lett*. **1989**, *164*, 185-192.
29. Griffiths, D. J. Time-independent Perturbation Theory. In Introduction to quantum mechanics. Pearson Prentice Hall: Upper Saddle River, NJ, 1995; pp 221.
30. Jensen, F. Møller–Plesset perturbation theory. In Introduction to Computational Chemistry, 2nd ed. Wiley: West Sussex, 2007; pp 164
31. Crèmer, D. Computational Molecular Science **2011**, 1, 509-530.
32. Hohenberg, P.; Kohn, W. *Phys. Rev.* **1964**, *136*, B864.
33. Kohn, W.; Sham, L. J. *Phys. Rev*. **1965**, *140*, A 1133–1138.
34. Koch, W.; Holthausen, M. C. A Chemist's Guide to Density Functional Theory, Wiley-VCH: New York, 2001.
35. Cremer, D.; Filatov, M.; Polo, V.; Kraka, E.; Shaik, S. *Int. J. Mol. Sci*. **2002**, *3*, 604-638.
36. Johnson, B. G.; Gonzales, C. A.; Gill, P. M. W.; Pople, J. A. *Chem. Phys. Lett.* **1994**, 221, 100.
37. Deng, L.; Branchadell, V.; Ziegler, T. *J. Am. Chem. Soc.* **1994**, 116, 10645.
38. Jursic, B. S. *Chem. Phys. Lett.* **1996**, 256, 603.
39. Truong, T. N.; Stefanovich, E. V. *J. Phys. Chem.* **1995**, 99, 14700.
40. Glukhovtsev, M. N.; Bach, R. D.; Pross, A.; Radom, L. *Chem. Phys. Lett.* **1996**, 260, 558.
41. Baker, J.; Andzelm, J.; Muir, M.; Taylor, P. R. *Chem. Phys. Lett.* **1995**, 237, 53.
42. Hrouda, V.; Roeselova, M.; Bally, T. *J. Phys. Chem. A* **1997**, 101, 3925.
43. Tsuneda, T.; Hirao, K. *J. Chem. Phys.* **2014**, 140, 18A513.
44. Perdew, J. P.; Ruzsinszky, A.; Tao, J. M.; Staroverov, V. N.; Scuseria, G. E.; Csonka, G. I. *J. Chem. Phys*. **2005**, *123*, 062201.
45. Perdew, J.P.; Burke, K.; Wang, Y. *Phys. Rev. B* **1996**, *54*, 16533-16539.
46. Perdew, J. P.; Kurth, S.; Zupan, A.; Blaha, P. *Phys. Rev. Lett*. **1999**, *82*, 2544.
47. Perdew, J. P.; Staroverov, V. N. ; Tao, J.; Scuseria, G. E. *Phys. Rev. A* **2008**, *78*, 052513.
48. Mori-S´anchez, P.; Cohen, A. J.; Yang, W. *J. Chem. Phys*. **2006**, *124*, 091102.
49. Becke, A. D. *J. Chem. Phys*. **2005**, *122*, 064101.
50. Grimme, S. *J. Chem. Phys*. **2006**, 124, 034108.
51. Cohen, A. J.; Mori-Sanchez, P.; Yang, W. *Chem. Rev.* **2012**, 112, 289-320.
52. Becke, A. D. *J. Chem. Phys*. **1993**, *98*, 5648.
53. Lee, C.; Yang, W.Parr, R. G. *Phys. Rev. B* **1988**, *37*, 785.
54. Becke, A. D. J. *Chem. Phys*. **1993**, *98*, 1372.
55. Zhao, Y.; Schultz, N. E.; Truhlar, D. G. *J. Chem. Phys*. **2005**, *123*, 161103.
56. Zhao, Y.; Truhlar, D. G. *Theor. Chem. Acc.* **2008**, *120*, 215.
57. Nguyen, M. T.; Creve, S.; Vanquickenborne, L.G. *J. Phys. Chem*. **1996**, *100*, 18422-18425.

58. Henderson, T. M.; Janesko, B. G.; Scuseria, G. E. *J. Phys. Chem. A*, **2008**, 112, 12530-12542.
59. Tsai, C-W.; Su, Y-C.; Lei, G-D; Chai, J-D. *Phys. Chem. Chem. Phys.* **2013**, 15, 8352-8361.
60. Slater, J. C. *Phys. Rev*. **1930**, *36*, 57.
61. Boys, S. F. Proceedings of the Royal Society of London **1950**, A200, 542.
62. Hehre, W. J.; Stewart, R. F.; Pople, J. A. *J. Chem. Phys*. **1969**, *51*, 2657.
63. Ditchfield, R.; Hehre, W. J.; Pople, J. A. *J. Chem. Phys*. **1971**, *54*, 724–728.
64. Dunning, T. H. *J. Chem. Phys*. **1989**, *90*, 1007.
65. Woon, D. E.; Dunning, T. H. *J. Chem. Phys*. **1993**, *98*, 1358.
66. Woon, D. E.; Dunning, T. H. *J. Chem. Phys*. **1995**, *103*, 4572.
67. Hehre, W. J.; Ditchfie, R.; Pople, *J. A. J. Chem. Phys.* **1972**, 56, 2257.
68. McLean, A. D.; Chandler, G. S. *J. Chem. Phys.* **1980**, 72, 5639.
69. Krishnan, R.; Binkley, J. S.; Seeger, R.; Pople, J. A. *J. Chem. Phys.* **1980**, 72, 650.
70. Woon, D. E.; Dunning, T. H. *J. Chem. Phys*. **1993**, *98*, 1358.
71. Kendall, R. A.; Dunning, T. H.; Harrison, R. J. *J. Chem. Phys*. **1992**, *96*, 6796.
72. Helgaker, T; Klopper, W.; Tew, D. P. Mol. Phys. 2008, 106, 2107-2143.
73. Whitten, J. L. *J. Chem. Phys.* **1973**, *58*, 4496.
74. Dunlap, B. I.; Connolly, J. W. D.; Sabin, J. R. *J. Chem. Phys.* **1979**, *71*, 3396.
75. Mintmire, J. W.; Sabin, J. R.; Trickey, S. B. *Phys. Rev. B* **1982**, *26*,1743.
76. Vahtras, O.; Alml¨of, J.; Feyereisen, M. W. *Chem. Phys. Lett.* **1993**, *213*, 514.
77. Feyereisen, M.; Fitzgerald, G.; Komornicki, A. *Chem. Phys. Lett.* **1993**, *208*,359.
78. Weigend, F.; H¨aser, M.; Patzelt, H.; Ahlrichs, R. *Chem. Phys. Lett*. **1998**, *294*, 143.
79. Weigend, F. *Phys. Chem. Chem. Phys.* **2002**, *4*, 4285.
80. Dahle, P.; Helgaker, T.; Jonsson, D.; Taylor, P. R. *Phys. Chem. Chem. Phys*. **2008**, *10*, 3377-3382.
81. Boys, S. F. Proc. Royal. Soc. A 1960, 258, 402; Singer, K. *Proc. Royal. Soc. A* **1960**, *258*, 412
82. Klopper, W.; Manby, F. R.; Ten-No, S.; Valeev, E. F. *International Reviews in Physical Chemistry* **2006**, *25*, 427-468.
83. Pedersen, T. B.; Aquilante, F.; Lindh, R. *Theor. Chem. Acc*. **2009**, *124*, 1-10.
84. Eichkorn, K.; Treutler, O. ; Ohm, H.; H¨aser, M.; Ahlrichs, R. *Chem. Phys. Lett.* **1995**, *240*, 283.
85. Eichkorn, K.; Weigend, F.; Treutler, O.; Ahlrichs, R. *Theor. Chem. Acc.* **1997**, *97*, 119.
86. Ren, X.; Rinke, P.; Blum, V.; Wieferink, J.; Tkatchenko, A.; Sanfilippo, A.; Reuter, K.; Scheffler, M. *New Journal of Physics* **2012**, *14*, 053020 (55pp).
87. Ishikawa, T. ; Kuwata, K. *Chem. Phys. Lett*. **2009**, *474*, 195-198.
88. Weigend, F. *Phys. Chem. Chem. Phys.* **2006**, *8*, 1057.
89. Weigend, F. *Phys. Chem. Chem. Phys*. **2002**, *4*, 4285.

90. Weigend, F.; K¨ohn, A.; H¨attig, C. *J. Chem. Phys*. **2002**, *116*, 3175.
91. H¨attig, C. *Phys. Chem. Chem. Phys*. **2005**, *7*, 59.
92. Peterson, K. A.; Adler, T. B.; Werner, H.-J. *J. Chem. Phys.* **2008**, *128*, 084102.
93. Halkier, A.; Helgaker, T.; Klopper, W.; Jorgensen, P.; Csaszar, A. G. *Chem. Phys. Lett.* **1999**, *310*, 385.
94. Schlegel, H. B. Wiley Interdisciplinary Reviews: Computational Molecular Science **2011**, 1, 790 - 809.
95. Broyden, C. G. Journal of the Institute of Mathematics and Its Applications **1970**, 6, 76.
96. Fletcher, R. *Comput. J.* **1970**, 13, 317.
97. Goldfarb, D. *Math. Comput.* **1970**, 24, 23.
98. Shanno, D. F. *Math. Comput.* **1970**, 24, 647.
99. Fletcher, R.; Powell, M. J. D. *Comput. J.* **1963**, 6, 163-168.
100. Schlegel, H. B. *J. Comp. Chem.* **1982**, 3, 214-218.
101. Frisch, M. J.; Trucks, G. W.; Schlegel, H. B.; Scuseria, G. E.; Robb, M. A.; Cheeseman, J. R.; Scalmani, G., Barone, V.; Mennucci, B.; Petersson, G. A.; et al. Gaussian 09, revision A.02; Gaussian, Inc.:Wallingford, CT, 2009.
102. Peng, C. Y.; Schlegel, H. B. *Israel Journal of Chemistry* **1993**, 33, 449.
103. Peng, C. Y.; Ayala, P. Y.; Schlegel, H. B.; Frisch, M. J. *J. Comp. Chem.* **1996**, 17, 49.
104. Halgren, T. A.; Lipscomb, W. N. *Chem. Phys. Lett.* **1977**, 49, 225.
105. Hratchian, H. P.; Schlegel, H. B. *J. Chem. Phys*. **2004**, *120*, 9918-9924.
106. Hratchian, H. P.; Schlegel, H. B. *J. Chem. Theory Comput*. **2005**, *1*, 61-69.
107. Collins, M. A. *Theor. Chem. Acc*. **2002**, *108*, 313-24.

Chapter 3.

Theoretical Chemical Kinetics

In the previous chapter, different quantum chemical methods used to obtain the relative electronic energies of reactants, transition states (TSs) and products are discussed. This chapter focuses on different theoretical methods for computing rate coefficients from relative electronic energies and molecular properties. In principle, quantum mechanics could be employed to solve the equation of motion of the species in a chemical reaction [1]. However, this would be very computationally expensive for simple systems [2]. As most molecular systems involved in reactions are large and consist of more than three or four atoms, the only solution is to employ classical mechanics to evaluate the rate coefficients [3].

3.1 Potential Energy Surface and Dynamics

The concept of potential energy surface (PES) introduced in section 2.1 is central to reaction dynamics as Born-Oppenheimer approximation separates the motion of electrons and nuclei. Thus, the nuclei are moving on the PES. The PES describes the electronic energy of molecules as a function of the molecular geometry, such as bond lengths and bond angles. The dimensionality of the PES of a molecule is the same as the number of degrees of freedom of the molecule (3N-5 for linear molecules or 3N-6 for non-linear molecules where N is the number of atoms in the system). The high dimensionality of a PES makes it difficult to visualize. A more convenient representation of a PES is to construct a contour plot (a two-dimensional PES) using two of the inter-nuclear distances of a molecule. Figure 3.1 shows a collinear triatomic molecule with inter-nuclear distances r_{AB} and r_{BC}.

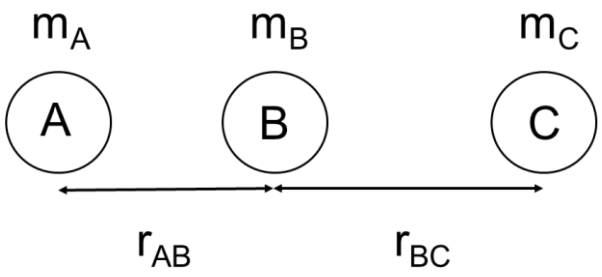

Figure 3.1 A collinear triatomic molecule ABC

This molecule may undergo dissociate to form AB and C and the process can be visualized using a contour plot as show in Figure 3.2.

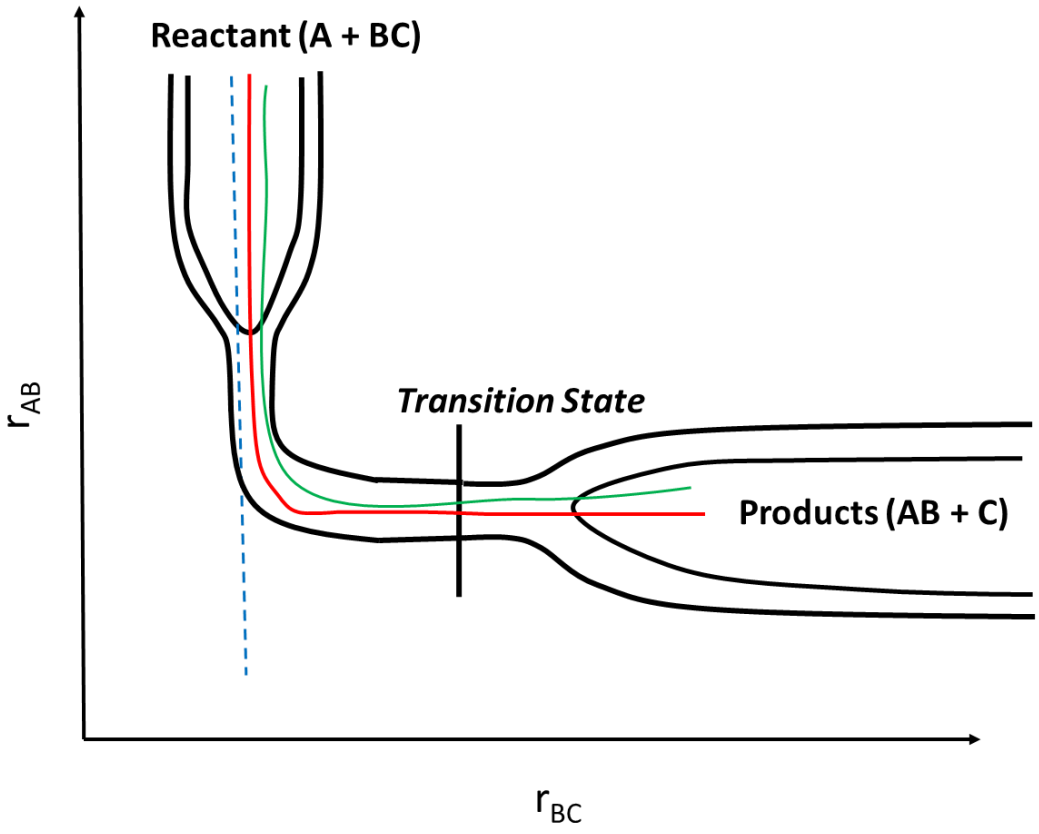

Figure 3.2 Potential contour diagram for the bimolecular reaction (from A + BC to AB + C)

The reactant region is on the left hand side in Figure 3.2 where A and BC are shown while the product region is on the right hand side. The red and green solid lines represent possible trajectories that connect the reactants (A and BC) to the products (AB and C) by crossing the transition state and this type of trajectory is known as reactive trajectory [11,

12]. Another type of trajectory is non-reactive trajectory [11, 12], which does not connect the reactants to the products, and it is represented by the blue dotted line in Figure 3.2 These trajectories are obtained by solving the equation of motion using classical mechanics.

Following the potential contour shown in Figure 3.2, the reaction coordinate (*s*) and its coordinate system need to be defined. For the transition state, it has 3N- η vibrational modes (where η = 6 for non-linear species and η = 5 for linear species) in which one of them has an imaginary vibrational frequency and the rest of them have real vibrational frequencies. The imaginary vibrational mode corresponds to the unbound normal mode whereas the rest of the real vibrational modes correspond to the bound normal modes. It is assumed that there is no coupling in all modes. The unbound normal mode is separated and taken as the reaction coordinate, and it is perpendicular to the bound normal modes. Then a mass-scaled coordinate system is used in the reaction coordinate because it has the following advantages [17].

1. The calculations of vibrational energies and partition functions can be simplified.
2. Kinetic energy can be obtained by a linear transformation of potential energy which is advantageous for the computation of the minimum energy path (MEP).
3. Convenient dynamical interpretation of the MEP is possible.
4. The unit of the mass-scale coordinate system is length, which is convenient for depicting the collinear motion.

The minimum energy path (MEP) is the reaction path of the steepest descent which connects from the transition state to the separate reactants and separate products in the negative and positive directions, respectively. It is also known as the intrinsic reaction coordinate (IRC). The vector of the unbound normal mode at a given point gives the direction of the barrier of the reaction and the direction of the MEP is given by the negative gradient of the potential. Throughout this thesis, the MEP is the reference reaction path for a reaction with a barrier (either positive or negative). With the use of the mass-scaled coordinate system, the MEP corresponds to a trajectory with potential energy only (i.e. kinetic energy = 0) [17]. By definition, separate reactants and products are located at -∞ and +∞ on the reaction coordinate (denoted as s) respectively. The transition state is located at $s = 0$, where it is the saddle point on the potential energy surface. In classical transition state theory, the dividing surface is located at the saddle point. The

potential energy along the MEP is denoted as the *VMEP* curve in which the maximum of the *VMEP* ($V^{\neq}_{MEP}$) curve is located at $s = 0$.

The molecular motion along the reaction coordinate is approximated using classical mechanics. In classical mechanics, the state of motion of a system is represented by its momentum and position. A two-dimensional space spanned by momentum and position is known as phase space. The state of motion of the system is represented by a point in phase space. Thus, the change of state of the system along a reaction path during the chemical reaction can be represented by a sequence of points in phase space. A curve can then be drawn to connect all these points together and this curve is known as a trajectory. The trajectory in the sense of classical mechanics is equivalent to a trajectory on the PES. Therefore, a chemical reaction can be described by trajectories.

In the phase space representation, the transition state of a reaction is the dividing surface [4] which separates the reactant region of phase space from the product region. There are many possible trajectories for the reactants to take in order to cross the dividing surface (i.e. the transition state) and form the products. For each trajectory of a reacting system, it is characterized by a physical quantity called action (*S*), which is defined as:

$$S = \int p(q)dq \tag{3.1}$$

where *S* is the classical action, *p* is the generalized momentum and *q* is the generalized reaction coordinate. For trajectories in phase space, their corresponding action, *S*, can be computed. Among all trajectories, the most favorable path for the reactants to take is given by the Principle of Least Action [5], which states that the trajectory with the smallest action value is favoured. Therefore, the most favoured trajectory taken by the reactants is the one with the smallest action which crosses the dividing surface and leads to the formation of the products. Finally, the rate coefficients can be computed from counting the number of trajectories which connect the reactants to the products [6].

In terms of the validity of the classical approach to reaction dynamics, large systems have large classical actions. So when a reaction proceeds, as the nuclei are heavy, the quantum effects would be less pronounced. As a result, quantum effects are considered to be minor and classical methods are valid for the evaluation of rate coefficients [7,8,9]. Therefore, the classical trajectory method is employed as an effective and powerful

method for large reaction systems [10]. However, in order to obtain reliable rate coefficients, large amounts of trajectories are required because there is more than one trajectory that connect reactants to products [11]. Thus, the classical trajectory method is not a practical method to calculate rate coefficients by accounting for all reactive trajectories because of its high computational costs. Hence, an alternative approach is adopted which considers a collection of reactants (i.e. a corresponding ensemble of reactants) and their own reactive trajectories rather than a single trajectory in order to reduce the computational cost and make the computations feasible. This approach makes statistical descriptions of the large amount of reactive trajectories in phase space possible. Consequently, by using statistical mechanics, the flux of reactive trajectories crossing the dividing surface only once in phase space can be derived to obtain the rate coefficients. This approach is discussed in the next section.

3.2 Transition State Theory

Transition state theory (TST) has served as the foundation for computing rate coefficients of chemical reactions by taking the thermal average of the reactive flux over an ensemble of reactive trajectories in phase space with Maxwell-Boltzmann weighting at a given temperature [13-16]. It was put forward by Eyring [13], Polanyi [14], Wigner [15] and others [16] in 1935, which evolved from the classical trajectory method. It is applicable to both unimolecular and bimolecular chemical reactions. In TST, the transition state is assumed to be in quasi-equilibrium with the reactants, and the transition state proceeds to the formation of separate products. The term, quasi-equilibrium, indicates that the TS is actually not at thermal equilibrium with the reactants because the transition state is not a real thermodynamic species since it has one less degree of freedom than the full reacting system. The assumed structure of a reaction in transition state theory (TST) is shown below:

$$Reactants \rightleftharpoons Transition\ State \rightarrow Products$$

There are four assumptions made in TST which are listed as below [16].

1. The reaction is electronically adiabatic, which means that the Born-Oppenheimer approximation (Chapter 2) is valid near the vicinity of the transition state. Hence,

the motion of the nuclei can be described by classical mechanics and quantum mechanical corrections can be introduced when necessary.

2. The reactants are in quasi-equilibrium with the transition state in a canonical (NVT) ensemble or a microcanonical (NVE) ensemble.
3. The populations of energy levels in the reagents and the TS (also termed the activated complex) are assumed to follow a Boltzmann distribution corresponding to the temperature of the reaction system.
4. Reactants can only cross the dividing surface (i.e. the transition state) once to form products.

The vibrational frequencies of the non-stationary points are also calculated along with IRC calculations performed in this thesis. The corresponding zero-point energy (ZPE) of an IRC point can then be calculated from its vibrational frequencies (ν_i) according to ZPE = $\Sigma_i (h\nu_i)/2$. Evaluation of the zero-point energy of each IRC point along the *VMEP* curve gives the zero-point energy curve. Subtraction the sum of zero-point energies of the reactants from the zero-point energy of each IRC point along the *VMEP* curve leads to the zero-point energy difference curve (ΔZPE curve). Finally, the vibrationally adiabatic ground-state potential (V_a^G) curve is obtained by summing up the *VMEP* curve and the ΔZPE curve. The V_a^G curve is central to the discussion of non-classical effects in variational transition state theory. The maximum of the V_a^G curve is denoted as $V_a^G(s^*)$ which is not necessarily located at $s = 0$. The *VMEP* curve plays an important role in TST calculations whereas the V_a^G curve plays an important role in VTST calculations, which are discussed in detail in section 3.4.

In principle, one would be able to obtain the exact rate constants with TST if every trajectory crossed the dividing surface only once and there are no non-reactive trajectories [19]. However, in reality, there are reactive trajectories which cross the dividing surface more than once and non-reactive trajectories. As a result, TST can only give an upper bound to the exact classical rate coefficient.

The TST rate coefficients are evaluated using the expression:

$$k(T) = \sigma \frac{kT}{h} \frac{Q_{TS}(T)}{\Phi_R(T)} \exp(-\beta V^{\neq}_{MEP}) \quad (3.2)$$

where σ is a symmetry factor which is discussed in the next paragraph, $V^{\neq}_{MEP}$ is the classical potential energy at the saddle point, $\beta=(k_BT)^{-1}$ where k_B is Boltzmann constant, h is Planck constant, Q_{TS} is the classical partition function of the TS with its zero of energy at the saddle point (i.e. s = 0 Å) and Φ_R is the classical partition function of the reactants with its zero of energy which is defined as the sum of Born-Oppenheimer electronic energies of the separated reactants.

The symmetry factor, σ, is the number of possible degenerate pathways to form the transition state from the reactants in a reaction. Fernández-Ramos and coworkers have developed a method [21] to calculate the symmetry factor of a reaction as:

$$\sigma = \frac{\sigma_{rot,R}}{\sigma_{rot,TS}} \quad (3.3)$$

where $\sigma_{rot,R}$ and $\sigma_{rot,TS}$ are the rotational symmetry numbers of the reactants and the transition state. For a bimolecular reaction, $\sigma_{rot,R}$ is the product of the individual symmetry numbers of the reactants. The symmetry number of a species is dictated by its point group according to Table 2 in the article of Fernández-Ramos and coworkers [21].

3.3 Microcanonical Transition State Theory

The previous section focuses on conventional transition state theory, which is implemented in a canonical ensemble. There is another form of transition state theory which is primarily used to calculate the rate coefficients of unimolecular and bimolecular reactions in a microcanonical ensemble. Consider the following reaction scheme:

$$A + M \rightleftharpoons A^* + M$$

$$A^* \rightarrow A^{\ddagger}$$

$$A^{\ddagger} \rightarrow \text{Products}$$

In this scheme, a molecule *A* collides with a bath gas M to be excited to *A** with the energy redistributed rapidly across different degrees of freedom. As a result, energy may

localize in a specific bond to form the transition state $A^{\ddagger}$, which can then move on to form the products. With the above reaction scheme, in 1952, Marcus with colleagues developed the RRKM (Rice- Ramsperger-Kassel-Marcus) theory [22, 23] by building on the work of other pioneers in the field of unimolecular reactions and transition state theory. RRKM theory has one more assumption than transition state theory, namely the ergodicity assumption [24]. It assumes that the vibrational energy will be randomized rapidly throughout all vibrational degrees of freedom compared with the timescale of the reaction, such that a statistical description of the rate process is possible [24]. In RRKM theory, the reactive flux, $F(E)$, is proportional to the total number of vibrational states of the transition state, $N(E^{\ddagger})$ [25, 26]. $F(E)$ is written as:

$$F(E) = \frac{N(E - E_0)}{h} = \frac{N(E^{\ddagger})}{h} \tag{3.4}$$

where E is the internal energy of the excited reactant, E_0 is the critical energy which is defined as the difference of enthalpy of formation at 0 K between the transition state and the reactant. $E^{\ddagger}$ is the available energy, defined as $E^{\ddagger} = E\text{-}E_0$. Then the microcanonical rate coefficient is given by

$$k(E) = \frac{\sigma F(E)}{\rho(E)} = \frac{\sigma N(E^{\ddagger})}{h\rho(E)} \tag{3.5}$$

where σ is the symmetry factor. $\rho(E)$ is the density of states of the reactant and it is related to the number of states of the reactant by:

$$\rho(E) = \frac{d\,N(E)}{dE} \tag{3.6}$$

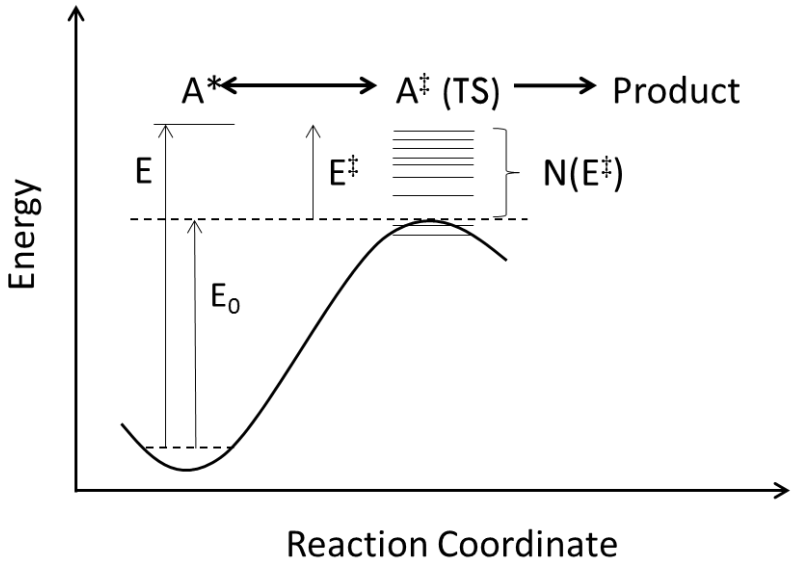

Figure 3.3 Pictorial representation of different quantities in RRKM theory, E (total energy), E_0 (threshold energy), $E^{\ddagger}$ (barrier height) and $N(E^{\ddagger})$ (number of available energy states).

Figure 3.3 shows a general unimolecular reaction of molecule *A*. Firstly A undergoes excitation by colliding with a bath gas to form A* (excited state). Upon collision, all vibrational modes of A are assumed to participate in the internal vibrational energy redistribution (IVR) [22, 23], that is, the energy of different quantum states of A* is redistributed, consistent with the ergodicity assumption. Then A* proceeds to the product by passing through the transition state, $A^{\ddagger}$. The transition state energy is lower than that of A*, consequently, there is an excess in energy ($E^{\ddagger}$). This is also known as the available energy and it basically determines the reactive flux of the reaction because the reactive flux is proportional to the number of available states of the transition state. The spacing of the energy levels of the transition state determines the density of states of the transition state. The advantage of this formulation of RRKM theory is that the zero-point energy can be incorporated into RRKM theory [22, 23]. Therefore, the barrier heights of all RRKM rate computations in this thesis are all zero-point corrected, which means that the barrier height is calculated as $(E_{TS} + ZPE_{TS}) - (E_{reactant} + ZPE_{reactant})$, where ZPE stands for zero-point energy.

The number of states, $N(E)$, and the density of states, $\rho(E)$, are the two central quantities in RRKM theory. Since RRKM theory is derived by employing classical mechanics, the two quantities can be approximated classically as:

$$N(E^{\ddagger}) = \frac{(E^{\ddagger})^{s}}{s! \prod_{i=1}^{s} h\nu_i} \tag{3.7}$$

$$\rho(E) = \frac{E^{s-1}}{(s-1)! \prod_{i=1}^{s} h\nu_i} \tag{3.8}$$

where s is the number of vibrational modes, E is the energy of the reactant and $E^{\ddagger}$ is the available energy of the transition state. However, the classical mechanical scheme is not an efficient method when there are a lot of energy states.

In order to circumvent this problem, Beyer and Swinehart developed an algorithm, which is known as the Beyer-Swinehart Direct Count Algorithm [28], to evaluate the number of states and the density of states exactly and efficiently for harmonic vibrations in molecules. The algorithm makes use of the vibrational frequencies of the reactants and the transition state to compute the number of ways of distributing a certain amount of energy among the bonds in the reactants and the transition state. This idea is consistent with the ergodicity assumption in RRKM theory. Finally, the number of vibrational states in the transition state is obtained by adding up all the vibrational levels with energy between 0 to $E^{\ddagger}$ (maximum possible energy) and the density of states is determined by the difference between the number of states at each energy. Beyer-Swinehart is the default algorithm used in VARIFLEX 1.0 [27] for evaluating the number of states and the density of states of harmonic vibrations in molecules.

The relationship between RRKM theory and transition state theory can be explained by inter-transformation of density of state and partition function as follows:

$$Q(T) = \int_0^{\infty} \rho(E) \exp(-\beta E)\, dE \tag{3.9}$$

$$\rho\,(E) = \frac{1}{2\pi i} \int_{-i\infty}^{+i\infty} Q(\beta) e^{-\beta E} d\beta \tag{3.10}$$

where $Q(T)$ is the partition function and β is defined as $1/(k_B T)$. Mathematically, the density of state relates to the corresponding partition function by a Laplace transform while the density of states is the inverse Laplace transform (ILT) [29] of the partition function. By using the Laplace transformation of density of states, one can show that RRKM is equivalent to unimolecular transition state theory in a microcanonical ensemble as expressed in equation (3.11):

$$k(T) = \frac{k_B T}{h Q_R} \int_{E_0}^{\infty} k(E) \exp\left(\frac{-E_0}{k_B T}\right) dE \tag{3.11}$$

where $k(T)$ is the TST rate coefficient and $k(E)$ is the RRKM rate coefficient.

3.3.1 Conservation of Angular Momentum

An important feature of the microcanonical formulation of RRKM theory allows the incorporation of angular momentum into rate coefficients, denoted as *E*,*J*-RRKM. This was implemented by Marcus [30, 31]. Radical-radical recombination reactions, bond fissions and ion-molecule reactions are reactions without a distinct barrier, so they are very sensitive to angular momentum. Conservation of angular momentum is therefore necessary in order to obtain reliable and accurate rate coefficients [32]. Suppose that two radicals interact through a long range attractive potential, then the Hamiltonian of the two radicals can be expressed in the Cartesian coordinates of one radical relative to another as:

$$H = \frac{1}{2\mu}\left(p_x{}^2 + p_y{}^2\right) + V(r) \tag{3.12}$$

where μ is the reduced mass of the two radicals and $V(r)$ is the attractive potential function. The pictorial description of the reacting system is shown in Figure 3.4.

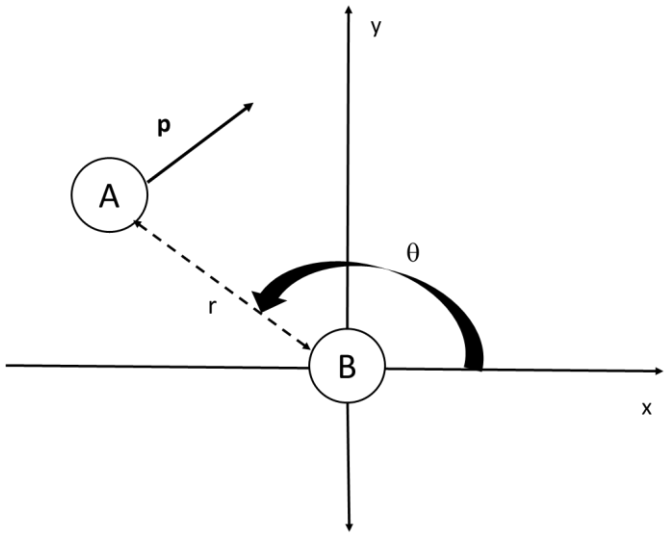

Figure 3.4 Cartesian coordinates and polar coordinates for two bodies (A and B) with relative momentum *p*

The Hamiltonian is then transformed to polar coordinate for convenience, using

$$x = r\cos\theta; y = r\sin\theta \tag{3.13}$$

Then the change of coordinate is performed for momentum as:

$$p_r = p_x cos\theta + p_y sin\theta \tag{3.14}$$

$$L = -p_x r sin\theta + p_y r cos\theta \tag{3.15}$$

where L is the angular momentum and finally the Hamiltonian in equation (3.12) is transformed to

$$H = \frac{1}{2\mu}\left(p_r{}^2 + \frac{L^2}{r^2}\right) + V(r) \tag{3.16}$$

The angular momentum of the reacting system is conserved because

$$\frac{dL}{dt} = -\frac{\partial H}{\partial \theta} = 0 \tag{3.17}$$

When the two radicals are far apart from each other, each radical has three degrees of translational energy. However, when they approach each together, some of their kinetic energy is transformed to rotational energy because of the conservation of angular momentum. With an intermediate non-zero angular momentum of the reacting system, a centrifugal barrier forms, which is known as the effective potential (V_{eff}) [33] along the reaction path (the center-of-mass distance between two radicals [34]) shown in Figure 3.5.

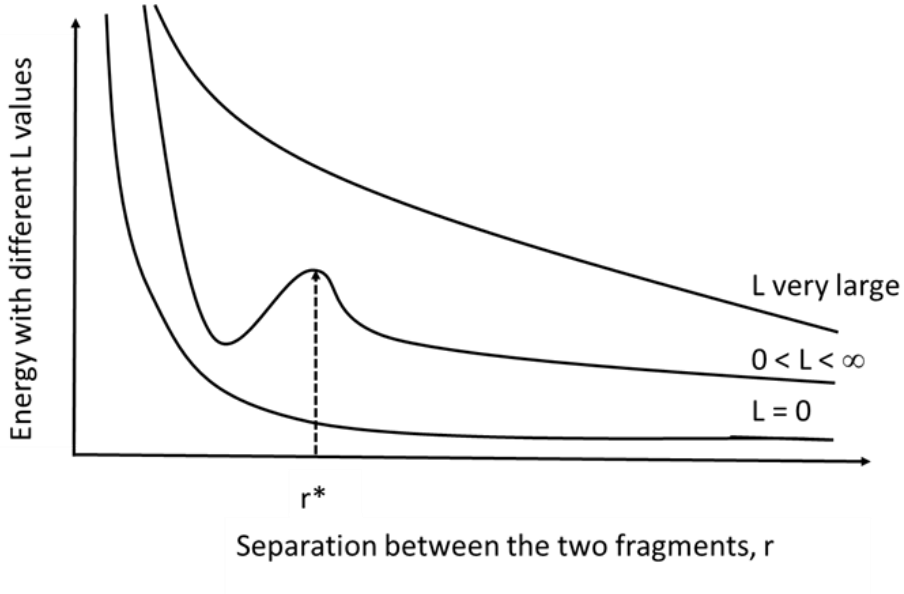

Figure 3.5 Centrifugal barrier along the reaction path under the conservation of angular momentum

Figure 3.5 shows three possible scenarios with different ranges of angular momentum values (L) [6]. The first case is that L is very large, so the potential energy is a monotonic decreasing function of inter-fragment distance, r. Another extreme case is that L goes to zero, which also leads to a monotonic decreasing function. The interesting case is when L is a non-zero intermediate value; this produces a centrifugal barrier in the potential energy function. The position that corresponds to the maximum of the centrifugal barrier is denoted as r^* and its value is determined by the variational principle which will be discussed in the next section.

The last step is to connect the effective potential to the evaluation of the number of states of the reacting system. By expanding the Hamiltonian in polar coordinates, the full Hamiltonian can be obtained as:

$$H = \frac{{p_r}^2}{2\mu} + \frac{L^2}{2\mu r^2} + V(r) = \frac{{p_r}^2}{2\mu} + V_{eff}(r) \tag{3.18}$$

$$V_{eff}(r) = \frac{L^2}{2\mu r^2} + V(r) = \frac{\hbar l(l+1)}{2\mu r^2} + V(r) = E_{rot} + V(r) \tag{3.19}$$

where E_{rot} is the rotational energy of the reaction system. Then the number of accessible energy states of the reacting system with energy greater than the effective potential is given by:

$$N(E^{\ddagger},J) = \int_0^{E-V_{eff}(r*)} \rho(E,J)dE \tag{3.20}$$

where E is the total energy of the reacting system. Finally, the rate coefficient at the E,J-RRKM level (RRKM theory implemented with the conservation of energy and angular momentum) is given by:

$$k(E^{\ddagger},J) = \frac{\sigma N(E^{\ddagger},J)}{h\rho(E)} \tag{3.21}$$

3.4 Variational Transition State Theory (VTST)

Transition state theory (TST) only gives the upper bound of the classical exact rate coefficient for a reaction. Although the evaluation of a TST rate coefficient is straight-forward, there are a few disadvantages of TST [35]:

1. The exact rate coefficient is overestimated because TST counts both non-reactive and reactive trajectories. The difference between a TST rate coefficient and an exact rate coefficient increases as temperature increases.
2. The shape and width of the potential energy surface near the saddle point region are not used in TST.
3. Quantum effects such as zero-point energy and tunneling are not considered in TST.

In order to overcome the above disadvantages, variational transition state theory (VTST) was developed. The key idea of VTST is to variationally minimize the reactive flux by moving the dividing surface [36]. Since the reactive flux is proportional to the number of reactive trajectories in phase space, one can eliminate some trajectories which re-cross the dividing surface if the reactive flux is minimized. Consequently, the dividing surface of VTST is not located at the saddle point anymore and the reaction system configuration with the minimum reactive flux along the reaction path is then known as a generalized transition state. VTST can be implemented in both a canonical ensemble and a microcanonical ensemble. There are three types of VTST employed in the work of this

thesis, namely, variational transition state theory (CVT), microcanonical variational transition state theory (μVT) and improved CVT (ICVT).

3.4.1 Canonical Variational Transition State Theory

The expression for the rate coefficient with a generalized transition state in a canonical ensemble is:

$$k_C^{GT}(T,s) = \sigma \frac{kT}{h} \frac{Q_{TS}(T,s)}{\Phi_R} \exp(-\beta V_{MEP}(s)) \tag{3.22}$$

The exponential factor in equation (3.22) accounts for the difference of the zero of energy between generalized transition state and the separate reactants. Φ_R has the same definition as that in the TST. $Q_{TS}(T,s)$ is the partition function of the generalized TS at s with the corresponding energy evaluated at $VMEP(s)$. Equation (3.22) can be rewritten in the thermodynamic form by employing the equilibrium constant ($K^{\neq}_{eq}$) and the reaction quotient at the standard state (K^0, 1 $cm^3 \cdot molecule^{-1}$).

$$K^{\neq}_{eq} = K^0 \exp\left(\frac{-\Delta G_C^{GT,0}(T,s)}{RT}\right) \tag{3.23}$$

Then equation (3.22) can be rewritten in terms of the standard-state Gibbs free energy change of the generalized transition state as:

$$k_C^{GT}(T,s) = \sigma \frac{kT}{h} K^0 \exp\left(\frac{-\Delta G_C^{GT,0}(T,s)}{RT}\right) \tag{3.24}$$

where

$$\frac{Q_{TS}}{\Phi_R} \exp\left(-\beta V_{MEP}(s)\right) = K^{\neq}_{eq} \tag{3.25}$$

Since the change in Gibbs free energy depends on both entropy and enthalpy, CVT rate coefficients include effects from enthalpic and entropic changes between the reactants and the generalized TS. In CVT, the minimum reactive flux criterion corresponds to the maximum Gibbs free energy change criterion [36, 37]. Therefore, the dividing surface is shifted to maximize the Gibbs free energy of activation along the reaction coordinate at each temperature and such location is denoted as $s_*^{CVT}(T)$. The CVT rate coefficient, k_C^{CVT}, is then given by the following expression:

$$k_C^{CVT} = \min k_C^{GT}(T,s) = k_C^{GT}[T, s_*^{CVT}] \tag{3.26}$$

In terms of implementation, a fourth degree polynomial fit to the free energy change of the generalized transition state at five values of reaction coordinate, which are nearest to the maximum of the free energy curve, is used to interpolate to obtain the $s_*^{CVT}(T)$ value [38].

3.4.2 Microcanonical Variational Transition State Theory

As an alternative to a canonical ensemble used in CVT, VTST can also be formulated in a microcanonical ensemble. This is characterized by constant total energy and such a formulation of VTST leads to microcanonical variational transition state theory (μVT). In μVT, a dividing surface along the minimum energy path in phase space is sought in order to minimize the reactive flux, which is proportional to the number of vibrational-rotational states with energy smaller than E (denoted as $N^{GT}{}_{vr}(E,s)$).

In μVT, the minimum reactive flux criterion corresponds to the minimum number of states criterion [39-41].

$$N^{\mu VT}(E) = \min\left(N^{GT}{}_{VT}(E,s)\right) \tag{3.27}$$

Therefore, the dividing surface is relocated to minimize the number of states along the reaction coordinate.

$$\frac{\partial N(E^{\ddagger},s)}{\partial s} = 0 \tag{3.28}$$

where s is the reaction coordinate. Then the microcanonical rate coefficient can be expressed as the Laplace transformation of the number of states, $N^{\mu VT}(E)$ as:

$$k(T) = \frac{Q_{el}(T)}{h\Phi_R}\int_0^{\infty} N^{\mu VT}(E)\exp(-\beta E)\,dE \tag{3.29}$$

It is very time consuming to evaluate the number of vibrational-rotational states for large molecules. In order to circumvent this problem, one can instead optimize the dividing surface (i.e. the generalized TS) up to the microcanonical threshold energy ($V_a{}^G(s^*)$) and

then use CVT for higher energy contributions. Such an approach is known as Improved Canonical Transition State Theory (ICVT), which will be discussed in section 3.4.3.

Variational RRKM theory is commonly used in computing the rate coefficients of barrierless association and dissociation reactions [34]. Then the variational RRKM rate coefficient is evaluated as:

$$k_{\mu VT}(E) = \frac{\sigma N(E^{\ddagger *})}{h\rho(E)} \tag{3.30}$$

3.4.2.1 Phase Space Theory

A variant of μVT, which builds on the *E*,*J*-RRKM approach, is phase space theory (PST) [42] introduced by Light in 1964. This aims to evaluate rate coefficients of radical-radical barrierless recombination reactions without using any information of the transition state. The effective potential in *E*,*J*-RRKM theory is defined as:

$$V_{eff}(r, l) = V(r) + \frac{\hbar l(l+1)}{2\mu r^2} \tag{3.31}$$

In PST, the long range isotropic attractive potential is approximated by:

$$V(r) = \frac{-C_6}{r^6} \tag{3.32}$$

where the coefficient, C_6, is approximated as:

$$C_6 = 1.5 \frac{\alpha_1 \alpha_2 IE_1 IE_2}{IE_1 + IE_2} \tag{3.33}$$

where α_i and IE_i are the polarizability and ionization energy of reactant i respectively. Then the number of states of the critical configuration at the peak of the centrifugal barrier in phase space theory can be evaluated quantum mechanically [43] as:

$$N(E,J) = (2J+1) \sum_{j_1,k_1,j_2,k_2 l,j,v_i} \Theta(E - E_1(e_1,v_1,j_1,k_1) - E_2(e_2,v_2,j_2,k_2) - V_{eff}(r,l) \times \Delta(J,j,l)\Delta(j,j_1,j_2)) \quad (3.34)$$

where e_i, v_i, j_i and k_i are the electronic state, vibrational state, angular momentum and the projection of angular momentum along a body-fixed axis for reactant I, respectively. E_i is the energy of reactant i, l is the orbital angular momentum, Δ is the triangle inequality and Θ is the Heaviside step function. The number of states can also be evaluated classically via:

$$N(E,J) = E^{(d-3)/2}\left(1 - \frac{2}{3\sqrt{3}}\left(\frac{J^2}{2\mu}E^{2/5}{C_6}^{-1/3}\right)^{3/2}\right)^{(d-3)/2} \quad (3.35)$$

where d is the number of rotational degrees of freedom and μ is the reduced mass of the reacting system. Finally, the PST rate coefficient can be evaluated as:

$$k(T) = \frac{1}{hQ}\int N(E,J)\exp\left(-\frac{E}{k_B T}\right)dEdJ \quad (3.36)$$

All rate coefficient calculations at RRKM, microcanonical TST and phase space theory levels in this work were performed using the software package, VARIFLEX 1.0 [27].

3.4.3 Improved Canonical Variational Transition State Theory

μVT gives a more accurate description of rate coefficients than CVT because it is implemented in the microcanonical ensemble in which the total energy is conserved. It gives rate coefficients which are in better agreement with the results of classical trajectory calculations than CVT because the energy near the threshold region is treated better in μVT than that in CVT [44]. The threshold energy in μVT is defined to be the maximum of the ${V_a}^G$ curve (${V_a}^G(s^*)$) (with quantum tunneling) [45] whereas the threshold energy of CVT is not at the saddle point [44, 45], which will be explained in detail in section 3.4.4.3. Consequently, there are some trajectories with less energy than the threshold energy but with positive momentum which are counted by CVT. Hence, CVT may overestimate rate coefficients. Although μVT yields more accurate results than CVT (especially at low temperatures), the evaluation of the density of states takes a long time. On the other hand,

the code of CVT is efficient, but its threshold energy is not as accurate as that in μVT. In order to take advantages of both μVT and CVT, Truhlar and coworkers compromised between efficiency and accuracy when they introduced the Improved Canonical Variational Transition State Theory (ICVT) [44]. In ICVT, the threshold energy is defined to be $V_a^G(s^*)$.

In ICVT, for energies below the threshold energy, the dividing surface is set at $s = 0$. For energies above threshold, the dividing surface is located at the maximum of the free energy of the improved generalized transition state. Then the resulting rate coefficient evaluated at the improved generalized transition state (k^{IGT}) is given by:

$$k^{IGT}(T,s) = \frac{k_B T}{h \Phi_R}\left\{\sum_{n=0}^{n_I^s} \exp\left[\beta V_a{}^G(s^*)\right] + \sum_{n=n_I^s+1}^{n_{\max}(s)} \exp\left[\beta V_a{}^G(n,s)\right]\right\} \quad (3.37)$$

where n is vibrational quantum number, n_I^s is the highest quantum number for which $V_a^G(s)$ at s is less than $V_a^G(s^*)$.

Finally, the rate coefficient at the ICVT level (k^{ICVT}) is evaluated as:

$$k^{ICVT}(T) = min\, k^{IGT}(T,s) \quad (3.38)$$

3.4.4 Incorporation of Quantum Effects

The classical mechanics has been used to develop TST and VTST to determine rate coefficients in the previous section. However, quantum mechanical effects may also be important in some reactions, such as in hydrogen transfer reactions where tunneling is important or low temperature reactions where quantum effects are significant. TST and VTST are formulated in the framework of classical mechanics so the state of the reaction system is defined by its momentum and position. However, in quantum mechanics, the momentum and the position of a system cannot be known simultaneously according to the Heisenberg uncertainty principle. In practice, only the vibrational partition functions of the molecules are evaluated quantum mechanically in TST and VTST and other quantum effects will be accounted by a multiplicative transmission coefficient.

3.4.4.1 Partition Functions

The evaluation of partition functions is central to the computation of rate coefficients. One way to introduce quantum mechanical effects to TST and VTST is to employ quantum mechanical partition functions instead of classical partition functions. This section is devoted to discussing the evaluation of different types of partition functions.

According to equation (3.2), Q_{TS} and Φ_R are necessary for the determination of rate coefficients. Φ_R is the reactant partition function. For example, in a bimolecular reaction (A + B $\rightarrow$ products), $\Phi_R(T)$ can be broken down into 3 components:

$$\Phi_R(T) = \Phi_{rel}^{A,B}(T) Q^A(T) Q^B(T) \tag{3.39}$$

where $Q^A(T)$ and $Q^B(T)$ are the total partition functions of the reactants (A and B) respectively and $\Phi_{rel}^{A,B}(T)$ is the relative translational partition function of the reactants which is evaluated as:

$$\Phi_{rel}^{A,B}(T) = \left(\frac{2\pi\mu}{\beta h^2}\right)^{\frac{3}{2}} \tag{3.40}$$

where μ is the reduced mass of the reactants.

For a polyatomic species, its electronic, vibrational, and rotational energy levels must be considered in the partition functions. If reactants A and B and the transition state are polyatomic species, their total partition functions can be written as:

$$Q^A(T) = Q_{ele}^A(T) Q_{vib}^A(T) Q_{rot}^A(T) \tag{3.41a}$$

$$Q^B(T) = Q_{ele}^B(T) Q_{vib}^B(T) Q_{rot}^B(T) \tag{3.41b}$$

$$Q^{TS}(T) = Q_{ele}^{TS}(T) Q_{vib}^{TS}(T) Q_{rot}^{TS}(T) \tag{3.41c}$$

where Q_{ele} is the electronic partition function, Q_{vib} is the vibrational partition function and Q_{rot} is the rotational partition function. If one of the reactants is an atom, only its electronic energy levels are considered.

3.4.4.1.1 Electronic Partition Function

The electronic partition function of a species, regardless of whether, it is an atom or a molecule, is evaluated quantum mechanically [46] as:

$$Q_{ele}(T) = \sum g \exp(-\beta \varepsilon_e) \tag{3.42}$$

where g is the degeneracy and ε_e is the energy of an electronic energy level. Since the spacing between electronic energy levels is usually much larger than thermal energy ($k_B T$), only energy levels of the lowest electronic state are usually considered.

3.4.4.1.2 Rotational Partition Function

The rotational partition function of a molecule is computed using classical mechanics because the rotational energy levels are usually closely spaced. Therefore, the rotational partition function can be approximated classically [47, 48] as:

$$Q_{rot}(T) = \frac{2I}{\hbar^2 \beta \sigma} \text{ for linear species} \tag{3.43}$$

$$Q_{rot}(T) = \frac{1}{\sigma}\left[\left(\frac{2}{\hbar^2 \beta}\right)^3 \pi I_x I_y I_z\right]^{\frac{1}{2}} \text{ for non-linear species} \tag{3.44}$$

where σ is the symmetry factor, I is a moments of inertia and the subscripts (x, y and z) represent the direction of the moments of inertia in Cartesian coordinate.

3.4.4.1.3 Vibrational Partition Function

All vibrational modes are assumed to behave as harmonic oscillators and no mode-mode couplings between vibrational modes are assumed. The vibrational partition functions are evaluated quantum mechanically [46] as:

$$Q_{vib}(T) = \prod_{m=1}^{3N-\eta} \sum_{n} \exp(-\beta E_{m,n}) \tag{3.45}$$

where m is the index of the degrees of freedom of the species and $E_{m,n}$ is the vibrational energy which is expressed as:

$$E_{m,n} = \hbar\omega_m \left(n_m + \frac{1}{2}\right) \tag{3.46}$$

where ω_m is the vibrational frequency of the *m-th* mode and n_m is the vibrational quantum number in the *m-th* mode.

For torsional vibrational modes which are anharmonic, Chuang and Truhlar derived a simple approximation for treating a torsional mode as a hindered rotation with a partition function [49-52] which is evaluated as:

$$Q_{hin} = \frac{\tanh\left(\pi W_j\right)^{0.5}}{2\sinh\left(0.5\beta\hbar\omega_j\right)} \tag{3.47}$$

In this equation, ω is the frequency of the torsional vibrational mode j and W_j is the torsional barrier height which is written as:

$$W_j = 2I_j \left(\frac{\omega_j}{M}\right)^2 \tag{3.48}$$

I_j is the moment of inertia of the groups of atoms responsible for the torsional motion and M is the number of minima of one complete cycle of hindered rotation. The above scheme for accounting for the torsional contribution to the partition function is known as the Rω scheme which was used in this thesis. The vibrational partition function with hindered rotations is calculated as $Q_{vib} \cdot Q_{hin}$.

The partition functions are normally evaluated classically, but in order to partially quantize TST and VTST, classical partition functions can be replaced by their quantum mechanical analogs. In practice, only the vibrational partition function is replaced by its quantum mechanical analog to account for the quantized vibrational energy levels and zero-point energy. The transition state has 3N-η degrees of freedom in which one of them is the unbound normal mode. For the 3N-η-1 bounded normal modes, quantum mechanical vibrational partition functions are used and the zero of energy is the Born-Oppenheimer electronic energy. For the electronic partition function, the potential energy surface is adiabatic so there is essentially no difference between using the classical partition function and using the quantum mechanical partition function. For the rotational

partition functions, since the levels of rotational energy are closely spaced (they are effectively continuous), little accuracy (1%) is lost if classical partition functions are used [53].

3.4.4.2 Tunneling

A multiplicative transmission coefficient accounts for two non-classical effects, namely tunneling and non-classical reflection. Mathematically, this can be broken down into two parts (κ^T and κ^{CAG}):

$$\kappa^{T/CAG} = \kappa^T \kappa^{CAG} \tag{3.49}$$

where κ^T and κ^{CAG} are the transmission coefficients for tunneling and non-classical reflection, respectively. Tunneling is likely to be significant for reactions which involve transfer of a hydrogen atom with a pronounced barrier height. Non-classical reflection arises from the fact that the reaction coordinate is not separable from the bounded normal modes in reality because of the curvature of the reaction path, although it is assumed to be separable.

There are three tunneling methods used in this thesis, namely one-dimensional Wigner tunneling correction [54], zero curvature tunneling (ZCT) correction [55] and small curvature tunneling (SCT) correction [56, 57] in which the latter two methods are multi-dimensional.

3.4.4.2.1 Wigner tunneling

Wigner tunneling is the simplest tunneling scheme. In Wigner tunneling, the potential function is assumed to be a parabolic function and the particle is considered to tunnel through the parabolic potential. It is a semi-classical method and the expression for κ^T in this case is

$$\kappa^{\neq/W} = 1 + \frac{1}{24}\left|\frac{\beta h \omega^{\neq}}{2\pi}\right|^2 \tag{3.50}$$

where $\omega^{\neq}$ is the vibrational frequency of the imaginary mode of the transition state. Although Wigner tunneling correction is simple, it is usually only significant at high temperatures.

3.4.4.2.2 Semi-classical adiabatic ground-state tunneling

Since both zero-curvature tunneling (ZCT) and small curvature tunneling (SCT) correspond to semi-classical adiabatic ground state tunneling correction factors, they are discussed in the same section. Wigner tunneling correction is a one-dimensional correction; however, an accurate treatment of tunneling corrections must involve multi-dimensional correction (i.e. multiple vibrational modes). In multi-dimensional tunneling corrections, the zero-point energy of all vibrational modes along the tunneling path must be considered [21]. Both SCT and ZCT are multi-dimensional tunneling correction methods and they require knowledge of the reactant, the reactant's reduced mass and the one dimensional effective potential for describing the tunneling process. $V_a{}^G(s^*)$ is used as the effective potential energy for tunneling.

With the potential function known, the next step is to construct the classical Hamiltonian function.

$$H(p,s) = \frac{{p_s}^2}{2\mu} + {V_a}^G(s) \tag{3.51}$$

The imaginary action integral is then constructed from the classical Hamiltonian.

$$S(E) = \hbar \int_{s<E}^{s>E} \left\{2\mu\left[E - {V_a}^G(s)\right]\right\}^{1/2} ds \tag{3.52}$$

The action integral, $S(E)$, is imaginary in the tunneling region because the system carries negative kinetic energy (hence negative momentum) along the tunneling path. Then the semi-classical adiabatic ground state (SAG) tunneling probability (P^{SAG}) for energies below the top of the effective potential (the maximum of the $V_a{}^G$ curve) is given by:

$$P^{SAG}(E) = \frac{1}{1 + \exp[2S(E)]} \tag{3.53}$$

Since equation (3.53) only takes care of the quantum effects below $V_a{}^G(s^*)$ but not the quantum mechanical effects above $V_a{}^G(s^*)$, it is modified with an assumption, which is that the shape of the potential near the top is parabolic, in order to derive an expression for P^{SAG} for a full range of energies, as:

$$P^{SAG} = \begin{cases} 0, & E < E_0 \\ \{1 + \exp[2S(E)]\}^{-1}, & E_0 \leq E \leq {V_a}^{AG} \\ 1 - P^{SAG}\left(2{V_a}^{AG} - E\right), & {V_a}^{AG} \leq E \leq 2{V_a}^{AG} - E_0 \\ 1, & 2{V_a}^{AG} - E_0 < E \end{cases} \tag{3.54}$$

where E_0 is the minimum amount of energy which makes tunneling possible. In a bimolecular reaction, E_0 is defined as:

$$E_0 = \max\left[{V_a}^{G}(s = -\infty), {V_a}^{G}(s = +\infty)\right] \tag{3.55}$$

Then the correction factor of tunneling correction in a canonical ensemble (P^{SAG}) is obtained by:

$$\kappa^{SAG} = \frac{\beta \int_0^{\infty} P^{SAG}(E) \exp(-\beta E)\ dE}{\exp(-\beta {V_a}^{AG})} \tag{3.56}$$

The difference between ZCT and SCT corrections lies in the evaluation of equation (3.52) which is the imaginary action integral. In the ZCT correction, since it does not account for the effect of the curvature of the reaction path on tunneling, the tunneling path is exactly the same as the MEP. Therefore, the reduced mass in equation (3.52) is a constant along the reaction coordinate. Since the reaction coordinate is intrinsically non-separable from the bound normal modes, the curvature of the reaction path must be accounted for in order to obtain a realistic tunneling correction factor. Therefore, the ZCT correction scheme always underestimates the tunneling contribution to the reaction rate [58]. Marcus and Coltrin [59] showed that the tunneling path was not necessarily the same path as the MEP. In fact, a coupling term in kinetic energy in the reaction path Hamiltonian arises due to the non-separability between the reaction coordinate and the bound normal modes. This coupling term corresponds to a negative centrifugal effect which increases the tunneling probability via a shorter path on the concave side of the MEP. Since the imaginary action is proportional to the length of the tunneling path and the tunneling path is shortened, the magnitude of the imaginary action decreases. Hence, the tunneling probability increases. This is known as the "corner-cutting" effect. The Marcus-Coltrin tunneling path is essentially an arc with arc length of $d\zeta$. The effective mass in Marcus-Coltrin's theory is:

$$\mu_{eff} = \mu \left(\frac{\mathrm{d}\xi}{\mathrm{ds}}\right)^2 \tag{3.57}$$

where *s* is the reaction coordinate and $d\zeta/ds$ is termed the Jacobian factor. Truhlar and coworkers introduced the small curvature tunneling (SCT) correction [56, 57]. This extends the Marcus-Coltrin tunneling path to a three dimensional potential energy surface for polyatomic reactions. They initially realized that the Jacobian factor in the implementation of the Marcus-Coltrin tunneling path would be unrealistic if they extended the potential surface to three dimensions. Therefore, they approximated the Jacobian factor in SCT with an expression which is a function of the coupling components between the reaction coordinate and the normal bound modes, and the vibrational turning points (vibrational turning points are where the extremities of a vibrational energy level meets the potential energy curve). Then the arc length (i.e. the SCT tunneling path) is approximated as

$$\frac{d\xi}{ds} = \{[1 - a(s)]^2 + (dt/ds)^2\}^{1/2} \tag{3.58}$$

where

$$a(s) = |\kappa(s)t(s)| \; and \; t(\quad) = \left[\frac{\hbar}{\mu\omega(s)}\right]^{1/2} \tag{3.59}$$

where $\kappa(s)$ is the curvature of the reaction coordinate, which is the square root of the coupling components between the reaction coordination and the bound normal modes, and $t(s)$ gives the vibrational turning points.

Since the Jacobian factor (equation (3.58)) is undefined when $t \geq 1/\kappa$, an exponential function is used to replace the arc length function, this is:

$$\frac{\mu_{eff}}{\mu} = \left(\frac{d\xi}{ds}\right)^2 = \min\left\{\exp\left\{-2a(s) - [a(s)]^2 + \left(\frac{dt}{ds}\right)^2\right\}\right. \tag{3.60}$$
$$1$$

$V_a^G(s^*)$ serves as the effective potential for tunneling. Therefore, $\kappa^{TST/CAG}$ needs to be included in the calculating of tunneling and it is discussed in details in the next section.

3.4.4.3 Classical adiabatic ground state (CAG) transmission coefficient

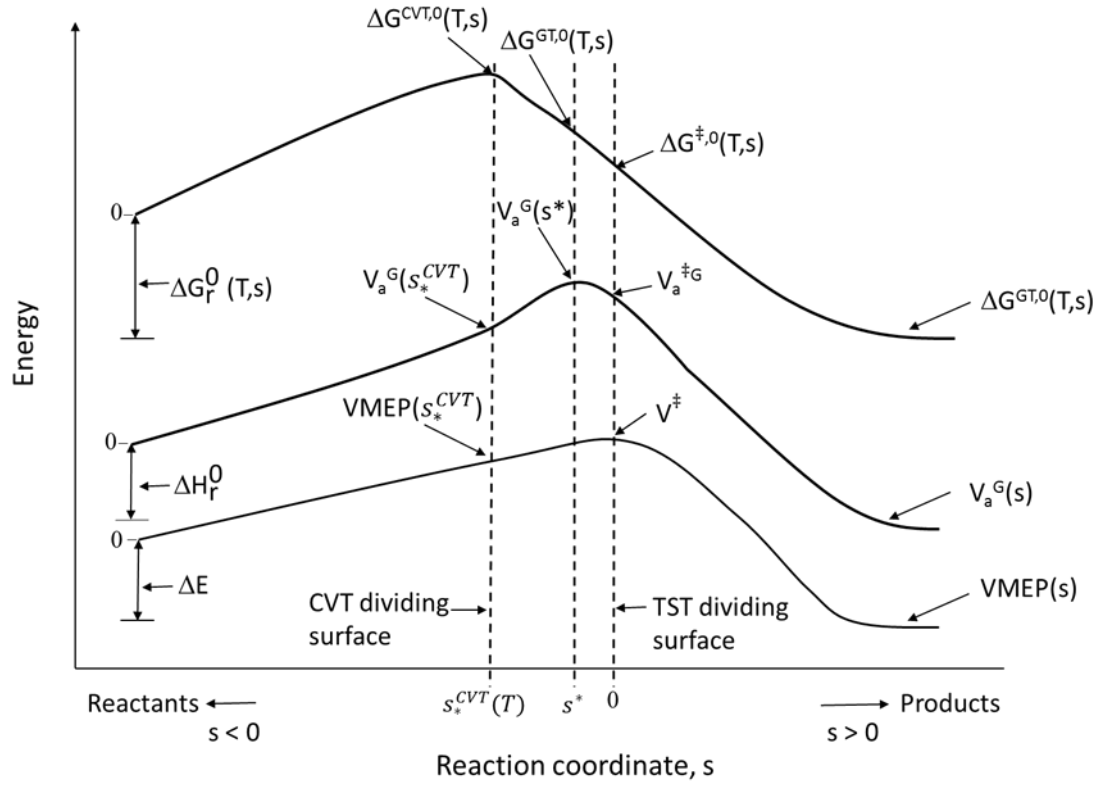

Figure 3.6 - Pictorial representation of some important quantities associated with energy on the classical potential energy curve (*VMEP*(*s*)), vibrationally adiabatic ground-state potential energy curve ($V_a^G(s)$) and the generalized free energy of activation curve ($\Delta G^{GT,0}(T,s)$).

Figure 3.6 shows various important quantities associated with energy in calculation of rate coefficients at the TST and CVT levels respectively. At the TST level, the barrier height used in the calculation is the classical potential energy at $s = 0$ (i.e. saddle point), $V^{\ddagger}$, on the *VMEP* curve. For RRKM/microcanonical TST calculations in general, the barrier height employed in the calculation is $V_a^{\ddagger G}$ on the V_a^G curve. At the CVT level, the barrier height used in calculations is $\Delta G^{CVT,0}(T,s)$ on the $\Delta G^{GT,0}$ curve. In the previous discussion on tunneling correction, the maximum of the V_a^G curve, $V_a^G(s^*)$, is used as the effective potential. Next, in the rest of this section, another role of $V_a^G(s^*)$ is discussed in detail which is crucial to obtain reliable rate coefficients.

There is another important aspect of tunneling correction, which involves the accurate treatment of classical threshold energy. Although the tunneling path has been treated in the previous section, quantum mechanical effects of the classical motion of the reaction coordinate have not yet been considered. In the previous section, $V_a^G(s^*)$ is

shown as the effective potential for the tunneling correction for VTST and it actually also serves as the classical threshold energy for VTST. However, the threshold energy of CVT is not $V_a^G(s^*)$ but $V_a(s_*^{CVT})$. Therefore, a classical adiabatic ground state (CAG) transmission coefficient [60, 61] is required and it is evaluated as:

$$\kappa^{CVT/CAG} = exp\{\beta[V_a{}^G(s_*^{CVT}(T)) - V_a{}^G(s^*)\} \quad (3.61)$$

For μVT and ICVT, their classical threshold energies are defined to be $V_a{}^G(s^*)$, and the generalized TS dividing surface is at $s^*(V_a^G)$ so they do not have any CAG factors. For TST, the transition state is located at the saddle point, so the maximum of the *VMEP*(s) curve is at $s = 0$. When the *VMEP* and the ΔZPE curves sum up to give the V_a^G curve, the location of ($V_a^G(s^*)$) is not necessarily at $s = 0$. Therefore, a CAG factor is necessary for TST [60, 61] to account for the accurate classical threshold energy. It is given by:

$$\kappa^{TST/CAG} = exp[V_a{}^G(s=0) - \beta(V_a{}^G(s^*)] \quad (3.62)$$

Therefore, the overall rate coefficient [60] is given by:

$$k(TST\ level\ with\ tunneling) = \kappa^T \kappa^{CAG} k^{TST\ level} \quad (3.63)$$

All rate coefficient calculations at the TST, the CVT, and the ICVT levels with tunneling corrections at the ZCT and the SCT levels in this work were performed using the software package, POLYRATE 2010-A [20].

3.5 Unified Statistical Theory and the Two Transition State Theory

A bimolecular reaction with a negative barrier is a class of reaction that is very common in combustion [62], atmospheric science [63, 64] and space science [65] in which kinetic modeling plays an important role. Usually this type of reaction involves radical-radical or ion-molecule reactions. This problem was first studied by Hirschfelder and Wigner [66]. They treated it as a trajectory recrossing problem in phase space and they came up with transmission and reflection coefficients of the reactive flux to account for the negative barrier situation. Miller built on the work of Hirschfelder and Wigner to

formulate the reflection coefficient and the transmission coefficient in terms of the number of states [67]. Then Miller considered that there are two bottlenecks in this type of reaction, as opposed to the fact that there is only one bottleneck in a typical unimolecular or bimolecular reactions with a pronounced barrier as determined by the maximum of the Gibbs free energy of activation or the minimum number of available states along the reaction coordinate. Figure 3.7 shows the typical contour plot of a bimolecular reaction with a negative barrier.

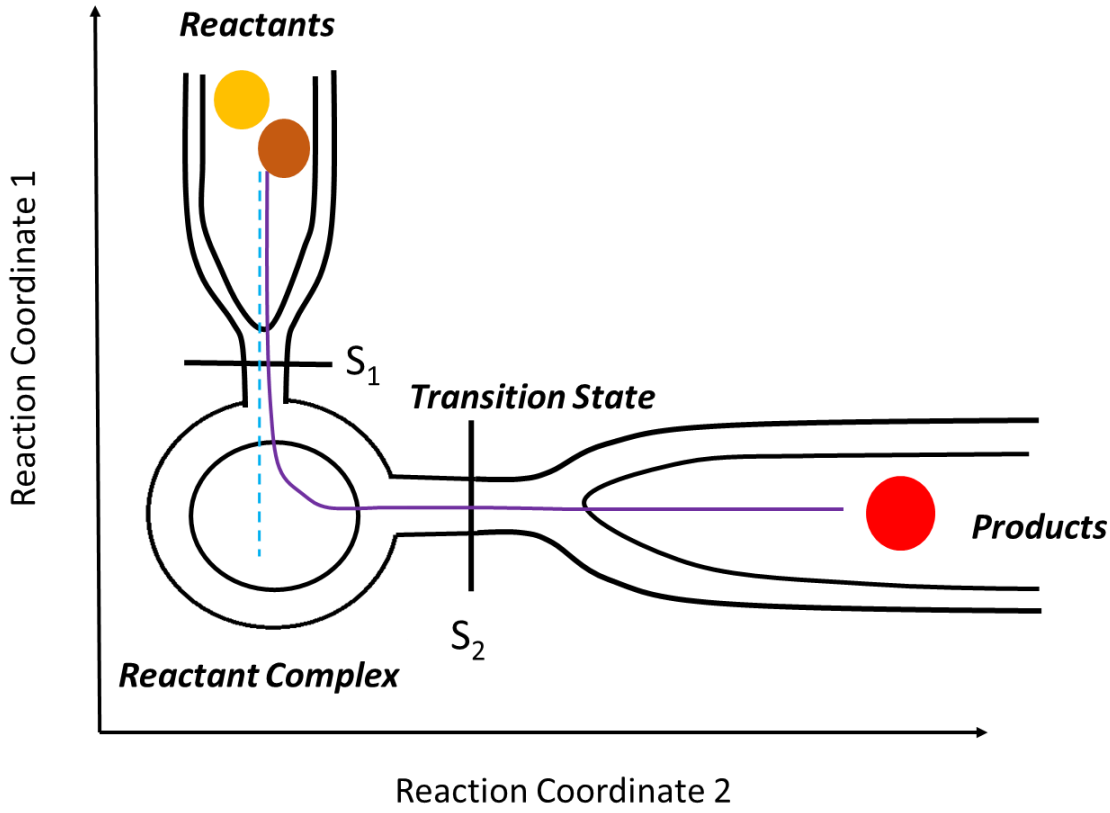

Figure 3.7 A contour plot of the potential energy surface of a bimolecular reaction with a negative barrier

In Figure 3.7, S_1 and S_2 are dividing surfaces. At low energy/temperature, the two reactants undergo barrierless association to cross the first dividing surface (S_1) to form the reactant complex (i.e. the dotted trajectory in the above figure) where the first dividing surface is actually the centrifugal barrier, as discussed, in phase space theory (section 3.4.2.1). Since the thermal energy is low at low temperature, the reacting system does not have enough energy to cross the second dividing surface (S_2, the transition state). At high temperature, the two reactants will cross the first dividing surface to form the reactant

complex (i.e. the purple solid trajectory) and the reacting system will have enough energy to cross the second dividing surface (S_2) to form the products but with a smaller velocity because it has to cross a pronounced barrier. Therefore, at low temperature, the major bottleneck is at the centrifugal barrier whereas the transition state is the major bottleneck at high temperature. At intermediate temperature range, both bottlenecks can contribute to the overall rate coefficients.

Miller uses PST and TST to obtain overall rate coefficients for the separate rate coefficients for the reactive fluxes passing through the centrifugal barrier and the saddle point respectively in a microcanonical ensemble and this approach is known as the unified statistical theory [67]. Garrett and Truhlar derived a canonical implementation of unified statistical theory, which is known as canonical unified statistical theory [67]. The overall rate coefficient at the CUS level is expressed as:

$$\frac{1}{k^{CUS}} = \frac{1}{k_{PST}} + \frac{1}{k_{TST}} \tag{3.64}$$

Greenwald, Klippenstein and Georgievskii derived a two-transition state theory [62, 63] which builds on Miller's unified statistical theory. They introduced two TSs, the outer transition state and the inner transition state respectively to represent S_1 and S_2 in Figure 3.7. They also emphasized the importance of conservation of angular momentum for treating bimolecular reactions with a negative barrier so the rate coefficients of the reactive fluxes passing through the outer and inner transition states should be evaluated at energy and angular momentum resolved levels. The outer transition state dominates at low temperatures and the inner transition state dominates at high temperatures, so both transition states can contribute to the overall rate coefficient at intermediate temperatures. The combined number of states contributed by both outer and inner transition states is given by:

$$\frac{1}{N_{eff}^{\neq}(E,J)} = \frac{1}{N_{outer}(E,J)} + \frac{1}{N_{inner}(E,J)} \tag{3.65}$$

Then the thermal rate coefficients of the two transition state theory are expressed as:

$$k(T) = \frac{1}{hQ_R}\int N_{eff}^{\neq}(E,J)\exp(-E\beta)dEdJ \tag{3.66}$$

3.6 Summary

Trajectories in phase space are used throughout this chapter as an illustration to introduce the classical mechanical basis of different levels of transition state theory (TST) and variational transition state theory (VTST), in both canonical and microcanonical ensembles. The methods of computing rate coefficients of reactions with and without barriers have also been discussed in detail. Different ways to enhance the accuracy of VTST (such as using quantum mechanical partition functions, accounting for tunnel corrections and obtaining accurate threshold energy) have also been reviewed. The methods described in this chapter have been used to compute rate coefficients of the $CH_3C(O)OCH_3$ + Cl reaction (Chapter 4) and the BrO + HO_2 reaction using the two transition state model (Chapter 5).

3.7 References

1. M. Baer, Ed. Theory of Chemical Reaction Dynamics. CRC Press: Boca Raton, Floria, 1985.
2. Miller, W.H. J. Phys. Chem. A 1998, 102, 793–806.
3. Wahnström, G.;Carmeli, B.; Metiu , H. J. Chem. Phys. 1988, 88, 2478-2491.
4. Fernandez-Ramos, A.; Miller, J.A.; Klippenstein, S.J.; Truhlar, D.G. Chem. Rev. 2006, 106, 4518-4584.
5. Goldstein, H. Classical Mechanics. Addison-Wesley: Reading MA., 1950.
6. Gilbert, R. G.; Smith, S. C. Theory of Unimolecular and Recombination Reactions. Blackwell Scientific Publications: Oxford, UK, 1990.
7. Child, M.S. Molecular Collision Theory. Academic: London, 1974.
8. Miller, W.H. Adv. Chem. Phys. 1974, 25, 69.
9. Miller, W.H. Adv. Chem. Phys. 1975, 30, 77.
10. Raff, L.M. and Thompson, D.L. The classical trajectory approach to reactive scattering. in Theory of chemical reaction dynamics, Vol. III; Baer, M., Ed. CRC Press: Boca Raton, FL, 1985.
11. Porter, R.N. Ann. Rev. Phys. Chem. 1974, 25, 317-355.
12. Garrett, B.C.; Truhlar, D.G. J. Phys. Chem. 1980, 84, 805-812.
13. H. Eyring, J. Chem. Phys. 1935, 3, 107.
14. Evans, M.G.; Polanyi, M. Trans. Faraday Soc. 1935, 31, 875.
15. Wigner, E. Trans. Faraday Soc. 1938, 34, 29.
16. Eyring, H.; Wynne-Jones, W. F. K. J. Chem. Phys. 1935, 3, 492.
17. Truhlar, D. G.; Isaacson, A. D.; Garrett, B. C. Generalized transition state theory. In Theory of Chemical Reaction Dynamics; Baer, M., Ed.; CRC Press: Boca Raton, FL, 1985; pp 71.
18. Garrett, B.C.; Truhlar, D.G. J. Phys. Chem. 1980, 84, 805-812.
19. Truhlar, D.G.; Garrett, B.C. Ann. RevIas. Phys. Chem. 1984, 35, 159-189.
20. Zheng, J.; Zhang, S.; Lynch, B. J.; Corchado, J. C.; Chuang, Y.-Y.; Fast, P. L.; Hu, W.-P.; Liu, Y.-P.; Lynch, G. C.; Nguyen, K. A. et al. POLYRATE version 2010-A (June, 2010), Copyright 1988-2010 D. G. Truhlar and Regents of the University of Minnesota, Minneapolis, Minnesota, U.S.A.
21. Fernandez-Ramos, A.; Ellingson, B. A.; Meana-Paneda, R.; Marques, J. M. C.; Truhlar, D. G. Theor. Chem. Acc. 2007, 118, 813.
22. Marcus, R.; Rice, O.K. J. Phys. Colloid. Chem. 1951, 55, 894.
23. Marcus, R.A. J. Chem. Phys. 1952, 20, 4658.

24. Oref, I.; Rabinovitch, B.S. Acc. Chem. Res. 1979, 12, 166-175.
25. Jarrod, M. F. Introduction to Statistical Reaction Rate Theories in Clusters of Atoms and Molecules, Theory, Experiment and Clusters of Atoms (Springer Series in Chemical Physics 52). Haberland, H. Ed; Springer: Berlin, 1994; pp 166.
26. Marcus, R.A. Phil. Trans. R. Soc. Lond. A 1990, 332, 283-296.
27. Klippenstein, S. J.; Wagner, A. F.; Dunbar, R. C.; Wardlaw, D. M.; Robertson, S. H. VARIFLEX , Version 1.0; Argonne National Laboratory: Argonne, IL, 1999.
28. Beyer, T. and Swinehart, D. F., Comm. ACM 1973, 16, 379.
29. Romanini, D.; Lehmann, K. K. J. Chem. Phys. 1993, 98, 6437-6444.
30. Marcus, R. A. J. Chem. Phys. 1965, 43, 2658.
31. Marcus, R. A. J. Chem. Phys. 1970, 52, 1018.
32. Pitt, I. G.; Gilbert, R. G.; Ryan, K. R. J. Phys. Chem. 1995, 99, 239-247.
33. Zhang, P.; Klippenstein, S. J.; Law, C. K. J. Phys. Chem. A 2013, 117, 1890-1906.
34. Klippenstein, S. J.; East, A. L. L.; Allen, W. D. J. Chem. Phys. 1996, 105, 118-140.
35. Garrett, B.C.; Truhlar, D. G. J. Phys. Chem. 1979, 83, 1052-1079.
36. Truhlar, D.G.; Garrett, B.C. Ann. Rev. Phys. Chem. 1984, 35, 159.
37. Wigner, E. J. Chem. Phys. 1937, 5, 720.
38. Truhlar, D. G.; Isaacson, A. D.; Garrett, B. C. Generalized transition state theory. In Theory of Chemical Reaction Dynamics; Baer, M., Ed.; CRC Press: Boca Raton, FL, 1985; pp 65.
39. Hase, W. L. J. Chem. Phys. 1972, 57, 730.
40. Hase, W. L. J. Chem. Phys. 1976, 64, 2442.
41. Garrett, B. C.; Truhlar, D. G. J. Chem. Phys. 1979, 70, 1593.
42. Light, J. C. J. Chem. Phys. 1964, 40, 3221-3229.
43. Klippenstein, S.J.; Cline, J. I. J. Chem. Phys. 1995, 103, 5451.
44. Garrett, B.C.; Truhlar, D.G.; Grev, R.S.; Magnuson, A.W. J. Phys. Chem. 1980, 84, 1730-1748.
45. Truhlar, D. G.; Issacson, A. D.; Skodje, R. T.; Garrett, B. C. J. Phys. Chem. 1982, 86, 2252-2261.
46. McQuarrie, D. A. Statistical Thermodynamics; New York: Harper and Row, 1973.
47. Garrett, B.C.; Truhlar, D.G. J. Chem. Phys. 1979, 70, 1593.
48. Miller, W.H.; Handy, N.C.l Adams, J.E. J. Chem. Phys. 1980, 72, 99.
49. Truhlar, D.G. J. Comp. Chem. 1991, 12, 266-270.
50. Chuang, Y.-Y; Truhlar, D.G. J. Chem. Phys. 2000, 112, 1221.
51. Chuang, Y.-Y; Truhlar, D.G. J. Chem. Phys. 2004, 121, 7036 (E).
52. Chuang, Y.-Y; Truhlar, D.G. J. Chem. Phys. 2006, 125, 084305.

53. Garrett, B. C.; Truhlar, D. G. J. Am. Chem. Soc. 1979, 101, 4534.
54. Wigner, E. P. Z. Physik. Chem. 1932, B19, 203.
55. Truhlar, D. G.; Kupperma. A. J. Am. Chem. Soc. 1971, 93, 1840.
56. Lu, D. H.; Truong, T. N.; Melissas, V. S.; Lynch, G. C.; Liu, Y. P.; Garrett, B. C.; Steckler, R.; Isaacson, A. D.; Rai, S. N.; Hancock, G. C.; Lauderdale, J. G.; Joseph, T.; Truhlar, D. G. Comput. Phys. Comm. 1992, 71, 235.
57. Liu, Y. P.; Lynch, G. C.; Truong, T. N.; Lu, D. H.; Truhlar, D. G.; Garrett, B. C. J. Am. Chem. Soc. 1993, 115, 2408.
58. Truhlar, D. G.; Kuppermann, A. J. Chem. Phys. 1972, 56, 2232-2252.
59. Marcus, R.A.; Coltrin, M.E. J. Chem. Phys. 1977, 67, 2609.
60. Fernández-Ramos, A.; Miller, J. A.; Klippenstein, S. J.; Truhlar, D. G. Modeling the Kinetics of Bimolecular Reactions Chem. Rev. 2006, 106, 4518-4584.
61. Fernandez-Ramos, A.; Ellingson, B. A.; Garret, B. C.; Truhlar, D. G. In Reviews in Computational Chemistry, Vol. 23; Lipkowitz, K. B.; Cundari, T. R. (Eds.) Wiley-VCH: Hoboken, NJ, 2007; pp. 125.
62. Greenwald, E. E.; North, S. W.; Georgievskii, Y.; Klippenstein, S. J. J. Phys. Chem. A 2005, 109, 6031-6044.
63. Greenwald, E.E.; North, S.W.; Georgievskii, Y.; Klippenstein, S.J. J. Phys. Chem. A 2007, 111, 5582-5592.
64. Daranlot, J.; Bergeat, A.; Caralp, F.; Caubet, P.; Costes, M.; Forst, W.; Loison, J-C.; Hickson, K. M. ChemPhysChem 2010, 11, 4002-4010.
65. Klippenstein, S.J.; Georgievskii, Y. J. Phys. Chem. A 2010, 114, 278-290.
66. Hirschfelder, J. O.; Wigner, E. J. Chem. Phys. 1939, 7, 616.
67. Miller, W. H. J. Chem. Phys. 1976, 65, 2216-2223.
68. Garrett, B. C.; Truhlar, D. G. J. Chem. Phys. 1982, 76, 1853-1858.

Chapter 4.

Theoretical Study of the Methyl Acetate with Cl atom reaction

4.1 Introduction

Volatile organic compounds (VOCs) are widely present in the atmosphere and the dominant atmospheric degradation pathways for VOCs are the reactions with the hydroxyl (OH) radical, which is a very important atmospheric oxidizing agent [1]. A major subclass of VOCs which contain oxygen are known as oxygenated volatile organic compounds (OVOCs), such as esters, alcohols and ketones. Fuel additives were developed in the 1970s after the prohibition of the use of tetraethyl lead in fuels in the late 1970s [2]. OVOCs were found to function as fuel additives because they could effectively reduce the emissions of carbon monoxide [3] effectively during gasoline combustion. Besides, OVOCs are also widely used as solvents in the industry. Apart from anthropogenic sources, OVOCs are also emitted naturally. OVOCs have low vapor pressure, so they can easily escape to the atmosphere [2]. Similar to other VOCs, the major degradation pathways of OVOCs are also the reactions with the OH radical [2]. An example of an atmospherically important esters is methyl acetate ($CH_3C(O)OCH_3$), which is widely used industrially, such as organic solvents, perfumes, flavorings, by-product formed in the incomplete combustion of biodiesel [4-7]. It is also formed naturally in vegetation.

Although VOCs are mainly oxidized by the OH radical as the major atmospheric fate, it turns out that the reactions between chlorine atom in the atmosphere and VOCs proceed 10 to 100 times faster than those with the hydroxyl radical [8]. Chlorine atom is an important oxidant [9] in the atmosphere and it is produced by photolysis of chlorine-containing compounds such as sea salt aerosols [10], nitrosyl chloride (ClNO), and nitryl chloride ($ClNO_2$) [11]. Its peak concentration in the marine boundary layer (MBL) have

been measured to be 10^3 - 10^6 atoms/cm^3, so the ratio of concentration of chlorine atoms to concentration of hydroxyl radical is 10^3 higher than usual [12, 13]. In this connection, the reactions between VOCs and chlorine atom are of atmospheric significance, especially in the MBL. Consequently, reliable rate coefficients of VOCs + Cl reactions are required for accurate atmospheric modelling.

The $CH_3C(O)OCH_3 + Cl \rightarrow HCl + CH_3C(O)OCH_2$ reaction was considered for this computational study for a number of reasons. First, as mentioned in the beginning, the reaction can be important in MBL where the concentration of Cl atom is high. Second, there has been some experimental studies on the kinetics on this reaction and they conclude that the hydrogen abstraction by Cl atoms almost solely occur (>95%) at the methoxy end of $CH_3C(O)OCH_3$ [6, 14-16] from product yield analyses. Thus there is essentially one channel of the reaction. The experimental rate coefficients at 298 K were measured to be between 1.93 ± 0.27 and 2.86 ± 0.35 x 10^{-12} $cm^3molecule^{-1}s^{-1}$ (the lower and upper bound values are taken from references 14 and 8 respectively; the value of 7.0 x 10^{-13} $cm^3molecule^{-1}s^{-1}$ which was misquoted in reference 13, was originally taken from reference 16). Moreover, Cuevas and co-workers (2005) determined the rate coefficients experimentally [5] with pulsed laser photolysis-resonance fluorescence technique (PLP-RF) from 264.5 K to 380 K to be k = (9.31 ± 1.02) x 10^{-12} exp [-(359 ± 70)/T] $cm^3molecule^{-1}s^{-1}$. There were no theoretical studies on the title reaction published in the early 2014. Chan and co-workers (2012) were the first group to study such type of reaction by using computational methods (*ab initio*/DFT for electronic structures and VTST for rate coefficients) to obtain the rate coefficients of 12 selected hydrogen abstraction reactions of hydrocarbons and substituted hydrocarbons by Cl atom [17]. Another study was conducted by Poutsma (2013) and it aimed to investigate the correlations between empirical structure and reactivity for approximating the rate coefficients at 298 K for variety of $Cl + HCR_3 \rightarrow HCl + CR_3$ reactions [18]. Their experimentally derived activation energy is very low (0.71 ± 0.14 $kcal.mol^{-1}$ based on the exponential term) [4] which could lead to some complicated effects in the calculation of rate coefficients.

The purposes of this study are to determine the rate coefficients (*k*) of the $CH_3C(O)OCH_3 + Cl \rightarrow HCl + CH_3C(O)OCH_2$ reaction in an *ab initio* manner and compare the resulting rate coefficient with the experimental results in literature, in order to elicit how computed barrier heights and imaginary vibrational frequencies affect the

tunneling contributions, the shapes of the Gibbs free energy curves, and computed rate coefficients which were computed at different levels of theories.

4.2 Methodology

4.2.1 *Ab initio*/DFT calculations

For the lower level of electronic structure theory calculations, MP2 (*ab initio*) and the DFT functionals (B3LYP, BH&HLYP, M05, M06 and M06-2X) with the 6-311++G** basis set were employed to perform geometry optimization, harmonic frequency calculations, transition state (TS) search and IRC calculations with Gaussian 09 [19] program suite, in which the B3LYP and BH&HLYP functionals are hybrid functionals while M05, M06 and M06-2X functionals are meta-hybrid GGA functionals. Geometry optimizations were initially performed with symmetry constraint in order to speed up the calculations. These calculations were then repeated with no symmetry constraint (using the keyword nosym in Gaussian 09) in order to align the coordinate systems of all optimized stationary points. Tables 4.1 and 4.2 show the computed barrier heights ($\Delta E_e^{\ddagger}$) of -0.49 to 6.58 kcal.mol^{-1} at MP2 (UMP2 and PUMP2) and DFT levels without spin-orbit correction of Cl atom. Table 4.1 also shows the computed harmonic frequencies of the imaginary mode of the TS, which range from 642i to 1077i cm^{-1}. Since the six lower level methods employed in this study contain different amount of Hartree-Fock exchange (20% - 54%), they yield different magnitudes of the computed barrier heights and imaginary frequencies of the same reaction and this enables an investigation between these properties and the resulting rate coefficients.

Higher level energies were obtained at the UCCSD(T)-F12x (x=a, b) [21] (an explicit correlation method) level using MOLPRO program suite [22, 23] with the geometries optimized at the MP2 and DFT levels. A major advantage of using the explicit correlation methods (UCCSD(T)-F12x) over the traditional correlation methods (such as CCSD(T)) is to achieve faster basis set convergence [24]. In order to accommodate for the F12 theory in UCCSD(T)-F12x calculations, a special atomic orbitals (AO) basis set designed for F12 calculations, cc-pVXZ-F12 [25], was used. In order to reduce the computational cost of the UCCSD(T)-F12x calculations, resolution of identity (RI) and density fitting (DF) were used in the calculations. Therefore, cc-pVXZ-F12_OPTRI (X =

D or T) [26] and aug-cc-pVXZ_MP2FIT (X = D or T) basis sets [27] were used for the RI and DF calculations respectively. A simple scaling factor, $\Delta E(T_{sc}) = \Delta E(T) \times E_{corr}^{MP2\text{-}F12}/E_{corr}^{MP2}$, which was the ratio of the computed correlation energies at the RMP2-F12 [28] level to those at the RMP2 level, was used to determine the scaled perturbative triples. They were then used throughout the UCCSD(T)-F12x calculations. All computationally demanding F12 calculations were carried out with symmetry in order to reduce the computational costs. By using basis sets of triple-zeta quality, the number of contracted Gaussian functions for the AO, RI and DF basis sets for the current reaction system were 435, 696 and 953 respectively. An important indicator of the reliability of single reference calculations with CCSD(T) is the T_1 diagnostics. All T_1 values were smaller than 0.018 for all species, so single-reference electronic structure theories were adequate for obtaining reliable electronic energies at the CCSD(T) level. The relative electronic energies with UCCSD(T)-F12x at the complete basis set (CBS) limit were obtained by using the $1/X^3$ extrapolation scheme [29, 30]. The best theoretical estimates (i.e. the benchmark values) of computed relative electronic energies (in Table 4.1) were computed as the average between the UCCSD(T)-F12a/CBS//MP2/6-311++G** and UCCSD(T)-F12b/CBS//MP2/6-311++G** relative electronic energies.

Since there are two methyl groups in $CH_3C(O)OCH_3$ and one methyl group in $CH_3C(O)OCH_2$, the torsional barriers due to the rotation of methyl groups were also computed at the aforementioned levels of theories. Rotation of the methyl group by 60° gave the approximated methyl torsional barrier of the TS.

In Cl atom, spin-orbit coupling leads to splitting of the ground state of Cl (^2P_J) to two electronic states ($^2P_{3/2}$ and $^2P_{1/2}$) with an energy difference of 882.35 cm^{-1} [31] (equivalent to 2.522 kcal/mol). Therefore, in order to include the spin-orbit splitting, the electronic energy of the unperturbed ^2P ground state of Cl atom was lowered by 0.84 $kcal.mol^{-1}$.

4.2.2 MEP Calculations

The IRC paths obtained at the six lower levels with Gaussian 09 served as the starting point of extrapolation/interpolation in order to obtain the minimum energy paths (MEP) for rate coefficient calculations in POLYRATE 2010-A. 15 IRC points on each side of the TS (i.e. a total of 31 IRC points) were computed with a step size of 0.1 $amu^{1/2}$-Bohr

at all single levels, and the gradients and Hessians of all IRC points were computed using the Hessian-based predictor-corrector (HPC) reaction path following method [32] in Gaussian 09. The details of the HPC was discussed in section 2.9. In particular, for the IRC calculations at the MP2, M05, M06 and BH&HLYP levels, with 31 IRC points for each level, the corresponding IRC ranges are at least $-1.56 \leq s \leq 1.56$ amu$^{1/2}$ Bohr (with $s = 0$ for the TS). Nonetheless, the IRC calculations at the B3LYP and M06-2X levels terminated at the thirteenth (−1.4717 amu$^{1/2}$ Bohr) and ninth points (−0.8763 amu$^{1/2}$ Bohr), respectively in the reactant direction because the default optimization threshold was reached in each case (i.e. a minimum was reached). The optimized structures in both cases clearly showed that distances between the hydrogen to be abstracted by Cl atom and the methoxy carbon in $CH_3C(O)OCH_3$ were 1.161 and 1.178 Å at B3LYP/6-311++G** and M06-2X/6-311++G** levels, respectively. However, Cl atom is still quite close to $CH_3C(O)OCH_3$, Cl and the hydrogen (to be abstracted) are apart by 1.818Å and 1.725Å at B3LYP/6-311++G** and M06-2X/6-311++G** levels, respectively. The distances were relatively short relative to those in the optimized reactant complex (2.986Å and 2.996Å at B3LYP and M06-2X levels, respectively), which implied that the B3LYP and M06-2X potential energy surfaces were very flat. Similar situations in other hydrogen abstractions by Cl atom have also been reported in literature [17]. In contrast, in the product direction, the IRC calculations with 15 points at the B3LYP and M06-2X levels extend to 1.8266 amu$^{1/2}$ Bohr and 1.6442 amu$^{1/2}$ Bohr, respectively. At some IRC points, many iterations were required to achieve convergence in the optimization step. The optimized structures of these IRC points might be very different from their initial structures. Hence, single point frequency calculations were performed for the converged geometries which required many iterations.

4.2.3 Kinetic Calculations

In POLYRATE 2010-A, the step size (denoted as SSTEP in POLYRATE) used for interpolating /extrapolating of classical potential energy of the minimum energy path (denoted as *VMEP* in POLYRATE) is 0.0002 amu$^{1/2}$ Å. By default, the SSTEP value is set as 0.000265 amu$^{1/2}$ Å. The choice of the range of reaction coordinate (s) for interpolating and extrapolating the *VMEP* curve, the V_a^G (vibrationally adiabatic ground-state potential) curve (=*VMEP* + ZPE) and the ΔG (free energy) curve can be different. In the section 4.3.3, it is evidenced that for some cases, the maximum of the ΔG (denoted

as s*(ΔG)) can be as far as -2.8 amu$^{1/2}$ Å from s= 0 amu$^{1/2}$ Å at certain temperature. When the range of reaction coordinate is not sufficient to cover *s**(ΔG) in the CVT calculations, the largest value of ΔG in the defined range of reaction coordinate is used, which is then taken as the false maximum. Thus, the resulting VTST rate coefficients could be very wrong.

A total of 10 TST levels were considered in this study, namely, TST, CVT, ICVT, TST/Wigner, TST/ZCT, CVT/ZCT, ICVT/ZCT, TST/SCT, CVT/SCT and ICVT/SCT. The symmetry number of this reaction was one. For the torsional modes in $CH_3C(O)OCH_3$ and $CH_3C(O)OCH_2$, they were considered as anharmonic modes. Chuang and Truhlar have derived a hindered-internal-rotator approximation [33, 34] for computing the partition functions of anharmonic modes and they have incorporated it into the POLYRATE 2010-A program. In this study, both Rω and RWO schemes [33] were used. The torsional barrier height was approximated in the Rω scheme by using the vibrational frequency of the torsional mode (see section 3.4.4.1.3 for detail) whereas that in the RWO scheme is required as an input in POLYRATE so no approximations are required. Computed rate coefficients by using both schemes were the same values at all temperatures. The underlying principle of hindered-internal-rotator approximation has been discussed in section 3.4.4.1.3 and it is not repeated here.

Higher level *VMEP* curves were initially obtained by using the corresponding lower level *VMEP* curves with electronic energy obtained at the higher level, and such approach is implemented as VTST-ISPE algorithm [35] in POLYRATE 2010-A. However, it turned out that the algorithm worked out unrealistically due to the low barriers. Therefore, a simple equation was devised to produce a higher level IRC path by using a lower level IRC path and the relative electronic energies of reactant and product complexes and transition state at both lower and higher levels as :-

$$E_s{}^{HL} = \left(E_s{}^{LL} - E_{RC}{}^{LL}\right) \times \frac{E_{TS}{}^{HL} - E_{RC}{}^{HL}}{E_{TS}{}^{LL} - E_{RC}{}^{LL}} + E_{RC}{}^{HL} \qquad (4.1)$$

where LL and HL denote lower level and higher level, respectively. The subscripts, RC, TS, s represent the reactant complex, the transition state, and an IRC point at reaction coordinate *s*, respectively. ($E_{TS}{}^{HL}$ - $E_{RC}{}^{HL}$)/($E_{TS}{}^{LL}$ - $E_{RC}{}^{LL}$) is used as the scaling factor . Equation (4.1) was used for scaling the IRC points on the reactant side (s < 0) to the

higher level. The relative energies of product complex at lower level and higher level were used to replace the relative energies of reactant complex in equation (4.1) for scaling IRC points on the product side. The number of stationary points in both lower level and higher level IRC paths was the same, that is, five stationary points were used in the calculations.

4.3 Results and Discussion

4.3.1 *Ab initio*/DFT results

Table 4.1 summarizes some DFT and *ab initio* results in terms of some optimized geometric parameters of the TS and imaginary vibrational frequency of the TS (ω_i) obtained at lower level calculations in addition to the barrier height ($\Delta E_e^{\ddagger}$) obtained at various lower and higher level calculations. One way to assess the reliability of the barrier height is to investigate the extent of spin contamination. Since both of the TS and $CH_3C(O)OCH_2$ are open-shell species, unrestricted wavefunctions are employed to obtain their electronic energies. In this case, the spin contamination in those radicals are negligibly small, where the computed $<S^2>$ values are 0.750 - 0.763 and 0.750 - 0.786 at the DFT and UMP2 levels, respectively. The lower level results can then be discussed in the following aspects: optimized geometries of the transition states at various lower levels, the magnitude of the imaginary vibrational frequencies, and computed barrier heights.

The optimized geometries of the reactant complex (RC), the TS, and the product complex (PC) are shown in Figures 4.1, 4.2 and 4.3, respectively. The optimized bond lengths of the RC, the TS, and the PC at the six lower levels are tabulated in Tables 4.2, 4.3 and 4.4, respectively. Regarding the optimized geometries of the transition states obtained at different lower levels, the differences in computed Cl…H distances (i.e. the distance between chlorine atom and the hydrogen to be abstracted) are relatively small (i.e. the difference between M05 level (1.446 Å, the upper limit) and B3LYP level (1.460 Å, the lower limit) is 0.08 Å. However, the difference in the computed C…H bond length (the bond length between the methoxy carbon and the hydrogen to be abstracted) obtained at different lower levels is relatively large (i.e. the difference between longest (1.446 Å by B3LYP) and the shortest (1.289 Å by UMP2) is 0.157 Å). Therefore, there is a general good agreement on Cl…H distance across different lower level results while there are

some disagreements on the C…H bond length. Since UMP2 yields the shortest C…H bond length, the resulting TS is more reactant-like comparing with other TS structures obtained with DFT functionals. The shortest C…H bond length obtained by DFT is 1.306 Å at M05 level, which is 0.017 Å longer than that at the UMP2 level. There is no way to conclude a trend from the computed geometrical parameters according to the lower level results since DFT lacks of a systematic way to improve the results because the exact exchange-correlation functional remains unknown.

The imaginary vibrational frequency has values between 642i (B3LYP) to 1077i (BH&HLYP) cm^{-1} (see Table 4.1) and the variation in the values obtained at different method is large. Once again, there is no apparent trend in these values. As for the computed barrier heights ($\Delta E_e^{\ddagger}$) at the six lower levels, they have values between 6.58 (UMP2) and -0.49 (B3LYP) $kcal.mol^{-1}$ with a range of 7 $kcal.mol^{-1}$. The magnitude of $\Delta E_e^{\ddagger}$ roughly correlates with the amount of Hartree-Fock exchange present in the corresponding methods. Electronic structure methods with larger Hartree-Fock exchange tend to yield larger $\Delta E_e^{\ddagger}$ values.

Regarding the higher level results (i.e. RMP2, RMP2-F12, UCCSD-F12x and UCCSD(T)-F12x, where x = a or b), there are a number of observations. First, significant contributions (~3.8 $kcal.mol^{-1}$) from the perturbative triple excitation are observed at the UCCSD(T)-F12x level. Second, the impacts of basis set effects on the barrier height (Table 4.7) are small. By using a VDZ-F12 basis set and a VTZ-F12 basis set, the difference in the computed relative energy is as small as ~0.8 $kcal.mol^{-1}$ which is expected in explicitly correlated F12 theory results. Another important aspect of the F12 calculation results is the effect of geometry on the computed barrier height. According to Table 4.1, the optimized TS at the MP2 level is not similar to that at the B3LYP level, so the computed barrier heights at the UCCSD(T)-F12x/CBS level with the two geometries are compared in order to assess the influence of geometry effects on the computed barrier heights. The barrier height at UCCSD(T)-F12x/CBS//B3LYP is lower than that at UCCSD(T)-F12x/CBS//MP2 level by 0.5 $kcal.mol^{-1}$, suggesting that the geometry effect indeed has an impact on the computed barrier height. This also suggests that the potential energy surface at the UCCSD(T)-F12x level is flat near the saddle point region. Although the TS with the MP2 geometry is not similar to that with the B3LYP geometry, the computed ΔZPE and thermal vibrational energies at those two levels agree very well. The differences in the zero-point corrected barrier height ($\Delta E_0^{\ddagger}$) and/or enthalpy of activation

($\Delta H_{298K}^{\ddagger}$) at those two levels at 298 K are smaller than 0.20 kcal.mol^{-1}. The differences in zero-point corrected reaction energy and/or reaction enthalpy at those two levels at 298 K are smaller than 0.54 kcal/mol.

Finally, the highest level results are discussed. MP2 is selected as the best-suited lower level because it is the only *ab initio* method used in the lower level calculations in this study and it can be used to keep the results as *ab initio* as possible. Detailed considerations of using MP2 as the best lower level are discussed in section 4.3.5. The UCCSD(T)-F12 theory is considered as the highest level in this study because the performance of it is comparable to that of CCSD(T) for obtaining accurate electronic energies while fast basis set convergence can be obtained. The advantages of using UCCSD(T)-F12 in electronic structure calculations are discussed in section 2.4.3. Thus, combining the MP2 method used the lower level calculation and the UCCSD(T)-F12 level in higher level calculations give the most accurate computed results in this study. In this study, the best computed barrier heights (at UCCSD(T)-F12/CBS//MP2/6-311++G** level; see footnote d of Table 4.1) in this work are 2.70± 0.31 ($\Delta E_e^{\ddagger}$) and -1.44 ± 0.72 kcal.mol^{-1} ($\Delta E_0^{\ddagger}$) respectively. With the inclusion of spin-orbit (SO) correction of Cl, the barrier heights are 3.54 kcal.mol^{-1} ($\Delta E_e^{\ddagger}$) and -0.60 kcal.mol^{-1} ($\Delta E_0^{\ddagger}$), respectively. The M06-2X gives the closest barrier height (1.83 or 2.67 kcal.mol^{-1} with SO correction of Cl) to the best computed barrier height, with a difference of 0.87 kcal.mol^{-1}. Barrier heights obtained at other lower levels deviate from the best computed value by more than 2 kcal.mol^{-1}.

Table 4.1 Some computed geometrical parameters (Å), imaginary vibrational frequencies (ω_i in cm^{-1}) and relative electronic energies ($\Delta E_e^{\ddagger}$ with respect to separate reactants in $kcal.mol^{-1}$) of the transition state (TS) of the reaction, $Cl + CH_3C(O)OCH_3 \rightarrow HCl + CH_3C(O)OCH_2$, obtained at different levels of calculations.

Methods[a]	Cl…H	H…C	ω_i	$\Delta E_e^{\ddagger}$
UMP2	1.516	1.289	1062i	6.58
PUMP2				4.31
BH&HLYP (hybrid GGA; 50% HF exchange)	1.495	1.353	1077i	5.95
M06-2X(meta hybrid GGA; 54% HF exchange)	1.486	1.372	823i	1.83
M06 (meta hybrid GGA; 27% HF exchange)	1.500	1.366	1017i	0.43
M05 (meta hybrid GGA; 28% HF exchange)	1.540	1.306	942i	-0.47
B3LYP (hybrid GGA; 20% HF exchange)	1.460	1.446	642i	-0.49
RMP2/VDZ-F12//MP2				2.02
RMP2-F12/VDZ-F12//MP2				-0.38
RHF-UCCSD-F12a/VDZ-F12//MP2				5.31
RHF-UCCSD-F12b/VDZ-F12//MP2				5.47
RHF-UCCSD(T)-F12a/VDZ-F12//MP2				1.56
RHF-UCCSD(T)-F12b/VDZ-F12//MP2				1.72
RHF-UCCSD(T)-F12a/VDZ-F12//B3LYP				1.08
RHF-UCCSD(T)-F12b/VDZ-F12//B3LYP				1.22
RMP2/VTZ-F12//MP2				0.26
RMP2-F12/VTZ-F12//MP2				-0.24
RHF-UCCSD-F12a/VTZ-F12//MP2				6.07
RHF-UCCSD-F12b/VTZ-F12//MP2				6.08
RHF-UCCSD(T)-F12a/VTZ-F12//MP2				2.38
RHF-UCCSD(T)-F12b/VTZ-F12//MP2				2.40
RHF-UCCSD(T)-F12a/VTZ-F12//B3LYP				1.84
RHF-UCCSD(T)-F12b/VTZ-F12//B3LYP				1.84
UCCSD(T)-F12a/CBS(VDZ-F12;VTZ-F12)[b]//MP2				2.73
UCCSD(T)-F12b/CBS(VDZ-F12;VTZ-F12)[b]//MP2				2.68
UCCSD(T)-F12a/CBS(VDZ-F12;VTZ-F12)[b]//B3LYP				2.16
UCCSD(T)-F12b/CBS(VDZ-F12;VTZ-F12)[b]//B3LYP				2.11

Best ΔE_e (average of UCCSD(T)-F12a,-F12b/CBS//MP2)[c]				2.70(31)
Best ΔE_{0K} (best ΔE_e + MP2 ΔZPE)[d]				-1.44(72)
Best ΔE_e + spin-orbit lowering in Cl				3.54
Best ΔE_{0K} + spin-orbit lowering in Cl				-0.60

[a] All MP2 and DFT calculations have employed the 6-311++G** basis set. The F12x//MP2 calculations were carried out employing MP2 geometries for all species involved, while F12x//B3LYP indicates that the B3LYP geometry of TS was used (all other species at MP2 geometries). The spin orbit contributions for the ^{2}P state of Cl have not been included in the evaluation of $\Delta E_e^{\ddagger}$ given in this table. The relative energies given are with the ^{2}P state of Cl (directly from *ab initio*/DFT calculations, using symmetry where appropriate; see also footnote a of Table 4.5).

[b] The $1/X^3$ extrapolation formula was used for CBS extrapolation (see text).

[c] The best estimates are averages of the CBS-F12a and CBS-F12b values. The estimated uncertainties (in parentheses) are the differences between the best and F12b/VTZ-F12 values.

[d] Without SO contributions from Cl; computed MP2 vibrational frequencies were used for zero-point energy corrections (ΔZPE) and 10% of ΔZPE was added to the uncertainties.

The relative energies of the reactant complex (ΔE^{RC}), TS ($\Delta E^{\ddagger}$), product complex (ΔE^{PC}), separate products (ΔE^{RX}) and reaction enthalpy at 298 K (ΔH_{298K}) with SO correction of Cl atom at the six lower levels are compiled in Table 4.5. According to Table 4.5, ΔE^{RC} and ΔE^{PC} spread over 3.49 and 5.75 kcal.mol^{-1}, respectively. No apparent trends can be deduced from these quantities. The best computed ΔE_e^{RC} and ΔE_e^{PC} are -2.60 and -1.81 kcal.mol^{-1}, respectively at the UCCSD(T)-F12b/CBS//MP2 level (see footnote b in Table 4.5). For the lower level results, ΔE_e^{RC} computed at the UMP2 and BH&HLYP levels are -2.88 and -2.43 kcal.mol^{-1}, respectively, which agree very well with the best computed value. Their differences with the best computed value are -0.28 kcal.mol^{-1} (UMP2) and 0.17 kcal.mol^{-1} (BH&HLYP), respectively. ΔE_e^{PC} computed at B3LYP (-1.25 kcal.mol^{-1}) and M06 (-2.68 kcal.mol^{-1}) levels agree very well with the best computed value, with a difference of 0.56 kcal.mol^{-1} and -0.87 kcal.mol^{-1}, respectively.

The next natural step is to compare the best computed $\Delta E_e^{\ddagger}$ (3.54 kcal.mol^{-1}) or $\Delta E_0^{\ddagger}$ (-0.60 kcal.mol^{-1}) with the experimentally derived activation energy (0.71 ± 0.14

kcal.mol^{-1}) [5]. According to reference 36, the activation energy cannot be directly measured in experiments, but it is a derived quantity. There are different modified forms of Arrhenius equation [37-40] which are utilized to derive the activation energies. Therefore, different forms of Arrhenius equation employed will give different values of the activation energies. Thus, it is more meaningful to compare the computed rate coefficients with the experimental rate coefficients (*vide infra*), rather than comparing the computed barrier heights with the experimentally derived activation energies.

The last quantity in Table 4.5 to be discussed is the computed ΔE_e^{RX} which spreads over 4.9 kcal/mol. The best computed ΔE_e^{RX} is 1.18 kcal.mol^{-1}, obtained at UCCSD(T)-F12/CBS//MP2 level. B3LYP yields the closest ΔE_e^{RX} value (1.37 kcal.mol^{-1}) to the best computed one among the six lower levels. The next best agreement is 1.81 kcal.mol^{-1}, given by the M06 functional. In terms of ΔH_{298K}^{RX} values, the best computed ΔH_{298K}^{RX} is -3.01 kcal.mol^{-1}, which is between the B3LYP value (-3.64 kcal.mol^{-1}) and the M06 value (-2.62 kcal.mol^{-1}). Again, different functionals used in this study lead to different values of harmonic frequencies, which in-turn lead to different zero-point energy corrections (ΔZPE). Hence, different thermal vibrational contributions to ΔH_{298K}^{RX} result. The impact of ΔZPE and the entropic contributions on the computed rate coefficients will be examined in the next section.

Figure 4.1. Optimized geometry of the reactant complex at MP2/6-311++G**, M05/6-311++G**, M06/6-311++G**, M06-2X/6-311++G**, B3LYP/6-311++G**, and BH&HLYP/6-311++G** with optimized bond lengths compiled in Table 4.2.

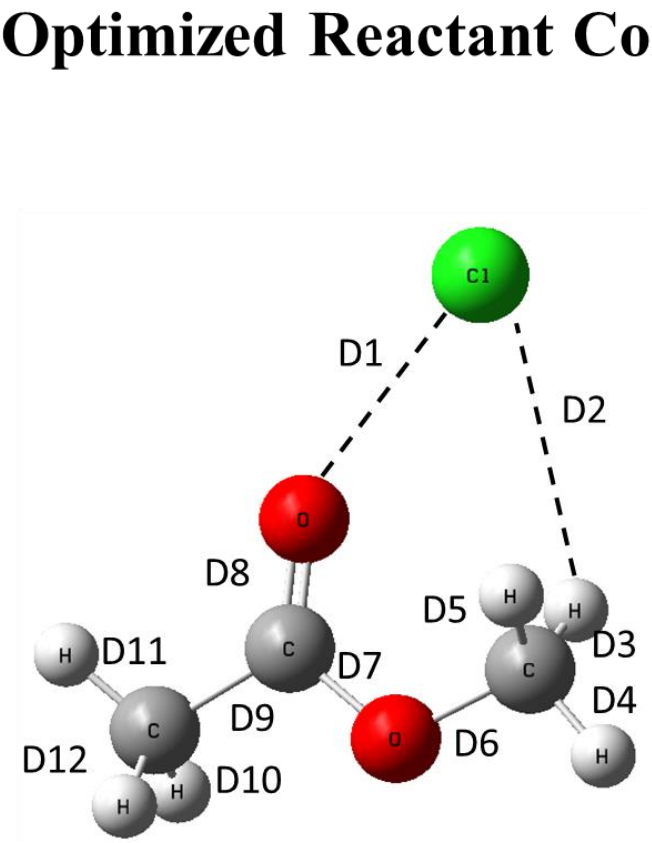

Table 4.2 Optimized geometries of the reactant complex obtained at MP2/6-311++G**, M05/6-311++G**, M06/6-311++G**, M06-2X/6-311++G**, B3LYP/6-311++G** and BH&HLYP/6-311++G**. All bond lengths are in Angstrom.

Bond	MP2	M05	M06	M06-2X	B3LYP	BH&HLYP
D1	2.82	2.63	2.60	2.66	2.59	2.71
D2	3.27	3.01	2.95	3.00	2.99	3.17
D3	1.09	1.09	1.09	1.09	1.09	1.08
D4	1.09	1.09	1.09	1.09	1.09	1.08
D5	1.09	1.09	1.09	1.09	1.09	1.08
D6	1.44	1.43	1.43	1.43	1.45	1.42
D7	1.35	1.33	1.33	1.33	1.33	1.33
D8	1.21	1.21	1.21	1.21	1.22	1.20
D9	1.51	1.50	1.49	1.50	1.51	1.50
D10	1.09	1.09	1.09	1.09	1.09	1.08
D11	1.09	1.09	1.09	1.09	1.09	1.08
D12	1.09	1.09	1.09	1.09	1.09	1.08

Figure 4.2. Optimized geometry of the transition state at MP2/6-311++G**, M05/6-311++G**, M06/6-311++G**, M06-2X/6-311++G**, B3LYP/6-311++G**, and BH&HLYP/6-311++G** with optimized bond lengths compiled in Table 4.3.

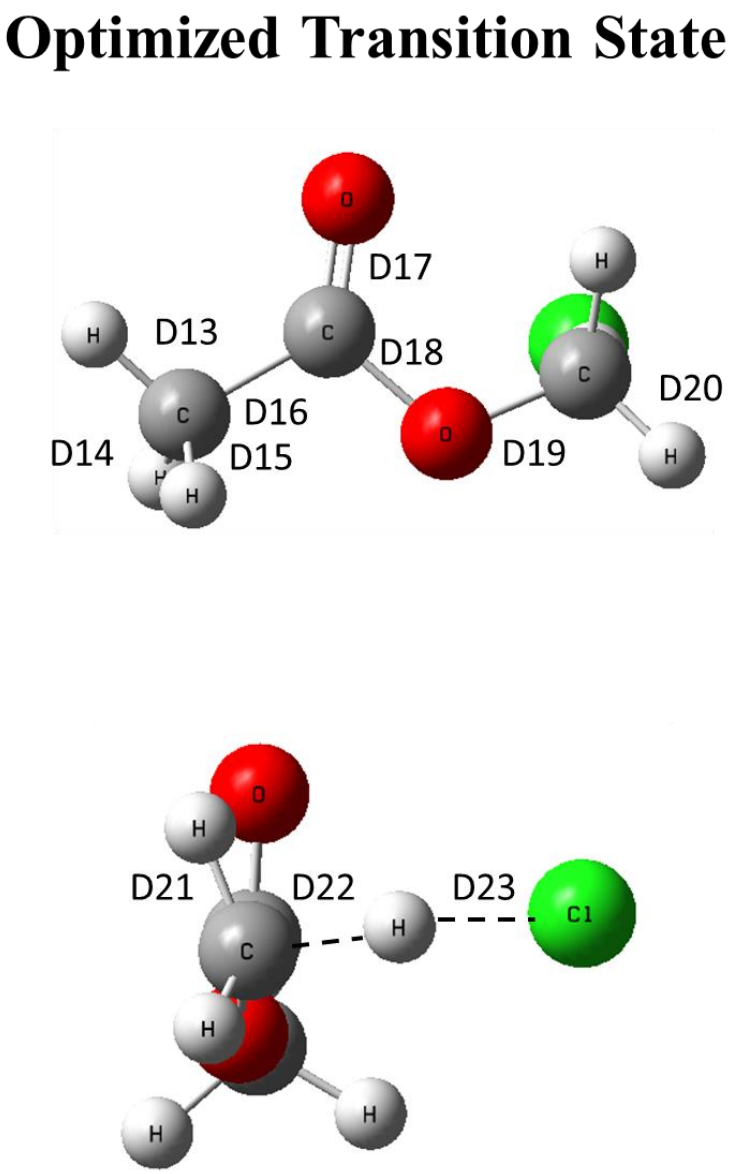

Table 4.3 Optimized geometries of the transition state obtained at MP2/6-311++G**, M05/6-311++G**, M06/6-311++G**, M06-2X/6-311++G**, B3LYP/6-311++G** and BH&HLYP/6-311++G**. All bond lengths are in Angstrom.

Bond	MP2	M05	M06	M06-2X	B3LYP	BH&HLYP
D13	1.09	1.09	1.09	1.09	1.09	1.08
D14	1.09	1.09	1.09	1.09	1.09	1.08
D15	1.09	1.09	1.09	1.09	1.09	1.08
D16	1.50	1.49	1.49	1.49	1.50	1.49
D17	1.20	1.19	1.19	1.19	1.20	1.18
D18	1.39	1.39	1.38	1.38	1.40	1.37
D19	1.38	1.36	1.36	1.36	1.37	1.36
D20	1.09	1.09	1.09	1.08	1.08	1.08
D21	1.09	1.09	1.09	1.09	1.09	1.08
D22	1.29	1.31	1.37	1.37	1.45	1.35
D23	1.52	1.54	1.50	1.49	1.46	1.50

Figure 4.3. Optimized geometry of the product complex at MP2/6-311++G**, M05/6-311++G**, M06/6-311++G**, M06-2X/6-311++G**, B3LYP/6-311++G**, and BH&HLYP/6-311++G** with optimized bond lengths compiled in Table 4.4.

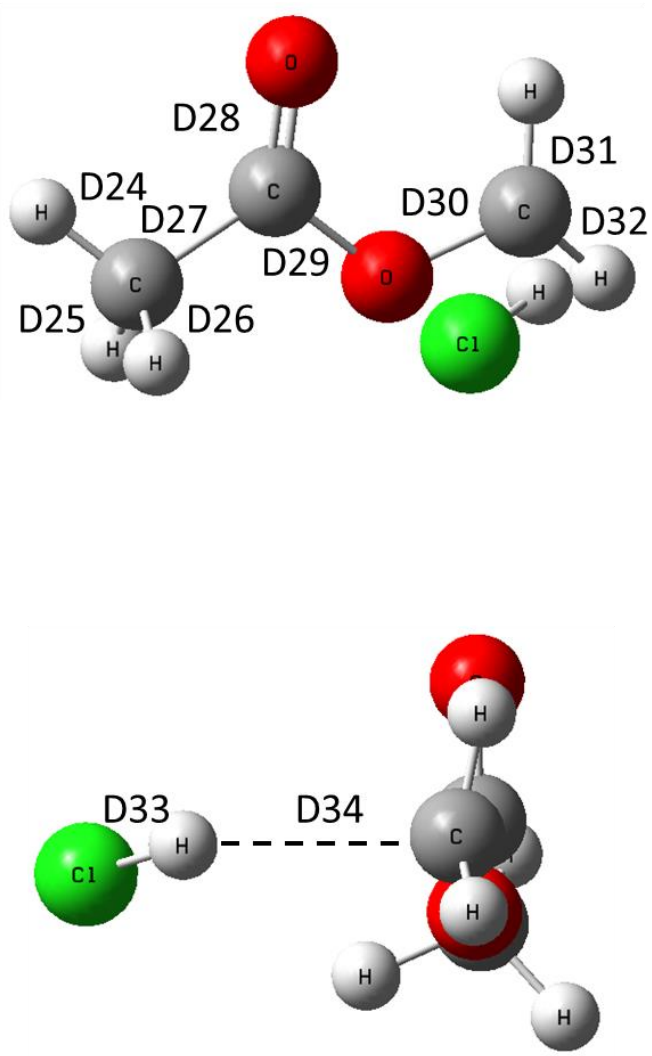

Table 4.4 Optimized geometries of the product complex obtained at MP2/6-311++G**, M05/6-311++G**, M06/6-311++G**, M06-2X/6-311++G**, B3LYP/6-311++G** and BH&HLYP/6-311++G**. All bond lengths are in Angstrom.

Bond	MP2	M05	M06	M06-2X	B3LYP	BH&HLYP
D24	1.09	1.09	1.09	1.09	1.09	1.08
D25	1.09	1.09	1.09	1.09	1.09	1.08
D26	1.09	1.09	1.10	1.09	1.09	1.09
D27	1.50	1.49	1.49	1.50	1.50	1.49
D28	1.20	1.19	1.19	1.20	1.20	1.19
D29	1.38	1.38	1.38	1.35	1.39	1.36
D30	1.37	1.35	1.35	1.37	1.36	1.35
D31	1.08	1.08	1.08	1.08	1.08	1.07
D32	1.08	1.08	1.08	1.08	1.08	1.07
D33	1.28	1.30	1.30	1.29	1.31	1.29
D34	2.47	2.11	2.22	3.26	2.10	2.26

Table 4.5 Computed relative energies ($\Delta E_0 = \Delta E_e + \Delta ZPE$; kcal.mol^{-1}) of the reactant complex (RC), transition state (TS; $\Delta E^{\ddagger}$), product complex (PC) and separate products (ΔE^{RX}), with respect to the separate reactants, of the Cl + $CH_3C(O)OCH_3$ → HCl + $CH_3C(O)OCH_2$ reaction obtained at different levels, used in the calculations of rate coefficients.

Methods[a]	RC		$\Delta E^{\ddagger}$		PC		ΔE^{RX}		
	ΔE_e	ΔE_0	ΔE_e	ΔE_0	ΔE_e	ΔE_0	ΔE_e	ΔE_0	ΔH_{298}^{RX}
UMP2	-2.88	-2.48	7.42	3.28	0.69	-2.96	4.86	0.12	0.68
BH&HLYP	-2.43	-2.11	6.79	2.35	2.17	-1.72	4.35	-1.02	-0.30
M06-2X	-4.77	-4.35	2.67	-1.85	-3.11	-7.00	3.12	-2.05	-1.35
M06	-5.92	-5.65	1.27	-3.20	-2.68	-6.05	1.81	-3.45	-2.62
M05	-4.91	-4.50	0.37	-3.86	-3.58	-7.02	-0.05	-5.09	-4.44
B3LYP	-4.10	-3.70	0.35	-3.97	-1.25	-4.77	1.37	-3.90	-3.64
Best ΔE_e (no SO)[b]	-3.44	-3.03	2.70	-1.44	-2.65	-6.31	0.34	-4.40	3.85
Best ΔE_e (with SO)[b]	-2.60	-2.19	3.54	-0.60	-1.81	-5.46	1.18	-3.56	
Best ΔH_{298K}[b]		-2.22		-1.17		-4.96			-3.01
Using ΔH_f values[c]									-2.70, -3.19
Fitted (present)[d]			1.34	-2.80					
Experiment[e]			0.71						

[a] All MP2 and DFT calculations have employed the 6-311++G** basis set. The UMP2 and DFT relative energies are from calculations with no symmetry constraint, and the ΔE_e and ΔE_0 values given are with respect to the $^2P_{3/2}$ spin orbit (SO) state of Cl (including the SO contribution of 0.84 kcal.mol^{-1} lowering from the unperturbed ^2P state to the $^2P_{3/2}$ SO state of Cl, unless otherwise stated; see also footnote b).

[b] The best ΔE_e values are the average of the UCCSD(T)-F12a/CBS//MP2 and UCCSD(T)-F12b/CBS//MP2 ΔE_e values (see footnote c of Table 4.1 and text), either with respect to the ^2P (no SO) or $^2P_{3/2}$ (with SO) state of Cl. The best ΔE_0 and ΔH_{298K} values were the best ΔE_e values with ΔZPE and/or vibrational thermal contributions, using computed MP2 harmonic vibrational frequencies. See also footnotes c and d of Table 4.1.

[c] Using available $\Delta H_{f,298K}$[e] values for the reactants and products

[d] Best match between experimental and computed k's (Figure 4.14) with a fitted barrier of $\Delta E_e^{\ddagger}$ = 0.5 or 1.34 kcal.mol^{-1} (without and with SO correction, respectively).

[e] Derived from the exponential term of the Arrhenius expression from reference 4.

Table 4.6 contains the enthalpies of formation ($\Delta H_{f,298K}^{o}$) values of the reactants and products in literature [38], which are useful in assessing the reliability of the relative energies in this computational study.

Table 4.6 Enthalpies of formation ($\Delta H_{f,298K}^{o}$) of methyl acetate, chlorine atom, $CH_3C(O)OCH_2$ and hydrogen chloride.

Species	ΔH_f^{298K} (kcal.mol^{-1})	Technique	Reference
Cl	28.992 ± 0.002		43
HCl	-22.06 ± 0.024		43
$CH_3C(O)OCH_3$	-98.00	Rotating bomb calorimetry	44
$CH_3C(O)OCH_3$	-97.51 ± 0.33	Computational study at MC-QCISD//MP2/6-311G** level	45
$CH_3C(O)OCH_2$	-49.65	Computational study at MC-QCISD//MP2/6-311G**)	45

Table 4.6 shows the difference in the enthalpy of formation of $CH_3C(O)OCH_3$ between the experimental value and computed value is ~0.5 kcal.mol^{-1}, which in-turn indicates that the $\Delta H_{f,298K}^{o}$ values of $CH_3C(O)OCH_3$ and $CH_3C(O)OCH_2$ come with an uncertainty of 0.5 kcal.mol^{-1}. By using the values in Table 4.6, ΔH_{298K}^{RX} are -2.70 kcal.mol^{-1} (by using experimental ΔH_f^{298K} of $CH_3C(O)OCH_3$ and -3.19 kcal.mol^{-1} (by using the computed ΔH_f^{298K} of $CH_3C(O)OCH_3$), respectively. These two values agree very well with the best computed ΔH_{298K}^{RX} (-3.01) in this work within 0.3 kcal.mol^{-1} (see Table 4.5).

All computed torsional barrier heights of methyl group in $CH_3C(O)OCH_3$ and $CH_3C(O)OCH_2$ obtained at various levels of theories are compiled in Table 4.7. There are two torsional modes in $CH_3C(O)OCH_3$ and one torsional mode in $CH_3C(O)OCH_2$. The best estimate of methyl torsional barrier heights of CH_3-C in $CH_3C(O)OCH_3$ and $CH_3C(O)OCH_2$ are 0.28 and 0.36 (± 0.04) kcal.mol^{-1}, respectively. Since the methyl torsional barrier heights are smaller than the thermal energy (i.e. k_BT at 300 K = 0.59 kcal.mol^{-1}), the two torsional modes are basically free internal rotors. Regarding another torsional mode in $CH_3C(O)OCH_3$, the CH_3-O mode, has the best computed value of 1.12 ± 0.02 kcal.mol^{-1}, which is larger than the thermal energy at 300 K, so it is essentially a

hindered internal rotor. There is also one torsional mode (CH_3-C) in the TS and its methyl torsional barrier height is obtained without optimization, so the value serves as an upper bound of the true methyl torsional barrier height. Moreover, geometry effects are observed as the methyl torsional barrier heights of the TS obtained with B3LYP geometry is about 0.8 kcal.mol^{-1} lower than that obtained with the MP2 geometry at higher level of theories (i.e. UCCSD-F12x/VTZ-F12, UCCSD(T)-F12x/VTZ-F12, UCCSD(T)-F12x/CBS where x = a, b). Therefore, the geometry effects cannot be ignored. Table 4.7 shows the computed methyl torsional barrier heights of the TS which range from ~0.2 to ~1.0 kcal.mol^{-1}. The average value of all highest level results (i.e. UCCSD(T)-F12x/CBS) is 0.54 ± 0.35 kcal.mol^{-1} which implies a free internal rotation. Regarding the methyl torsional barrier heights of $CH_3C(O)OCH_3$ in literatures, their computed values are 1.18 and 0.28 kcal.mol^{-1} for CH_3-O and CH_3-C respectively at the CCSD(T)/cc-pVTZ level. Their experimentally derived values are 1.21 and 0.29 kcal.mol^{-1}, respectively. This shows that both our computed values agree with the experimental and computed values in literature very well, so our computed values are reasonably reliable.

Table 4.7 Computed methyl torsional barrier heights (ΔE_e in kcal.mol^{-1}) obtained at different levels of calculations.

Methods	$CH_3C(O)OCH_3$[a]		TS[b]	$CH_3C(O)OCH_2$[a]
	CH_3-O	CH_3-C	CH_3-C	CH_3-C
B3LYP/6-11++G**	0.811	0.174	0.639	0.211
BH&HLYP/6-311++G**	1.015	0.313		0.389
M05/6-311++G**	0.681	0.141		0.162
M06/6-311++G**	0.919	0.217		0.246
M06-2X/6-311++G**	1.237	0.313		0.392
MP2/6-311++G**	1.437	0.223	0.897	0.223
RMP2/VDZ-F12//MP2	1.174	0.232	0.912	0.336
RMP2-F12/VDZ-F12//MP2	1.168	0.200	0.872	0.301
UCCSD-F12a/VDZ-F12//MP2	1.218	0.310	0.958	0.395
UCCSD-F12b/VDZ-F12//MP2	1.231	0.320	0.967	0.402
UCCSD(T)-F12a/VDZ-F12//MP2	1.134	0.233	0.890	0.318
UCCSD(T)-F12b/VDZ-F12//MP2	1.146	0.243	0.879	0.325
RMP2/VDZ-F12//B3LYP[c]	1.234	0.327	0.195	0.444
RMP2-F12/VDZ-F12//B3LYP	1.244	0.336	0.199	0.417
UCCSD-F12a/VDZ-F12//B3LYP	1.167	0.306	0.187	0.420
UCCSD-F12b/VDZ-F12//B3LYP	1.199	0.334	0.188	0.420
UCCSD(T)-F12a/VDZ-F12//B3LYP	1.187	0.337	0.190	0.426
UCCSD(T)-F12b/VDZ-F12//B3LYP	1.193	0.341	0.190	0.426
RMP2/VTZ-F12//MP2	1.188	0.207	0.875	0.307
RMP2-F12/VTZ-F12//MP2	1.162	0.197	0.864	0.296
UCCSD-F12a/VTZ-F12//MP2	1.206	0.307	0.950	0.391
UCCSD-F12b/VTZ-F12//MP2	1.212	0.312	0.955	0.394
UCCSD(T)-F12a/VTZ-F12//MP2	1.127	0.237	0.887	0.319
UCCSD(T)-F12b/VTZ-F12//MP2	1.132	0.241	0.891	0.323
RMP2/VTZ-F12//B3LYP	1.266	0.340	0.197	0.424
RMP2-F12/VTZ-F12//B3LYP	1.227	0.322	0.199	0.397
UCCSD-F12a/VTZ-F12//B3LYP	1.139	0.284	0.188	0.398
UCCSD-F12b/VTZ-F12//B3LYP	1.142	0.286	0.188	0.409

UCCSD(T)-F12a/VTZ-F12//B3LYP	1.161	0.320	0.192	0.409
UCCSD(T)-F12b/VTZ-F12//B3LYP	1.164	0.322	0.191	0.410
UCCSD(T)-F12a/CBS(1/X^3)//MP2	1.124	0.238	0.886	0.320
UCCSD(T)-F12b/CBS(1/X^3)//MP2	1.126	0.241	0.896	0.323
UCCSD(T)-F12a/CBS(1/X^3)//B3LYP	1.150	0.313	0.193	0.403
UCCSD(T)-F12b/CBS(1/X^3)//B3LYP	1.151	0.314	0.193	0.403
Average of all CBS values	1.14(2)	0.28(4)	0.54(35)	0.36(4)
CCSD(T)/cc-pVTZ[d]	1.18	0.28		
Experimental[e]	1.21	0.29		

[a] The relevant methyl group was rotated by 60° from the true minimum, followed by full geometry optimization of the rest of the geometrical parameters. The optimized structures have only one a″ imaginary mode, which is that of the methyl torsional mode at all levels, except for CH_3COOCH_2 at the BH&HLYP, M06-2X and MP2 levels, where the optimized structures have two a″ imaginary modes corresponding to the CH_2-O and CH_3-C torsions.

[b] The methyl group was rotated by 60° from the true minimum, without further optimization.

[c] The structures at the torsional barriers were from B3LYP calculations, while those at the minima were from MP2 (same for all labels with B3LYP below).

[d] Computed vibrationally corrected barriers (413.1 and 99.2 cm^{-1}) from reference 41.

[e] 422 and 102 cm^{-1}; derived from a fit to microwave and millimetre wave transitions of cis-methyl acetate (reference 42).

4.3.2 Reaction Paths at Single Levels

Figure 4.4 shows the computed IRC, classical potential energy (*VMEP*), change in zero-point energy (ΔZPE) and adiabatic ground state potential energy (V_a^G = *VMEP* + ΔZPE) curves which are plotted against the reaction coordinate (*s*) at the six lower levels. Only the IRC versus *s* curves in Figure 4.4 are obtained by using Gaussian 09 whereas the rest of the curves are obtained by using POLYRATE 2010-A. Each *VMEP* curve is obtained by interpolating/extrapolating the corresponding IRC path by using POLYRATE 2010-A. All relative energy quantities present in Figure 4.4 are calculated with respect to separate reactants (i.e. the zero of energy is defined as the sum of the energies of the reactants). In rate coefficient calculations, the reactant complex (RC) is considered in all cases. Since RC is in lower energy than separate reactants in all lower level results, the maxima of *VMEP* and V_a^G curves shift toward the reactant complex (i.e. reactant side, $s < 0$). The existence of the reactant complex leads to some IRC points

having negative relative electronic energies (relative to the separate reactants). Thus, even though the transition state corresponds to a positive barrier height, there are some non-stationary points with negative relative electronic energies along the intrinsic reaction coordinate. For each ΔZPE curve, there is a dip near the TS (i.e. at $s \approx 0$). The dips in all ΔZPE curves reflect the gradual changes of the vibrational frequency of a mode along the reaction paths. An imaginary vibrational mode and two low frequency intermolecular modes in the TS correspond to three translational modes in the separate reactants and products. The vibrational mode, which is responsible for the dramatic change of the ΔZPE curves along the reaction coordinate, is identified to be the C-H stretching mode in the methyl group of $CH_3C(O)OCH_3$. During the course of the reaction, chlorine atom approaches the C-H stretching mode (3100 cm^{-1}) to form the C..H..Cl intermolecular mode (~500 cm^{-1}, between 459 (M05) and 553 (B3LYP) cm^{-1}) in the TS and finally it dissociates to the HCl stretching mode (3000 cm^{-1}) in HCl. In terms of energy, the dips of all ΔZPE curves near $s = 0$ translate to ~4 kcal/mol, which essentially account for half of the difference in vibrational frequency between the aforementioned CH stretching mode and C..H..Cl mode (i.e. ~1300 cm^{-1} or ~3.7 $kcal.mol^{-1}$). Regarding the minima position of all ΔZPE curves in Figure 4.4, they are near $s = 0$ but they are not necessarily at exactly $s = 0$ whereas the maximum of each *VMEP* curve must be at $s = 0$. When *VMEP* curves and ΔZPE curves add up to obtain the V_a^G curves, the maxima of all V_a^G curves are not necessarily at $s = 0$. Moreover, depending on the shapes of the *VMEP* curves and ΔZPE curves, the resulting dips of the V_a^G curves can be bumpy. Therefore, the V_a^G curves obtained at the six lower levels, shown in Figure 4.4, can be quite different.

There are some features of the V_a^G curves. First, for each V_a^G curve, the dip comes with two maxima on both sides. However, for lower levels with high barrier heights, such as MP2 and BH&HLYP ($\Delta E_e^{\ddagger}$ = 7.42; 6.79 $kcal.mol^{-1}$. See Table 4.8), the dips in the V_a^G curves are less significant than those in the ΔZPE curves at the corresponding levels. As the barrier height decreases, the dips in the V_a^G curves are more significant. Second, generally, the dips of the V_a^G curves are at $s \approx 0$ since the minima of ΔZPE curves are at $s \approx 0$. Third, for the two maxima in the V_a^G curves, for most cases, the maximum of the V_a^G curve of the dip on the reactant side is higher in energy than that in the product. The underlying reason is that the PC is generally lower in energy than the RC (except for BH&HLYP; see Table 4.5) and/or the ΔZPE curve is lower in energy on the reactant side than the product side. Finally, the locations of global maxima of the V_a^G curves (denoted

as $s^*(V_a^G)$), are labeled by dotted lines in Figure 4.4 and their values are compiled in Table 4.8. According to Figure 4.4 and Table 4.8, $s^*(V_a^G)$ is always on the reactant side for the title reaction, its value depends on the size of the barrier height and the fine differences between the shapes of the *VMEP* and ΔZPE curves near $s = 0$, especially for cases with very low barrier height.

Figure 4.4 IRC (black squares; from G09 calculations), *VMEP*, ΔZPE, and V_a^G (from POLYRATE interpolation/extrapolation) curves at six single levels. Energies in kcal.mol^{-1} are with respect to separate reactants, which are set to zero.

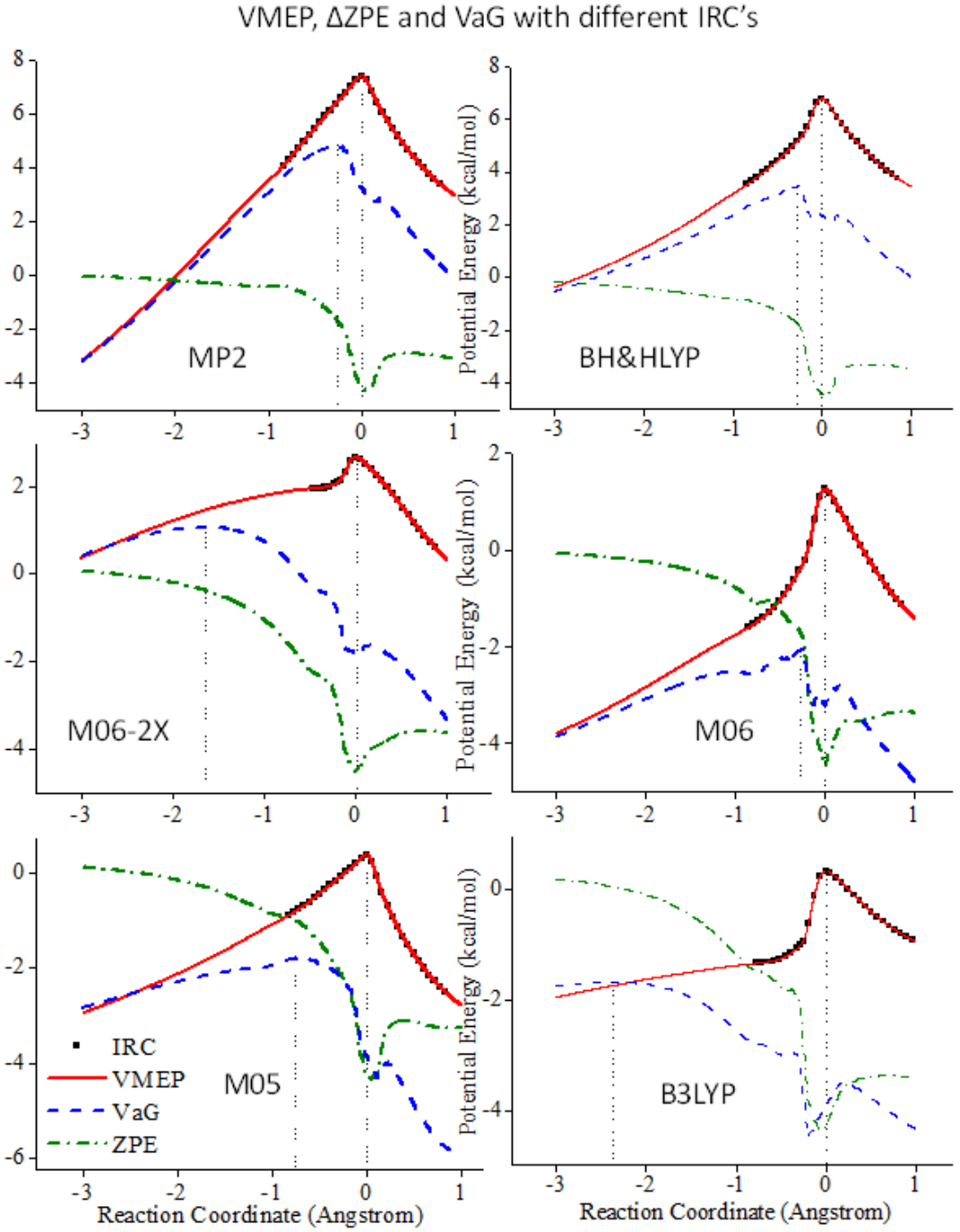
VMEP, ΔZPE and VaG with different IRC's
MP2
BH&HLYP
M06-2X
M06
M05
B3LYP
IRC
VMEP
VaG
ZPE
Potential Energy (kcal/mol)
Reaction Coordinate (Angstrom)

Table 4.8 Some single level results employing different IRCs (energies in kcal.mol^{-1} and rate coefficients in cm^3.molecule^{-1}.s^{-1}).

	B3LYP	M05	M06	M06-2X	BH&HLYP	UMP2
$\Delta E_e^{\ddagger}$	0.35	0.37	1.27	2.67	6.70	7.42
$\Delta E_0^{\ddagger}$	-3.97	-3.86	-3.20	-1.85	2.35	3.28
$s^*(V_a^G)$	-2.37	-0.76	-0.28	-1.64	-0.28	-0.27
ΔV_a^G	-2.30	-2.05	-1.13	-2.92	-1.12	-1.54
$k^{CVT}=k^{ICVT}$	Yes	Yes	Yes	Yes	Yes	Yes
$\kappa^{ZCT}\approx\kappa^{SCT}\approx1.0$	Yes	Yes	Yes	Yes	$T\geq$750K	$T\geq$750K
$\kappa^{TST/CAG,200K}$	3.09E-3	5.75E-3	5.88E-2	6.50E-4	6.00E-2	2.09E-2
$\kappa^{CVT/CAG,200K}$	9.99E-1	9.88E-1	1.00E0	9.96E-1	1.00E0	9.99E-1
$k^{TST,200K}$	1.65E-8	1.00E-8	3.13E-9	1.07E-10	2.30E-15	1.54E-16
$k^{TST/CAG,200K}$	5.10E-11	5.76E-11	1.84E-10	6.98E-14	1.38E-16	3.22E-18
$k^{CVT,200K}$	3.85E-11	1.05E-10	1.71E-10	4.66E-14	2.02E-16	4.58E-18
$k^{ICVT/SCT,200K}$	3.85E-11	1.05E-10	1.71E-10	4.80E-14	4.51E-16	1.02E-17
$\kappa^{TST/CAG,1500K}$	4.63E-1	5.03E-1	6.85E-1	3.76E-1	6.87E-1	5.97E-1
$\kappa^{CVT/CAG,1500K}$	9.81E-1	7.25E-1	9.97E-1	9.29E-1	1.00E0	9.87E-1
$k^{TST,1500K}$	1.49E-10	1.25E-10	1.18E-10	8.40E-11	1.63E-11	1.04E-11
$k^{TST/CAG,1500K}$	6.88E-11	6.27E-11	8.07E-11	3.16E-11	1.12E-11	6.23E-12
$k^{CVT,1500K}$	1.98E-11	3.36E-11	3.06E-11	7.67E-12	7.48E-12	4.37E-12
$k^{ICVT/SCT,1500K}$	1.98E-11	3.36E-11	3.06E-11	7.67E-12	7.60E-12	4.43E-12
$s^*(\Delta G)^{200K}$	-2.34	-0.54	-0.27	-1.69	-0.27	-0.27
$s^*(\Delta G)^{1500K}$	-1.94	-2.88	-0.27	-2.34	-0.27	-0.23
ω_i/cm^{-1}	642i	942i	1017i	823i	1077i	1062i
T/K with $\kappa^{TST/W}\leq1.2$	≥~500	≥~650	≥~700	≥~600	≥~750	≥~700

[a] Computed activation energies, $\Delta E_e^{\ddagger}$ (electronic energy differences at s = 0, including spin-orbit contribution for Cl), and ΔV_a^G values (V_a^G = *VMEP* + ZPE; ΔV_a^G is the difference between the V_a^G energy at s = 0 and the maximum of V_a^G at $s^*(V_a^G)$) are in kcal.mol^{-1} (negative for $V_a^G(s = 0)$ smaller than $V_a^G(s^*)$). Computed rate coefficients, k's, are in cm^{3}molecule^{-1}s^{-1}. Reaction coordinate, s, is in amu$^{1/2}$-Å. The maximum of *VMEP* is at s = 0, the maximum of V_a^G is at $s^*(V_a^G)$, and the maximum of ΔG at a certain temperature, T, is at $s^*(\Delta G)^{TK}$. Computed imaginary harmonic vibrational frequency, ω_i, at the TS (s = 0) is in cm^{-1}.

4.3.3 Computed CAG factors and Rate Coefficients

An immediate consequence of the deviation of $s^*(V_a^G)$ from 0 is the introduction of a classical transmission coefficient (known as a CAG factor) which corrects the fact that the maximum of V_a^G is not at $s = 0$. Reliable computed rate coefficients require accurate treatment of threshold energies, especially in the case of multi-dimensional tunneling correction (MT; e.g. ZCT and SCT) where the threshold energy dominates the extent of the tunneling contributions to the rate coefficients. Generally, the classical transmission coefficients correct the rate coefficients at the TST and CVT levels with MT in form of a multiplicative factor which is known as κ^{CAG} and the overall rate coefficients [46] are computed as :

$$k(tunneling) = \kappa^{CAG} \times \kappa(tunneling) \times k(without\ tunneling) \qquad (4.2)$$

i.e. $$k^{(TST\ or\ CVT)/MT} = \kappa^{(TST\ or\ CVT)/CAG} \times \kappa^{ZCT\ or\ SCT} \times k^{TST\ or\ CVT} \qquad (4.3)$$

At the TST level, $\kappa^{TST/CAG} = \exp(\beta[V_a^G(s=0) - V_a^G(s^*)])$ [46, 47] while $\kappa^{CVT/CAG} = \exp(\beta(V_a^G(s^*(\Delta G)) - V_a^G(s^*))$ [46, 47] at the CVT level, where $\beta = (k_B T)^{-1}$.

For the computed $\kappa^{TST/CAG}$, $V_a^G(s^*)$ is the global maximum of the V_a^G curve so it is generally larger than $V_a^G(s=0)$, so $\kappa^{TST/CAG}$ is always less than or equal to unity. The quantity, $V_a^G(s=0) - V_a^G(s^*)$, in $\kappa^{TST/CAG}$ is denoted as ΔV_a^G. The ΔV_a^G and the corresponding $s^*(V_a^G)$ values obtained at the six lower levels are reported in Table 4.8. The former quantity ranges from -2.92 to -1.12 kcal.mol^{-1}, leading to $\kappa^{TST/CAG}$ which ranges from 6.50×10^{-4} to 6.00×10^{-2} at 200 K and 3.76×10^{-1} to 6.87×10^{-1} at 1500 K respectively. The computed $\kappa^{TST/CAG}$, k^{TST} and $k^{TST/CAG}$ (i.e. $k^{TST/CAG} = \kappa^{TST/CAG} \times k^{TST}$) values at 200 K and 1500 K are also reported in Table 4.8. The interrelations among ΔV_a^G, $\kappa^{TST/CAG}$, k^{TST} and $k^{TST/CAG}$ are as expected because they simply follow the equations (4.2) and (4.3). The most significant observation is the impact of small $\kappa^{TST/CAG}$ (as small as 6.5×10^{-4}) on the computed $k^{TST/CAG}$. This situation is particularly prominent at low temperature, where the $k^{TST/CAG}$ values are actually more than three orders of magnitude smaller than the corresponding k^{TST} values (see the M06-2X V_a^G at 200 K) because of the very small $\kappa^{TST/CAG}$ values. In summary, small $\kappa^{TST/CAG}$ values originate from the large differences between $V_a^G(s^*)$ and $V_a^G(s=0)$, which arise from the ΔZPE changes along the

reaction path. This reflected the gradual change of the CH stretching mode in $CH_3CO(O)CH_3$ (reactant) and to the intermolecular C..H..Cl mode in the TS.

For the $\kappa^{CVT/CAG}$ values, the generalized TS is located at the maximum of the ΔG curve, and the corresponding V_a^G value is $V_a^G(s^*(\Delta G))$, which may or may not be the same as $V_a^G(s^*)$. The computed $\kappa^{CVT/CAG}$ values at 200 and 1500 K are reported in Table 4.8 and they are almost exactly 1.0 at 200 K and near 1.0 at 1500 K for all cases except for the M05 level ($\kappa^{CVT/CAG,1500K}$ = 0.725), which is not far from 1. Regarding the ΔG curves at the six lower levels, they generally behave as the corresponding V_a^G curves. In these 6 cases, one can observe the locations of the maxima of ΔG are near the maxima of V_a^G (i.e. $s^*(\Delta G) \approx s^*(V_a^G)$) and all $s^*(\Delta G)$ at both 200 K and 1500 K are reported in Table 4.8. Actually, the $s^*(\Delta G)$ values at both 200 K and 1500 K are near the corresponding $s^*(V_a^G)$ values, except for the M05, M06-2X and B3LYP levels. Their $s^*(\Delta G)^{1500K}$ values are -2.88, -2.34 and -1.94 amu$^{1/2}$-Å respectively whereas their $s^*(V_a^G)$ values are -0.76, -1.64 and -2.37 amu$^{1/2}$-Å, respectively. Therefore, the differences between the $s^*(\Delta G)^{1500K}$ and the $s^*(V_a^G)$ are -2.12, 0.70 and +0.43 amu$^{1/2}$-Å, respectively. The above comparisons show that the maxima of ΔG curves at 200 K and 1500 K are generally close to the maxima of V_a^G curves, except for the M05 level, which will be discussed later. For the cases at the M06-2X and B3LYP levels, their $s^*(V_a^G)$ values are different from their $s^*(\Delta G)$ values, even though their $\kappa^{CVT/CAG}$ at 1500 K are still close to 1.0. Considering both ΔG and V_a^G curves at the two levels are quite flat and $\kappa^{CVT/CAG}$ only accounts for the difference in energy, the large difference between $s^*(V_a^G)$ and $s^*(\Delta G)$ makes no contribution to the $\kappa^{CVT/CAG}$ value. In summary, even though the $s^*(\Delta G)$ is very different from $s^*(V_a^G)$, as long as the ΔG and V_a^G curves are relatively flat, $\kappa^{CVT/CAG}$ will still be very close to 1.0. Hence, $\kappa^{TST/CAG}$ values actually move $k^{TST/CAG}$ values close to k^{CVT} values, which are like accounting for variational effects as in CVT.

The changes of $s^*(\Delta G)$ with temperature at the six lower levels are shown in Figure 4.5. Smooth changes of $s^*(\Delta G)$ with increasing temperature are observed in Figure 4.5 except at the M05 level, where sudden changes are identified at 400/500 K and 900/1000 K. The $s^*(\Delta G)$ value moves toward -3.0 amu$^{1/2}$-Å (more negative s which means closer to the reactant complex) with increasing temperature.

Figure 4.5 The positions (reaction coordinate, s, in amu$^{1/2}$-Å) of the global maxima in the free energy (ΔG)) curves, $s^*(\Delta G)$, versus temperature (T in K) at six single levels (note that the BH&HLYP plot is almost exactly on top of the M06 plot).

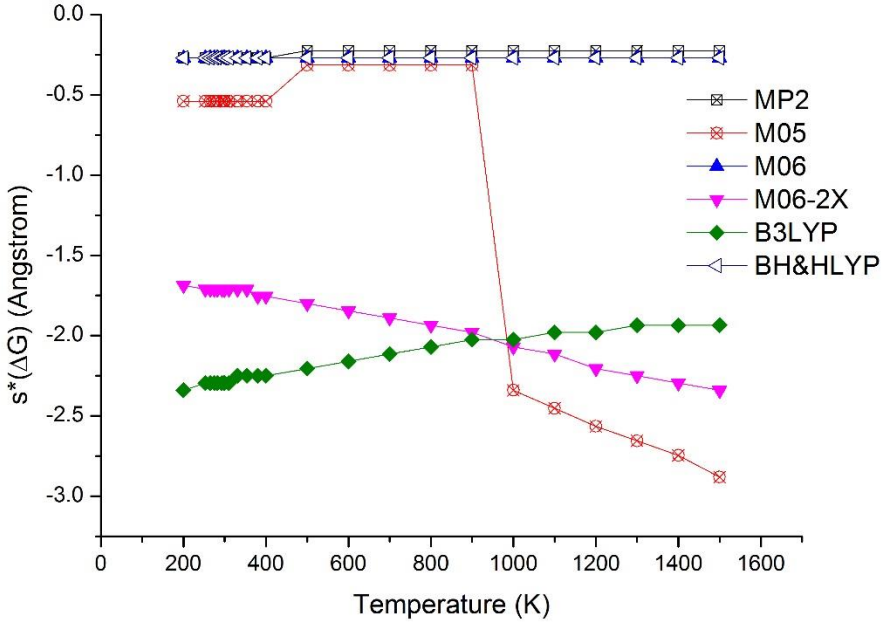

Figure 4.5 shows the changes of $s^*(\Delta G)$ with temperature at the MP2, BH&HLYP and M06 levels (M06 data points are exactly underneath the BH&HLYP data points), and these levels show negligibly small changes with temperature. The MP2, BH&HLYP and M06 levels have $s^*(\Delta G)$ values which are very close to their $s^*(V_a^G)$ values (see Table 4.8). As temperature increases, $s^*(\Delta G)$ obtained with the B3LYP IRC path moves toward $s = 0$ but it moves away from $s = 0$ for the M06-2X IRC path. A significant observation in Figure 4.5 is that at the levels of B3LYP, M06-2X and M05 (which will be discussed in details later), the $s^*(\Delta G)$ values keep decreasing as temperature increase (at the M06-2X and M05 levels) or decreases (at the B3LYP level). Similar situations in hydrogen abstraction reactions with Cl atom have also been reported in reference 17 and the authors need to extend the IRC path beyond the computed range in order to locate a maximum along the reaction paths (VTST, IRCmax and ZK-IRCmax). Therefore, the problems with the CVT calculations are twofold. First, the range of reaction coordinate employed must cover the maximum of ΔG, otherwise one would not be able to obtain accurate rate coefficients. Second, for flat potential energy surface, $s^*(\Delta G)$ could be very far away

from the saddle point. A similar situation is also reported in Figure 4 in reference 17 where the $s^*(\Delta G)$ value of the $(CH_3)_2CH_2 + Cl \rightarrow (CH_3)_2CH + HCl$ reaction keeps decreasing. Thus, the validity of CVT could remain a question, which indicates that the same problem can also be present in this case.

The sudden transitions of $s^*(\Delta G)$ at M05 level at 400/500 K and 900/1000 K are identified in Figures 4.5 and 4.6. In Figure 4.6, the ΔG versus s curves at 400 K, 500 K, 900 K and 1000 K are plotted with the maxima values of ΔG labeled as s^*. The sudden change of the $s^*(\Delta G)$ value between 400 K (bottom trace) and 500 K (top trace) shown in the top plot of Figure 4.6 and it is caused by a slight shift of the maximum value on the flat plateau. Regarding the sudden change of the $s^*(\Delta G)$ value between 900 K and 1000 K (the bottom plot of Figure 4.6), the global maximum of the flat plateau at -0.315 amu$^{1/2}$-Å at 900 K is exchanged with another flatter plateau at -2.34 amu$^{1/2}$-Å at 1000 K. In summary, for all the lower levels, although the shifts of $s^*(\Delta G)$ are not small, the differences in the corresponding ΔG values are small because the ΔG curves are relatively flat in the range of reaction coordinate considered. Moreover, in Figure 4.6, the very flat plateau of the ΔG curve beyond -2 amu$^{1/2}$-Å is likely the result of slightly unsmooth extrapolation of the *VMEP*, ΔZPE and V_a^G curves with the computed IRC path (see Figure 4.4). If there is an extra dip (not the one at near $s = 0$) which has led to the formation of another plateau in the ΔG curve which is closer to the reactant complex, it is the consequence of an error in the extrapolation of the V_a^G curve from the IRC path. The ΔG curve would then be presumed to proceed without the dip and be very flat in the reactant region without this extrapolation error.

Figure 4.6 The free energy (ΔG in kcal.mol^{-1}) versus reaction coordinate (s in amu$^{1/2}$-Å) plots at 400 and 500 K (top), and at 900 and 1000 K (bottom); the global maxima at four temperatures are indicated.

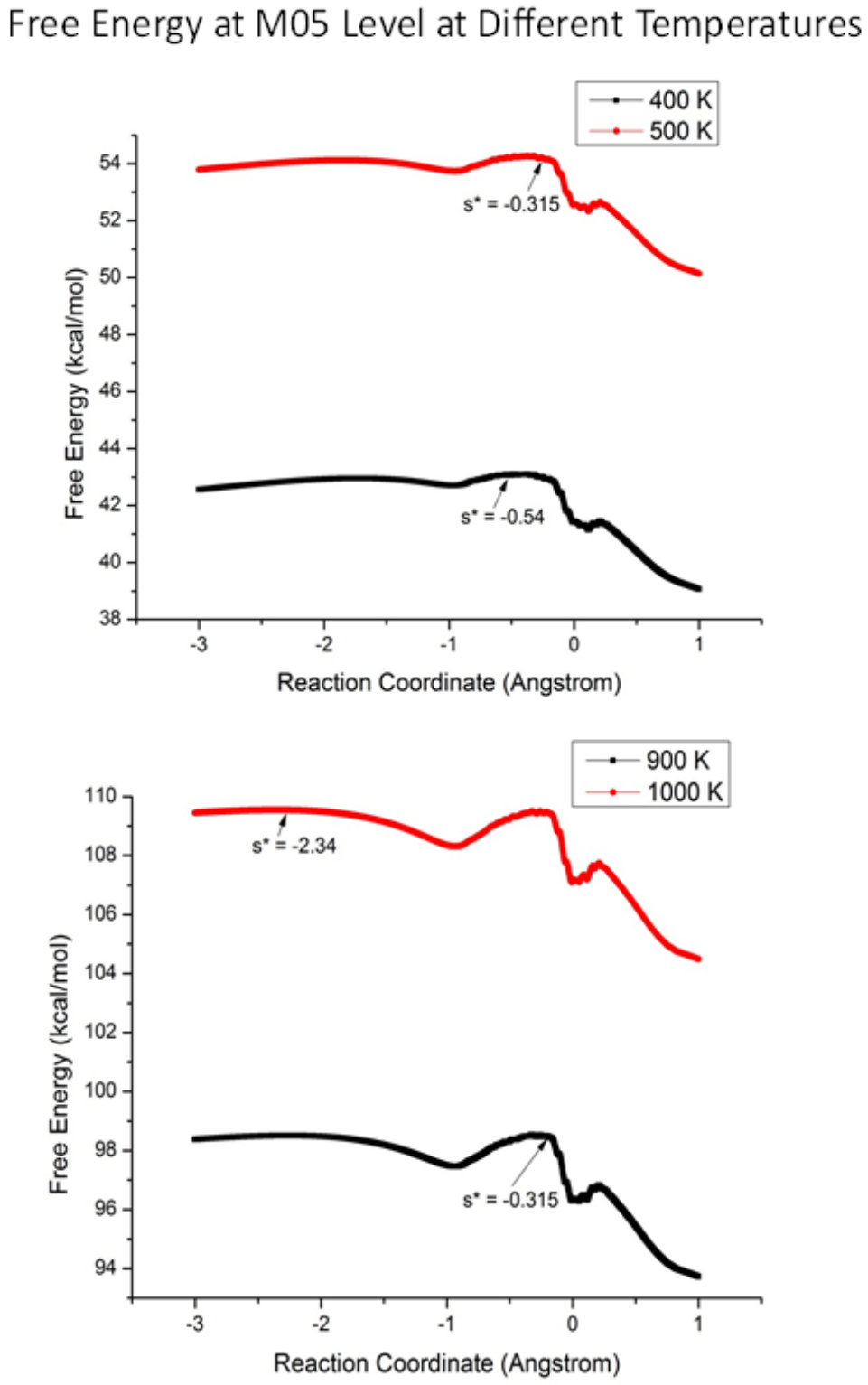

4.3.4 Rate Coefficient Calculations at Single Levels

The rate coefficients computed at various TST levels with and without tunneling corrections at 200 K and 1500 K obtained at the six lower levels are provided in Table 4.8. The important findings are as follows. First, the computed k^{CVT} values are the same as the k^{ICVT} values so the microcanonical correction of the threshold energy is negligible. Second, for the one-dimensional Wigner tunneling correction, the $\kappa^{TST/W}$ values are ≥ 1.2 at temperature higher than 500 K (for B3LYP IRC) while the same situation is observed for the IRCs at MP2 and the rest of the DFT levels at temperature higher than ~700 K (see Table 4.8). According to reference 46, the Wigner tunneling correction is no longer valid when $\kappa^{TST/W} >\sim 1.2$, so it is not considered further. Third, the multi-dimensional tunneling corrections at ZCT and SCT levels are basically unimportant (i.e. $\kappa^{ZCT} = \kappa^{SCT} = \sim 1.0$) in the temperature range considered except for the IRC paths obtained at the MP2 and BH&HLYP levels. Their κ^{ZCT} and κ^{SCT} values are smaller than 1.5 at 298 K, so the tunneling corrections at 298 K are small at the MP2 and BH&HLYP levels. Fourth, although k^{CVT} are the same as k^{ICVT} and κ^{ZCT} are the same as κ^{SCT} in most cases, $k^{CVT/SCT}$ values can be different from $k^{ICVT/SCT}$. Since $k^{CVT/SCT}$ is computed according to equation (4.3) and $k^{ICVT/SCT} = \kappa^{SCT} \times k^{ICVT}$, $\kappa^{CVT/CAG}$ determines the difference between $k^{CVT/SCT}$ and $k^{ICVT/SCT}$ at the same temperature. Hence, if the $\kappa^{CVT/CAG}$ value is significantly small (< 1.0), computed rate coefficients at the CVT/SCT level are different those at the ICVT/SCT levels at the same temperature. A small $\kappa^{CVT/CAG}$ value corresponds to a significant correction of the threshold energy. Finally, the plot of k^{TST} versus temperature using the six lower level IRC paths is plotted in Figure 4.7. Figure 4.8 is similar to Figure 4.7 except that the computed rate coefficients were obtained at ICVT/SCT level. According to Table 4.5, since the computed barrier height at the M06-2X level is the closest one to the experimentally derived barrier height, computed rate coefficients obtained at different TST levels (with and without tunneling) using the M06-2X IRC path are shown in Figure 4.9. Experimental rate coefficients are also shown in Figures 4.7, 4.8 and 4.9 for comparison purposes.

Figure 4.7 Computed k^{TST} ($cm^3molecule^{-1}s^{-1}$) versus T (K) curves (top) and $\log_{10}k^{TST}$ versus $1000/T$ curves (bottom) obtained with different single level IRC paths (experimental values from reference 4).

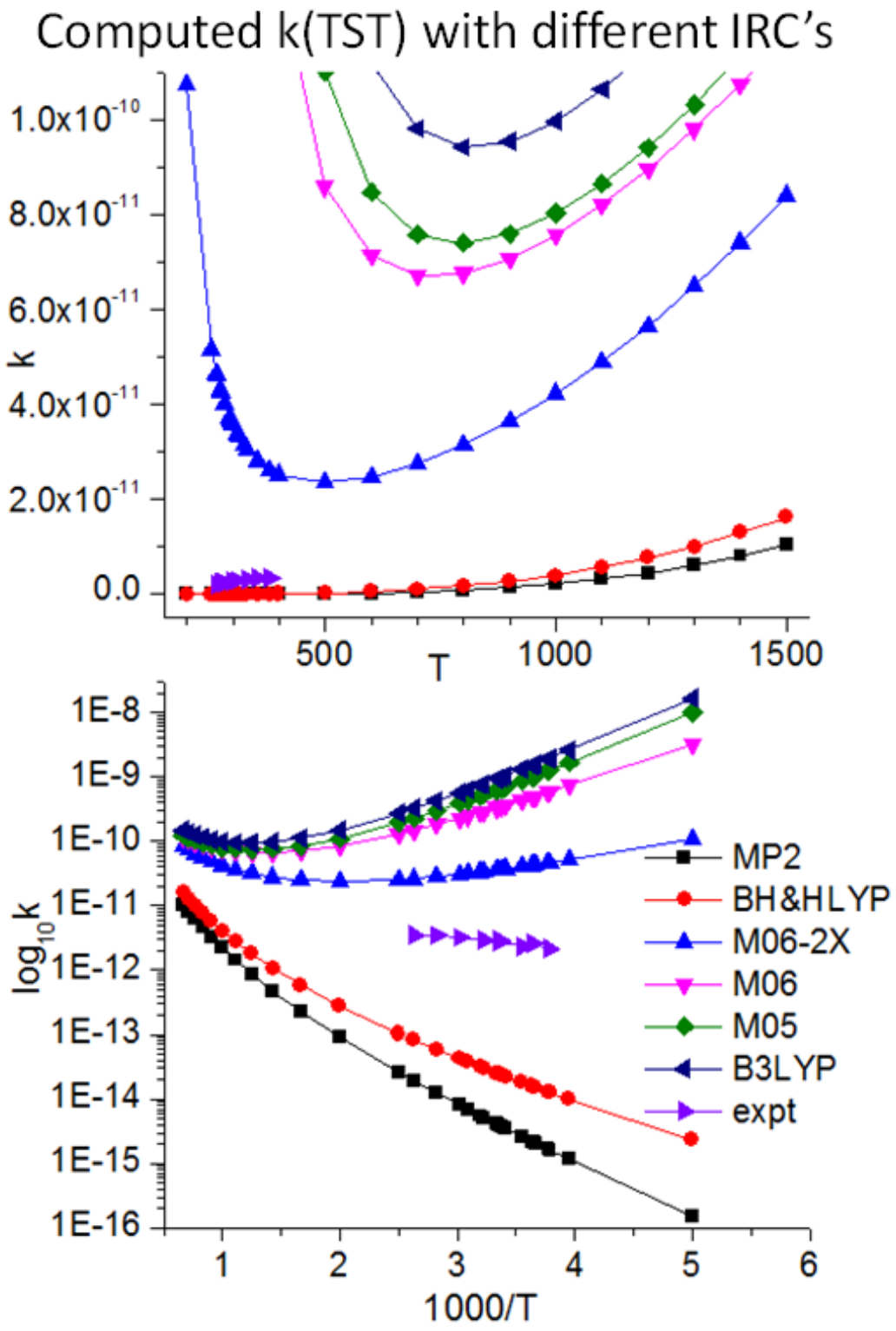

Figure 4.8 Computed $k^{ICVT/SCT}$ ($cm^3molecule^{-1}s^{-1}$) versus T (K) curves (top) and $\log_{10}k^{ICVT/SCT}$ versus $1000/T$ curves (bottom) obtained with different single level IRC paths (experimental values from reference 4).

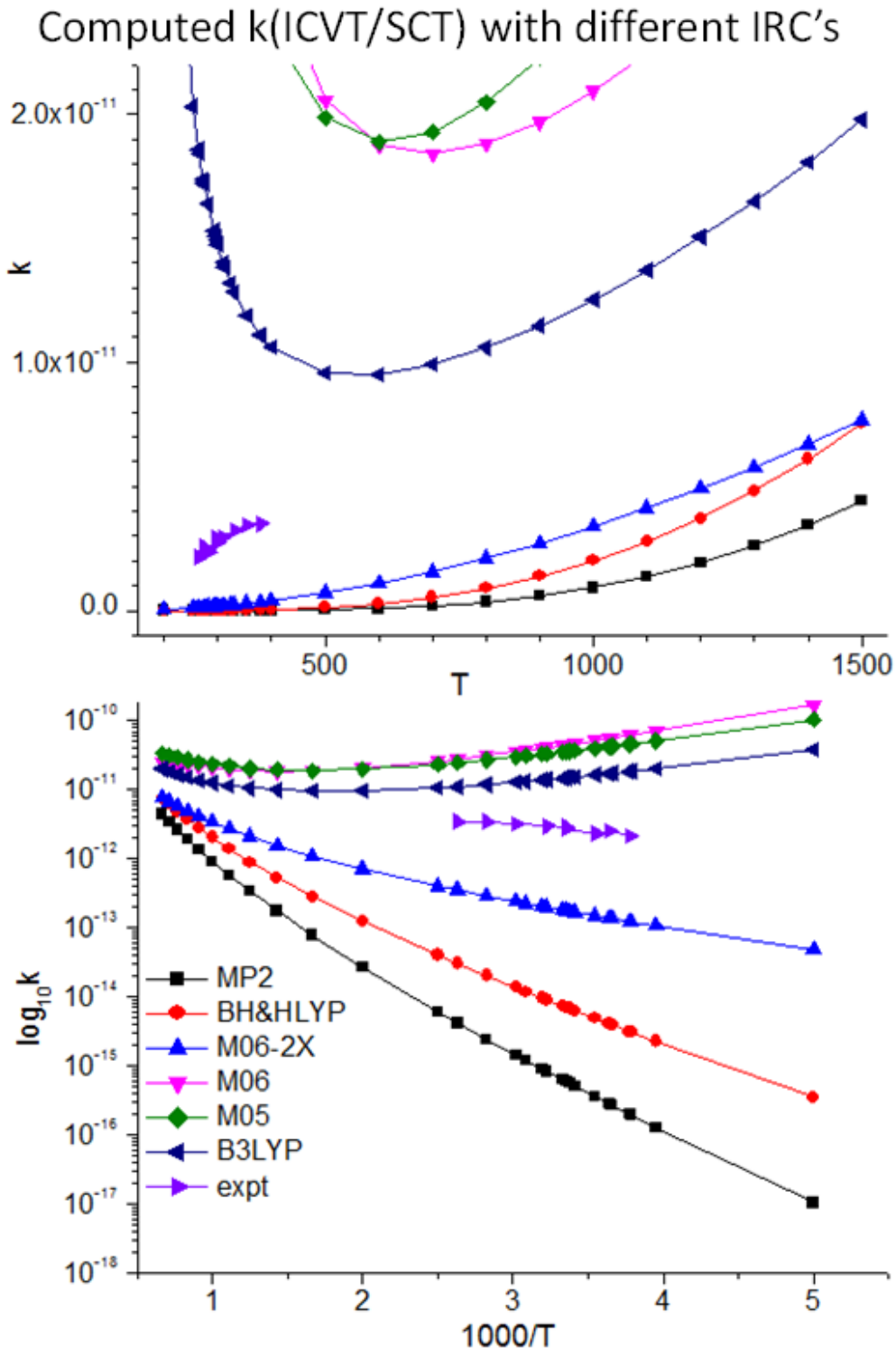

In Figure 4.7, the behaviors of the computed rate coefficients at the TST level obtained with different lower levels IRC clearly follow the computed barrier heights, that is, a high barrier height gives smaller k^{TST}. It can be seen that the experimental k value is bounded by the computed k^{TST} values at the BH&HLYP and M06-2X levels. In Figure 4.8, once variational effects and tunneling contributions to the rate coefficients are considered at the ICVT/SCT level, the trend of computed k values at the ICVT/SCT level does not follow that at the TST level. For example, the barrier heights obtained at the M06, M05 and B3LYP levels are 1.27, 0.37, and 0.35 kcal.mol^{-1} respectively, which are relatively low. Their k^{TST} values have order B3LYP > M05 > M06. At the ICVT/SCT level, their $k^{ICVT/SCT}$ values have order M05 > M06 > B3LYP. Clearly there is another factor which can influence the trend of $k^{ICVT/SCT}$ values, which implies that the pre-exponential entropic term ($\Delta S/R$ where ΔS is a function of vibrational frequencies and R is the universal gas constant) may play an important role in the rate coefficients of reactions with low barrier heights. The experimental rate coefficient falls between the computed $k^{ICVT/SCT}$ values at the M06-2X and B3LYP levels. If barrier height is the only factor considered in comparison, a barrier height that has values between those at the M06-2X and B3LYP levels ($\Delta E_e^{\ddagger}$ = 0.35 and 2.67 kcal.mol^{-1} respectively; Table 4.8) may have a better agreement between the computed $k^{ICVT/SCT}$ and the experimental values. In Figure 4.9, k^{TST} values are the largest among all the TST levels, however, with the inclusion the small $\kappa^{TST/CAG}$ values, $k^{TST/CAG}$ values are close to the computed rate coefficients at the VTST levels as the variational effects at the CVT and ICVT levels are similar to the impacts of $\kappa^{TST/CAG}$ on k^{TST}.

Figure 4.9 Computed k ($cm^3molecule^{-1}s^{-1}$) versus T (K) curves (top) and $\log_{10}k$ versus 1000/T curves (bottom) obtained at various TST levels with the M06-2X IRC path (experimental values from reference 3); since $k^{CVT} = k^{ICVT}$ and $\kappa^{ZCT} = \kappa^{SCT}$ (= ~1), computed k's with s with the same values are not plotted; for those plotted, the $k^{TST/CAG}$ curve essentially overlaps with the $k^{TST/SCT}$ curve, while the $k^{CVT/CAG}$, k^{ICVT}, $k^{CVT/SCT}$ and $k^{ICVT/SCT}$ curves overlap with each other.

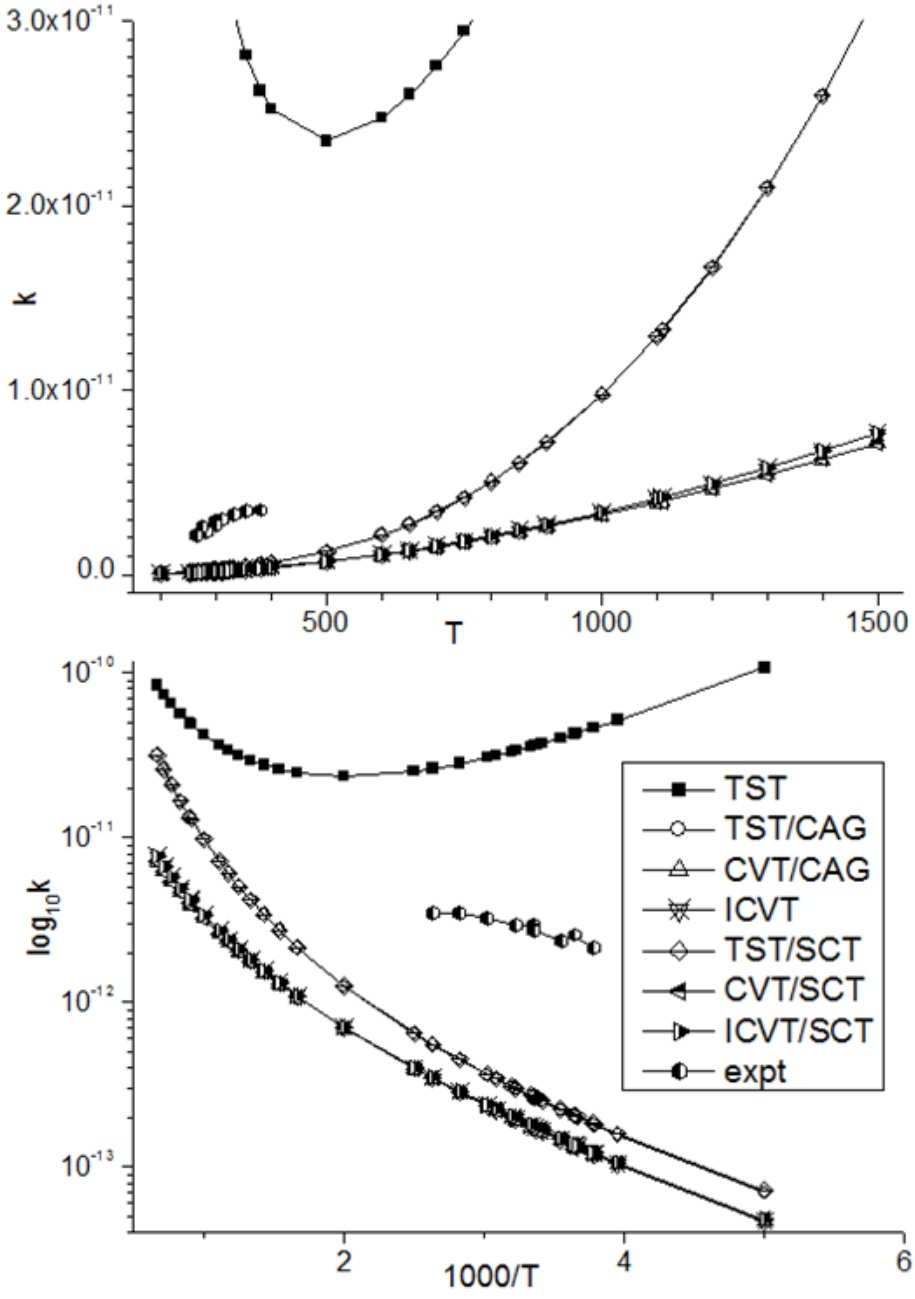

4.3.5 Rate Coefficient Calculations at Dual Levels

The computed *VMEP* curves at the six lower levels and their corresponding higher levels are shown in Figure 4.10 where the higher level *VMEP* curves were obtained by using equation (4.1) and the barrier height obtained at the UCCSD(T)-F12b/CBS level. Hence, all higher level *VMEP* curves in Figure 4.10 have the same barrier height and all of their appearances mimic the corresponding lower level *VMEP*s closely. Then the higher level *VMEP* curves are then used for rate coefficient calculations at various TST levels and the resulting k^{TST} and $k^{ICVT/SCT}$ values are plotted against temperature as shown in Figures 4.11 and 4.12, respectively. First, although all higher level *VMEP*s have the same barrier height, their k^{TST} and $k^{ICVT/SCT}$ values differ by more than 1 order of magnitude, indicating the effects from the lower level *VMEP*s on the computed *k* are not negligible. Although the relative energies in the dual level dynamic calculations are obtained at higher level, the vibrational frequencies used are still the ones obtained at lower levels. Hence, the pre-exponential terms actually have values obtained in the lower levels and they can affect the computed *k* with higher level results. Second, the lower levels with magnitudes of k^{TST} values are ranked, M06-2X > M06 > BH&HLYP > M05 > MP2 > B3LYP whereas those at ICVT/SCT levels are ranked, M06 > BH&HLYP > B3LYP > M05 > MP2 > M06-2X in which no obvious trends can be devised. Third, in terms of the agreement between the computed *k* values and experimental *k* values, k^{TST} computed at dual levels with MP2 and M05 as lower levels agree very well with the experimental *k* values; however, all $k^{ICVT/SCT}$ values are approximately one order of magnitude smaller than the experimental *k* values. Hence, the barrier height at UCCSD(T)-F12/CBS//MP2 level (3.54 kcal.mol^{-1}, see Table 4.5) is too high with respect to $k^{ICVT/SCT}$ calculations. Finally, the computed *k* at various TST levels versus *T* plots obtained with the UCCSD(T)-F12/CBS//MP2 VMEP are shown in Figure 4.13. This figure shows that k^{TST} values are the largest among all TST levels, which are similar to the situations discussed previously.

Figure 4.10 *VMEP*s at both single levels and dual level (UCCSD(T)-F12/CBS).

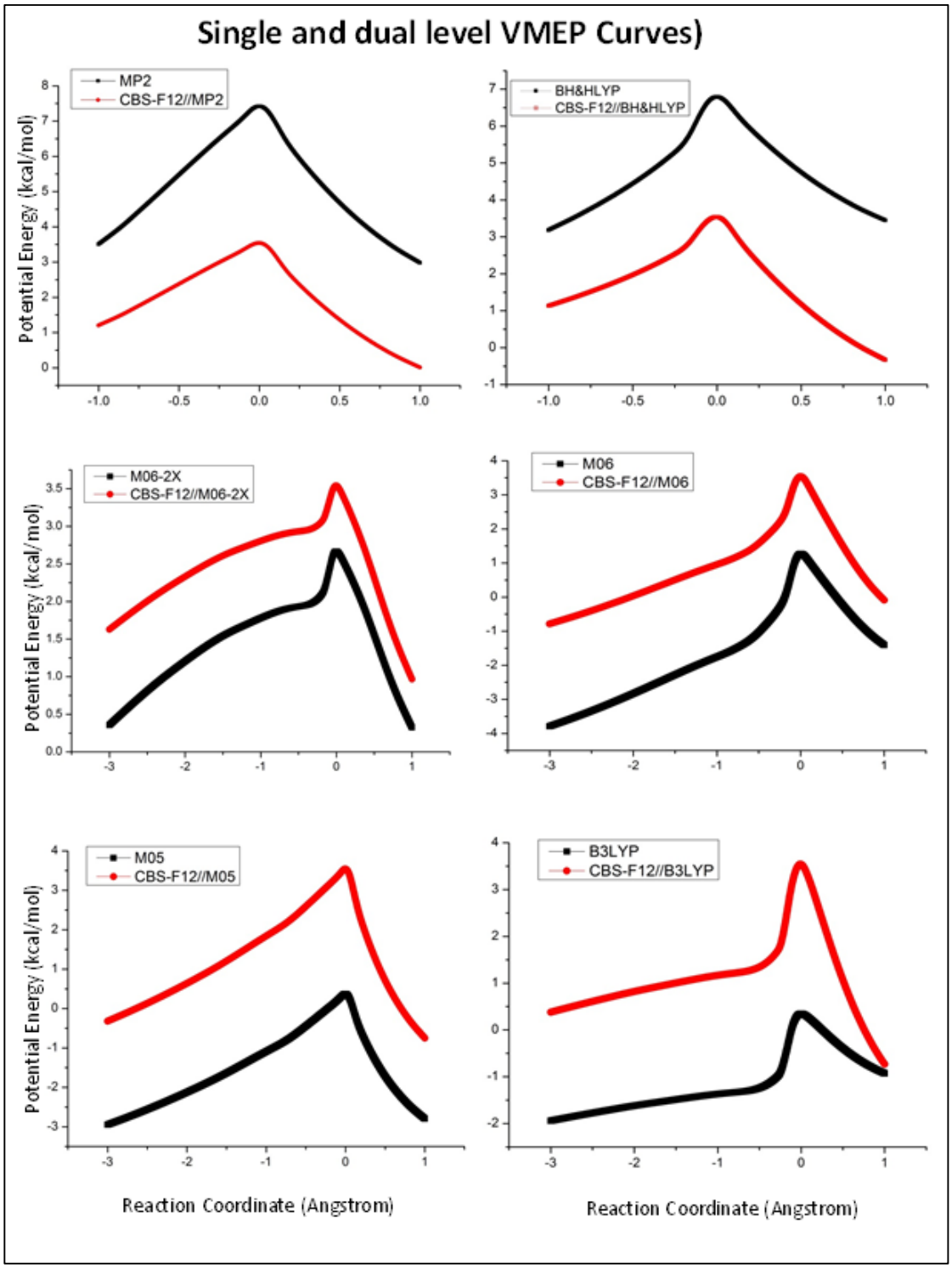

Figure 4.11 Computed k^{TST} ($cm^3molecule^{-1}s^{-1}$) versus T (K) curves (top) and $\log_{10}k^{TST}$ versus $1000/T$ curves (bottom) obtained at different dual levels: F12/CBS//MP2 higher level with different lower levels (experimental values from reference 4).

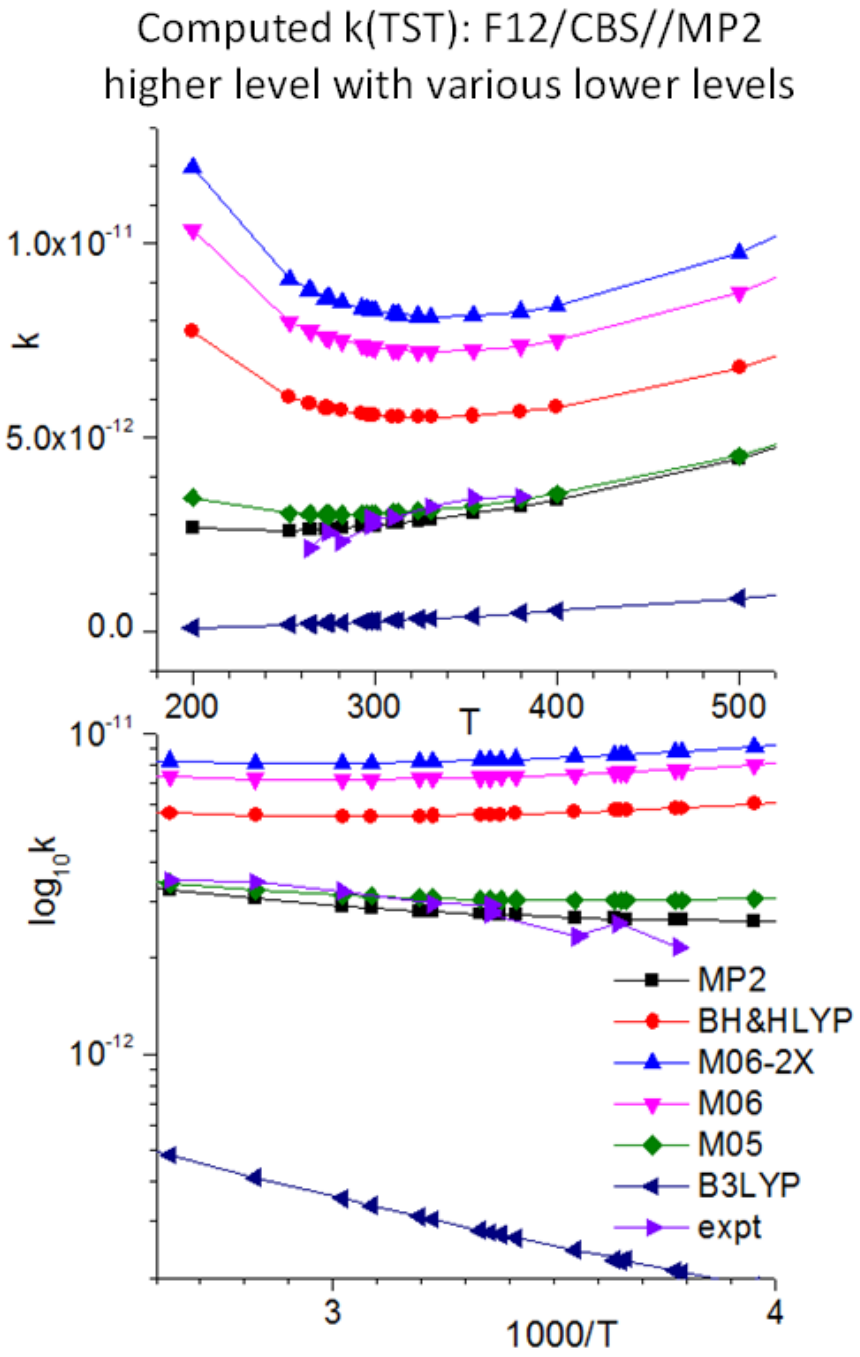

Figure 4.12 Computed $k^{ICVT/SCT}$ ($cm^3molecule^{-1}s^{-1}$) versus T (K) curves (top) and $\log_{10}k^{ICVT/SCT}$ versus $1000/T$ curves (bottom) obtained at different dual level: F12/CBS//MP2 higher level with different lower levels (experimental values from reference 4).

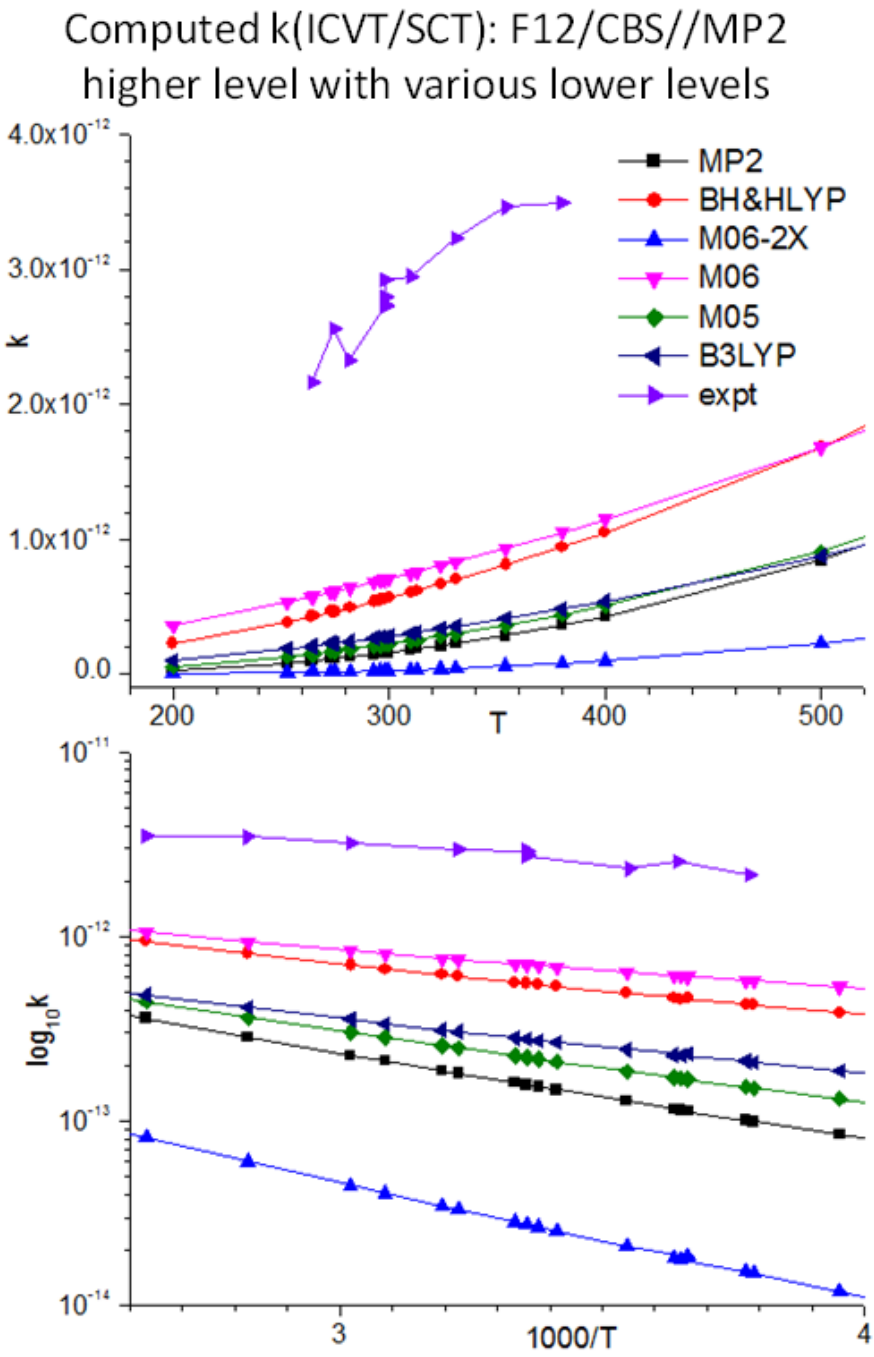

Figure 4.13 Computed k ($cm^3molecule^{-1}s^{-1}$) versus T (K) curves (top) and $\log_{10} k$ versus $1000/T$ curves (bottom) obtained at various TST levels with the dual level: F12/CBS//MP2 higher level and MP2 lower level (experimental values from reference 4); since $k^{CVT} = k^{ICVT}$

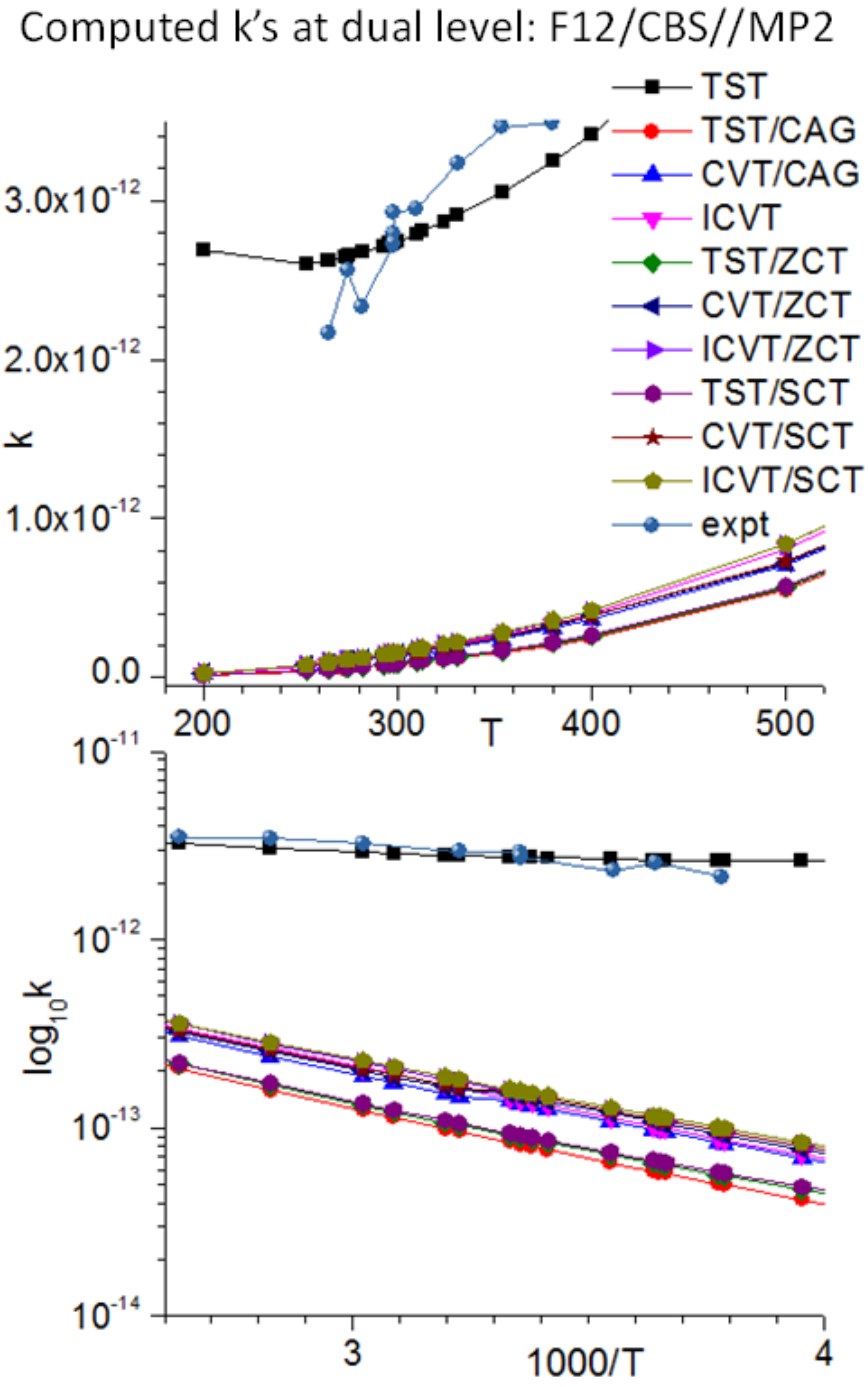

In view of matching the computed rate coefficients with the experimental rate coefficients, adjustments are made empirically to the barrier height at the higher level, so the following considerations have been made in order to achieve this. Since ICVT/SCT is the highest TST level, only $k^{ICVT/SCT}$ values will be adjusted. Second, F12/CBS//MP2 is the only pure *ab initio* level of the *VMEP* curve which has been used, other than the barrier height which is modified empirically. Third, the lower level method used in the dual level approach for the empirical adjustments of barrier heights needs to be determined. The considerations of choosing the most suitable lower level method cover three aspects: computed barrier heights, geometry optimization, and vibrational frequency results. In terms of barrier height ($\Delta E_e^{\ddagger}$), the M06-2X functional yields the closest value to the best estimate but the situation is the opposite for reaction energy (ΔE_e^{RX}). Indeed, none of the DFT functionals can yield relative electronic energies of the five stationary points which are comparable to the best estimates (see Table 4.5). In terms of geometry optimizations and vibrational frequency calculations, among the six lower levels, the MP2 method is the only *ab initio* method and it also comes with analytical first and/or second derivatives. For higher level *ab initio* methods (such as the QCISD and the CCSD(T) methods), they do not come with analytical first and/or second derivatives so it will be very computationally expensive to carry out geometry optimization and frequency calculations using those methods. Hence, no geometry optimizations and vibrational frequency calculations can be carried out with higher *ab initio* levels and it is difficult to justify whether the MP2 results are treated as benchmark results [35]. In summary, none of the lower levels is best suited according to the considerations of computed relative energies, geometries and vibrational frequencies. However, as mentioned before, the geometry effects from different lower levels on the computed barrier height are small (~0.5 kcal/mol). Lastly, the current $k^{ICVT/SCT}$ results show that the MP2 lower level yields values which are approximately in the middle of the results among all six lower levels (see bottom plot in Figure 4.12). After considering all of the above factors, the MP2 method is chosen as the lower level. Besides, the MP2 level can be used to keep all computational levels as *ab initio* as possible.

The resulting rate coefficients with modified barrier height (0.5 kcal.mol^{-1} without spin-orbit corrections of Cl, or 1.34 kcal.mol^{-1} with the spin-orbit corrections of Cl) are plotted against temperature as shown in Figure 4.14. Even with the reduced barrier height, k^{TST} values are still very large comparing with the experimental rate coefficients. With

the consideration of tunneling, $k^{TST/SCT}$ values are smaller than the experimental rate coefficients. At the highest TST level, $k^{ICVT/SCT}$ values agree very well with the experimental rate coefficients and the temperature behavior of the computed rate coefficients is consistent with that of the experimental *k*. The empirically adjusted barrier height is 1.34 kcal.mol^{-1}, which is 1.16 kcal.mol^{-1} larger than the experimentally derived activation energy (0.71±0.14 kcal.mol^{-1}) from the Arrhenius expression [3]. Comparing the adjusted barrier height with the best estimate (3.54±0.37 kcal.mol^{-1}, with the uncertainty given by the difference between the best and F12b/VTZ-F12 values see footnote c of Table 4.1), it is smaller than the benchmark value by 2.2 kcal.mol^{-1}. With the inclusion of the uncertainty error associated with the geometry effects (0.5 kcal.mol^{-1}), the overall uncertainty of the best estimate is then around ±0.9 kcal.mol^{-1} (i.e. 3.54±0.9 kcal.mol^{-1}), whereas the experimentally derived activation energy and the empirically adjusted value are 0.71±0.14 and 1.34 kcal.mol^{-1} respectively.

Finally, only out-of-plane hydrogen abstraction channel has been studied as experimental results suggest that it is the major channel but not the in-plane hydrogen abstraction at the methoxy group. However, there is a similar reaction, OH + $CH_3C(O)OCH_3$ with both in-plane and out-of-plane hydrogen abstractions which has been studied computationally. The results suggest that the out-of-plane hydrogen abstraction channel is the major channel according to the computed branching ratios of >~ 0.5 below 1000 K and ~0.5 above 500 K [44]. Besides, the $\Delta E_e^{\ddagger}$ of the out-of-plane channel in the OH + $CH_3C(O)OCH_3$ reaction is 1.66 kcal.mol^{-1}, which is slightly higher than the empirically adjusted barrier height of 1.34 kcal.mol^{-1} for the corresponding Cl + $CH_3C(O)OCH_3$ reaction studied in this work. The barrier height of the in-plane hydrogen abstraction channel of the OH + $CH_3C(O)OCH_3$ reaction, which is 3.24 kcal.mol^{-1} higher than the out-of-plane channel [44]. All these factors suggest that the out-of-plane channel of this class of reaction more kinetically favorable than the in-plane channel.

Figure 4.14 Computed k ($cm^3molecule^{-1}s^{-1}$) versus T (K) curves (top) and $\log_{10}k$ versus $1000/T$ curves (bottom) obtained at various TST levels with the dual level: F12/CBS//MP2 higher level and MP2 lower level, except with a fitted barrier height of 0.5 or 1.34 $kcal.mol^{-1}$ without and with SO contribution, respectively (experimental values from reference 4); note that some TST levels are not plotted, because they have the same computed k values as those plotted, as $\kappa^{ZCT} = \kappa^{SCT} = 1$, $k^{CVT} = k^{ICVT}$ and $k^{TST/CAG} = k^{TST/SCT}$.

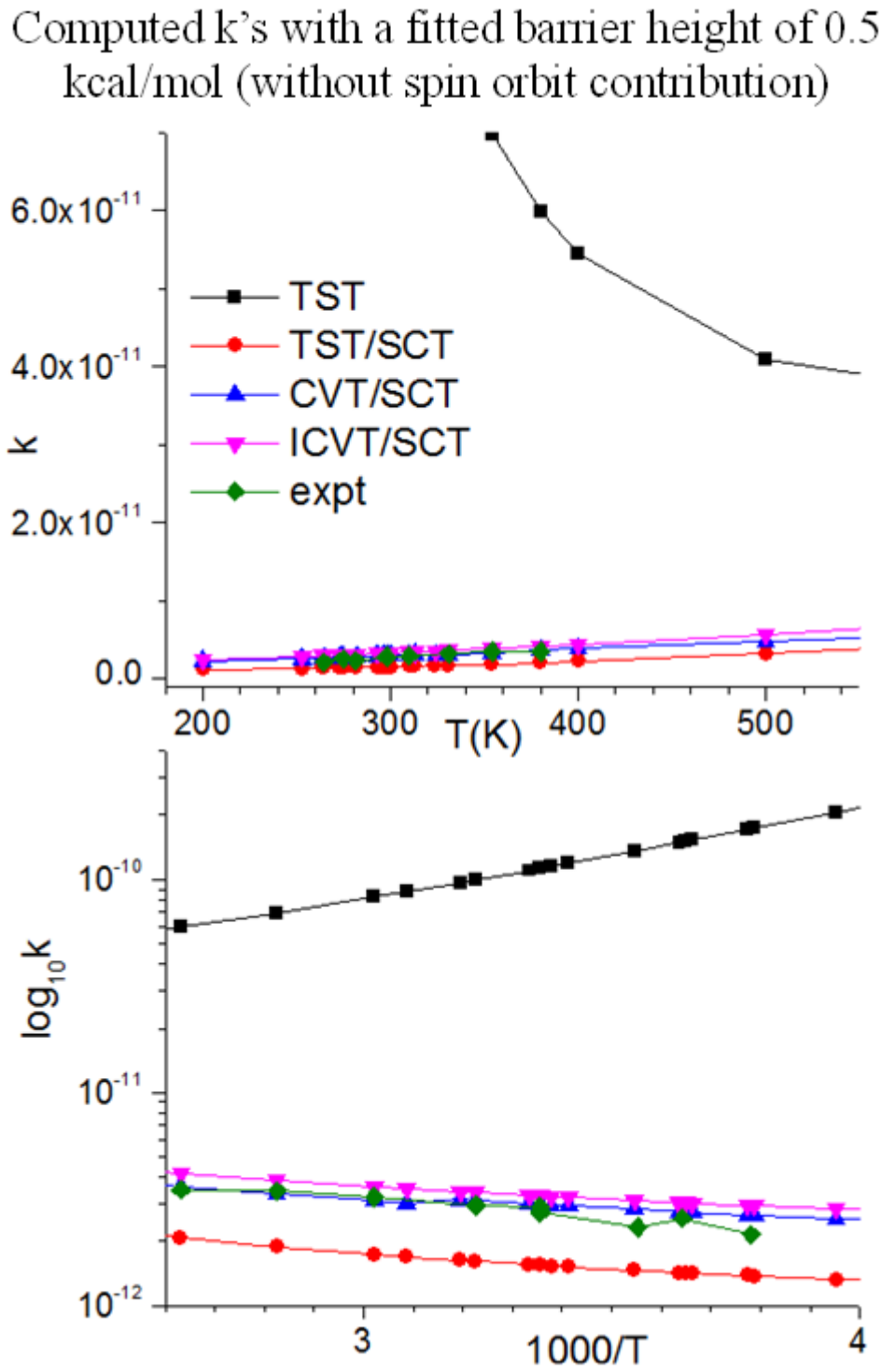

4.4 Conclusion

The Cl + $CH_3C(O)OCH_3$ → HCl + $CH_3C(O)OCH_2$ reaction has been investigated computationally. High level quantum chemistry calculations are used to construct potential energy surfaces which are then subsequently employed for carrying out rate coefficient calculations with single and dual level dynamics at different TST levels from 200 K to 1500 K. The most important results in the investigations on the interrelationships between various quantities and rate coefficients are summarized as follows.

First, the significant impacts of changes of computed harmonic frequency of one vibrational mode along the reaction path on the computed rate coefficients have been observed. The change in the vibrational frequency along the reaction path arising from the CH mode in the reactant (methyl acetate) to the C..H..Cl mode in the TS and then it becomes H-Cl in the product and these observations are common to all hydrogen abstraction reactions by Cl in the investigations. The drastic change of vibrational frequencies leads to the fact that the dip of the ZPE curve may be near $s = 0$ which in-turn leads to a small CAG correction factor (i.e. significant correction of the threshold energy). In the title reaction, $\kappa^{TST/CAG}$ can be much smaller than 1.0 (6.5×10^{-4}) , especially at low temperature. These effects are more obvious for reactions with low barrier height, as shown in the study. The introduction of $\kappa^{TST/CAG}$ is similar to the ZK-IRCmax approach in reference 17.

Second, once the variational effects are considered in CVT, the location of ΔG maximum can be very far away from the saddle point in the direction of reactants, especially when the barrier height is small. Therefore, one must be cautious about the choice of the range of the reaction coordinate, which must cover the maximum of the ΔG curve, otherwise, the VTST rate coefficients would be meaningless. Similar scenarios have also been investigated in reference 17 for hydrogen abstraction reactions by Cl with low barrier height.

Third, normally the barrier height is the dominant factor of the magnitude of the rate coefficients; however, it has been found that pre-exponential factor (i.e. the entropic contribution) can also have significant impacts on the computed rate coefficients, especially for reactions with low barriers. In the dual level dynamics calculations with the same barrier height but different lower level IRCs, it has been found that the discrepancies

in the rate coefficients (regardless at TST or ICVT/SCT levels) between different lower levels can be as large as one order of magnitude, which means that the uncertainties associated in the computed rate coefficients in higher levels due to uncertainties in lower levels can be also of an order of magnitude. Therefore, only improving the reliability of the computed barrier height may not be adequate to improve the computed rate coefficients. Hence, it is also crucial to benchmark optimized geometries and computed harmonic vibrational frequencies along the reaction path, as discussed in reference 17. However, considering the size of reacting system similar to the one in this study, for higher level *ab initio* methods other than the MP2 method, their analytical energy derivatives, especially second derivatives for calculating harmonic vibrational frequencies, are also mandatory.

Finally, a scaling equation for obtaining the higher level IRC paths from lower level IRC paths has been devised for carrying dual level dynamics calculations and they mimic the corresponding lower level IRC paths very well. The computed rate coefficients at ICVT/SCT level agree very well with the experimental values of the $Cl + CH_3C(O)OCH_3 \rightarrow HCl + CH_3C(O)OCH_2$ reaction when an empirically adjusted barrier height of 1.34 $kcal.mol^{-1}$ was employed in the dual level calculation. The adjusted barrier height of 1.34 $kcal.mol^{-1}$ is in between the best estimate value (3.54 ± 0.90 $kcal.mol^{-1}$) at UCCSD(T)-F12/CBS//MP2/6-311++G** level and the experimentally derived activation energy (0.71 ± 0.14 $kcal.mol^{-1}$ [5]).

4.5 References

1. Atkinson, R.; Arey, J. Atmospheric Degradation of Volatile Organic Compounds. *Chem. Rev.* **2003**,*103*, 4605-4638.
2. Mellouki, A.; Wallington, T. J.; Chen, J. Chem. Rev. 2015, 115, 3984-4014.
3. Yao, Y-C.; Tsai, J-H.; Chou, H-H. Aerosol and Air Quality Research 2011, 11, 547-559.
4. Christensen, L. K.; Ball, J. C.; Wallington, T. J. Atmospheric Oxidation Mechanism of Methyl Acetate *J. Phys. Chem. A* **2000**, *104*, 345– 351.
5. Cuevas, C. A.; Notariob, A.; Martineza, E.; Albaladejo, J. Influence of Temperature in the Kinetics of the Gas-phase Reactions of a series of Acetates with Cl atoms Atmos. Environ. 2005, 39, 5091– 5099
6. Andersen, V. F.; Nilsson, E. J. K.; Jørgensen, S.; Nielsen, O. J.; Johnson, M. S. Methyl Acetate Reaction with OH and Cl: Reaction Rates and Products for a Biodiesel Analogue Chem. *Phys. Lett.* **2009**, *472*, 23– 29.
7. Schutze, N.; Zhong, X.; Kirschbaum, S.; Bejan, I.; Barnes, I.; Benter, T.Relative Kinetic Measurements of Rate Coefficients for the Gas-phase Reactions of Cl atoms and OH radicals with a series of Methyl Alkyl Esters *Atmos. Environ.* **2010**, *44*, 5407– 5414.
8. De Haan, D. O.; Brauers, T.; Oum, K.; Stutz, J.; Nordmeyer, T.; Finlayson-Pitts, B.Heterogeneous Chemistry in the Troposphere: Experimental Approaches and Applications to the Chemistry of Sea Salt Particles *J Int. Rev. Phys. Chem.* **1999**, *18*, 343– 385.
9. Finlayson-Pitts, B.; Pitts, J. R. Chemistry of the Upper and Lower Atmosphere; Academic Press: San Diego, CA, **2000**
10. Finlayson-Pitts, B.; Pitts, J. R. *Chemistry of the Upper and Lower Atmosphere*; Academic Press: San Diego, CA, **2000**.
11. Raff, J. D.; Njegic, B.; Chang, W. L.; Gordon, M. S.; Dabdub, D.; Gerber, B.; Finlayson-Pitts, B. J.Chlorine Activation Indoors and Outdoors via Surface-mediated Reactions of Nitrogen Oxides with Hydrogen Chloride *Proc. Natl. Acad. Sci. U. S. A.* **2009**, *106*, 13647– 13654.
12. Pszenny, A. A. P.; Moldanov, J.; Keene, W. C.; Sander, R.; Maben, J. R.; Martinez, M.; Crutzen, P. J.; Perner, D.; Prinn, R. G.Halogen Cycling and Aerosol pH in the Hawaiian Marine Boundary Layer *Atmos. Chem. Phys.* **2004**, *4*, 147– 168.
13. Wayne, R. P. *Chemistry of Atmospheres*, 3rd ed.; Oxford University Press: Oxford, U.K., **2000**.

14. Tyndall, G. S.; Pimentel, A. S.; Orlando, J. J.Temperature Dependence of the Alpha-ester Rearrangement Reaction *J. Phys. Chem. A* **2004**, *108*, 6850– 6856.
15. Middala, S.; Campell, S.; Olea, C.; Scruggs, A.; Hasson, A. S.Kinetics and Mechanism of the Reaction of Propylene Oxide with Chlorine Atoms and Hydroxy Radicals *Int. J. Chem. Kinet.* **2011**, *43*, 507– 521.
16. Notario, A.; Le Bras, G.; Mellouki, A. Absolute Rate Constants for the Reactions of Cl atoms with a series of Esters J. Phys. Chem. A 1998, 102, 3112-3117.
17. Chan, B.; Radom, L. Approaches for Obtaining Accurate Rate Constants for Hydrogen Abstraction by a Chlorine Atom *J. Phys. Chem. A* **2012**, *116*, 3745– 3752.
18. Poutsma, M. L. Evolution of Structure-Reactivity Correlations for the Hydrogen Abstraction Reaction by Chlorine Atom *J. Phys. Chem. A* **2013**, *117*, 687– 703.
19. Frisch, M. J.; Trucks, G. W.; Schlegel, H. B.; Scuseria, G. E.; Robb, M. A.; Cheeseman, J. R.; Scalmani, G.; Barone, V.; Mennucci, B.; Petersson, G. A.; *GAUSSIAN 09*, revision A.02; GAUSSIAN, Inc.: Wallingford, CT, **2009**.
20. Zheng, J.; Zhang, S.; Lynch, B. J.; Corchado, J. C.; Chuang, Y.-Y.; Fast, P. L.; Hu, W.-P.; Liu, Y.-P.; Lynch, G. C.; Nguyen, K. A. POLYRATE version 2010-A (June, 2010), Copyright 1988–2010 D. G. Truhlar and Regents of the University of Minnesota, Minneapolis, MN, U.S.A.
21. Adler, T. B.; Knizia, G.; Werner, H. J. A Simple and Efficient CCSD(T)-F12 Approximation *J. Chem. Phys.* **2007**, *127*, 221106.
22. Werner, H.-J.; Knowles, P. J.; Knizia, G.; Manby, F. R.; Schütz, M.Molpro: a General-Purpose Quantum Chemistry Program Package WIREs *Comput. Mol. Sci.* **2012**, *2*, 242–253.
23. Werner, H.-J.; Knowles, P. J.; Knizia, G.; Manby, F. R.; Schutz, M.; MOLPRO, version 2010.1.
24. Helgaker, T.; Klopper, W.; Tew, D. P. *Quantitative Quantum Chemistry Molecular Physics* **2008**, *106*, 2107-2143.
25. Hill, J. G.; Mazumder, S.; Peterson, K. A. Correlation Consistent Basis Sets for Molecular Core-valence Effects with Explicitly Correlated Wavefunctions: The Atoms B-Ne and Al-Ar *J. Chem. Phys.* **2010**, *132*, 054108.
26. Peterson, K. A.; Adler, T. B.; Werner, H.-J. Optimized Auxiliary Basis Sets for Explicitly Correlated Methods *J. Chem. Phys.* **2008**, *128*, 084102.
27. Weigend, F.; Köhn, A.; Hättig, C. Efficient Use of the Correlation Consistent Basis Sets in Resolution of the Identity MP2 Calculations *J. Chem. Phys.* **2002**, *116*, 3175-3183.
28. Knizia, G.; Adler, T. B.; Werner, H.-J. Local Explicitly Correlated Second-order Perturbation Theory for the Accurate Treatment of Large Molecules *J. Chem. Phys.* **2009**, *130*, 054104.

29. Helgaker, T.; Klopper, W.; Koch, H.; Noga, J. Basis-set Convergence of Correlated Calculations on Water *J. Chem. Phys.*, **1997**, *106*, 9639-9646.
30. Halkier, A.; Helgaker, T.; Klopper, W.; Jorgensen, P.; Csaszar, A. G. Comment on "Geometry Optimization with an Infinite Basis Set" [*J. Phys. Chem. A* **1999**, *103*, 651.] and "Basis-set Extrapolation" [*Chem. Phys. Lett.* **1998**, *294*, 45.)] *Chem. Phys. Lett.* **1999**, *310*, 385-389.
31. Radziemski Jr., L. J.; Kaufman, V. *Journal of the Optical Society of America* **1969**, *59*, 424.
32. Hratchian H. P.; Schlegel, H. B. Using Hessian Updating to Increase the Efficiency of a Hessian based Predictor-corrector Reaction Path following Method *J. Chem. Theory Comput.* **2005**, *1*, 61-69.
33. Chuang, Y.-Y.; Truhlar, D. G. Statistical Thermodynamics of Bond Torsional Modes *J. Chem. Phys*. **2000**, *112***,** 1221-1228; Erratum, *J. Chem. Phys*. **2004**, *121*, 7036.
34. Ellingson, B. A.; Lynch, V. A.; Mielke, S. L.; Truhlar, D. G. Statistical Thermodynamics of Bond Torsional Modes: Tests of Separable, Almost-separable, and Improved Pitzer-Gwinn Approximations *J. Chem. Phys.* **2006**, *125*, 084305.
35. Truhlar, D.G. (1995). *The Reaction Path in Chemistry*. Dordrecht, The Netherlands :Kluwer.
36. Ng, M.; Mok, D.K.W.; Lee, E.P.F.; Dyke, J.M. *Journal of Computational Chemistry* **2013**,*34*,545–557.
37. Donahue, N. M.; Anderson, J. G.; Demerjian, K. L. New Rate Constants for Ten OH Alkane Reactions from 300 to 400 K: An Assessment of Accuracy *J. Phys. Chem. A* **1998**, *102*, 3121-3126.
38. IUPAC. Compendium of Chemical Terminology, 2nd ed. (the "Gold Book"). Compiled by A. D. McNaught and A. Wilkinson. Blackwell Scientific Publications, Oxford (1997). XML on-line corrected version: http://goldbook.iupac.org (2006-) created by M. Nic, J. Jirat, B. Kosata; updates compiled by A. Jenkins. ISBN 0-9678550-9-8. doi:10.1351/goldbook.
39. Hamborg, E. S.; Versteeg, G. F. Absorption and Desorption Mass Transfer rates in Chemically Enhanced Reactive Systems. Part II: Reverse Kinetic Rate Parameters *Chemical Engineering Journal*, **2012**, *198–199*, 561-570.
40. Aquilanti, V.; Mundim, K. C.; Cavalli, S.; De Fazio, D.; Aguilar, A.; Lucas, J. M. Exact Activation Energies and Phenomenological Description of Quantum Tunneling for Model Potential Energy Surfaces. The F + H-2 Reaction at Low Temperature *Chemical Physics* **2012**, *398*, 186-191.

41. Senent, M. L.; Domínguez-Gómez, R.; Carvajal M.; Kleiner, I. Highly Correlated *Ab initio* Study of the Far Infrared Spectra of Methyl Acetate *J. Chem. Phys*. **2013**, *138*, 044319.
42. Tudorie, M.; Kleiner, I.; Hougen, J. T.; Melandri, S.; Sutikdja, L. W.; Stahl, W. A fitting program for Molecules with Two Inequivalent Methyl Tops and a Plane of Symmetry at Equilibrium: Application to New Microwave and Millimeter-wave Measurements of Methyl Acetate *J. Mol. Spectrosc*. **2011** *269*, 211-225.
43. Cox, J. D.; Wagman, D. D.; Medvedev, V. A. *CODATA Key Values for Thermodynamics*, Hemisphere Publishing Corp., New York, **1984**, 1.
44. Hall, H. K., Jr.; Baldt, J. H. Thermochemistry of Strained-Ring Bridgehead Nitriles and Esters *J. Am. Chem. Soc.* **1971**, *93*, 140–145.
45. Yang, L.; Liu, J.-y.; Li, Z.-s. Theoretical Studies of the Reaction of Hydroxyl Radical with Methyl Acetate *J. Phys. Chem. A* **2008**, *112*, 6364– 6372.
46. Fernández-Ramos, A.; Miller, J. A.; Klippenstein, S. J.; Truhlar, D. G. Modeling the Kinetics of Bimolecular Reactions *Chem. Rev.* **2006**, *106*, 4518-4584.
47. Fernandez-Ramos, A.; Ellingson, B. A.; Garret, B. C.; Truhlar, D. G. In *Reviews in Computational Chemistry, Vol. 23*; Lipkowitz, K. B.; Cundari, T. R. (Eds.) Wiley-VCH: Hoboken, NJ, **2007**; pp. 125.

Chapter 5.

Theoretical Studies of the BrO with HO_2 reaction

5.1 Introduction

Bromine monoxide (BrO) has been well recognized for its ability to destroy the stratosphere ozone layer effectively and it mainly comes from volcanic eruption [1]. Yung and coworkers [2] found that a catalytic cycle, which involves bromine and chlorine atoms, may play a role in the destruction of the stratospheric ozone layer:

$$Br + O_3 \rightarrow BrO + O_2$$

$$Cl + O_3 \rightarrow ClO + O_2$$

$$BrO + ClO \rightarrow Br + Cl + O_2$$

$$\text{Net: } 2O_3 \rightarrow 3O_2$$

The major removal mechanism of atmospheric BrO radical is its reaction with hydroperoxyl radical (HO_2):

$$BrO + HO_2 \rightarrow \begin{cases} HOBr + O_2 \text{ (a)} \\ HBr + O_3 \ (b) \end{cases}$$

There are two channels of this reaction which are widely considered in literature [3-12]. The major channel, which involves the production of HOBr, is coincidently also the first step in the catalytic ozone destruction cycle. HOBr then undergoes photolysis to generate radicals and the full catalytic cycle is outlined as follows [3-5, 7]:

$$BrO + HO_2 \rightarrow HOBr + O_2$$

$$HOBr + h\nu \rightarrow OH + Br$$

$$OH + O_3 \rightarrow HO_2 + O_2$$

$$Br + O_3 \rightarrow BrO + O_2$$

$$\text{Net: } 2O_3 \rightarrow 3O_2$$

In the above cycle, the rate determining step is the first step, where atomic oxygen is not present. However, the opposite is observed in the ozone removal mechanisms by bromine and chlorine atoms. The following shows the catalytic ozone removal cycle by chlorine atoms:

$$Cl + O_3 \rightarrow ClO + O_2$$

$$ClO + O \rightarrow Cl + O_2$$

$$\text{Net: } O_3 + O \rightarrow 2O_2$$

Consequently, the $BrO + HO_2$ reaction may take part in the ozone removal process in the lower stratosphere, which is of lower concentration of atomic oxygen than that in the higher stratosphere. Since the $BrO + HO_2$ reaction is of atmospheric importance, extensive experimental and theoretical studies have been carried out. The experimental rate coefficients (k) of this reaction obtained at various pressure (P) and temperature (T) compiled in Table A1 in the appendix.

Some experimental observations of performing reactions (a) and (b) are summarized as follows. First, HOBr was the only detected product [3-5, 7-12] and no ozone was detected [11]. Second, the negative temperature dependence of the rate coefficient of reaction (a) was observed [6, 7]. Thus, a weak complex ($HBrO_3$ complex) was purposed to be responsible for this behavior [6, 7]. Third, reaction (a) was independent from pressure [8-10].

In view of the large differences in the existing experimental rate coefficients of the BrO + HO_2 reaction, Atkinson and coworkers [13] compiled and carefully evaluated the experimental rate coefficients of this reaction. They concluded that channel (a) was the major channel and channel (b) essentially had no effect on the overall rate coefficient. They recommended the Arrhenius expression of reaction (a) to be $4.5\times 10^{-12}\exp(500/T)$ over the temperature range of 210 – 360 K [13]. Since the recent studies of the BrO + HO_2 reaction show that it proceeds faster than the recommended value at 298 K (which is 2.4×10^{-11} cm^3/molecule-second). Moreover, the experimental measurements over 210 – 360 K show a negative temperature dependence of rate coefficient and it has been proposed that a reactant complex could be responsible for this observation [6].

In the BrO + HO_2 reaction, the ground states of both reactants are doublet. According to the spin conservation, the reaction can proceed on a triplet (producing HOBr ($\tilde{X}^1A'$) + $O_2(\tilde{X}^3\Sigma^-_g)$) or a singlet reaction surface (producing HOBr ($\tilde{X}^1A'$) + $O_2(\tilde{a}^1\Delta_g)$). For the singlet surface, the reactant complex (RC) and the transition state (TS) are expected to be open-shell singlets whereas the product complex (PC) and products are expected to be closed-shell singlets. The same pattern is observed in a previous study on the BrO + $CH_3O_2 \rightarrow$ HOBr + CH_2O_2 reaction studied by our group [14]. In this study, various density functionals and the MP2 method were employed to locate the open-shell singlet TS but only the M06-2X functional could locate the TS. In this connection, the results suggested that most functionals and the underlying UHF wavefunction used in MP2 method were not able to capture the multi-reference effects in open-shell singlet species (see reference 14 for details). Guha and Francisco performed computational study on the BrO + $CH_3O_2 \rightarrow$ HOBr + CH_2O_2 reaction [15] using QCISD method and they failed to locate the TS because the underlying HF wavefunction is inadequate in describing the electronic structures of open-shell singlet species. In view of the failure of the methods employed in the previous studies of the reaction with similar nature to the title reaction, UHF-based correlation methods do not deem appropriate for locating open-shell singlet species but M06-2X functional is a more feasible choice.

The first computational investigation of the potential energy surface of reactions (a) and (b) was conducted by Kaltsoyanni and Rowley [16]. Three channels in the BrO + HO_2 reaction were considered in their study, namely,

(i) $BrO + HO_2 \rightarrow HOBr + O_2 (\tilde{X}^3\Sigma_g^-)$

(ii) $BrO + HO_2 \rightarrow HOBr + O_2 (\tilde{a}^1\Delta g)$

(iii) $BrO + HO_2 \rightarrow HBr + O_3$

and they generally optimized the stationary points at the CCD/6-311G** (where CCD means coupled-cluster double) level and refined the single point energies at the CCSD(T)/6-311G** level. The barrier heights and reaction enthalpies are obtained as (i) -2.9, -52.6 kcal.mol^{-1}, (ii) 15.8, -37.3 kcal.mol^{-1} and (iii) 8.1, -10.0 kcal.mol^{-1}. This study concludes that the channel with the largest rate coefficient is reaction (i) which comes with a negative barrier. The barrier of reaction (iii) was too high so the formation of HBr and O_3 was not kinetically favoured [16]. Although reaction (ii) involves open-shell singlet species, Kaltsoyanni and Rowley appeared to have used restricted wavefunctions in the study so closed-shell species have indeed been optimized on the singlet surface. There were no rate coefficient calculations in their work [16] so no comparisons can be made with the experimental results. Following the suggestion by Mellouki *et al*. [6] and Larichev *et al*. [7], Guha and Francisco employed computational techniques to investigate different possible $HBrO_3$ isomers and their structures, relative energies, and vibrational spectra [17-19] with the stationary points optimized at the QCISD level and electronic energy computed at the QCISD(T) level.

In this work, the following five channels of the $BrO + HO_2$ reaction were studied:

$$BrO + HO_2 \rightarrow HOBr + O_2 (\tilde{X}^3\Sigma_g^-) \quad (1a)$$

$$BrO + HO_2 \rightarrow HOBr + O_2 (\tilde{a}^1\Delta_g) \quad (1b)$$

$$BrO + HO_2 \rightarrow HBr + O_3 \quad (2)$$

$$BrO + HO_2 \rightarrow OBrO + OH \quad (3)$$

$$BrO + HO_2 \rightarrow BrOO + OH \quad (4)$$

Channels (1a) and (1b) correspond to the major channel as reported in the literature. Channel (2) can be important since it produces O_3. Channels (3) and (4) are included in this study because they produce OH radicals. More importantly, if their rate coefficients are near or even larger than those of channels (1a) and (1b), they could be crucial to atmospheric chemistry.

This work aims to investigate the reaction mechanisms of the BrO + HO_2 reaction, locate the stationary points (reactants, RC, TS, PC and products), and compute their relative energies in the individual channels by using state-of-the-art wavefunction and DFT methods. Rate coefficient calculations have also been performed for the channel with the lowest barrier height in the atmospherically important temperature range, 200 - 400 K, and they are then compared with the experimental values. This work is the first work to compute rate coefficients for the BrO + HO_2 reaction from the potential energy surfaces obtained using electronic structure calculations. Since the previous literature [13] has reported that the major product of the reaction is HOBr and no O_3 has been detected in the temperature range, 300 – 441 K, channels (1a) and (1b) are expected to the most important kinetically. Therefore, a limit can be placed on the rate coefficient ratio $k_2/k_{(1a+1b)} < 1.5 \times 10^{-2}$ [7].

5.2 Methodology

5.2.1 *Ab initio*/DFT Calculations

Geometry optimization and harmonic frequencies of stationary points, transition state (TS) search, intrinsic reaction coordinate (IRC, also known as MEP, minimum energy path) and relative energy calculations were performed with the meta-hybrid GGA density functional, M06-2X, for all channels with the aug-cc-pVDZ (for H, C and O) and aug-cc-pVDZ-PP (for Br) basis sets (collectively denoted as AVDZ from now on) in the Gaussian 09 suite [20]. The M06-2X functional was selected for current study because studies have shown it to be able to obtain reliable barrier height and perform well in geometry optimization in various benchmark studies [21-25]. For each transition state, it had only one imaginary vibrational frequency. IRC calculations were performed to ensure that the TS connects from appropriate reactants to appropriate products. Moreover, some TS search and harmonic frequency calculations were also computed at the BD/AVDZ level (*vide infra*).

Among the five channels considered in the title reaction, there are three triplet channels (channels (1a), (3) and (4)) and two singlet channels (channels (1b) and (2)). Due to the nature of different channels, the methods employed could be slightly different. For channel (2), an open-shell singlet state of the RC was initially explored using

unrestricted wavefunction with the guess=mix keyword in Gaussian 09 [20]. However, geometry optimization led to a closed-shell singlet intermediate (*vide infra*). As a result, TS and PC were optimized as closed-shell singlet species in this channel. For channel (1b), RC and TS have been optimized as open-shell singlet states. As mentioned previously, UHF-based methods generally give unsatisfactory relative electronic energies for O_2 ($\tilde{a}^1\Delta_g$). Obtaining reliable O_2 ($\tilde{a}^1\Delta_g$) – O_2 ($\tilde{X}^3\Sigma_g^-$) energy gap has been known to be very challenging [26], so electronic energy of O_2 ($\tilde{a}^1\Delta_g$) in this work is obtained by adding the experimental value of the O_2 ($\tilde{a}^1\Delta_g$) – O_2 ($\tilde{X}^3\Sigma_g^-$) energy gap to the computed electronic energy of O_2 ($\tilde{X}^3\Sigma_g^-$) at individual levels in channel (1b). The same approach was adopted to compute the relative energy of PC in the same channel, assuming that the interaction between HOBr and O_2 ($\tilde{X}^3\Sigma_g^-$) in the triplet PC is similar to the interaction between HOBr and O_2 ($\tilde{a}^1\Delta_g$) in the singlet PC, as well as both PCs have similar geometries.

High level *ab initio* methods were employed to improve the relative energies of stationary points. RHF/UCCSD(T), as implemented in MOLPRO [27], was initially used with the AVTZ (aug-cc-pVTZ for H and O and aug-cc-pVTZ-PP for Br) and the AVQZ (aug-cc-pVQZ for H and O and aug-cc-pVQZ-PP for Br) basis sets. The $1/X^3$ formula was employed to extrapolate the electronic energies obtained at the AVTZ and the AVQZ levels to the CBS limit. For channel (1a), although the convergence of the CCSD iterations in the UCCSD(T) calculations for RC and TS was achieved, the resulting T1 diagnostic values tended to be high (~0.05 and ~0.1 respectively). In order to circumvent this problem, Brueckner theory was employed to treat the TS, as Brueckner doubles (BD) has a T_1 value of exactly 0. The relative energies obtained at BD/AVDZ level were then improved by using the BD(T) with basis sets AVTZ and AVQZ, which were then extrapolated to the CBS limit (i.e. BD(T)/CBS level) using the $1/X^3$ formula. Finally, the relative energy obtained at the highest *ab initio* level in this work is BD(TQ)/CBS, which was obtained by adding BD(T)/CBS and the quadrupole contribution from the difference in the relative energy between BD(TQ) and BD(T) levels.

The equilibrium experimental separation of $\tilde{X}_2{}^2\Pi_{1/2}$ and $\tilde{X}_1{}^2\Pi_{3/2}$ electronic states of BrO is 975.43 cm^{-1} [28], so the $\tilde{X}_2{}^2\Pi_{3/2}$ SO state of BrO is lower than the unperturbed $\tilde{X}^2\Pi$ state by 487.7 cm^{-1}, or 1.3944 $kcal.mol^{-1}$ in order to account for the spin-orbit splitting. This value is then used as the spin-correction correction in all relative energy

and reaction enthalpy (ΔH_{298K}^{RX}) calculations. For each ΔH_{298K}^{RX} value in each channel, it is reduced by the same amount.

The two spin-orbit electronic states of BrO have been considered in all rate coefficient calculations.

5.2.2 Reaction Enthalpies in Literature

In order to assess the reliability of the results of the relative electronic energies, both experimental and computed heats of formation (ΔH_f) of the individual species at 0 K and 298 K in the 5 channels in the literature were compiled in Table A2 in the appendix. The available heats of formation of individual reactants and products at 298 K were then averaged (see Table A2 for details). Finally, the reaction enthalpies were computed using the average of both experimental and computed heats of formation and the average of computed heats of formation at 298 K.

5.2.3 Computing Rate Coefficients

As will be discussed, among the five channels, only channel (1b) has a negative barrier height while the rest of the channels have positive barrier heights. Consequently, channel (1b) is supposed to have the largest rate coefficients from 200 K to 400 K. The majority of rate coefficient calculations was performed for channel (1b) and there are also some rate coefficient results for channel (1a). In order to give the correct orientations of the optimized stationary points of the rate coefficient calculations, geometry optimizations of the stationary points were redone using the no-symmetry constraint ('nosym' keyword in Gaussian 09 [20]). Cartesian coordinates were employed in all geometries for all *ab initio* and DFT calculations. Rate coefficient calculations were carried out at high pressure limit by using POLYRATE 2010-A [104] and VARIFLEX 1.0 [105].

For computing the rate coefficient of a chemical reaction with a negative barrier, there are two bottlenecks in the reaction. The first bottleneck is at the barrierless entrance of the association reaction of the two reactants, in which they need to overcome a centrifugal barrier in order to form the reactant complex. The second barrier is at the conventional transition state (i.e. the saddle point). Klippenstein and coworkers [106] have introduced the two-transition state theory which emphasizes on the importance of

treating the two barriers at the energy and angular momentum resolved levels in order to obtain reliable rate coefficients of a chemical reaction with a negative barrier. In the language of the two-transition state theory, the centrifugal barrier is known as the outer transition state and the saddle point was known as the inner transition state. At the intermediate range of temperature, both outer transition state and inner transition state can contribute to the overall reactive flux of the reaction. The overall rate coefficient ($k_{overall}$) can be obtained by combining the rate coefficients passing through the reactive fluxes at the outer and inner transition states respectively:

$$\frac{1}{k_{overall}} = \frac{1}{k_{outer}} + \frac{1}{k_{inner}} \tag{5.1}$$

In this work, there are two ways to determine $k_{overall}$ because there are two ways to treat k_{inner} as follows:

(i) Both k_{outer} and k_{inner} were computed by using VARIFLEX [105], labeled as $k_{overall(i)}$

(ii) k_{outer} was computed by using VARIFLEX [105] and k_{inner} was computed by using POLYRATE [104]

For (i), k_{outer} was computed by using the phase space theory (PST) [107]. The long-range isotropic potential which is approximated by $V(r) = -C_6/r^6$ where $C_6 = 1.5\alpha_1\alpha_2E_1E_2/(E_1+E_2)$ [108] in which α_i is the isotropic polarizability and E_i is the ionization energy of the two reactants (i=1,2). In the PST calculations, the isotropic polarizability of the two reactants were computed at the M06-2X/AVDZ level and the ionization energies of BrO and HO_2 radicals were taken from investigations using UV photoelectron spectroscopy (10.46 eV for BrO [109] and 11.35 eV for HO_2 [110]). For computing k_{inner}, the *E*,*J*-TST (the transition state theory at energy and angular momentum resolved levels) approach with the rigid-rotor harmonic-oscillator (RRHO) approximation for all degrees of freedom was employed. In the *E*,*J*-TST calculations, the barrier height obtained at BD(TQ)/CBS//M06-2X/AVDZ level was zero-point corrected.

For (ii), k_{inner} values were evaluated at different TST levels by using POLYRATE, including conventional transition state theory (TST), canonical variational transition state theory (CVT) and improved canonical variational transition state theory (ICVT) with

different tunneling schemes, namely Wigner tunneling correction (W), zero-curvature tunneling (ZCT) and small curvature tunneling (SCT) corrections.

For channel (1b), the minimum energy path (MEP) obtained at the BD(TQ)/CBS//M06-2X/AVDZ level was obtained by scaling the MEP at the M06-2X/AVDZ level according to the equation (4.1).

5.3 Results and Discussion

5.3.1 *Ab initio*/DFT results

The optimized geometries of the stationary points in the five channels considered are shown in Figures 5.1 to 5.7 and their relative electronic energies obtained at various levels are compiled in Tables A3, A5 to A8 in the appendix. The values of available heats of formation ($\Delta H_{f,298K}^{RX}$) of the reactants and products are compiled in Table A2, and they were then used to compute the reaction enthalpies of individual channels and they are listed in Table A9. The zero-point corrected barrier height (ΔE(0K)), which is the difference between the electronic energy of the TS with ZPE correction and the sum of electronic energies of the reactants with ZPE correction, is reported in the following sections.

5.3.1.1 Channel (1a): $BrO + HO_2 \rightarrow HOBr + O_2$ ($\tilde{X}^3\Sigma_g^-$)

The optimized geometries of RC, TS, and PC at the M06-2X/AVDZ level are shown in Figure 5.1 whereas the optimized geometries of TSs located at the M06-2X/AVDZ and the BD/AVDZ levels are shown in Figure 5.2. The TS optimized at the M06-2X/AVDZ level had a relatively small imaginary vibrational frequency of 162i cm^{-1} which corresponded to the bending motions of both BrO and HO_2 moieties. When the UCCSD(T) was used to improve the electronic energy of this transition state, a large T_1 value (~0.1) resulted which suggested significant multi-reference character of the TS. In order to circumvent this problem, the BD method was utilized to optimize the TS of the same channel and compute its harmonic frequencies with the AVDZ basis set. It was found that the TS had an imaginary vibrational frequency of 399i cm^{-1} which pertained to the vibrational mode of O-H bond in the Br[O]…[H]O_2 unit. However, the RC and the PC have not been optimized at the BD/AVDZ level because of their shallowness on the

potential energy surface, which requires high computational costs. Thus, the highest level of relative electronic energies of both RC and PC was obtained at the CCSD(T)/CBS//M06-2X/AVDZ level whereas that of TS was obtained at the BD(TQ)/CBS//BD/AVDZ level. According to Table A3, the reaction energies (ΔE^{RX}) obtained at the CCSD(T)/CBS and the BD(TQ)/CBS levels agree very well with each other and this excellent agreement should remain valid for RC and PC.

Significant geometrical differences of the TSs optimized at the two levels are revealed in Figure 5.2. The Br[O]…[H]O_2 bond in the TS optimized at the M06-2X/AVDZ level is 1.77Å, which is slightly shorter than the equivalent bond length in the RC of 1.87Å, while it is 1.49Å in the TS optimized at the BD/AVDZ level. Besides, the TS optimized at the BD/AVDZ level has a dihedral angle (∠(Br-O-O-O)) of 0.2° (essentially planar) whereas the M06-2X/AVDZ geometry has a dihedral angle (∠(Br-O-O-O)) of 24.0°. Despite the significant difference in the dihedral angles of the two TSs, the difference in their computed ΔE(0K) is small (2.23 kcal.mol^{-1}; see Table A3). The relative energy of TS is negative at the BD/AVDZ level (-1.78 kcal.mol^{-1}) but it becomes positive when larger basis sets are employed (4.19 kcal.mol^{-1} at the BD/AVTZ level and 4.42 kcal.mol^{-1} at the BD/AVQZ level). Due to the prominent change of the relative energies of TS with increasing size of basis sets, this suggests that the AVDZ basis set is probably too small for obtaining a reliable barrier. By using larger basis sets, better agreement in the relative energies of TS was achieved between the BD(T)/AVTZ//BD/AVDZ and the BD(T)/AVQZ//BD/AVDZ levels (2.06 kcal.mol^{-1} and 2.20 kcal.mol^{-1} respectively). For the computed reaction energy, it increases when the basis set expands from the AVDZ level to the AVTZ level but it decreases when the basis set further expands from the AVTZ level to the AVQZ level (Table A3). Since the changes in reaction energy with respective to the sizes of the two basis sets employed oppose to each other, a CBS extrapolation scheme with the $1/X^3$ formula deems inappropriate. In this connection, the BD(T)/CBS value is obtained as taking the average relative energies between the BD(T)/AVTZ and the BD(T)/AVQZ levels. Moreover, the nearness between the BD(T)/AVTZ and BD(T)/AVQZ values indicate that their values are close to the value at basis set saturation. Furthermore, the reaction energy computed at the BD(TQ)/CBS level obtained using this approach agrees very well with that obtained at the CCSD(T)/CBS level. Summing up, this channel has a pronounced recommended barrier height of 2.53 kcal.mol^{-1} (ΔE(0K) value) and a large exothermicity characterized

by a reaction enthalpy (ΔH_{298K}^{RX}) of -47.5 kcal.mol^{-1} at the BD(TQ)/CBS level with spin-orbit correction of BrO (see Table A2).

Figure 5.1 Triplet reactant complex (RC), triplet transition state (TS) and triplet product complex (PC) of channel (1a) at the M06-2X/AVDZ,AVDZ-PP level. Bond distances are shown Angstroms (Å).

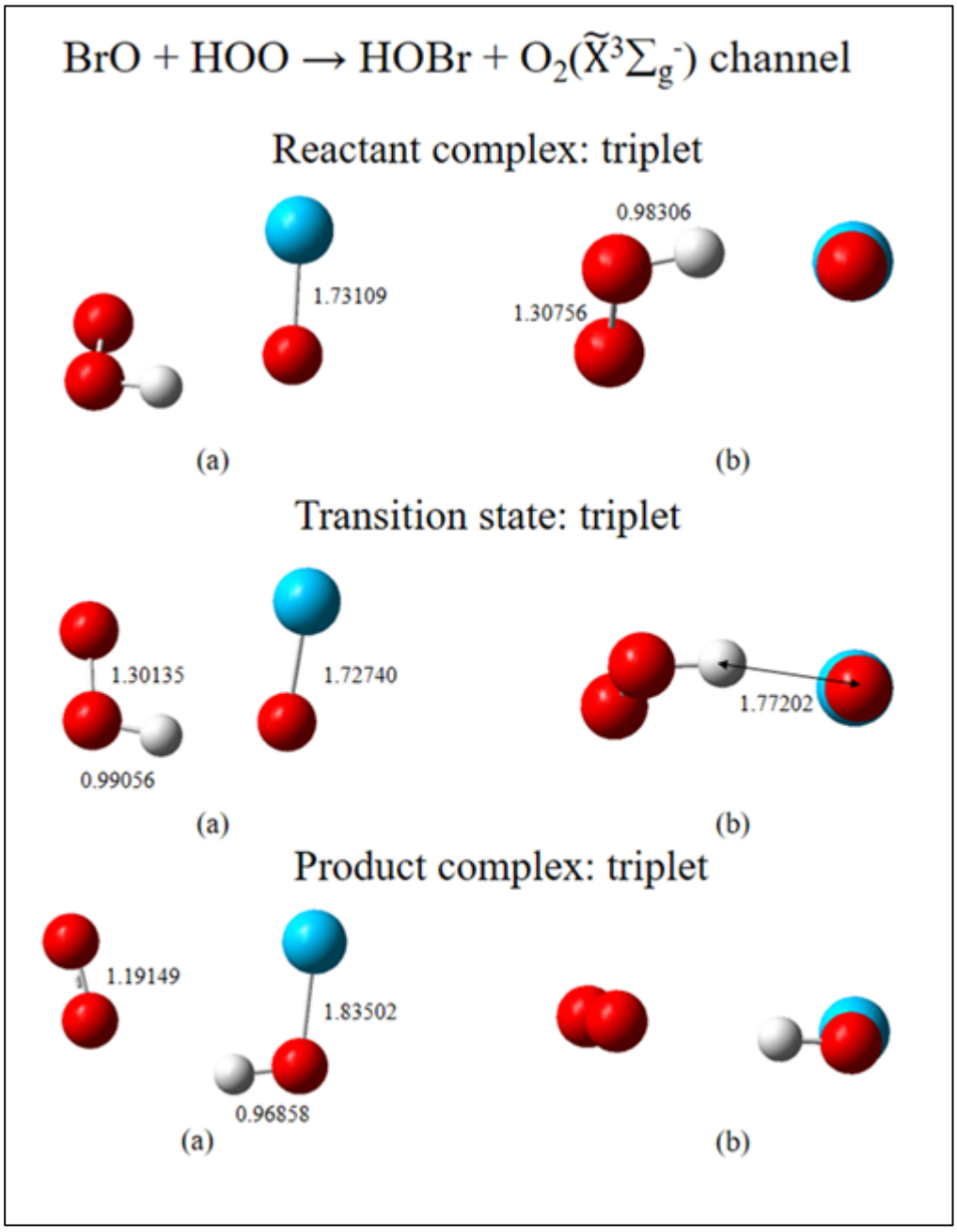

Figure 5.2 Triplet transition states (TSs) of channel (1a) at the M06-2X/AVDZ, AVDZ-PP (upper) and BD/AVDZ,AVDZ-PP levels (lower). Bond distances are shown in Angstroms (Å).

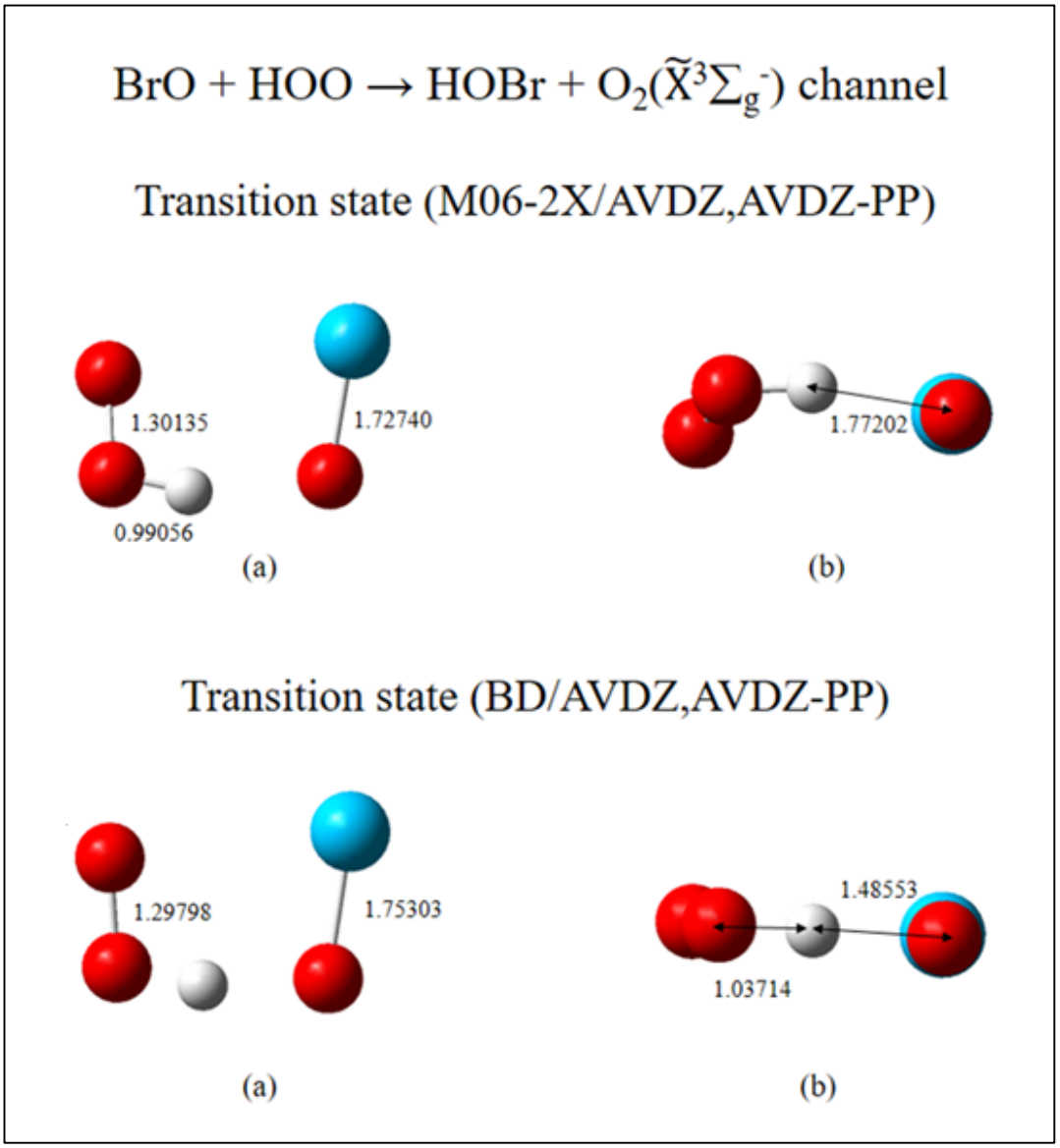

5.3.1.2 Channel (1b): $BrO + HO_2 \rightarrow HOBr + O_2(\tilde{a}^1\Delta_g)$

The optimized geometries of RC, TS and PC are shown in Figure 5.3, whereas the optimized geometries of TSs located at the M06-2X/AVDZ and the BD/AVDZ levels are shown in Figure 5.4. In order to explore the open-shell singlet states of RC and TS, unrestricted wavefunctions were employed with 'guess=mix' keyword as mentioned in section 5.2.1. The open-shell singlet states of RC and TS were confirmed by checking the computed spin density values which are compiled in Table A4. The Br[O]…[H]O_2

distance in the RC was 1.87Å and it decreased to 1.58Å and 1.36Å in the TSs optimized at the M06-2X/AVDZ (with imaginary frequency of 229i cm^{-1}) and the BD/AVDZ levels (with imaginary frequency of 1391i cm^{-1}), respectively. The dihedral angle (∠Br-O-O-O) of the transition states were 2.76° and 0.02° at the M06-2X/AVDZ and the BD/AVDZ levels, respectively. The difference in the ΔE(0K) between two TSs is 0.05 $kcal.mol^{-1}$. The M06-2X/AVDZ and BD/AVDZ TSs were analogous to each other. In terms of the difference between the TSs in the channels (1b) and (1a), the dihedral angle (∠Br-O-O-O) of (1b) was smaller than that of (1a) and the Br[O]…[H]O_2 distance was shorter in (1b) than (1a).

The computed relative energies obtained at different levels of theories are compiled in Table A5. Regarding the state of the TS, Brueckner wavefunctions yielded an open-shell singlet state with AVDZ basis set as confirmed by the non-zero computed spin densities on the atomic centers. However, with the AVTZ and the AVQZ basis sets for the BD/AVDZ geometry, the BD(TQ)/AVTZ and BD(TQ)/AVQZ calculations yielded closed-shell singlet states. These results give much higher relative energies (see Table A5). In contrast, Brueckner wavefunctions yielded non-zero spin density values with AVTZ and AVQZ basis sets for the M06-2X/AVDZ TS, which can be considered as a more accurate description of the TS. Therefore, the TS with M06-2X/AVDZ geometry was used for higher level Brueckner theory calculations (i.e. BD(T) and BD(TQ)).

Summing up, channel (1b) is a channel with a recommended barrier height (ΔE(0K) value) of -3.07 $kcal.mol^{-1}$. It is an exothermic channel with a reaction enthalpy (ΔH_{298K}^{RX}) of -25.0 $kcal.mol^{-1}$.

Figure 5.3 Open-shell singlet reactant complex (RC), open-shell singlet transition state (TS), and closed-shell singlet product complex (PC) of channel (1b) at the M06-2X/AVDZ,AVDZ-PP level. Bond distances are shown in Angstroms (Å).

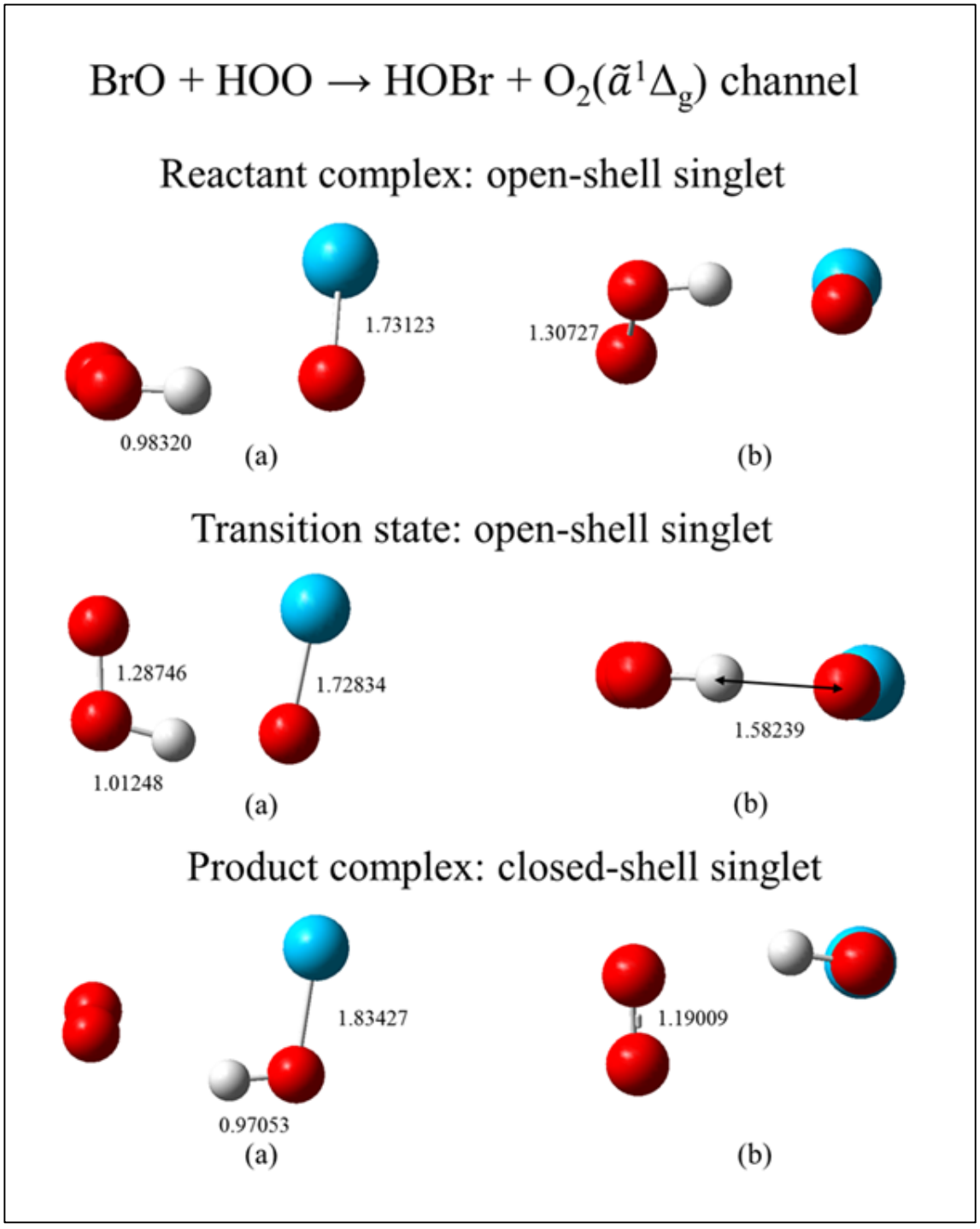

Figure 5.4 Triplet transition states (TSs) of channel (1b) at the M06-2X/AVDZ, AVDZ-PP (upper) and BD/AVDZ,AVDZ-PP levels (lower). Bond distances are shown in Angstroms (Å).

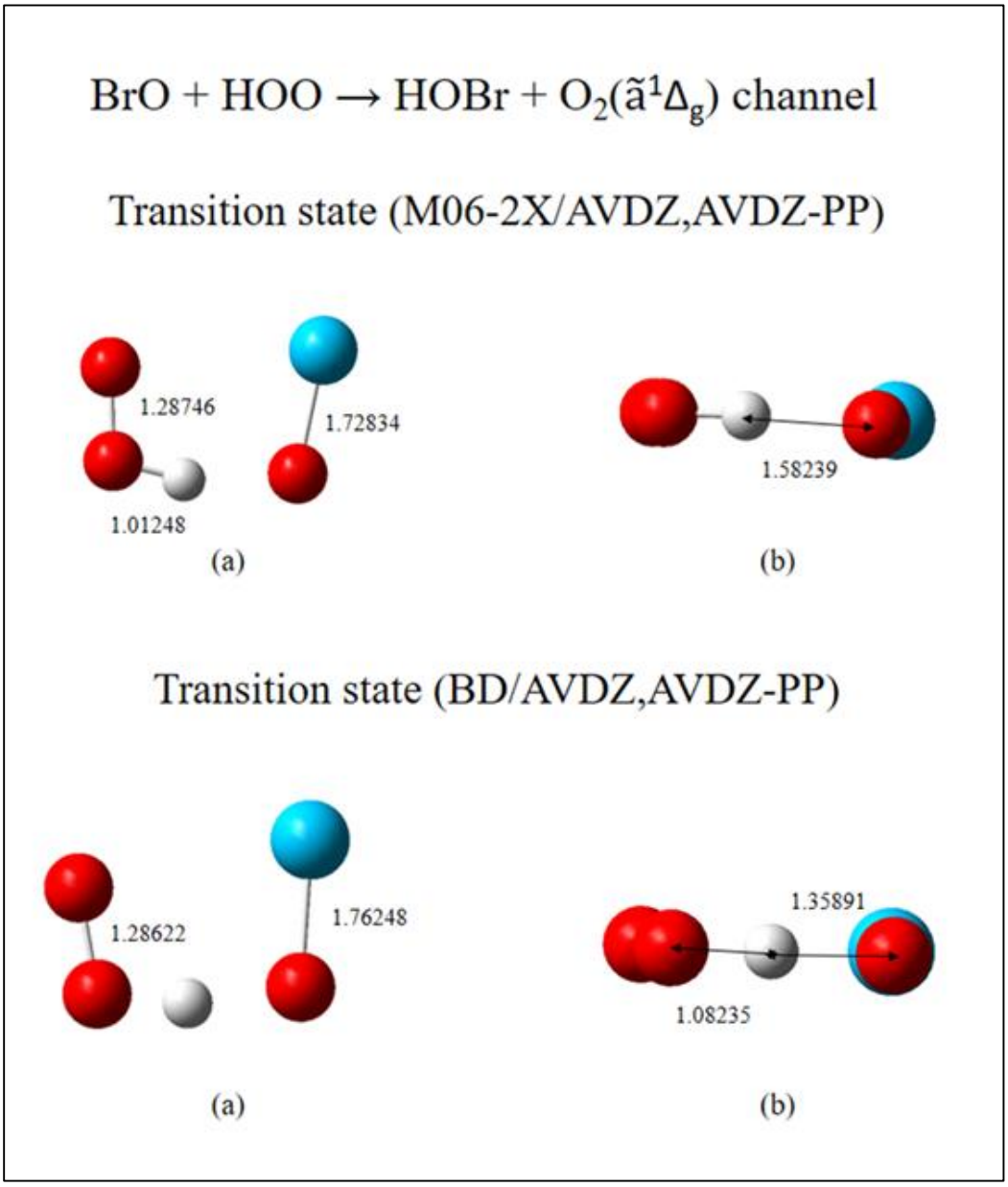

5.3.1.3 Channel (2): BrO + HO2 → HBr + O_3

The optimized geometries of the RC, the TS (with an imaginary frequency of 1191i cm^{-1}) and the PC are shown in Figure 5.5. The RC is actually optimized to an intermediate, HOOOBr (labeled as IM2 in Figure 5.8). The computed relative electronic energies of the stationary points in this channel are tabulated in Table A6. The barrier height (ΔE(0K) value) of this channel is 10.93 kcal.mol^{-1} at the BD(TQ)/CBS//M06-2X/AVDZ level

(with spin-orbit correction of BrO) and it is much higher than the barrier heights of the reactions (1a) and (1b) respectively. The results obtained for channel (2) was generally analogous to the same channel in reference 16. The current study and reference 16 show that BrO and HO_2 formed a HOOOBr intermediate which then proceeded to the TS to form HBr and O_3. The optimized TS in this study is essentially the same as that in reference 16 optimized at the CCD/6-311G** level. There is a small difference in the geometry of the RC between our work and reference 16 in which the H and Br atoms in our RC were *trans* to each other whereas the H and Br atoms in the RC of reference 16 are *cis* to each other. The relative energies of the RC, the TS and the separate products in reference 16 were calculated to be -17.21, 8.13, and -9.09 kcal.mol^{-1} respectively at the CCSD(T)/6-311G**//CCD/6-311G** level where the equivalent values obtained in this work are -19.57, 11.83 and -3.00 kcal.mol^{-1} at the BD(TQ)/CBS//M06-2X/AVDZ level (with spin-orbit correction of BrO) respectively. Both works conclude that reaction (2) is exothermic and it proceeds over a pronounced energy barrier. The significant discrepancy in the reaction energy (> 6 kcal.mol^{-1}) between this work and reference 16 is likely associated with the smaller basis sets employed in reference 16. Moreover, although ozone is a closed-shell singlet species, its significant multi-reference effect is well-known [112]. Consequently, the BD(TQ) method is expected to outperform the CCSD(T) method.

Figure 5.5 Open-shell singlet reactant complex (RC), open-shell singlet transition state (TS), and closed-shell singlet product complex (PC) of channel (2) at the M06-2X/AVDZ, AVDZ-PP level. Bond distances are shown in Angstroms (Å).

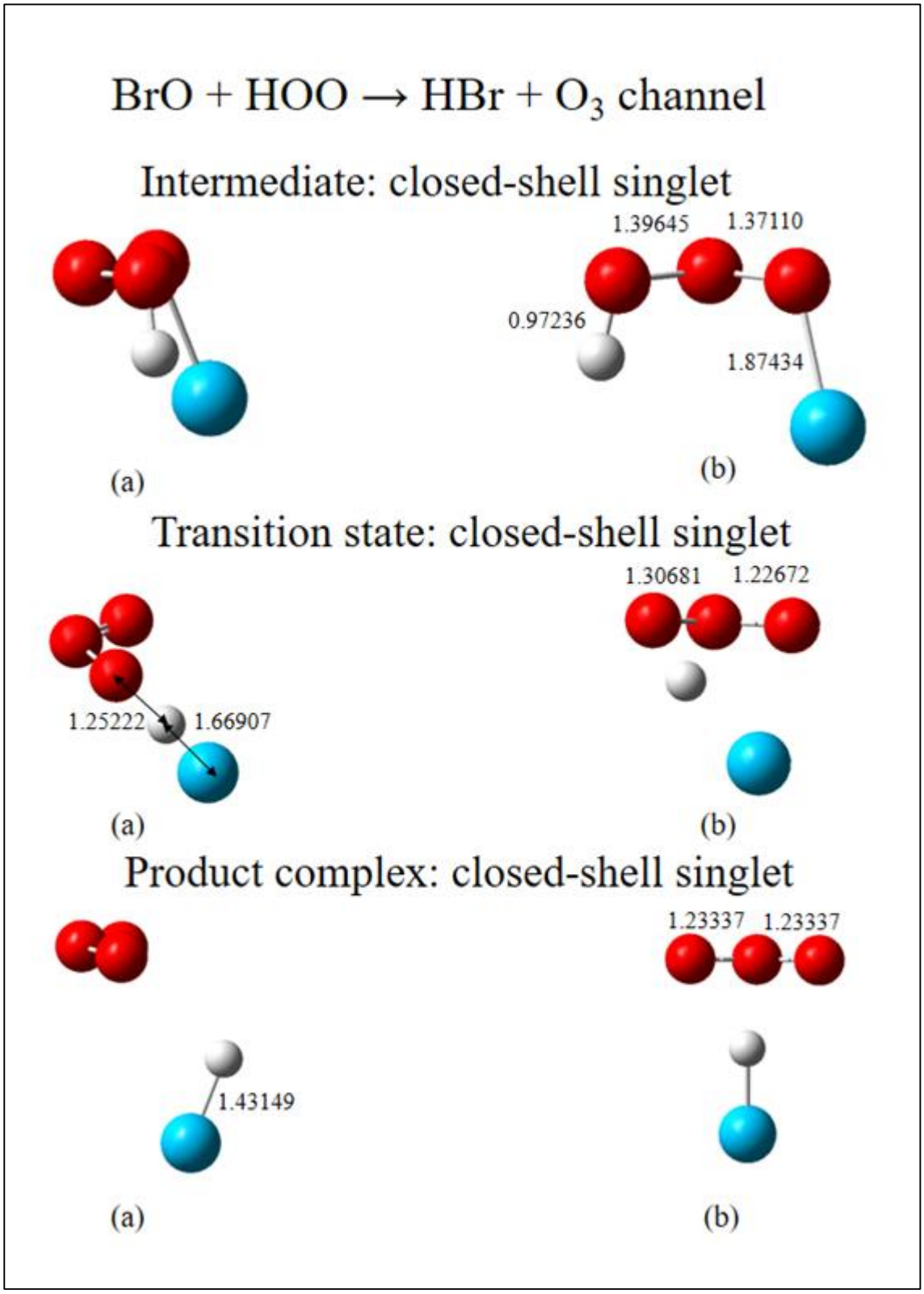

In summary, channel (2) has a recommended barrier height of 10.93 kcal.mol^{-1} (ΔE(0K)) and its reaction enthalpy (ΔH_{298K}^{RX}) is -4.3 kcal.mol^{-1} at the BD(TQ)/CBS//M06-2X/AVDZ level with spin-orbit correction of BrO. The barrier height of channel (2) is much higher than that of channels (1a) and (1b) so the rate coefficient is expected to be much lower than those of (1a) and (1b). This is consistent with the experimental results that HOBr has been observed as the major product of the BrO + HO_2 reaction and no ozone has been detected experimentally. Although trace amounts of HBr have been detected, the presence of HBr can be due to secondary reactions of HOBr or wall reactions [7, 9, 11].

An equilibrium is assumed to be established between the reactants and the intermediate (IM2) for this channel. Besides, since the relative energy of the TS is as high as 10.93 kcal.mol^{-1}, this channel will have no effect on the overall rate coefficient (*vide infra*).

5.3.1.4 Channel (3): BrO + HO_2 → OBrO + OH

This work is the first theoretical work to cover reaction (3) which proceeds via a triplet potential energy surface. The optimized geometry of the TS (with an imaginary frequency of 1074i cm^{-1}) is shown in Figure 5.6. The reaction enthalpy (ΔH_{298K}^{RX}) at the BD(TQ)/CBS//M06-2X/AVDZ level with spin-orbit correction of BrO is 14.9 kcal.mol^{-1} (Tables A7 and A9) while that at the M06-2X/AVDZ level is 29.9 kcal.mol^{-1} (Table A7). The large discrepancy in the reaction enthalpies between the M06-2X/AVDZ and the BD(TQ)/CBS levels came down to the electronic energy of ground-state OBrO, which has a strong multi-reference character [113]. This shows that the M06-2X functional is not capable of accounting the electronic structure of ground-state OBrO accurately. Again, this showed the importance of using Brueckner theory for treating multi-reference species. It is satisfactory for the ΔH_{298K}^{RX} value calculated using the available heats of formation (15.3 ± 2.8 kcal.mol^{-1}; see Tables A2 and A9) is in excellent agreement with that obtained at the BD(TQ)/CBS level in this work. Regarding the barrier height (ΔE(0K) value) of this channel, it is very high (34.98 kcal.mol^{-1}; see Table A7). Consequently, the rate coefficients of this channel are expected to be much smaller than those of channels (1a), (1b) and (2) so they are not supposed to affect the overall rate coefficient in the temperature range of 200 – 400 K considered of the BrO + HO_2 reaction.

Figure 5.6 Separate reactants, triplet transition state (TS) and separate products of channel (3) at M06-2X/AVDZ, AVDZ-PP level. Bond distances are shown in Angstroms (Å).

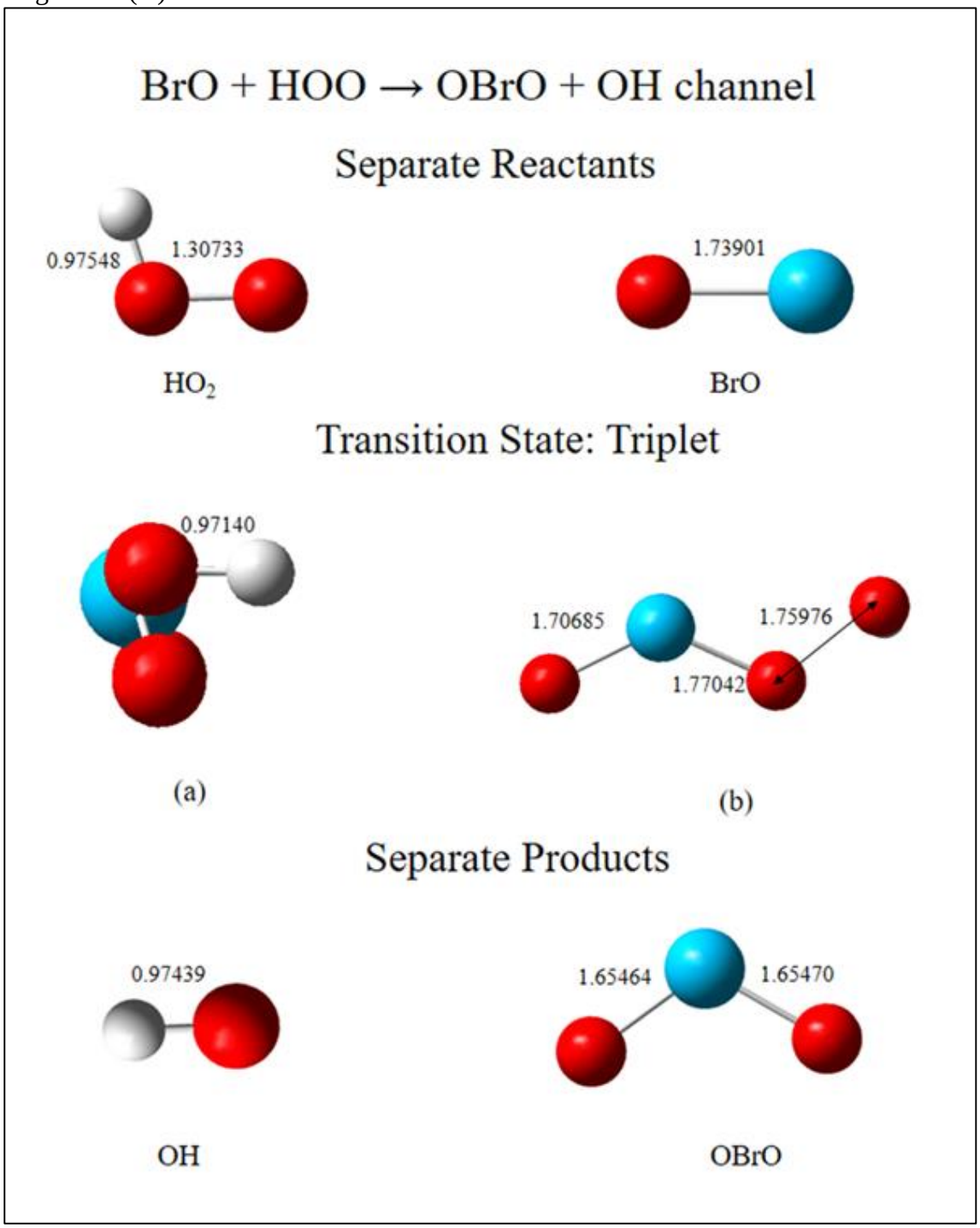

5.3.1.5 Channel (4): $BrO + HO_2 \rightarrow BrOO + OH$

Together with channel (3), this work is the also first theoretical work to investigate the potential energy surface of reaction (4). The results of this channel are similar to those of channel (3). Also, this channel will not affect the overall rate coefficient of $BrO + HO_2$ reaction in the temperature range of 200 – 400 K considered. The optimized geometry of the TS (with an imaginary frequency of 1228i cm^{-1}) is shown in Figure 5.7. The calculated reaction enthalpy (ΔH_{298K}^{RX}) at the BD(TQ)/CBS//M06-2X/AVDZ level with spin-orbit correction is 5.9 $kcal.mol^{-1}$ (see Tables A8 and A9), which agrees with the reaction enthalpy obtained by using available heats of formation (2.9 ± 3.5) $kcal.mol^{-1}$ (Table A9). In contrast, the reaction enthalpy obtained at the M06-2X/AVDZ level is -4.9 $kcal.mol^{-1}$. The source of discrepancy can be attributed to the ground-state energy of BrOO obtained at the M06-2X/AVDZ level. Since BrOO has some multi-reference character [113], BD is a more appropriate method for obtaining a reliable electronic energy than the M06-2X functional. The barrier height (ΔE(0K) value) of this channel is as high as 37.8 $kcal.mol^{-1}$ and the reaction enthalpy (ΔH_{298K}^{RX}) is 5.9 $kcal.mol^{-1}$ at the BD(TQ)/CBS//M06-02X/AVDZ level with spin-orbit correction of BrO.

Figure 5.7 Separate reactants, triplet transition state (TS) and separate products of channel (4) at the M06-2X/AVDZ, AVDZ-PP level. Bond distances are shown in Angstroms (Å).

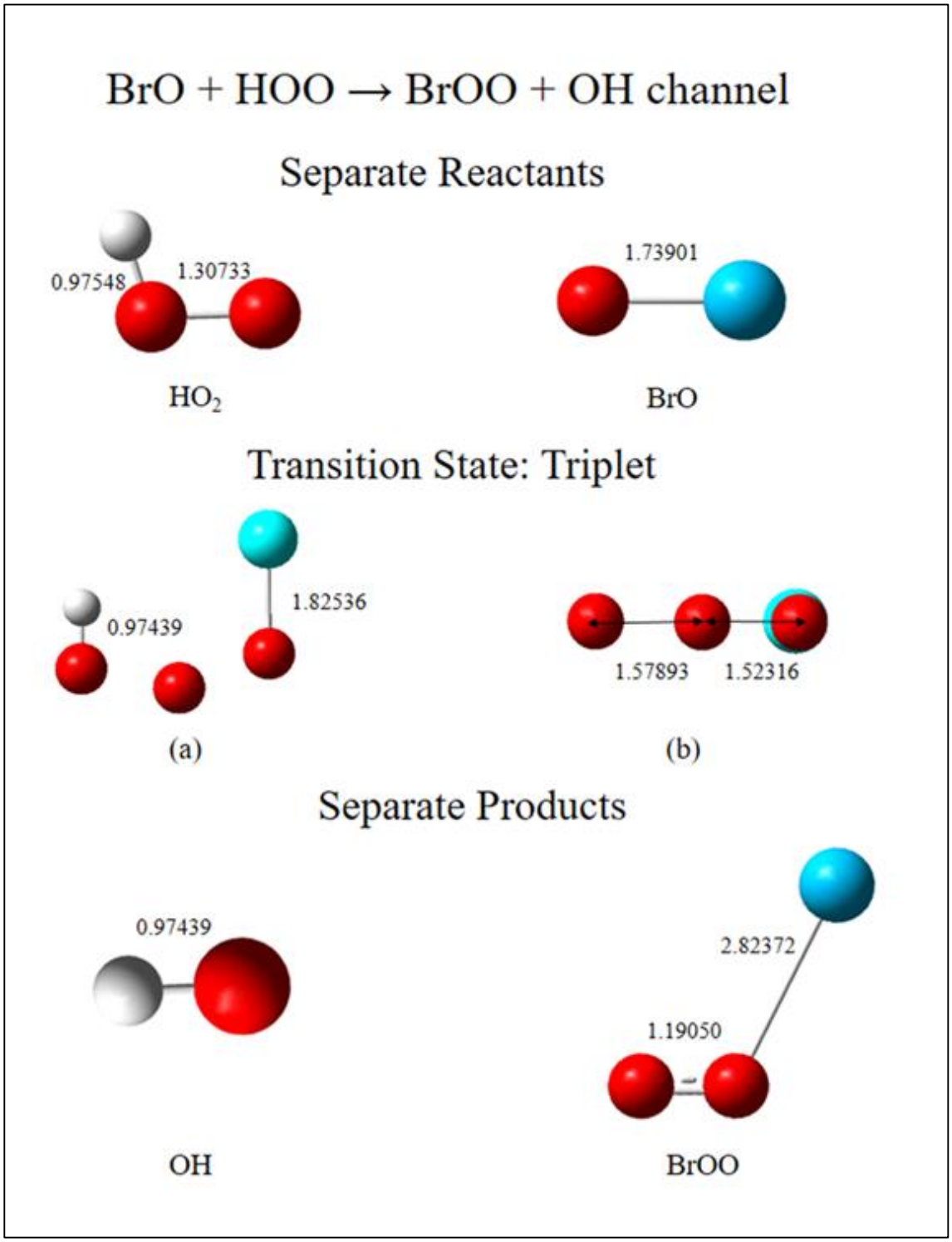

5.3.2 Summary and Comparison with Other Work

In order to assess the reliability of the computed values in this work, the reaction enthalpies (ΔH_{298K}^{RX}) of the individual channels are evaluated by employing available heats of formation ($\Delta H_{f,298K}$) of the reactants and products, which serve as the reference values. The resulting ΔH_{298K}^{RX} values obtained using the average literature values (tabulated in Table A9) are (1a) (-47.5 ± 2.1), (1b) (-25.0 ± 2.1), (2) (-7.1 ± 3.3), (3) (2.9 ± 3.5) and (4) (15.3 ± 2.8) kcal.mol^{-1} and they agree very well with the computed values of -47.5, -25.0, -4.3, 14.9 and 5.9 kcal.mol^{-1} computed at the BD(TQ)/CBS//M06-2X/AVDZ level with spin-orbit correction of BrO in this work (see Table A9). The reaction enthalpies in reference 16 are computed at the CCSD(T)/6-311G** level agree well with the reference values for channels (1a) and (2) but their computed reaction enthalpy of channel (1b) at the same level is too low by 12.3 kcal.mol^{-1} with respect to the reference value of (-25.0 ± 2.1) kcal.mol^{-1}. Regarding the barrier height (ΔE(0K) value), the recommended values are (1a) 2.53, (1b) -3.07 (2) 10.93, (3) 35.0 and (4) 37.81 kcal.mol^{-1} at the BD(TQ)/CBS level with spin-orbit correction of BrO. The barrier heights of channels (1a), (1b) and (2) obtained in reference 16 are -2.9, 15.8 and 8.1 kcal.mol^{-1} respectively at the CCSD(T)/6-311G** level. In this work, the barrier height of channel (1a) is positive while it is negative in reference 16 with a difference of 5.43 kcal.mol^{-1}. Generally, the barrier heights of channels (1a) and (2) obtained in this work agree moderately with those obtained in reference 16 but the agreement on the barrier height of channel (1b) is very poor, with a difference of 18.9 kcal.mol^{-1}.

5.3.3 Rate Coefficient Results

Figure 5.8 - Schematic pathways of the five channels (1a,1b,2,3,4) in the BrO + HO_2 reaction showing the stationary points with their relative electronic energies with zero-point correction at 0 K in kcal.mol^{-1} at the BD(TQ)/CBS level (incl. SO correction for BrO)) in brackets (note before ZPE correction RC(1b) is lower than TS(1b), but with ZPE correction RC(1b) is slightly above TS(1b)).

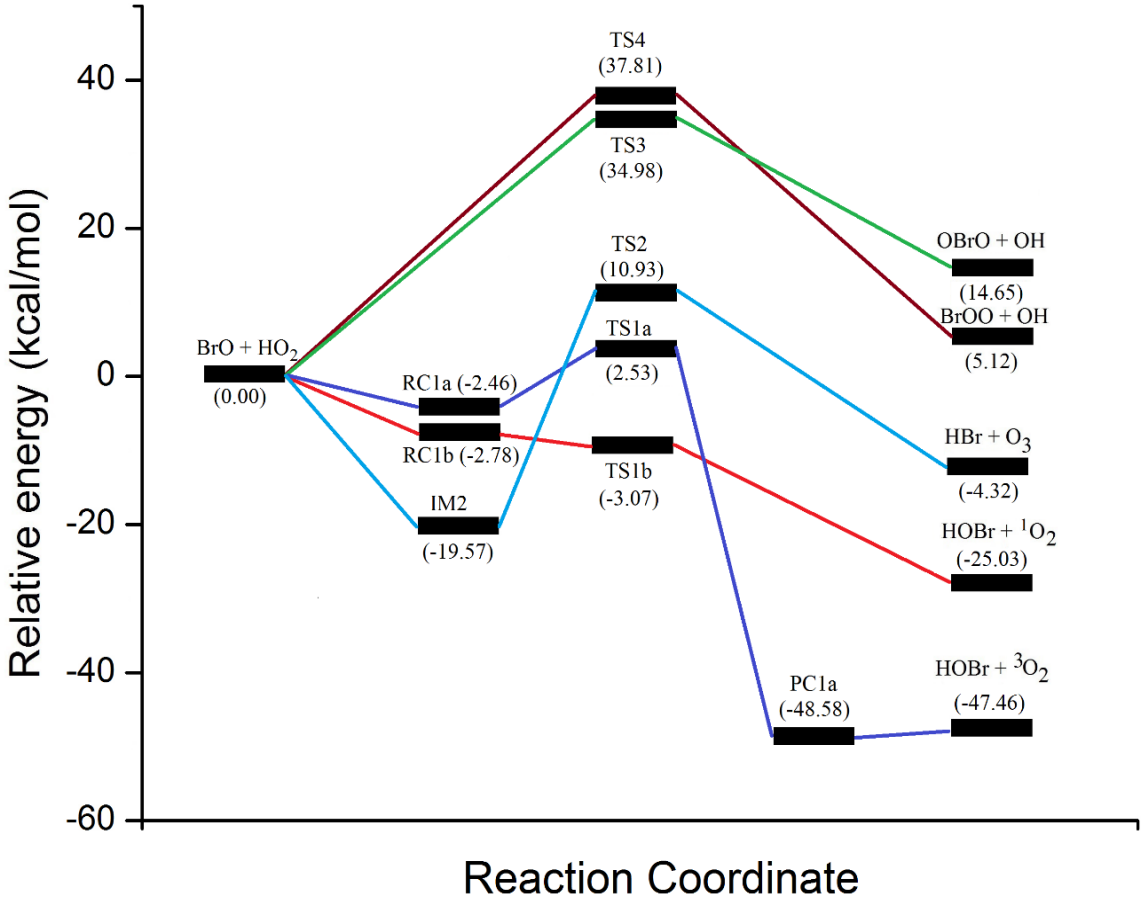

Figure 5.8 shows the schematic energy diagram of the considered channels in the BrO + HO_2 reaction, according to the calculated relative energies of the stationary points. As shown in Figure 5.8, channel (1a) has the largest exothermicity while channel (1b) had the lowest barrier height. Hence, channel (1b) is expected to have the largest rate coefficient and rate coefficients calculations were computed for this channel in the temperature range of 200 – 400 K, where the minimum energy path (MEP) was obtained at the BD(TQ)/CBS//M06-2X/AVDZ level with spin-orbit correction of BrO. Channel

(1a) comes with the second lowest barrier height and rate coefficient calculations were also performed by using its own MEP (see Table A3 for the best estimate values of the relative energies of the stationary points).

The higher level *VMEP* curve of channel (1b) at the BD(TQ)/CBS level was obtained by scaling the lower level *VMEP* curve at M06-2X/AVDZ level according to equation (4.1).

The classical potential energy (*VMEP*), zero-point energy difference (ΔZPE) and ground-state vibrationally adiabatic energy (ΔV_a^G = *VMEP* + ΔZPE) curves obtained at the BD(TQ)/CBS//M06-2X/AVDZ level with spin-orbit correction of BrO are shown in Figure 5.9. Since the reactant complex is far away from the saddle point, it is not shown in Figure 5.9. The *VMEP* curve indicates a very flat potential energy surface. There is a dip of ΔZPE curve at near s = +0.5Å and it is caused by bond-breaking and bond-forming processes of the reaction. In particular, the major contribution of ΔZPE arises from the O-H bond in the reacting system in addition to the gradual changes of other computed harmonic frequencies. In the reactant, the O-H stretching mode in HO_2 has a computed harmonic frequency of 3680 cm^{-1} and it transforms to an OO-H stretching mode in the TS with a computed harmonic frequency of 2661 cm^{-1}. When the TS dissociates, the H from the OO-H stretching mode in the TS transferred to the BrO moiety to form HOBr molecule in the product with a computed frequency of 3839 cm^{-1}. Given that *VMEP* was almost a flat curve, the dip in the ΔZPE curve was reflected in the ΔV_a^G curve because ΔV_a^G = *VMEP* + ΔZPE. The maximum of the *VMEP* curve had to be at s= 0 but the maximum of ΔV_a^G curve did not have to be at s = 0 because it depended on the shapes of the ΔZPE curve and the V_{MEP} curve. For this reaction, the maximum of ΔV_a^G curve (denoted as $s^*(\Delta V_a^G)$) is located at =-0.509Å.

Figure 5.9 *VMEP*, ΔZPE and V_a^G curves of channel (1b) BrO + HO_2 → HOBr + O_2 ($\tilde{a}^1\Delta_g$) from POLYRATE calculations at the BD(TQ)/CBS//M06-2X/AVDZ level (incl. SO correction for BrO; energies are in kcal.mol^{-1} with respect to separate reactants).

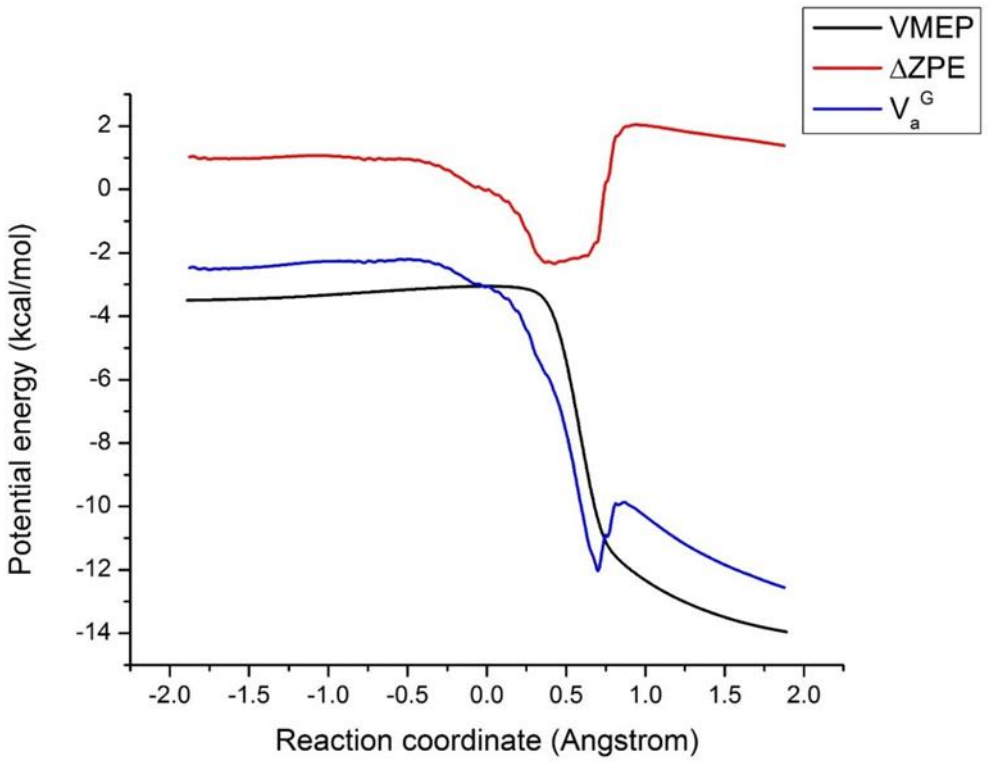

5.3.3.1 Computed rate coefficients

As discussed in the section 5.2, there are two bottlenecks in channel (1b). Initially, $k_{overall(i)}$ was calculated by using k_{outer} and k_{inner} values in a microcanonical ensemble using VARIFLEX [105]. In these computations, k_{outer} was evaluated using the PST method while k_{inner} was evaluated by using the *E*,*J*-TST method. Figure 5.10 and Table A10 show the rate coefficients of the outer TS (k_{outer}), inner TS (k_{inner}) and the overall rate coefficients ($k_{overall(i)}$) from 200 K to 400 K. The outer TS does not contribute significantly to the overall rate coefficient, even at low temperature. Essentially, the major bottleneck is the inner transition state throughout the temperature range considered. Thus, TST can give a good prediction of the rate coefficient. The next step is to explore the variational effect on k_{inner} by performing calculations with variational transition state theory using POLYRATE [104]. In this approach, k_{outer} was still evaluated by using the PST and $k_{overall(ii)}$ was obtained by using equation (5.1). Before proceeding to computing $k_{overall(ii)}$ values, the k_{inner} values obtained by using *E*,*J*-TST method were compared with those obtained by using the TST method (see Table A11 and Figure 5.11). It is found that the

E,*J*-TST method yields slightly larger k_{inner} values than those computed using the TST method because of two reasons. The first reason is that the energy distribution of reactants and the TS are treated differently in the *E*,*J*-TST and the TST methods, such as the choice of statistical ensembles and the constraints applied in treating the association reactions. The second reason is the barrier height used. The barrier height is zero-point corrected (ΔE(0K)) in the *E*,*J*-TST approach, whereas the barrier height is classical electronic barrier height in the TST approach (see footnote of Table A10). The computed k_{inner} values with various levels of the TST theories (TST, CVT and ICVT) with different tunneling methods are compiled in Figure 5.13 and Tables A12 and A13.

Since the ICVT method ($k^{ICVT/SCT}$) represents the highest level of the variational transition state theory employed in this work, k_{inner} values are set to the computed $k^{ICVT/SCT}$ values in the calculation of $k_{overall(ii)}$. Figure 5.12 shows the plots of k_{outer}, k_{inner} and $k_{overall(ii)}$ values as a function of temperature in which the k_{outer} and k_{inner} values are tabulated in Tables A10 and A13, respectively. Since the k_{inner} values are about 2 orders of magnitude smaller than the k_{outer} values, the inner TS is the major bottleneck of the reaction. Since the inner TS dominates the bottleneck at high temperature [106], the $k_{overall(ii)}$ values are very close to the k_{inner} values and these two curves overlap with each other at high temperature (see Figure 5.12).

Figure 5.10 Computed (BD(TQ)/CBS//M06-2X/CBS incl. SO correction for BrO) k_{outer}, k_{inner}, and $k_{overall(i)}$ ($cm^3molecule^{-1}s^{-1}$) versus T (K) curves of the channel (1b) BrO + HO_2 → HOBr + O_2 ($\tilde{a}^1\Delta_g$). k_{outer} was evaluated at the PST level with VARIFLEX, k_{inner} was evaluated at the *E*,*J*-TST level with VARIFLEX and $k_{overall(i)}$ was calculated from k_{outer} and k_{inner} with equation (5.1).

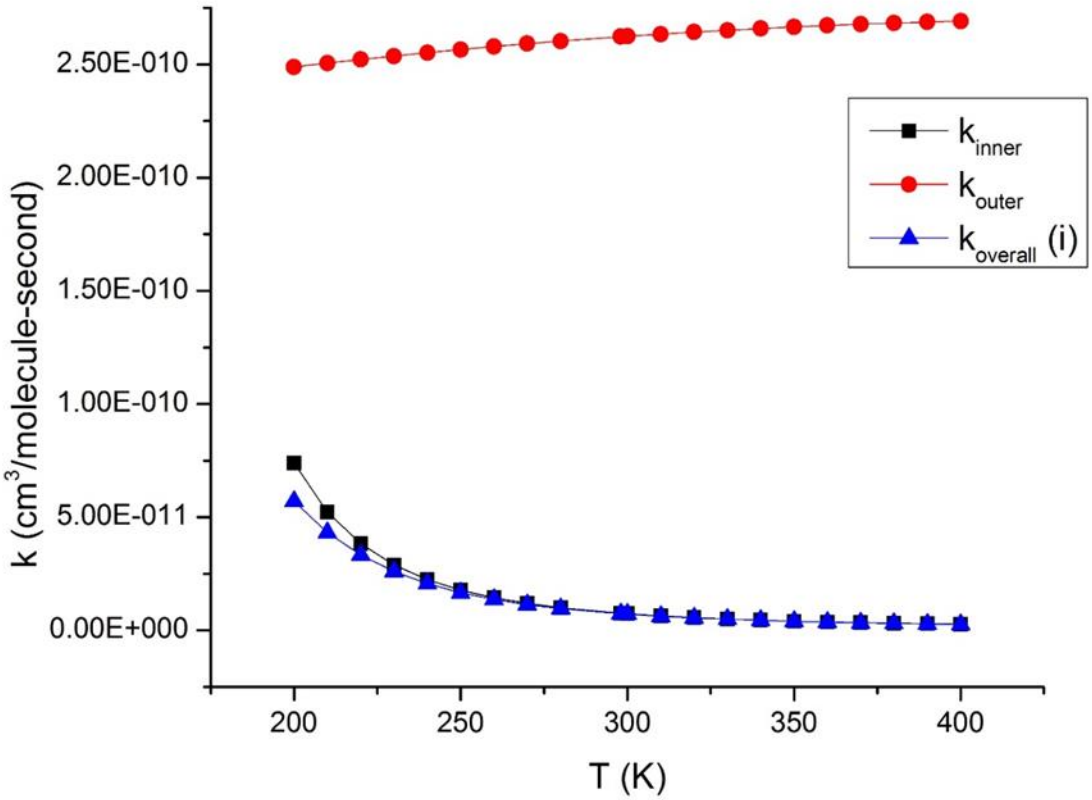

Figure 5.11 Computed k_{inner} (BD(TQ)/CBS//M06-2X/CBS incl. SO correction for BrO) values ($cm^3molecule^{-1}s^{-1}$) with TST for channel (1b) BrO + HO_2 → HOBr + O_2 ($\tilde{a}^1\Delta_g$). *E,J*-TST (with zero-point corrected barrier height) values were obtained with VARIFLEX and TST values (with the classical barrier height, which does not include zero-point correction) were obtained with POLYRATE.

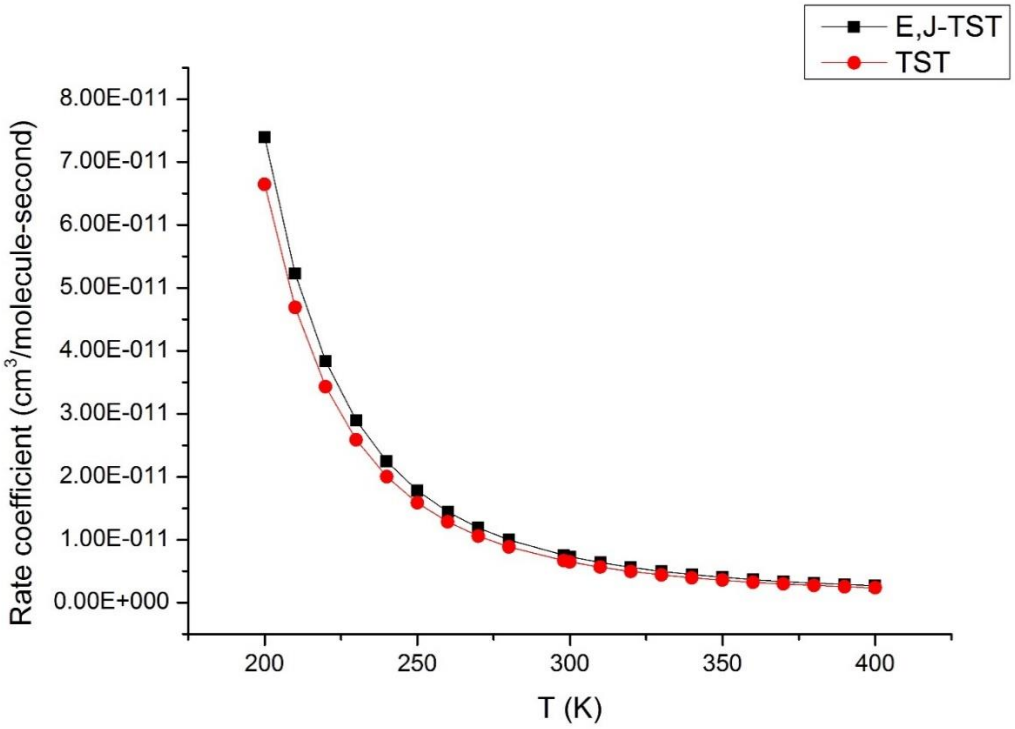

Figure 5.12 - Computed (BD(TQ)/CBS//M06-2X/CBS incl. SO correction for BrO) $k_{overall(ii)}$. ($cm^3molecule^{-1}s^{-1}$) versus T (K) curves for channel (1b) BrO + HO_2 → HOBr + O_2 ($\tilde{a}^1\Delta_g$). k_{outer} is evaluated with PST using VARIFLEX and k_{inner} is evaluated using ICVT/SCT with POLYRATE. $k_{overall(ii)}$ is obtained from k_{outer}, and k_{inner} , using equation (5.1). (The $k_{overall(ii)}$ values (blue triangles) are virtually superimposed on the k_{inner} values (red circles in this figure).

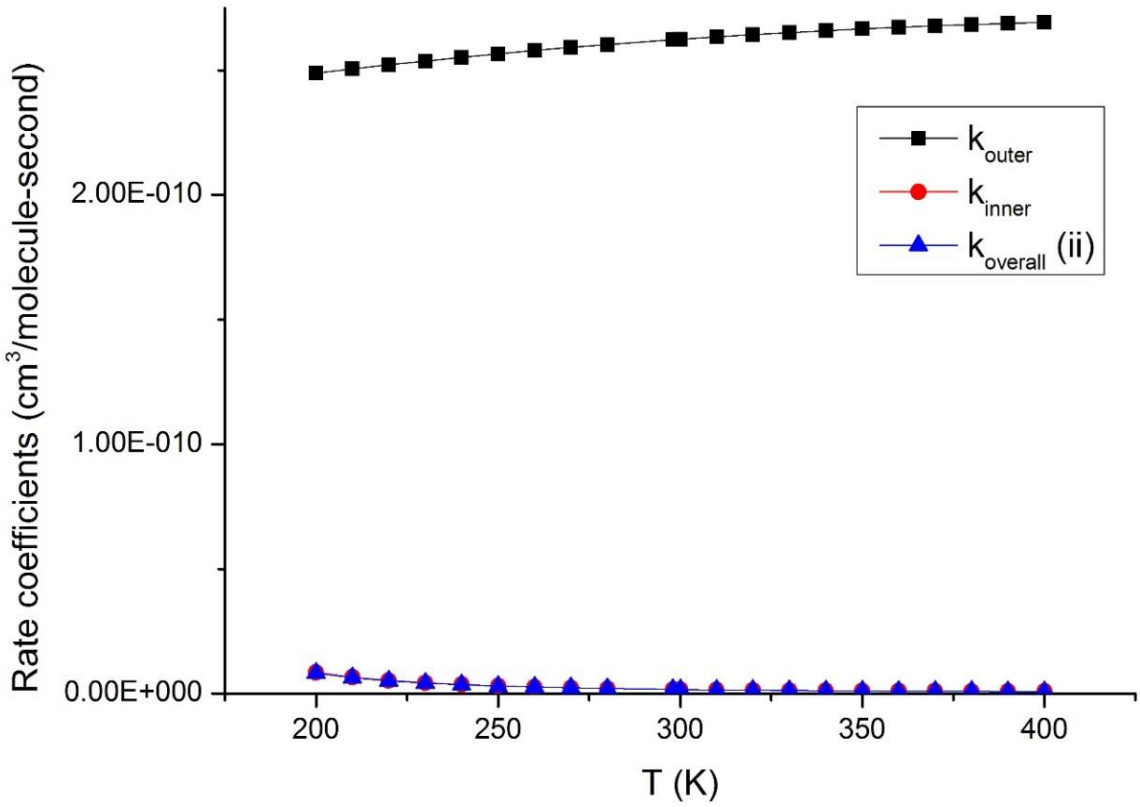

5.3.3.2 Computed κ and k values

As shown in Figure 5.9, the maximum of the ΔV_a^G curve ($s^*(\Delta V_a^G)$) is not located at s = 0 although the maximum of the *VMEP* curve is at s = 0. A direct consequence of the deviation of $s^*(\Delta V_a^G)$ from 0 implies that the classical transmission coefficient (known as CAG factor) is not negligible. The CAG factor is introduced to correct for the fact that the conventional TS is not located at $s^*(\Delta V_a^G) = 0$. Computed rate coefficients at the TST (or CVT) level with a CAG factor for [114, 115] threshold correction and a multi-dimensional tunneling (MT) correction method (e.g. ZCT or SCT) is related to k^{TST} (or k^{CVT}) as follows:

k(with tunneling) = κ^{CAG} x κ(tunneling) x k(without tunneling),

i.e. $k^{(\text{TST or CVT})/\text{MT}} = \kappa^{(\text{TST or CVT})/\text{CAG}} \times \kappa^{\text{MT}} \times k^{(\text{TST or CVT})}$

At the TST level, $\kappa^{\text{TST/CAG}} = \exp(\beta[V_a^G(s=0) - V_a^G(s^*)]$ [114, 116], where $\beta = 1/k_BT$. Generally, $V_a^G(s^*) \geq V_a^G(s=0)$, so $\kappa^{\text{TST/CAG}}$ is always ≤ 1. Similarly, $\kappa^{\text{CVT/CAG}}$ is introduced to correct for the fact that the maximum of the ΔG curve is different from that of the V_a^G curve. It is evaluated as $\kappa^{\text{CVT/CAG}} = \exp(\beta(V_a^G[s^{*\text{CVT(T)}}] - V_a^G(s^*))$ at the CVT level [114, 116].

Computed k, CAG factors, tunneling correction factors at Wigner, ZCT, and SCT levels are compiled in Table A14. From the table, $(V_a^G(s=0) - V_a^G(s^*))$ gives 0.856 kcal.mol^{-1}, the corresponding values of $\kappa^{\text{TST/CAG}}$ range from 0.112 at 200 K to 0.335 at 400 K. In principle, if $V_a^G(s^*)$ is the same as $V_a^G(s=0)$, $\kappa^{\text{TST/CAG}}$ is 1. Hence, the more $\kappa^{\text{TST/CAG}}$ deviates from 1, the more significant the correction is. As temperature increases, $\kappa^{\text{TST/CAG}}$ approaches 1 because β decreases as temperature increases. For $\kappa^{\text{CVT/CAG}}$, it depends on V_a^G at where maximum value of ΔG is. The value of $(V_a^G[s^{*\text{CVT(T)}}] - V_a^G(s^*))$ is smaller than that of $(V_a^G(s=0) - V_a^G(s^*))$, so $\kappa^{\text{CVT/CAG}}$ is closer to unity than $\kappa^{\text{TST/CAG}}$. $\kappa^{\text{CVT/CAG}}$ ranges from 0.974 at 200 K to 0.9114 at 400 K. At the ICVT level, its threshold energy is defined at $V_a^G(s^*)$ so there is no classical transmission coefficient for the ICVT method. Hence, $k^{\text{ICVT/MT}}$ is calculated from k^{ICVT} as below:

$$k^{ICVT} = \kappa^{MT} \times k^{ICVT} \qquad (5.2)$$

Regarding the magnitude of rate coefficients at the same temperature, the trend of $k^{\text{TST}} \geq k^{\text{CVT}} \geq k^{\text{ICVT}}$ is observed and expected (see Figure 5.13 and Table A12). The k^{CVT} values are almost identical to the k^{ICVT} values from 200 K to 400 K so the microcanonical correction of the threshold energy is negligible. The tunneling corrections were calculated at the Wigner, ZCT and SCT levels. Since Wigner tunneling correction only depends on the magnitude of the imaginary frequency of the conventional TS, it only works with k^{TST}. The Wigner tunneling correction factor is denoted as $\kappa^{\text{TST/W}}$. It is only valid when it is < 1.2 [35]. In our case, $\kappa^{\text{TST/W}}$ is < 1.2 in the temperature range considered because the magnitude of the imaginary frequency is small. Since the tunneling factors (κ^{ZCT} and κ^{SCT}) are exactly 1.0 from 200 K to 400 K, the remaining correction factor is then the classical transmission coefficients ($\kappa^{\text{TST/CAG}}$ and $\kappa^{\text{CVT/CAG}}$). $\kappa^{\text{TST/CAG}}$ is around 0.1 while $\kappa^{\text{CVT/CAG}}$ is around 0.9 so $\kappa^{\text{TST/CAG}}$ leads to a large reduction of k^{TST} whereas $\kappa^{\text{CVT/CAG}}$ leads to a

small reduction of k^{CVT}. By considering the tunneling corrections, the trend of $k^{TST} \geq k^{CVT} \geq k^{ICVT}$ is actually reversed in our case, which is $k^{ICVT/SCT} \geq k^{CVT/SCT} \geq k^{TST/SCT}$ (or $k^{ICVT/ZCT} \geq k^{CVT/ZCT} \geq k^{TST/ZCT}$). Another aspect of kinetics is the extent of variational effect of the rate coefficients, which can be measured by the ratio, k^{CVT}/k^{TST}. The closer the ratio is to unity, the smaller the variational effect is. The ratios are 0.127 and 0.352 at 200 K and 400 K respectively. Since both values significantly deviate from unity, large variational effect is observed throughout the temperature range considered. This is consistent with the small $\kappa^{TST/CAG}$ in the calculations that leads to the large reduction of k^{TST}. Figure 5.13 clearly shows that there are essentially two sets of rate coefficients. The larger set of rate coefficients is essentially the non-variational rate constant which consists of the k^{TST} and $k^{TST/W}$ curves. The Wigner tunneling correction is not significant even at low temperature. The lower set of rate coefficients consists of the VTST rate coefficients (with and without tunneling). Since the contributions of nonreactive trajectories are minimized in VTST, the lower set of computed rate coefficients should be more reliable.

Figure 5.13 Computed (BD(TQ)/CBS//M06-2X/AVDZ incl. SO correction for BrO) k ($cm^3molecule^{-1}s^{-1}$) (k_{inner} values) versus T (K) curves (upper) and $\log_{10}k$ versus $1000/T$ curves (lower) of channel (1b) $BrO + HO_2 \rightarrow HOBr + O_2$ ($\tilde{a}^1\Delta_g$) obtained at TST and various VTST levels (CVT, ICVT, TST/ZCT, CVT/ZCT, ICVT/ZCT, TST/SCT, CVT/SCT, and ICVT/SCT) using POLYRATE. As $k^{CVT} \sim= k^{ICVT}$ and $\kappa^{ZCT} = \kappa^{SCT} = 1$, k^{CVT}, k^{ICVT}, $k^{CVT/ZCT}$, $k^{ICVT/ZCT}$, $k^{CVT/SCT}$ and $k^{ICVT/SCT}$ curves overlap with each other. Also, since $k^{TST/CAG} = k^{TST/SCT} = k^{TST/ZCT}$, only $k^{TST/SCT}$ is plotted.

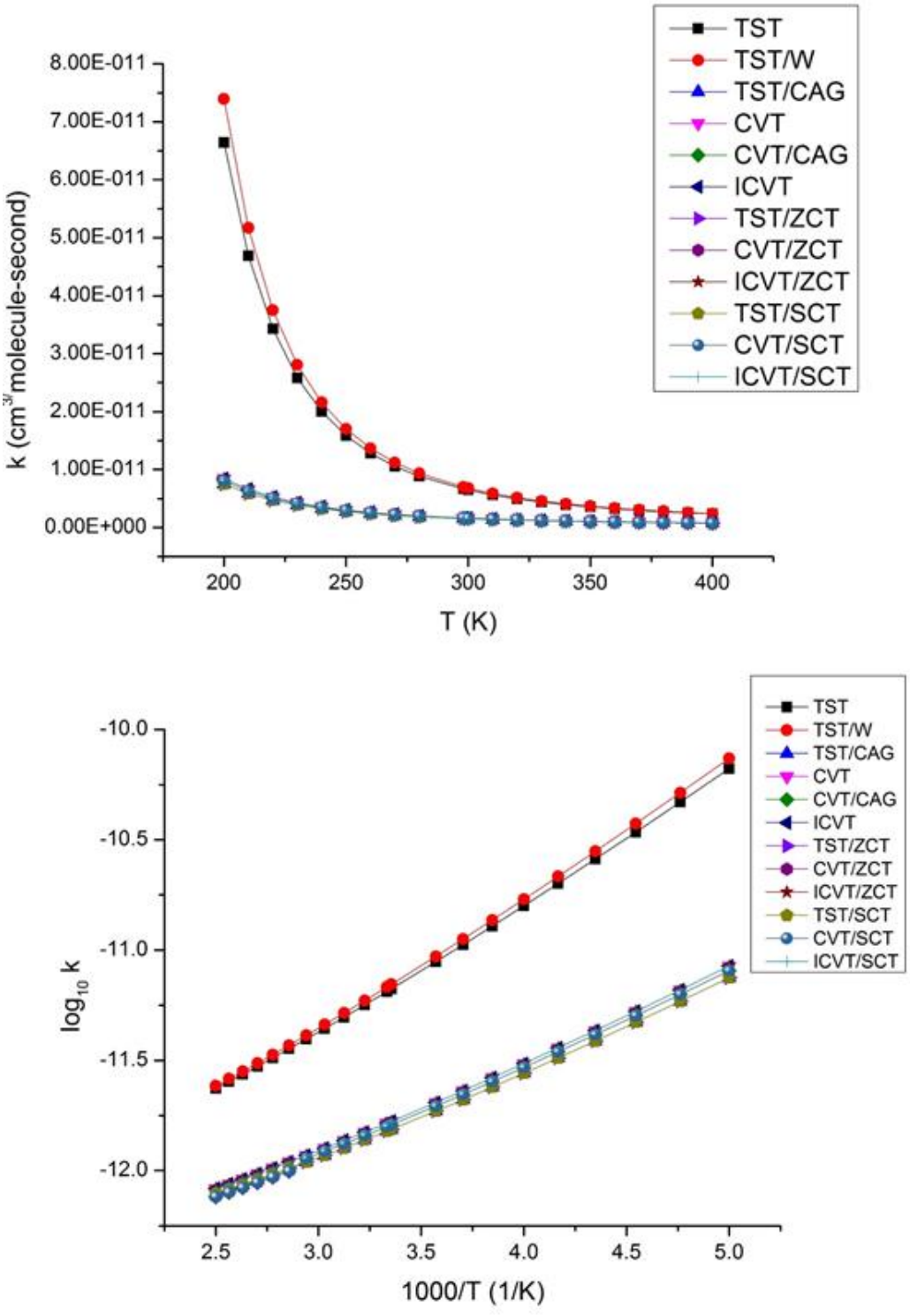

5.3.3.3 Enthalpy of activation and entropy of activation contributions to the TST rate coefficient (k_{inner}) of channel (1b)

All rate coefficients of channel (1b) are tabulated in Tables A12 and A13 in which the k_{inner} values were computed by using POLYRATE. These rate coefficients exhibit a negative temperature dependent at all TST levels, such as the TST, the CVT, the ICVT and the CVT/SCT levels. To inspect such behavior of the rate coefficients, the impacts of the entropy of activation and the enthalpy of activation at different temperatures on the rate coefficients are analyzed. Since the rate coefficients evaluated at the TST level is simpler than the corresponding ones obtained at the CVT level, only the former ones are considered.

The rate coefficient of a bimolecular reaction can be computed at the TST level according to:

$$k = \frac{k_B T}{hc^0} \exp\left(\frac{-\Delta G^{\#}}{k_B T}\right) = \frac{k_B T}{hc^0} \exp\left(\frac{\Delta S^{\#}}{k_B}\right) \exp\left(\frac{-\Delta H^{\#}}{k_B T}\right) \quad (5.3)$$

where c^0 is the standard-state concentration (the concentration at 1 bar and 298.15 K), $\Delta H^{\#}$ is the standard-state enthalpy of activation, and $\Delta S^{\#}$ is the standard-state entropy of activation. $\Delta G^{\#}$ is the standard-state free energy of activation and it is related to $\Delta H^{\#}$ and $\Delta S^{\#}$ by $\Delta G^{\#} = \Delta H^{\#} - T\Delta S^{\#}$. By taking the natural logarithm of k in equation (5.3), the following expression is then obtained:

$$\ln k = ln\left(\frac{k_B T}{hc^0}\right) + \frac{\Delta S^{\#}}{k_B} - \frac{\Delta H^{\#}}{k_B T} \quad (5.4)$$

Both of $\Delta H^{\#}$ and $\Delta S^{\#}$ are negative in channel (1b). The behaviors of the individual terms on the right hand side of equation (5.4) are as follows. The first term, $\ln(k_B T/hc^0)$, increases as temperature increases. Tables A15 to A17 and Figure 5.14 show that $\Delta S^{\#}/k_B$ decreases slightly with temperature while $-\Delta H^{\#}/(k_B T)$ decreases significantly with temperature. Figure 5.14 also shows that the behavior of $\ln k$ with temperature is determined by that of $-\Delta H^{\#}/(k_B T)$ with temperature. The variations of the terms in equation with temperature with respect to the corresponding values at 400 K are shown in Figure 5.14. Tables A15 to A17 show that the bottleneck of the reaction is given by the $-\Delta G^{\#}/(k_B T)$ term, which is in-turn dominated by the $\Delta S^{\#}/k_B$ term. Consequently, lowering

$\Delta H^{\#}$ by 1.0 kcal.mol^{-1} has a little effect (<2%) on the computed k^{TST} values but the temperature dependence of ln$k$ is given by the $-\Delta H^{\#}/(k_B T)$ term. It is observed that the magnitude of ln$k$ of the radical-radical reaction is determined by the entropy ($\Delta S^{\#}/k_B$) term, which is one of the major conclusions in this study. The rate coefficient of channel (1b) decreases with increasing temperature. In this situation, Figure 5.14 shows that the slope of ln$k$ versus 1000/T is positive while those of $\Delta S^{\#}$ and $-\Delta H^{\#}$ versus 1000/T are negative and positive respectively. Since the $-\Delta H^{\#}/k_B T$ determines the behaviour of ln$k$ with temperature and its slope is positive with respect to 1000/T, the ln$k$ term increases as temperature increases.

Figure 5.14 Plots of $\Delta \ln k$, $\Delta(\ln(k_B T/hc^0))$, $\Delta(-\Delta H^{\#}/k_B T)$ and $\Delta(\Delta S^{\#}/k_B T)$ vs 1000/T of the channel (1b) BrO + HO_2 $\rightarrow$ HOBr + O_2 ($\tilde{a}^1\Delta_g$) obtained by using POLYRATE. (The rate coefficients are k_{inner} values). In this figure, $\Delta \ln k = \ln k - \ln k|_{T=400K}$, $\Delta(-\Delta H^{\#}/k_B T) = -\Delta H^{\#}/k_B T + \Delta H^{\#}/k_B T|_{T=400K}$, $\Delta(\Delta S^{\#}/k_B) = -\Delta S^{\#}/k_B + \Delta S^{\#}/k_B|_{T=400K}$ and $\Delta(\ln(k_B T/hc^0)) = \ln(k_B T/hc^0) - \ln(k_B T/hc^0)|_{T=400K}$ where # refers to TS and k refers to k^{TST}. All calculations are based on the BD(TQ)/CBS//M06-2X/AVDZ potential energy surface (incl. SO correction for BrO) (see Table A17).

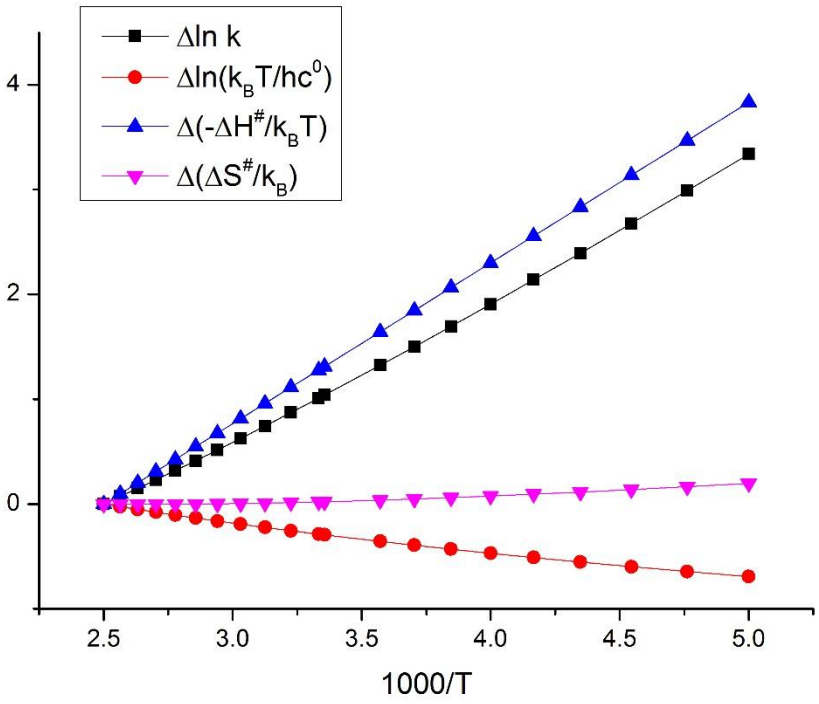

5.3.3.4 Effect of channel (2) on the overall rate coefficient

As mentioned in the introduction, channel (2) is the ozone production channel. More importantly, the impact of this channel on the overall rate coefficient of the BrO + HO_2 reaction is of concern to the atmospheric chemistry community. Channel (2) proceeds via a reaction intermediate (-19.57 kcal.mol^{-1}) and then it passes the TS (10.93 kcal.mol^{-1}). The TS then dissociates to form the products (HBr and O_3). In the experimental studies, only the overall rate coefficients of the BrO + HO_2 reaction were measured from 200 K to 400 K in the pressure range considered (1 – 760 Torr) and only HOBr have been detected as the major product. No intermediate (HOOOBr) and HBr have been detected using mass spectrometry [7-9, 11]. These experimental results suggest that the contribution of channel (2) to the overall rate coefficient of the BrO + HO_2 reaction is negligible. Moreover, according to Figure 5.8, the zero-point corrected barrier height of channel (2) is 10.93 kcal.mol^{-1}, which is much higher than that of channel (1b). Thus, the computational results are consistent with the experimental results, in which HOBr is the major product and HBr is not likely to form due to high barrier. In view of all these experimental and computational results, channel (2) is a minor channel, so no rate coefficient calculations have been performed for channel (2). The intermediate, HOOOBr, is expected to be stabilized at high pressure limit and then the rate coefficient of the BrO + HO_2 reaction would be enhanced as a result. However, all available experiment results suggest that this reaction is independent of pressure so the intermediate could be insignificant in the atmospherically important pressure range. In this connection, the intermediate may not be relevant to atmospheric chemistry. However, the investigations of the intermediate could give valuable information and it can be studied using infrared matrix isolation spectroscopy or other types of spectroscopies in a molecular beam experiment.

5.3.3.5 Comparison of computed $k_{overall}$ values with experimental rate coefficients

Atkinson and coworkers have compiled the available experimental rate coefficients of the BrO + HO_2 reaction. The first measurement of the rate coefficient of this reaction, performed by Cox and coworkers, was neglected because its value is very small. The rest of the available experimental rate coefficients spread over a factor of two. The recommended value at 298 K in reference 13 is $(2.4 \pm 0.8)\times10^{-11}$ cm^3 molecule^{-1}s^{-1}, which is the average value of references [5, 7-12]. The recommended E_a/R value in the Arrhenius

expression of this reaction has been obtained by using the average of the E_a values taken from references [7-9, 11] while the recommended value of the pre-exponential factor in the recommended Arrhenius expression has been obtained by adjusting to yield the recommended rate coefficient at 298 K. The recommended values provided in reference 13 from 210 K to 360 K are listed in Table A19. Table A18 also shows the computed rate coefficients, k_{outer} (evaluated at the PST level), k_{inner} (evaluated at the ICVT/SCT level), and $k_{overall(ii)}$ from 200 K to 400 K. According to this table, the k_{inner} values are very similar to the $k_{overall(ii)}$ values because the inner transition state is the major bottleneck of the reaction. Figure 5.15 shows a comparison between the $k_{overall(ii)}$ values and the available experimental rate coefficients obtained by different research groups. The experimental and the computed rate coefficients (k^{TST}, $k^{ICVT/SCT}$, and $k_{overall(ii)}$) are tabulated in Table A19 and their values are plotted against temperature in Figure 5.16. According to Table A19, the $k^{ICVT/SCT}$ values are significantly lower than the experimental rate coefficients by a factor of 8 and an order at 210 K and high temperature respectively. Although the negative temperature dependence of $k_{overall(ii)}$ has been observed in Figure 5.16, the extent of the negative temperature dependence is less pronounced than that of the experimental rate coefficients. In contrast, the k^{TST} values exhibit much pronounced negative temperature dependence than the $k_{overall(ii)}$ values and they also come in better agreement with the experimental rate coefficients, especially in the low temperature region (200 – 300 K). Although the underlying reason for the differences in the computed and experimental rate coefficients is unknown, they likely arise from the inaccuracies in both $\Delta H^{\#}$ and $\Delta S^{\#}$ values. Both quantities have been obtained using the lower level results (MEP, geometries and vibrational frequencies of both stationary and non-stationary points) obtained at the M06-2X/AVDZ level. The work in Chapter 4 has shown that different lower level results could actually lead to different rate coefficients, even the same barrier has been employed. This observation suggests that the entropic term, which depends on vibrational frequencies and geometries obtained at the lower level, can play an important role in rate coefficient calculations. Moreover, the zero-point energy curve obtained by using vibrational frequencies of both stationary and non-stationary points can affect the V_a^G curve. Hence, there could also be an inaccuracy in the detailed shape of the potential energy curve obtained at higher level which leads to large differences in the computed and experimental rate coefficients in this study. In summary, the sources of

errors in this kinetic study are inaccuracies of the activation enthalpy and the activation entropy terms and the detailed shape of the potential energy curve at the higher level.

VTST calculations at the CVT and the ICVT levels were also carried out for channel (1a) using the best computed relative energies of the stationary points tabulated in Table A3 and the MEP obtained at the BD(TQ)/CBS//BD/AVDZ level. A high classical barrier (2.58 kcal.mol^{-1}) of this channel leads to rate coefficients which are at least 4 orders of magnitude smaller than those of channel (1b).

This work has revealed the reaction mechanisms and energetics of all atmospherically important channels of the BrO + HO_2 reaction, in particular, channel (1b) is the major channel, rather than channel (1a) as identified in reference 16. Therefore, channel (1b) is expected to have the largest rate coefficient among the investigated channels. A similar study is required for the ClO + HO_2 reaction as HOCl ($\tilde{X}^1$A′) + O_2($\tilde{a}^1\Delta_g$), rather than HOCl ($\tilde{X}^1$A′) + O_2($\tilde{X}^3\Sigma^-_g$), could be the most favoured channel kinetically. Since the experimental rate coefficients of the ClO + HO_2 reaction are smaller than those of the BrO + HO_2 reaction by five times [13], the ClO + HO_2 reaction may be less significant than the BrO + HO_2 reaction regarding stratospheric ozone depletion.

Figure 5.15 Computed (BD(TQ)/CBS//M06-2X/CBS incl. SO correction for BrO) and experimental [3-5, 7-11] k ($cm^3molecule^{-1}s^{-1}$) versus T (K) curves (upper) and $\log_{10} k$ versus $1000/T$ curves (lower) of channel (1b) $BrO + HO_2 \rightarrow HOBr + O_2$ ($\tilde{a}^1\Delta_g$). $k_{overall}$ values are evaluated from equation (5.1) with (ii) k_{outer} from PST (VARIFLEX) and k_{inner} from E,J-TST(VARIFLEX) and (ii) k_{outer} from PST (VARIFLEX) and k_{inner} from ICVT/SCT (POLYRATE). Also plotted are k_{inner} values (k^{TST} and $k^{ICVT/SCT}$) from POLYRATE. The k_{inner} ($k^{ICVT/SCT}$) and $k_{overall}$ (ii) plots are superimposed in this figure.

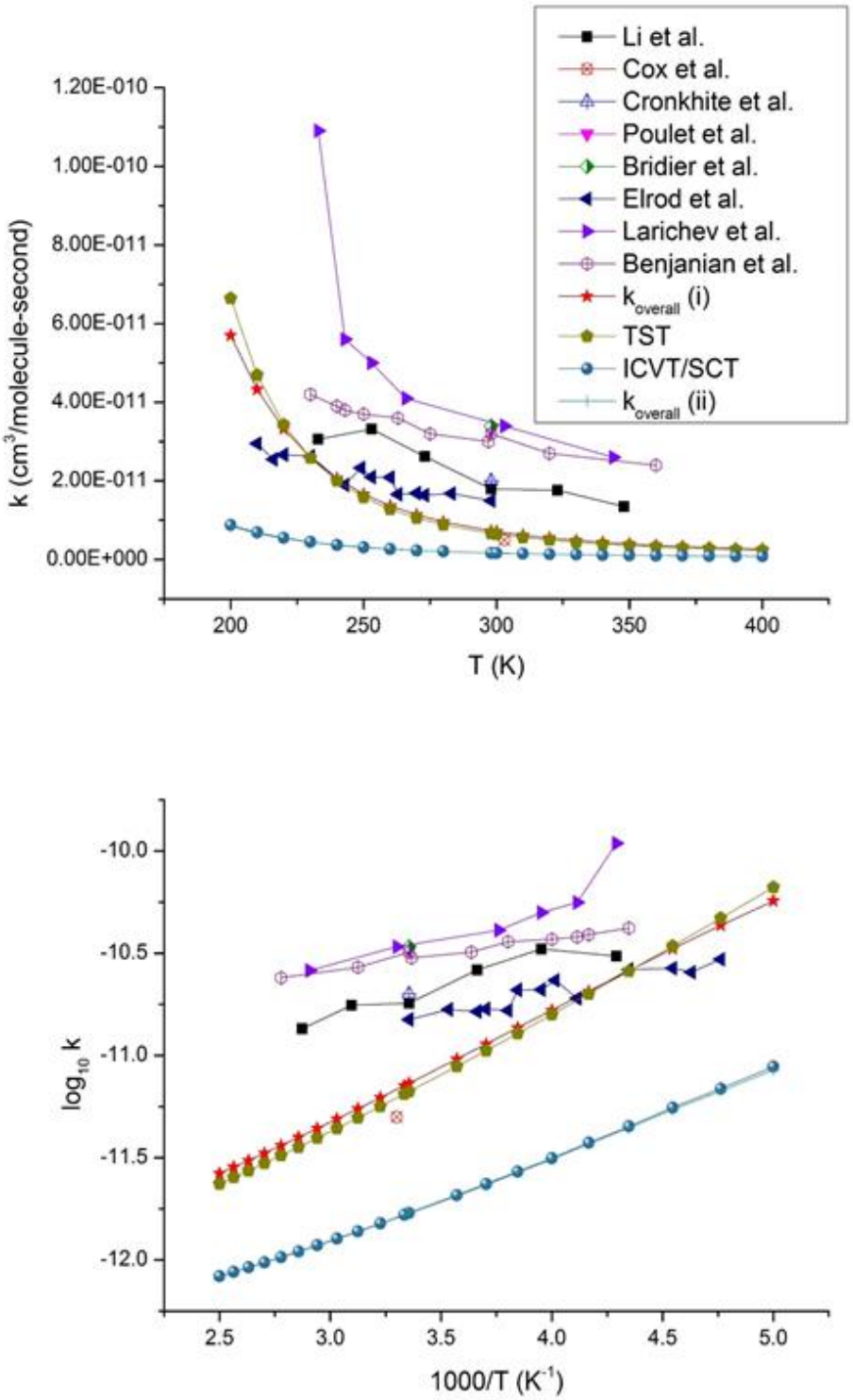

Figure 5.16 Computed (BD(TQ)/CBS//M06-2X/CBS incl. SO correction for BrO) and recommended experimental k ($cm^3molecule^{-1}s^{-1}$) values from ref.(13) versus T (K) curves (upper) and $\log_{10}k$ versus $1000/T$ curves (lower) of channel (1b) $BrO + HO_2 \rightarrow HOBr + O_2$ ($\tilde{a}^1\Delta_g$).

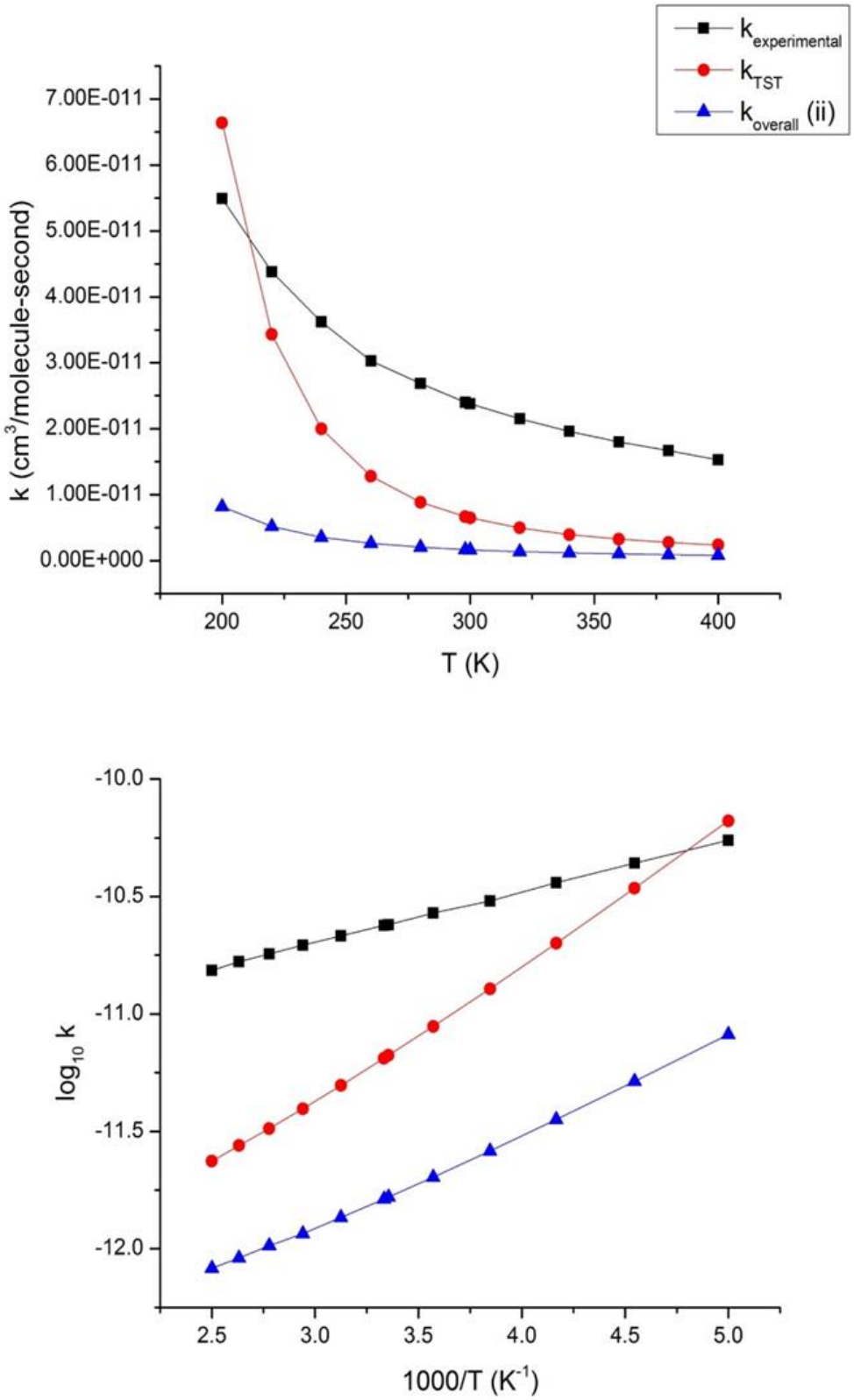

5.4 Conclusion

We have performed *ab initio*/DFT calculations of five channels in the BrO + HO_2 reaction, namely BrO + HO_2 → HOBr + O_2 ($\tilde{X}^3\Sigma_g^-$), BrO + HO_2 → HOBr + O_2 ($\tilde{a}^1\Delta_g$), BrO + HO_2 → HBr + O_3, BrO + HO_2 → OBrO + OH and BrO + HO_2 → BrOO + OH. The singlet O_2 production channel (channel (1b)) is found to have the smallest barrier while channel (1a) is the most exothermic channel. It is expected that channel (1b) will proceed with the highest rate. In contrast of a previous computational study carried out by Kaltsoyanni and Rowley [16] where channel (1a) was the major channel. This difference in these two computational studies lies in the treatment of the TS in channel (1b), that is, it was treated as a closed shell singlet in reference 16 rather than an open-shell singlet in this study. The open-shell singlet state of the TS has been confirmed by using spin densities of each atom in the TS. Non-zero spin densities have been obtained for each atom in the TS of channel (1b) using unrestricted wavefunction (converged), suggesting an open-shell singlet TS. Besides, Brueckner theory is found to be very effective in capturing the non-dynamical correlation in optimized multi-reference stationary points in this work.

This study is the first theoretical kinetic study of channels (1a) and (1b) at high pressure limit. Since channel (1b) is a bimolecular reaction with a negative barrier, the two transition state theory was employed to combine the k_{outer} and k_{inner} values, which were evaluated by using the phase space theory and the microcanonical transition state theory family, respectively. The inner transition state was identified to be the major bottleneck of the reaction whereas the outer transition state has essentially no effect on the overall rate coefficient at 200 – 400 K. An investigation on the activation entropy, activation enthalpy and activation free energy terms has revealed that the activation free energy term is dominated by the activation entropy term but the activation enthalpy term determines the temperature dependence of ln$k$. Rate coefficients were also calculated for channel (1a) and it has been found that channel (1a) proceeds much more slowly than channel (1b) at 200 – 400 K. The computed rate coefficient ($k_{overall(ii)}$) at the highest TST level (i.e. ICVT/SCT) exhibits negative temperature dependence but its values are smaller than the experimental rate coefficient by approximately an order of magnitude. Klippestein and coworkers [105] have found that the outer transition state dominates the reactive flux of a reaction with a negative barrier at low temperatures while the inner

transition state dominates it at high temperature. They have also found that both transition states can contribute to the overall reactive flux at intermediate temperature. However, the case observed in channel (1b) is different in which the entropic contributions dominate the reaction rate in the temperature range considered. The dual level approach was employed in computing the rate coefficients for channels (1a) and (1b) using the MEPs at the BD(TQ)/CBS//BD/AVDZ and BD(TQ)/CBS//M06-2X/AVDZ levels, respectively. The activation entropy term is computed by using vibrational frequencies and rotational constants of the optimized transition state and those of the reactants at the lower level (M06-2X/AVDZ for channel (1b)). Hence, inaccuracies in the lower level results can lead to an inaccurate activation entropy term, which is considered to be the major factor for the differences in the computed and the experimental rate coefficients.

The dual level approach employed in carrying out rate coefficients using POLYRATE has a lot in common with composite methods in electronic structure calculations. Both approaches involve using a larger basis set with a higher level method for computing electronic energies and a smaller basis set with a lower level method for computing geometries and vibrational frequencies. Since a near state-of-the-art method has been employed as the higher level for computing the relative energies of the stationary points, their values are expected to be within the accepted chemical accuracy (1 kcal.mol^{-1}). In principle, systematic improvements of the single point energy calculations can be made and the corresponding uncertainties can be approximated using stepwise improvements in the correlation methods and/or basis sets. The geometry and frequency calculations can be computationally expensive, so the availability of the first and the second derivatives for different methods limits further investigation on systematic improvements on the calculated quantities [117]. It is important to note that geometries and vibrational frequencies obtained at the lower level can lead to a large difference (~ 1 order of magnitude) in computed rate coefficients with the same barrier height. In Chapter 4, the rate coefficients of the $CH_3C(O)OCH_3 + Cl \rightarrow HCl + CH_3C(O)OCH_2$ reaction was computed and its best computed barrier height was found to be positive. It was also found that the bottleneck of the rate coefficients was dominated by the activation enthalpy. In contrast, the major channel of the $BrO + HO_2$ reaction, $BrO + HO_2 \rightarrow HOBr + O_2(\tilde{a}^1\Delta_g)$, has a negative barrier and its bottleneck is found to be dominated by the activation entropy. Hence, the differences in computed and experimental rate coefficients arise from the inadequacies of geometry and frequencies obtained at the lower levels. A surprising

finding of the major channel is that the overall reactive flux is dominated by the inner transition state, rather than the outer transition state. This situation arises from the fact that the entropy of activation is much greater than the enthalpy of activation. Thus, even the barrier of the inner transition state is reduced by a few kcal.mol^{-1}, this has negligible effects on the computed rate coefficients (k_{inner} and/or $k_{overall}$). Therefore, one has to be cautious to match the experimental rate coefficients with computed rate coefficients if the bottleneck of the reaction is dominated by entropy of activation. In summary, entropic effects can be prominent in computing rate coefficients as it can be more significant than the enthalpic effects is in the free energy of the $BrO + HO_2 \rightarrow HOBr + O_2$ ($\tilde{a}^1\Delta_g$) reaction, where the magnitude of computed rate coefficients is given by the activation entropy whereas the temperature dependence of computed rate coefficients is given by the activation enthalpy.

5.5 References

1. Bobrowski1, N.; Hönninger, G.; Galle, B.; U. Platt1. Detection of Bromine Monoxide in a Volcanic Plume. *Nature* **2003**, *423*, 273-276.
2. Yung, Y. L.; Pinto, J. P.; Watson, R. T.; Sander, S. P. Atmospheric Bromine and Ozone Perturbations in the Lower Stratosphere. *J. Atmos. Science* **1980**, *37*, 339-353.
3. Cox, R.A.; Sheppard, D.W. Rate Coefficient for the Reaction of BrO with HO_2 at 303 K. *J. Chem. Soc., Faraday Trans 2*, **1982**, *78*, 1383-1389
4. Poulet, G.; Pirre, M.; Francoise, M.; Ramaroson R.; Le Baras G. Role of the BrO + HO_2 reaction in the stratospheric chemistry of bromine *Geophys. Res. Lett*. **1992**, *19*, 2305-2308.
5. Bridier, I.; Veyret, B.; Lesclaux, R. Flash photolysis kinetic study of reactions of the BrO radical with BrO and HO_2. *Chem. Phys. Lett*. **1993**, *201*, 563-568.
6. Mellouki, A.; Talukdar, R.; Howard, C.J. Kinetics of the reactions of HBr with O_3 and HO_2: The yield of HBr from HO_2 + BrO. *J. Geophys. Res*. **1994**, *99*, 22949-22954.
7. Larichev, M.; Maguin, F.; Le Bras, G.; Poulet, G. Kinetics and Mechanism of the BrO + HO_2 Reaction. *J. Phys. Chem*. **1995**, *99*, 15911–1591
8. Elrod, M. J.; Meads, R.F.; Lipson, J.B.; Seeley, J.V.; Molina, M.J. Temperature Dependence of the Rate Constant for the HO_2+BrO Reaction. *J. Phys. Chem*. **1996**, *100*, 5808-5812.
9. Li, Z.; Friedl, R.R.; Sander, S.P. Kinetics of the HO_2 + BrO reaction over the temperature range 233 – 348 K. *J. Chem. Soc., Faraday Trans* **1997**, *16*, 2683-2691.
10. Cronkhite, J.M.; Stickel, R.E.; Nicovich, J.M.; Wine, P.H. Laser Flash Photolysis Studies of Radical-Radical Reaction Kinetcs: The HO_2 + BrO Reaction. *J. Phys. Chem. A* **1998**, *102*, 6651-6658.
11. Bedjanian, Y.; Riffault, V.; Pilet, G. Kinetic Study of the Reactions of BrO Radicals with HO_2 and DO_2. *J. Phys. Chem. A* **2001**, *105*, 3167-3175.
12. Bloss, W.J.; Rowley, D.M.; Cox, R.A.; Jones, R.L. Rate coefficient for the BrO + HO_2 reaction at 298 K. *Phys. Chem. Chem. Phys*. **2002**, *4*, 3639–3647
13. Atkinson, R.; Baulch, D. L.; Cox, R. A.; Crowley, J. N.; Hampson, J. N. et al. Evaluated kinetic and photochemical data for atmospheric chemistry Vol III Gas-phase reactions of inorganic halogens. *Atmos. Chem. Phys*. **2007**, *7*, 981-1191.
14. Shallcross, D. E.; Leather, K. E.; Bacak, A.; Xiao, P.; Lee, E. P. F.; Ng, M.; Mok, D. K. W.; Dyke, J. M.; Hossaini, R.; Chipperfield, M. P.; Khan, M. A. H.; Percival, C. J. Reaction between CH_3O_2 and BrO radicals: a new source of upper troposphere lower stratosphere hydroxyl radicals. *J. Phys. Chem. A* **2015**, *119*, 4618-4632.

15. Guha, S.; Francisco, J. S. An *ab initio* study for the pathways for the reaction of CH_3O_2 and BrO radicals. *J. Chem. Phys*. **2003**, *118*, 1779-1793.
16. Kaltsoyannis, N.; Rowley, D.M. *Ab initio* investigations of the potential energy surfaces of the XO + HO_2 reaction (X=chlorine or bromine). *Phys. Chem. Chem. Phys*. **2002**, *4*, 419–427.
17. Guhua, S.; Francisco, J.S. Structures, Vibrational Spectra, and Relative Energetics of $HBrO_3$ Isomers. *J. Phys. Chem. A* **1998**, *102*, 2072-2079.
18. Guhua, S.; Francisco, J.S. An Examination of the Reaction Pathways for the HOOOBr and HOOBrO Complexes Formed from the HO_2 + BrO Reaction. *J. Phys. Chem. A*, **1999**, *103*, 8000-8007.
19. Guhua, S.; Francisco, J.S. A Theoretical Examination of the Isomerization Pathways for $HBrO_3$ Isomers. *J. Phys. Chem. A* **2000**, *104*, 9321-9327.
20. Frisch, M. J.; Trucks, G. W.; Schlegel, H. B.; Scuseria, G. E.; Robb, M. A.; Cheeseman, J. R.; Scalmani, G.; Barone, V.; Mennucci, B.; Petersson, G. A.; Nakatsuji, H.; Caricato, M.; Li, X.; Hratchian, H. P.; Izmaylov, A. F.; Bloino, J.; Zheng, G.; Sonnenberg, J. L.; Hada, M.; Ehara, M.; Toyota, K.; Fukuda, R.; Hasegawa, J.; Ishida, M.; Nakajima, T.; Honda, Y.; Kitao, O.; Nakai, H.; Vreven, T.; Montgomery, J., J. A.; Peralta, J. E.; Ogliaro, F.; Bearpark, M.; Heyd, J. J.; Brothers, E.; Kudin, K. N.; Staroverov, V. N.; Keith, T.; Kobayashi, R.; Normand, J.; Raghavachari, K.; Rendell, A.; Burant, J. C.; Iyengar, S. S.; Tomasi, J.; Cossi, M.; Rega, N.; Millam, J. M.; Klene, M.; Knox, J. E.; Cross, J. B.; Bakken, V.; Adamo, C.; Jaramillo, J.; Gomperts, R.; Stratmann, R. E.; Yazyev, O.; Austin, A. J.; Cammi, R.; Pomelli, C.; Ochterski, J. W.; Martin, R. L.; Morokuma, K.; Zakrzewski, V. G.; Voth, G. A.; Salvador, P.; Dannenberg, J. J.; Dapprich, S.; Daniels, A. D.; Farkas, Ö.; Foresman, J. B.; Ortiz, J. V.; Cioslowski, J.; Fox, D. J. Gaussian 09; Revision B.01 ed.; Gaussian, Inc.: Wallingford CT, 2010.
21. Goerigk, L. ; Grimme, S. A thorough benchmark of density functional methods for general main group thermochemistry, kinetics, and noncovalent interactions. *Phys. Chem. Chem. Phys.* **2011**, *13*, 6670-6688.
22. Zheng, J. J.; Zhao, Y.; Truhlar, D. G. The DBH24/08 Database and Its Use to Assess Electronic Structure Model Chemistries for Chemical Reaction Barrier Heights. *Journal of Chemical Theory and Computation* **2009**, *5*, 808-821.
23. Zhao, Y.; Truhlar, D. G. Density functionals with broad applicability in chemistry. *Accounts of Chemical Research* **2008**, *41*, 157-167.
24. Xu, X. F.; Alecu, I. M.; Truhlar, D. G. How well can modern density functionals predict internuclear distances at transition states? *Journal of Chemical Theory and Computation* **2011**, *7*, 1667-1676.

25. Balaganesh, M. and Rajakumar, B. Rate Coefficients and Reaction Mechanism for the Reaction of OH Radicals with (E)-CF3CH=CHF, (Z)-CF3CH=CHF, (E)-CF3CF=CHF, and (Z)-CF3CF=CHF between 200 and 400 K: Hybrid Density Functional Theory and Canonical Variational Transition State Theory Calculations. *J. Phys. Chem. A*, **2012**, *116*, 9832-9842.
26. Drougas, E.; Kosmas, A. M. Computational studies of (HIO_3) isomers and the HO_2 + IO reaction pathways. *J. Phys. Chem. A* **2005**, *109*, 3887-3892.
27. Werner, H.-J. ; Knowles, P. J.; Knizia, G.; Manby, F. R.; Schütz, M.; Celani, P.; Korona, T.; Lindh, R.; Mitrushenkov, A.; Rauhut, G.; Shamasundar, K. R.; Adler, T. B.; Amos, R. D.; Bernhardsson, A.; Berning, A.; Cooper, D. L.; Deegan, M. J. O.; Dobbyn, A. J.; Eckert, F.; Goll, E.; Hampel, C.; Hesselmann, A.; Hetzer, G.; Hrenar, T.; Jansen, G.; Köppl, C.; Liu, Y. ; Lloyd, A. W.; Mata, R. A.; May, A. J.; McNicholas, S. J.; Meyer, W.; Mura, M. E.; Nicklass, A.; O'Neill, D. P.; Palmieri, P.; Peng, D.; Pflüger, K.; Pitzer, R.; Reiher, M.; Shiozaki, T.; Stoll, H.; Stone, A. J.; Tarroni, R.; Thorsteinsson, T.; Wang, M. MOLPRO, version 2012.1, a package of *ab initio* programs, see http://www.molpro.net.
28. Drouin, B.J.; Miller, C.E.; Muller, H. S. P.; Cohen, E. A. The Rotational Spectra, Isotopically Independent Parameters, and Interatomic Potentials for the $X_1{}^2\Pi_{3/2}$ and $X_2{}^2\Pi_{1/2}$ States of BrO. *J. Mol.Spectrosc.* **2001**, *205*, 128-138.
29. Grant, D. J. ; Garner III, E. B.; Matus, M. H.; Nguyen, M. T.; Peterson, K. A.; Francisco, J. S. and Dixon, D. A. Thermodynamic Properties of the XO_2, X_2O, XYO, X_2O_2, and XYO_2 (X, Y = Cl, Br, and I) Isomers. J. Phys. Chem. A 2010, 114, 4254–4265.
30. Ornellas, F. R. Thermochemistry of New Molecular Species: SBr and HSBr. *J. Chem. Phys*. **2007**, 126,204314; DOI: 10.1063/1.2737776.
31. Peterson, K. A.; Shepler, B. C.; Figgen, D.; Stoll, H. On the Spectroscopic and Thermochemical Properties of ClO, BrO, IO, and Their Anions. *J. Phys. Chem. A* **2006**, *110*, 13877−13883.
32. Kim, H., Dooley, J. S.; Johnson, E. R. and North, S. W. Photodissociation of the BrO radical using velocity map ion imaging: Excited state dynamics and accurate $D_0{}^0$(BrO) evaluation. *J. Chem. Phys*. **2006**, *124*, 134304.
33. Denis, P. A. On the Performance of CCSD(T) and CCSDT in the Study of Molecules with Multiconfigurational Character: Halogen Oxides, HSO, BN and O_3. *Chem. Phys. Lett.* **2004**, *395*, 12−20.

34. Wilmouth, D. M.; Hanisco, T. F.; Donahue, N. M.; Anderson, J. G. Fourier Transform Ultraviolet Spectroscopy of the a A $^2\Pi_{3/2} \leftarrow X^2\Pi_{3/2}$ Transition of BrO. *J. Phys. Chem. A* **1999**, *103*, 8935−8945.
35. Chase, M. W., Jr. NIST-JANAF Thermochemical Tables, 4th ed.; *J. Phys. Chem. Ref. Data*, Monograph **1998**, *9*.
36. Bedjanian, Y.; LeBras, G.; Poulet, G. Kinetic Study of the Br+IO, I+BrO and Br+I_2 Reactions. Heat of Formation of the BrO Radical. *Chem. Phys. Lett*. **1997**, *266*, 233−238.
37. Orlando, J. J.; Tyndall, G. S. Rate Coefficients for the Thermal Decomposition of $BrONO_2$ and the Heat of Formation of $BrONO_2$. *J. Phys. Chem*. **1996**, *100*, 19398−19405.
38. Chase, M. W., "NIST-JANAF Thermochemical Tables for the Bromine Oxide," *J. Phys. Chem. Ref. Data* **1996**, *25*, 1069-1111.
39. Ganyecz, Á.; Csontos, J.; Nagy, B. and Kállay, M. Theoretical and Thermochemical Network Approaches To Determine the Heats of Formation for HO_2 and Its Ionic Counterparts. *J. Phys. Chem. A* **2015**,*119*,1164-1176.
40. Active Thermochemical Tables, http://atct.anl.gov/ (accessed October 13, 2014).
41. Goldsmith, C.F.; Magoon, G.R. and Green, W.H. Database of Small Molecule Thermochemistry for Combustion. *J. Phys. Chem. A* **2012**, *116*, 9033−9057.
42. Ruscic, B. Active Thermochemical Tables: version Alpha 1.110 of the Core (Argonne) Thermochemical Network, release date 04.02.2011.
43. da Silva, G. Kinetics and Mechanism of the Glyoxal + HO_2 Reaction: Conversion of HO_2 to OH by Carbonyls. *J. Phys. Chem. A* **2011**,*115*, 291-297.
44. Karton, A.; Daon, S.; Martin, J. M. L. W4-11: A high-confidence benchmark dataset for computational thermochemistry derived from first-principles W4 data. *Chem. Phys. Lett.* **2011**, *510*, 165–178.
45. A. Burcat, B. Ruscic, Third Millennium Ideal Gas and Condensed Phase Thermochemical Database for Combustion with Updates from Active Thermochemical Tables, Chemistry Division, Argonne National Laboratory, Argonne, Illinois, September 2005, (last update: March 15, 2010); this database is available in electronic form at: ftp://ftp.technion.ac.il/pub/supported/aetdd/thermodynamics.
46. Csaszar, A.G. and Furtenbacher, T. From a Network of Computed Reaction Enthalpies to Atom-Based Thermochemistry (NEAT). *Chem. Eur. J.* **2010**, *16*, 4826 – 4835.
47. Grant, D. J .; Dixon, D. A .; Francisco, J. S .; Feller, D .; Peterson, K. A . Heats of Formation of the $H_{1,2}O_mS_n$ (m, n = 0−3) Molecules from Electronic Structure Calculations. *J. Phys. Chem. A* **2009**,*113*, 11343–11353.
48. Karton, A.; Parthiban, S. and Martin, J.M.L. Post-CCSD(T) *ab Initio* Thermochemistry

of Halogen Oxides and Related Hydrides XOX, XOOX, HOX, XO_n, and HXO_n (X = F, Cl), and Evaluation of DFT Methods for These Systems. *J. Phys. Chem. A* **2009**, *113*, 4802–4816.

49. Active Thermochemical Tables (ATcT) using the Core (Argonne) Thermochemical Network Version 1.064. Harding, M. E.; Va´zquez, J.; Ruscic, B.; Wilson, A. K.; Gauss, J.; Stanton, J. F. *J. Chem. Phys.* **2008**, *128*, 114111. Ruscic, B.; Pinzon, R. E.; Morton, M. L.; Laszewski, G. v.; Bittner, S.; Nijsure, S. G.; Amin, K. A.; Minkoff, M.; Wagner, A. F. *J. Phys. Chem. A* **2004**, *108*, 9979. Ruscic, B.; Pinzon, R. E.; Laszewski, G. v.; Kodeboyina, D.; Burcat, A.; Leahy, D.; Montoya, D.; Wagner, A. F. *J. Phys. Conf. Ser.* **2005**, *16*, 561. Ruscic, B.; Pinzon, R. E.; Morton, M. L.; Srinivasan, N. K.; Su, M.-C.; Sutherland, J. W.; Michael, J. V. *J. Phys. Chem. A* **2006**, *110*, 6592.
50. Feller, D.; Peterson, K.; Dixon, D. A Survey of Factors Contributing to Accurate Theoretical Predictions of Atomization Energies and Molecular Structures. *J. Chem. Phys.* **2008**,*129*, 204105.
51. Ruscic, B.; Pinzon, R. E.; Morton, M. L.; Srinivasan, N. K.; Su, M.-C.; Sutherland, J. W.; Michael, J. V. Active Thermochemical Tables: Accurate Enthalpy of Formation of Hydroperoxyl Radical, HO_2. *J. Phys. Chem. A* **2006**,*110*, 6592-6601.
52. Tajti, A.; Szalay, P. G.; Csaszar, A. G.; Kállay, M.; Gauss, J.; Valeev, E. F.; Flowers, B. A.; Vázquez, J. and Stanton, J. F. HEAT: High accuracy extrapolated *ab initio* thermochemistry. *J. Chem. Phys*. **2004**, *121*, 11599 – 11613.
53. Flowers, B. A.; Szalay, P. G.; Vazquéz, J.; Stanton, J. F.; Kállay, M.; Gauss, J.; Császár, A. G. Benchmark Thermochemistry of the Hydroperoxyl Radical. *J. Phys. Chem. A* **2004**,*108*, 3195−3199.
54. Henry, D.J.; Parkinson, C.J. and Radom, L. *J. Phys. Chem. A* **2002**, *106*, 7927-7936.
55. Ramond, T.; Blanksby, S.; Kato, S.; Bierbaum, V.; Davico, G.; Schwartz, R.; Lineberger, W.; Ellison, G. Heat of Formation of the Hydroperoxyl Radical HOO Via Negative Ion Studies. *J. Phys. Chem. A* **2002**, *106*, 9641−9647.
56. Litorja, M.; Ruscic, B. A Photoionization Study of the Hydroperoxyl Radical, HO_2, and Hydrogen Peroxide, H_2O_2. *J. Electron Spectrosc. Relat. Phenom*. **1998**, *97*, 131−146.
57. Espinosa-Garcia, J. Theoretical Enthalpies of Formation of RO_x (R = H, CH_3; X = F, Cl, Br) Compounds. *Chem. Phys. Lett*. **1999**, *315*, 239−247.
58. Hills, A.J. and Howard, C.J. Rate coefficient temperature dependence and branching ratio for the OH+ClO reaction. J. Chem. Phys. 1984, 81, 4458. http://dx.doi.org/10.1063/1.447414.
59. Shum, L.; Benson, S. Review of the Heat of Formation of the Hydroperoxyl Radical. *J. Phys. Chem*. **1983**, *87*, 3479−3482.
60. Denis, P. A. Thermochemistry of the Hypobromous and Hypochlorous Acids, HOBr

and HOCl. *J. Phys. Chem. A* **2006**, *110*, 5887−5892.

61. Joens, J. A. The Dissociation Energy of OH($X^2\Pi_{3/2}$) and the Enthalpy of Formation of OH($X^2\Pi_{3/2}$), ClOH, and BrOH from Thermochemical Cycles. *J. Phys. Chem. A* **2001**, *105*, *11041−11044*.
62. Espinosa-Garcia, J. Theoretical Enthalpies of Formation of RO_x (R = H, CH_3; X = F, Cl, Br) Compounds. *Chem. Phys. Lett.* **1999**, *315*, 239−247.
63. Jursic, B. S. High Level *Ab Initio* and Density Functional Theory Study of Bond Dissociation Energy and Enthalpy of Formation for Hypochloric and Hypobromic Acids. *J. Mol. Struct.: THEOCHEM* **1999**, *467*, 173−179.
64. Messer, B. M.; Elrod, M. J.; Theoretical, A. Study of RO_x (R = H, CH_3; X = F, Cl, Br) Enthalpies of Formation, Ionization Potentials and Fluoride Affinities. *Chem. Phys. Lett*. **1999**, *301*, 10−18.
65. Hassanzadeh, P. and Irikura, K. K. Nearly *ab Initio* Thermochemistry: The Use of Reaction Schemes. Application to IO and HOI. *J. Phys. Chem. A* **1997**, *101*,1580.
66. Lock, M.; Barnes, R. J.; Sinha, A. Near-Threshold Photodissociation Dynamics of Hobr: Determination of Product State Distribution, Vector Correlation, and Heat of Formation. *J. Phys. Chem*. **1996**, *100*, 7972−7980.
67. Orlando, J. J.; Tyndall, G. S. Rate Coefficients for the Thermal Decomposition of $BrONO_2$ and the Heat of Formation of $BrONO_2$. *J. Phys. Chem*. **1996**, *100*, 19398−19405.
68. M.A. Grela, A.J. Colussi, *J. Phys. Chem*. **1996**, *100*, 10150.
69. Chase, M. W.; Davies, C. A.; Downey, J. R.; Frurip, D. J.; McDonald, R. A.; Syverud, A. N. *J. Phys. Chem. Ref. Data Suppl*.**1985**, 1.
70. DeMore, W.B.; Sander, S.P.; Golden, D.M. ; Hampson, R.F.; Kurylo, M.J.; Howard, C.J.; Ravishankara, A.R.; Kolb, C.E. and Molina, M. Chemical kinetics and Photochemical Data for Use in Stratospheric Modeling, Jet Propulsion Lab., Pasadena, CA, 1994, *JPL Publ*. 94-26.
71. Ruscic, B.; Berkowitz, J. Experimental determination of ΔH^0_f(HOBr) and ionization potentials (HOBr): Implications for corresponding properties of HOI. *J. Chem. Phys.* **1994**, *101*, 7795-7803.
72. McGrath, M.P. and Rowland, F.S. *J. Phys. Chem*. **1994**, *98*, 4773.

64: Messer, B. M.; Elrod, M. J.; Theoretical, A. Study of RO*x* (R = H, CH_3; X = F, Cl, Br) Enthalpies of Formation, Ionization Potentials and Fluoride Affinities. *Chem. Phys. Lett*. **1999**, *301*, 10−18.

73. Huie, R. E.; Laszlo, B. The Atmospheric Chemistry of Iodine Compounds. In Halon Replacements: Technology and Science; ACS Symposium Series 611; American Chemical Society: Washington, DC,1995; p 31.

74. Feller, D.; Peterson, K.A.; de John, W.A. and Dixon, D.A. Performance of coupled cluster theory in thermochemical calculations of small halogenated compounds. *J. Chem. Phys*. **2003**, *118*, 3510.
75. Cox, J. D., D. D. Wagman and V. A. Medvedev CODATA Key Values for Thermodynamics; Hemisphere Publishing Corp.: New York, 1989.
76. Gurvich, L. V., I. V. Veyts and C. B. Alcock Thermodynamic Properties of Individual Substances,, Fourth ed.; Hemisphere Publishing Corp.: New York, 1991; Vol. 2.
77. Morgon, N.H. Enthalpies of Formation of Phosphorus and Oxygen Compounds Determined by the Correlation Consistent Composite Approach. *Int. J. Quantum Chemistry* **2012**, *112*, 3256–3260.
78. Fabian, W. M. F.; Kalcher, J. and Janoschek, R. Stationary points on the energy hypersurface of the reaction $O_3 + H\bullet \rightarrow [\bullet O_3H]^* \leftrightarrows O_2 + \bullet OH$ and thermodynamic functions of $\bullet O_3H$ at G3MP2B3, CCSD(T)-CBS (W1U) and MR-ACPF-CBS levels of theory. *Theor. Chem. Acc*. **2005**, *114*, 182-188.
79. Ruscic, B.; Pinzon, R.E.; Morton, M.L.; von Laszevski, G.; Bittner, S.J.; Nijsure, S.G.; Amin, K. A.; Minkoff, M. and Wagner, A.F. Introduction to Active Thermochemical Tables: Several "Key" Enthalpies of Formation Revisited. *J. Phys. Chem. A* **2004**, *108*, 9979-9997.
80. Haworth, N.L. and Bacskay, G.B. Heats of formation of phosphorus compounds determined by current methods of computational quantum chemistry. *J. Chem. Phys*. **2002**, *117*, 11175.
81. Taniguchi, N.; Takahashi, K.; Matsumi, Y.; Dylewski, S.M.; Geiser, J.D. and Houston, P.L. Determination of the heat of formation of O_3 using vacuum ultraviolet laser-induced fluorescence spectroscopy and two-dimensional product imaging techniques. *J. Chem. Phys*. **1999**, *111*, 6350.
82. Gurvich, L. V., I. V. Veyts and C. B. Alcock Thermodynamic Properties of Individual Substances,, Fourth ed.; Hemisphere Publishing Corp.: New York, 1991; Vol. 2.
83. Ruscic, B.; Feller, D.; Peterson, K. A. Active Thermochemical Tables: Dissociation Energies of Several Homonuclear First-Row Diatomics and Related Thermochemical Values. *Theor. Chem. Acc*. **2014**, *133*, 1415/1−12.
84. Ruscic, B. Active Thermochemical Tables: Sequential Bond Dissociation Enthalpies of Methane, Ethane, and Methanol and the Related Thermochemistry. *J. Phys. Chem. A* **2015**, *119*,7810−7837.
85. Ruscic, B.; Wagner, A.F.; Harding, L.B.; Asher, R.L.; Feller, D.; Dixon, D.A.; Peterson, K.A.; Song, Y.; Qian, X.; Ng, C-Y.; Liu, J.; Chen, W. and Schwenke, D.W. On the Enthalpy of Formation of Hydroxyl Radical and Gas-Phase Bond Dissociation Energies of Water and Hydroxyl. *J. Phys. Chem. A* **2002**, *106*, 2727-2747.

86. Herbon, J.T.; Hanson, R.K.; Golden, D. M. and Bowman, C. T. Proceedings of the Combustion Institute, 2002, 29, 1201–1208.
87. Wiedmann, R.T.; Tonkyn, R.G. and White, M.G. Rotationally resolved threshold photoelectron spectra of OH and OD. *J. Chem. Phys*. **1992**, *97*, 768.
88. Pople, J.A.; Luke, B.T.; Frisch, M.J. and Binkley, J.S. Theoretical Thermochemistry. 1. Heats of Formation of Neutral AH, Molecules (A = Li to CI). *J. Phys. Chem*. **1985**, *89*, 2198-2203.
89. Barrow, R. F. *Ark. Fys*. **1956**, *11*, 281.
90. Pacios, L.F. and Geomez, P.C. Bonding in bromine oxides: Isomers of BrO_2, Br_2O_2 and BrO_3. *J. Mol. Struct. Theochem* **1999**, *467*, 223-231.
91. Lee, S.Y. Computational Study of Enthalpies of Formation of OXO (X = Cl, Br, and I) and Their Anions. *J. Phys. Chem. A* **2004**, *108*, 10754-10761.
92. Klemm, R. B.; Thorn, R.P.; Stief, L.J.; Buckley, T.J. and Johnson, R.D. Heat of Formation of OBrO: Experimental Photoionization Study. *J. Phys. Chem. A* **2001**, *105*, 1638-1642.
93. Alcami, M. and Cooper, I. L. *Ab initio* calculations on bromine oxide and dioxides and their corresponding anions. *J. Chem. Phys*. **1998**, *108*, 9414.
94. Workman, M.A. and Francisco, J.S. Molecular structure and energetics of BrO_x radicals (where x =1, 2, and 3). *Chem. Phys. Lett.* **1998**, *293*, 65–71.
95. Huie, R. E.; Laszlo, B. The Atmospheric Chemistry of Iodine Compounds. In Halon Replacements: Technology and Science; ACS Symposium Series 611; American Chemical Society: Washington, DC,1995; p 31.
96. Cottrell, T. L.The Strength of Chemical Bonds; Butterworth: London, 1954; P.221-81.
97. S. P. Sander, R. R. Friedl, D. M. Golden, M. J. Kurylo, R. E. Huie, V. L. Orkin, G. K. Moortgat, A. R. Ravishankara, C. E. Kolb, M. J. Molina and B. J.Finlayson-Pitts, JPL Publication 02-25, Chemical Kinetics and Photochemical Data for Use in Atmospheric Studies, Evaluation Number 14, National Aeronautics and Space Administration, Jet Propulsion Laboratory, California Institute of Technology.
98. Ruscic, B.; Feller, D.; Dixon, D.A.; Peterson, K.A.; Harding, L.B.; Asher, R.L. and Wagner, A.F. Evidence for a Lower Enthalpy of Formation of Hydroxyl Radical and a Lower Gas-Phase Bond Dissociation Energy of Water. *J. Phys. Chem. A* **2001**, *105*, 1-4.
99. Sander, S. P., J. Abbatt, J. R. Barker, J. B. Burkholder, R. R. Friedl, D. M. Golden, R. E. Huie, C. E. Kolb, M. J. Kurylo, G. K. Moortgat, V. L. Orkin and P. H. Wine "Chemical Kinetics and Photochemical Data for Use in Atmospheric Studies, Evaluation No. 17," JPL Publication 10-6, Jet Propulsion Laboratory, California Institute of Technology**,** Pasadena, 2011.
100. Santos, C. M. P.; Faria, R. B.; Machuca-Herrera, J. O.; Machado, S. D. Equilibrium

Geometry, Vibrational Frequencies, and Heat of Formation of HOBr, $HBrO_2$, and $HBrO_3$ Isomers. *Can. J. Chem.-Rev. Can. Chim.* **2001**, *79*, 1135−1144.

101. Aranda, A.; LeBras, G.; LaVerdet, G.; Poulet, G. The BrO + CH3O2 Reaction: Kinetics and Role in the Atmospheric Ozone Budget. *Geophys. Res. Lett*. **1997**, *24*, 2745−2748. 40: Active Thermochemical Tables, http://atct.anl.gov/ (accessed October 13, 2014).
102. Canneaux, S.; Hammaecher, C.; Cours, T.; Louis, F. and Ribaucour, M. Theoretical Study of H-Abstraction Reactions from CH_3Cl and CH_3Br Molecules by ClO and BrO Radicals. *J. Phys. Chem. A* **2012**, *116*, 4396−4408.
103. Ornellas, F. R. Thermochemistry of New Molecular Species: SBr and HSBr. *J. Chem. Phys.* **2007**, *126*, 204314; DOI: 10.1063/1.2737776.
104. Zheng, J.; Zhang, S.; Lynch, B. J.; Corchado, J. C.; Chuang, Y.-Y.; Fast, P. L.; Hu, W.-P.; Liu, Y.-P.; Lynch, G. C.; Nguyen, K. A. *et al*. POLYRATE version 2010-A (June, 2010), Copyright 1988-2010 D. G. Truhlar and Regents of the University of Minnesota, Minneapolis, Minnesota, U.S.A..
105. Klippenstein, S.J.; Wagner, A.F.; Robertson, S.H.; Dunbar, R.; Wardlaw, D.M. Variflex software, Version 1.0, http://chemistry.anl.gov/variflex
106. Greenwald, E.E.; North, S.W.; Georgievskii, Y.; Klippenstein, S.J. A Two Transition State Model for Radical-Molecule Reactions: A Case Study of the Addition of OH to C_2H_4. *J. Phys. Chem. A* **2005**, *109*, 6031-6044.
107. Georgievskii, Y.; Klippenstein, S.J. Long-range transition state theory. *J. Chem. Phys*. **2005**, *122*, 194103.
108. Zhang, P.; Klippenstein, S.J.; Law, C.K. Ab Initio Kinetics for the Decomposition of Hydroxybutyl and Butoxy Radicals of n-Butanol. *J. Phys. Chem. A* **2013**, *117*, 1890-1906.
109. Gilles, M.K.; Polak, M.L.; Lineberger, W.C. Photoelectron Spectroscopy of the Halogen Oxide Anions FO^-, ClO^-, BrO^-, IO^-, $OClO^-$, and OIO^-, *J. Chem. Phys.*, **1992**, *96*, 11, 8012.
110. Dyke, J.M.; Jonathan, N.B.H.; Morris, A.; Winter, M. Vacuum ultraviolet photoelectron spectroscopy of transient species. Part 13. Observation of the X^3A state of HO_2, *Mol. Phys.*, **1981**, *44*, 1059-1066.
111. R. Chow,M. Ng, D. K.W. Mok, E.P.F. Lee, and J.M. Dyke Rate coefficients of the Cl + CH3C(O)OCH3 → HCl + CH3C(O)OCH2 reaction at different temperatures calculated by transition state theory with ab initio and DFT reaction paths. *J. Phys. Chem. A* **2014**, *118*, 2040-2055.
112. Laidig, W. D.; Schaefer, H. F. *J. Chem. Phys*. **1981**, *74*, 3411.
113. Pacios, L.F.; Gomez, P.C. Bonding in bromine oxides: Isomers of BrO_2, Br_2O_2 and

BrO_3. *J. Mol. Struct. A* **1999**, *467*, 223-231.

114. Fernández-Ramos, A.; Miller, J. A.; Klippenstein, S. J.; Truhlar, D. G. Modeling the Kinetics of Bimolecular Reactions. *Chem. Rev.* **2006**, *106*, 4518-4584.

115. Fernandez-Ramos, A.; Ellingson, B. A ; Garret, B. C.; Truhlar, D. G. Variational transition state theory with multidimensional tunneling in Reviews in Computational Chemistry Vol. 23; Chapter 3 pp. 125-232, 2007 Lipkowitz, K. B.; Cundari, T. R. (Eds.) Wiley-VCH: Hoboken, NJ.

116. Hall, Jr., H. K.; Baldt, J. H. Thermochemistry of Strained-Ring Bridgehead Nitriles and Esters. *J. Am. Chem. Soc*. **1971**, *93*, 140.

117. M. Ng, D.K.W. Mok, E. P.F. Lee, and J. M. Dyke Rate coefficients of the $CF_3CHFCF_3 + H \rightarrow CF_3CFCF_3 + H_2$ reaction at different temperatures calculated by transition state theory with *ab initio* and DFT reaction paths. *J. Computational Chemistry* **2013**, *34*, 545-557.

Chapter 6.

Conclusion

The goal of this thesis was to establish reliable and practical methods to compute the rate coefficients with low and negative barriers. Generally, a theoretical study of reaction dynamics involves two parts. The first part involved the construction of the reaction surfaces using electronic structure theory calculations, namely *ab initio* methods and density functional theory (DFT) while the second part involved the calculation of rate coefficient using the transition state theory (TST) and its variant, the variational transition state theory (VTST), with the energetics and the reaction surfaces obtained in the first part. Two atmospherically important reactions were selected for the theoretical studies in this thesis, namely the $CH_3C(O)OCH_3$ + Cl reaction and the BrO + HO_2 reaction. Experimental studies showed that the former reaction had a small activation energy while the second one had a negative activation energy. There were some experimental studies for both reactions so the experimental rate coefficients of them were available before the theoretical studies began. The reliability of computationally methodologies employed in the two theoretical studies were assessed by comparing the computed rate coefficients with the experimental rate coefficients. In addition, some precautions in computing rate coefficients arose in these studies, which would be valuable for other coworkers in the same field who aimed to compute rate coefficients for reactions with similar nature in the future. In the rest of this chapter, the major findings of the two theoretical studies are briefly reviewed and they are followed by an overall summary on the main findings.

The $CH_3C(O)OCH_3$ + Cl reaction had only 1 channel, namely, the $CH_3C(O)OCH_3$ + Cl $\rightarrow$ $CH_3C(O)OCH_2$ + HCl reaction, which had an experimentally derived activation energy of 0.71 kcal.mol^{-1}. Various DFT functionals (B3LYP, BH&HLYP, M05, M06, M06-2X) and MP2 were employed as the lower level methods to obtain the molecular properties (vibrational frequencies and geometries) while the state-of-the-art ab initio method, UCCSD(T)-F12, were employed to obtain the reliable relative energies of the reaction surfaces. It was found that the vibrational frequency of a vibrational mode, the

C-H bond, changed dramatically along the reaction coordinate, leading to dramatic changes of the ΔZPE curve. Consequently, the maxima of the V_a^G versus reaction coordinate curves at all lower levels were all on the reactant side (s < 0), resulting in significant corrections of the threshold energies which were characterized by small $\kappa^{TST/CAG}$ factors. This effect was particularly prominent when the computed barrier height was low. The rate coefficients obtained with the $\kappa^{TST/CAG}$ factors, $k^{TST/CAG}$, had values which were comparable to the k^{CVT} values. This showed that the effect of the $\kappa^{TST/CAG}$ factor for correcting the threshold energy of the reaction was similar to the variational effects as in the VTST. With the consideration of the contribution of temperature to the reaction surfaces, Δ*G* versus *s* curves were considered instead of V_a^G versus *s* curves. The locations of the maxima of Δ*G* versus *s* curves at a certain temperature were far away from the saddle point, especially when the computed barrier heights were low. In order to obtain reliable rate coefficients, the choice of reaction coordinate had to cover the maxima of Δ*G* along the reaction coordinate. Typically, the barrier height of a reaction dominated the magnitude of the rate coefficients. However, for a reaction with a low barrier, it was found that the pre-exponential term, which was computed using vibrational frequencies and geometries (i.e. rotational constants) of the reactants and transition states, had an impact on the computed rate coefficients. Therefore, obtaining accurate barrier heights only was not adequate for obtaining accurate rate coefficients because the accuracies in geometrical parameters and vibrational frequencies also played important roles. In consideration of the availability of analytical energy derivatives and the system size of this reaction, MP2 was recommended for geometry optimizations and vibrational frequency calculations. Finally, a simple formula was devised to obtain a higher level VMEP curve by scaling the corresponding lower level VMEP curve. The best computed barrier height was 3.54 ± 0.90 kcal.mol^{-1} obtained at the UCCSD(T)-F12/CBS//MP/6-311++G** level in this study, which gave computed rate coefficients at ICVT/SCT level which were about an order of magnitude smaller than the experimental ones. Thus, the computed barrier height was adjusted to 1.34 kcal.mol^{-1} empirically in order to match the computed rate coefficients with the experimental rate coefficients.

For the BrO + HO_2 reaction, 5 channels were studied: (1a) HOBr + O_2 ($\tilde{X}^3\Sigma_g^-$), (1b) HOBr + O_2 ($\tilde{a}^1\Delta_g$), (2) HBr + O_3, (3) OBrO + OH, and (4) BrOO + OH. Some stationary points had moderate multi-reference characters so Brueckner theory was employed as the lower level in order to obtain reliable optimized geometries and

vibrational frequencies. For channel (1b), its transition state was treated as open-shell singlet species while it was treated as a close-shell singlet species in previous literature. It was found that channel (1b) had the lowest barrier height of -3.07 kcal.mol^{-1} at the BD(TQ)/CBS//M06-2X/AVDZ level hence it was the major channel. Since the computed barrier heights of channels (2), (3) and (4) are high (> 10 kcal.mol^{-1}), the productions of O_3 and OH in the atmosphere from this reaction were not likely and this conclusion was consistent with the experimental results. Due to the negative barrier height of the major channel, the contributions of the outer transition state and the inner transition state to the overall reactive flux had to be considered in order to obtain reliable rate coefficients for reaction with a negative barrier. The outer transition state was found to have little effects on the computed overall rate coefficient in the temperature range considered, 200-400 K, so the inner transition state was identified as the bottleneck of channel (1b). From the analyses of different contributions to the ΔG term, it was found that the entropy of activation determined the magnitude of the computed rate coefficients while the enthalpy of activation determined the temperature dependence of the computed coefficients. Rate coefficient calculations were also performed for channel (1a) and it was found that channel (1a) proceeded much slower than channel (1b) in the temperature range considered. The negative temperature dependence of the experimental rate coefficients was reproduced in the computed rate coefficients at the ICVT/SCT level of the major channel but the computed values were about an order of magnitude smaller than the experimental values. The discrepancies between the computed and the experimental rate coefficients were due to the inaccuracies in the vibrational frequencies and rotational constants because the magnitude of the computed rate coefficients was determined by the entropy of activation. Therefore, the entropy of activation played a more important role than the enthalpy of activation in channel (1b) of the BrO + HO_2 reaction.

In summary, the major findings of this work are summarized as follows:

- For a chemical reaction with a small or negative barrier, the large variational effects arising from the shape and the dip of a zero-point energy curve could be prominent. The true bottleneck of this type of reaction may not be necessarily located at the saddle point, so the CAG factor or variational transition state theory must be employed in order to obtain reliable rate coefficients (in Chapters 4 and 5).
- The maximum of the free energy versus reaction coordinate curve can be far away from the saddle point for a reaction with a low or negative barrier. The choice of

the range of IRC should cover the global maximum of the reaction profile in order to obtain reliable rate coefficients.

- The contribution of the entropy of activation to the free energy of activation can be significant in a chemical reaction with a low or negative barrier. Therefore, in addition to obtaining an accurate barrier height, the accuracies in both vibrational frequencies and rotational constants may also be crucial in obtaining accurate rate coefficients.
- For a chemical reaction with a negative barrier, the contributions of the two transition states (the inner and the outer transition states) to the overall reactive flux should be considered in calculating the overall rate coefficients using the Two transition state theory.
- Brueckner theory can be employed to provide a way for obtaining reliable electronic energies of species with moderate multi-reference characters.

Appendix. Supplementary Materials of the Theoretical Studies of the BrO with HO_2 reaction

Table A1 Experimental rate coefficients of the BrO + HO_2 reaction. (a)+(b) refers to the simultaneous measurements of the rate coefficients of reactions (a) and (b).

Authors (Year)	Technique	*P* (Torr)	*T* (K)	Reaction	*k* (cm^3/molecule-second)	Ref
Yung *et al*. (1980)	Photochemical modeling studies	760	298	(a)+(b)	4×10^{-12}	2
Cox and Sheppard (1982)	Molecular-modulation/UV-absorption	760	303	(a)+(b)	5×10^{-12}	3
Poulet *et al*. (1992)	Discharge flow/mass spectrometry	760	298	(a)+(b)	3.3×10^{-11}	4
Bridier *et al*. (1993)	Flash photolysis/UV absorption	760	298	(a)	3.4×10^{-11}	5
Mellouki *et al*. (1994)	Discharge flow / laser magnetic resonance	3	300	(b)	$\leq 1 \times 10^{-15}$	6
		3	441	(b)	$\leq 5 \times 10^{-17}$	
Larichev *et al*. (1995)	Discharge flow / mass spectrometry	1	233 - 344	(a)+(b)	$(4.77\pm0.32) \times 10^{-12}$ exp[(580±100)/T]	7
Elrod *et al*. (1996)	Turbulent flow / chemical ionization mass spectrometer	100	210 - 298	(a)	$(2.5\pm0.8) \times 10^{-12}$ exp[(520±80)/T]	8
Li *et al*. (1997)	Discharge flow / molecular beam mass spectrometry	1-3	233 - 348	(a)	$(3.13\pm0.33) \times 10^{-12}$ exp[(536±206)/T]	9
Cronkite *et al*. (1998)	Flash photolysis	12	298	(a)	$(2.0 \pm 0.6) \times 10^{-11}$	10
		25			$(2.0 \pm 0.6) \times 10^{-11}$	
Bedjanian *et al*. (2001)	Turbulent discharge flow / mass spectrometry	1	230 - 260	(a)+(b)	$(9.4\pm2.3) \times 10^{-12}$ exp[(345±60)/T]	11
Bloss *et al*. (2002)	Flash photolysis / time resolved UV spectroscopy	760	298	(a)	$(2.35\pm0.82) \times 10^{-11}$	12

Table A2 Heats of formation ($\Delta H_{f,298K;}$ 0 K values in square brackets; best computed values in *italics*) used for calculating the reaction enthalpy (ΔH_{298K}^{RX}) of the BrO + HO_2 reaction channels (1a,1b, 2,3 and 4).

kcal.mol^{-1}	$\Delta H_{f,298K}$	Reference	Remarks
BrO	30.8	29	from atomization energies at R/UCCSD(T)/CBS+CV+SR+SO)
	[32.6]	29	
	[31.4]	30	UCCSD(T)/CBS+CV+SO+rel+T+TQ from 31
	29.6± 0.4	31	from computed D_0 at UCCSD(T)/CBS+CV+SO+rel+T+TQ
	29.5±0.1	32	ion imaging D_0; quoted in 99
	[31.3±0.1]	32	
	30.4±1.0	33	CCSD(T)+CV+T+SO+rel
	30.2±0.4	34	FT-UV D_0; quoted in 102 suppl. material
	30.1±0.4	35	
	28.6±1.4	36	Quoted in 101
	30.4±2	37	average from most direct measurements
	30.1±0.6	38	Quoted in 45
	30.1±0.7		(average of all 298 K values, except 67)
HO_2	2.85±0.05	39	a thermo-chemical network, 14 experimental and 7 theoretical reaction enthalpies
	[3.55±0.05]	39	(as above)
	2.84±0.05	*39*	*CCSDTQP/CBS+SR+DBOA*
	2.93±0.04	40	ATcT; quoted in 39
	2.7±0.9	41	RQCISD(T)/cc-PV ∞ QZ//B3LYP/6-311++G(d,p) + bond additivity correction; previous values: 0.5 to 3.0 kcal.mol^{-1}
	2.9	42	Quoted in 41
	3.3	43	No reference given
	3.17	44	using W4.2 TAE_{0K}=165.98kcal.mol^{-1} and CODATA $\Delta H_{f,298K}$'s
	2.94±0.06	45	ATcT
	[3.61±0.55]	46	NEAT
	2.91±0.05	47	ATcT; quoted in 39
	2.96±0.14	48	W4.2; quoted in 45, 39

	2.91±0.05	49	ATcT; quoted in 47
	3.0±0.2	50	UCCSD(T)/CBS(Q;5)+CV+SR+SO; quoted in 47, 39
	2.94±0.06	51	ATcT; quoted in 48, 99, 39
	[3.58±1.5]	52	ATcT; quoted in 46
	2.96±0.10	53	CCSD(T)/aug-cc-pCV5Z; quoted in 39
	[3.97]	54	G3X-RAD
	3.2±0.5	55	Photoelectron detachment; quoted in 39
	3.3±0.8	56	photoionization mass spectrum.; quoted in 39
	2.32±0.72	35	
	4.0±0.6	57	MP4/TZ(2df,p)+post-MP4 correction
	3.0	58	From T dependent rate coefficients; quoted in 45
	3.5±1.0	59	Review; quoted in 39
	3.0±0.5		(averaged of all 298 K values, except the smallest 35, the largest MP4 57 values and earlier values quoted in 39 with large uncertainties)
HOBr	*-15.3±0.60*	*60*	*CCSD(T)+CV+T+SO+rel; quoted by 99*
	[-11.4±0.4]	61	Thermochemical cycle
	-15.2±1.1	62	Best average theoretical value
	-14.5	62	CCSD(T)/CBS
	-19.4	63	MP4/CBS//MP2/6-31G(d')
	[-14.8]	63	B3LYP/6-311G(3df,3pd); recommended
	-18.2	63	B3LYP/6-311G(3df,3pd)
	-17.5	64	G2
	-14.5±0.3	65	Recommended value; quoted in 102 suppl. Material and JPL-NASA (reference 99)
	-14.3±1	66	Quoted and favoured by 103 & 100; quoted by 60
	[-11.8±1]	66	
	-14.1±2	67	Average from most direct measurements
	-15.8	68	Bond additivity; quoted in 64
	[-10.9±1]	69	Quoted in 18 and 63
	-14±2	70	Quoted in 62
	-13.59±0.42	71	Corrected for ΔH_f(OH) given in 100; quoted in 65
	-13.9±0.5	71	Quoted by 60 as the accepted value

	-14.2	72	G2; quoted in 100
	-14.4±0.9		(average of 298 K values >-13.5 and <-15.5 kcal.mol^{-1})
O_2 ($\tilde{X}^3\Sigma_g^-$)	0		By definition for the ground $\tilde{X}^3\Sigma_g^-$ electronic state.
O_2 ($\tilde{a}^1\Delta_g$)	22.54±0.01	73	Infrared solar spectrum; quoted in 99
	22.54		
HBr	-8.64±0.04	45	ATcT
	-8.6	*74*	*CCSD(T)/CBS with aug-cc-pVnZ where n = T,Q, and 5*
	-8.71	35	Absorption spectrum
	-8.67±0.04	75	CODATA
	-8.67±0.04	76	Quoted in 45
	-8.66±0.06		(average of all 298 K values)
O_3	38.1	77	ccCA
	34.9	77	G3
	33.88±0.04	45	ATcT
	35.4	45	G3MP2B3
	36.8	*78*	*W1U; quoted in 77 and 45*
	33.87±0.01	79	ATcT; quoted in 99
	36.8	*80*	*CCSD(T)/CBS+SR//B3LYP/6-31G(2df,p); quoted in 77*
	33.89	81	VUV laser-induced fluorescence spectroscopy
	34.1	35	calorimetric measurements
	33.9±0.5	82	Calorimetric measurement of the enthalpy of dissociation (O_3)
	33.9	76	Quoted in 45
	34.7±2.0		(average of all 298 K values; except the ccCA value)
OH	8.96±0.01	83; 84	ATcT (agree with earlier values in Ref. 30 and 31)
	8.9±0.9	41	RQCISD(T)/cc-PV ∞ QZ//B3LYP/6-311++G(d,p) + bond additivity correction; previous values: 8.9 to 9.4 kcal.mol^{-1}
	9.0	42	ATcT; quoted in 41
	8.89±0.09	42	Position ion cycle (photoionization and photoelectron measurements) for 98
	8.93±0.01	45	ATcT
	8.91± 0.07	85	Recommended value at 298 K; quoted in 45

	[8.85±0.07]	85	Recommended value at 0 K
	[8.85±0.18]	85	CCSD(T)(FC)/CBS with unc-cc-pVnZ basis set; FCI for further corrections in the atomization energy.
	[8.85±0.18]	85	PIMS experiment
	[8.86±0.18]	85	PFI-PE30 experiment
	[8.83±0.12]	85	PFI-PEPICO experiment
	[8.92±0.03]	85	photodissociation of water
	8.92±0.16	86	Shock tube measurement
	[8.68]	54	W2
	9.319	35	
	[9.18±0.29]	35	Spectroscopic determination
	[8.83±0.18]	87	Positive ion cycle
	8.89±0.09	82	D_0(H-OH)
	[9.35±0.05]	76	Spectroscopic determination of D_0(OH)
	9.8	88	MP4/6-311+G(2df,p)//UHF/6-31G(d)
	[9.26±0.29]	89	measurement of D_0(OH, $A^2\Sigma^+$); quoted in 98
	8.97±0.35		(average of all 298 K values; except the MP4 value of 88)
BrOO	*28.9±1.5*	*29*	RCCSD(T)/CBS(Q5)+CV+SR+SO; quoted in 97
	26±1	90	CCSD(T)/AREP/TZ(2df)//UMP2/AREP/TZ(2df); quoted in 29
	[28±1]	90	
	26.0±9.6	38	Based on a trend analysis of $\Delta_fH_0°$(OClO)/$D_0°$(ClO) and the accepted value of $D_0°$(BrO); quoted in 45 and 97 from 38.
	[27.8±9.6]	38	
	27.0±1.9		(average of all 298 K values)
OBrO	*40.6±1.5*	*29*	RCCSD(T)/CBS(Q5)+CV+SR+SO; also in 99
	39.2±1.7	91	CCSD(T, Full)/6-311+G(3d,f)
	39.2±1.1	92	From appearance energy of BrO^+ from OBrO; quoted in 99
	[41.4±1.0]	92	
	[39.6±1.9]	92	Corrected G2 value of 93 (spin-orbit contribution for BrO).
	38.9±1.9	92	Corrected CCSD(T) value of ref. 19 (spin-orbit contribution for BrO).

	[39.4±1.9]	92	As above
	30±3	90	CCSD(T)/AREP/TZ(2df)//UMP2/AREP/TZ(2df); quoted in 29
	[32±3]	90	
	[37.5]	93	G2; quoted in 92
	34.4±3	94	CCSD(T)/6-311+G(3df)//CCSD(T)/6-311G(2df); quoted in 92
	[34.5±3]	94	
	36.3±6.0	38	Quoted in 45 from 38.
	39.2±1.1	38	Quoted in 97 from 38.
	[38.6±6]	38	Based on a trend analysis of $\Delta_fH_0°$(OClO)/$D_0°$(ClO) and the accepted value of $D_0°$(BrO); quoted in 92
	[31.55]	95	Quoted in 92; estimated from $\Delta G(BrO_2(aq))$
	[20.79]	96	Quoted in 92; derived from D(O-BrO)
	39.4±1.2		(average of all 298 K values, except the values of 38 (the lower value of 36.3), 90 & 94)
ΔH_{298K}^{RX} (channel (1))	-47.5±2.1		using the averaged $\Delta H_{f,298K}$ values
	-47.7±1.1		using the best theoretical $\Delta H_{f,298K}$ values
	-47.7		(present study; UCCSD(T)/CBS + SO(BrO))
	-47.5		(present study; BD(TQ)/CBS + SO(BrO))
ΔH_{298K}^{RX} (channel (1))	-25.0±2.1		using $\Delta H_{f,298}$ of O_2 $\tilde{a}^1\Delta_g$ =22.5 kcal.mol^{-1} from 99
	-25.2±1.5		using the best theoretical $\Delta H_{f,298K}$ values
	-25.0		(present study; BD(TQ)/CBS + SO(BrO))
ΔH_{298K}^{RX} (channel 2)	-7.1±3.3		using the averaged $\Delta H_{f,298K}$ values
	-4.2(>±0.5)		using the best theoretical $\Delta H_{f,298K}$ values
	-4.3		(present study; BD(TQ)/CBS + SO(BrO))
ΔH_{298K}^{RX} (channel 3)	15.3±2.8		using the averaged $\Delta H_{f,298K}$ values
	17.1±2.0		using the best theoretical $\Delta H_{f,298K}$ values
	14.9		(present study; BD(TQ)/CBS + SO(BrO))
ΔH_{298K}^{RX} (channel 4)	2.9±3.5		using the averaged $\Delta H_{f,298K}$ values
	5.4±2.0		using the best theoretical $\Delta H_{f,298K}$ values
	5.9		(present study; BD(TQ)/CBS + SO(BrO))

Table A3 Computed relative energies (kcal.mol^{-1}) of the reactant complex (RC), transition state (TS) (ΔE(0K)) for relative energy of TS with zero-point correction), product complex (PC), separate products (ΔE^{RX}), and reaction enthalpy at 298 K ($\Delta H_{298K}{}^{RX}$) with respect to the separate reactants, of channel (1a) BrO + HO_2 → HOBr + O_2 ($\tilde{X}^3\Sigma_g^-$) obtained at different levels (all values in the table have been corrected for a spin-orbit correction in BrO) [a]. All relative energies are obtained at the CCSD(T)/CBS//M06-2X/AVDZ level apart from the relative energy of the TS which is obtained at the BD(TQ)/CBS//BD/AVDZ level.

Level	RC	TS	ΔE(0K)	PC	ΔE^{RX}	$\Delta H_{298K}{}^{RX}$
M06-2X/AVDZ	-5.07	-5.06	-4.01[b]	-52.26	-50.89	-50.4[d]
BD/AVDZ		-1.74	-1.78[c]		-49.62	-49.1[e]
BD/AVTZ		4.24	4.19[c]		-48.24	-47.8[e]
BD/AVQZ		4.47	4.42[c]		-48.54	-48.1[e]
BD(T)/AVTZ// BD/AVDZ		2.11	2.06[c]		-47.82	-47.3[e]
BD(T)/AVQZ// BD/AVDZ		2.25	2.20[c]		-47.99	-47.5[e]
BD(T)/CBS// BD/AVDZ		2.35[f]	2.30[c,f]		-47.91[g]	-47.4[e]
BD(TQ)/AVTZ// BD/AVDZ		2.35	2.30[c]		-47.19	-46.7[e]
(Q) contribution[h]		0.22			-0.050	
Composite BD(TQ)/CBS[i]// BD/AVDZ		2.58	2.53[c]		-47.96	-47.5[e]
CCSD(T)/AVTZ// M06-2X/AVDZ	-4.02			-48.96	-47.38	-46.9[d]
CCSD(T)/AVQZ// M06-2X/AVDZ	-3.83			-49.33	-47.86	-47.3[d]
CCSD(T)/CBS// M06-2X/AVDZ (1/X^3:AVTZ/AVQZ)[j]	-3.68			-49.62	-48.20	-47.7[d]
Best estimates	-3.68	2.58	2.53[c]	-49.62	-47.96 -47.46[k]	-47.5[e]

[a] For BrO, the ground electronic state is $\tilde{X}^2\Pi$, and the experimental equilibrium spin-orbit (SO) separation between the $\tilde{X}\ ^2\Pi_{1/2}$ and $\tilde{X}\ ^2\Pi_{3/2}$ states is 975.43 cm^{-1} (or 2.7889 kcal.mol^{-1}) (ref.32). Using this SO splitting, the $\tilde{X}\ ^2\Pi_{3/2}$ SO state of BrO is lower than the unperturbed $\tilde{X}^2\Pi$ state by 1.39 kcal.mol^{-1}.

[b] The zero-point energy corrections were computed at M06-2X/AVDZ level.

[c] The zero-point energy corrections were computed at BD/AVDZ level.

[d] Using $\Delta ZPE+\Delta E_{298K}^{vib}$ from M06-2X frequency calculations (=0.505 kcal.mol^{-1})

[e] Using $\Delta ZPE+\Delta E_{298K}^{vib}$ from BD frequency calculations (=0.474 kcal.mol^{-1})

[f] The BD(T)/CBS value was obtained by using the $1/X^3$ formula with the reaction energy at BD(T)/AVTZ and BD(T)/AVQZ levels respectively.

[g] The BD(T)/CBS value was taken as the average of the relative energy at BD(T)/AVTZ and BD(T)/AVQZ levels respectively (see text).

[h] The (Q) contribution was calculated as: BD(TQ)/AVTZ – BD(T)/AVTZ

[i] Assuming additivity in a composite approach: BD(TQ)/CBS = BD(T)/CBS + (Q)

[j] The CCSD(T)/CBS value was obtained by using the $1/X^3$ formula with the reaction energy at CCSD(T)/AVTZ and CCSD(T)/AVQZ levels respectively.

[k] Zero-point corrected value computed by using frequencies obtained at BD/AVDZ level

Table A4 Computed spin densities with unrestricted wavefunctions of all atoms in the transition state of channel (1b).

Levels of theory	Atom				
	Br	O	H	O	O
M06-2X/AVDZ	0.365983	0.525253	-0.011192	-0.273028	-0.607017
BD/AVDZ	0.337768	0.404465	-0.026403	-0.220575	-0.495256
BD(T)/AVTZ// M06-2X/AVDZ	0.370982	0.565513	-0.015772	-0.242201	-0.678522
BD(T)/AVTZ// BD/AVDZ	0.000000	0.000000	0.000000	0.000000	0.000000
BD(T)/AVQZ// M06-2X/AVDZ	0.368173	0.569491	-0.011449	-0.255235	-0.670981
BD(T)/AVQZ// BD/AVDZ	0.000000	0.000000	0.000000	0.000000	0.000000

Table A5 Computed relative energies (kcal.mol^{-1}) of the reactant complex (RC), transition state (TS) (ΔE(0K)) for relative energy of TS with zero-point correction), separate products (ΔE^{RX}), and reaction enthalpy at 298 K ($\Delta H_{298K}{}^{RX}$) with respect to the separate reactants, of channel (1b) BrO + HO_2 → HOBr + O_2 ($\tilde{a}^1\Delta_g$) obtained at different levels, used in the calculations of rate coefficients (all values in the table have been corrected for a spin-orbit correction in BrO) [a] .All relative energies are obtained at the CCSD(T)/CBS//M06-2X/AVDZ level apart from the relative energy of the TS which is obtained at the composite BD(TQ)/CBS level.

Level	RC	TS[b]	ΔE(0K)[c,d]	ΔE^{RX} [a]	$\Delta H_{298K}{}^{RX}$
M06-2X/AVDZ	-5.07	-3.50	-3.47	-36.81	-36.3[e]
BD/AVDZ		-3.50 ; (2.05)	-3.52 ; (0.97)	-26.97[f]	-26.6[f,g]
BD/AVTZ		-0.49; (15.58)	-0.51 ; (14.50)	-25.81[h]	-25.3[e,h]
BD/AVQZ		-0.44; (15.86)	-0.46 ; (14.78)	-26.11[h]	-25.6[e,h]
BD(T)/AVTZ	-4.35	-3.32; (2.93)	-3.34 ; (1.85)	-25.18[h]	-24.7[e,h]
BD(T)/AVQZ	-4.25	-3.38; (3.10)	-3.40 ; (2.02)	-25.31[h]	-24.8[e,h]
BD(T)/CBS (1/X^3 :AVTZ/AVQZ)	-4.18	-3.42; (3.23)	-3.44 ; (2.15)	-25.48[h]	-25.0[e,h]
BD(TQ)/AVTZ	-4.20	-2.95; (4.21)	-2.97 ; (3.13)	-25.23[h]	-24.7[e,h]
(Q) contribution[i]	0.15	0.37; (1.28)		-0.050[h]	
Composite BD(TQ)/CBS[j]	-4.03	-3.05; (4.52)	-3.07; (3.43)	-25.53[h]	-25.0[e,h]
CCSD(T)/AVTZ// M06-2X/AVDZ				-24.75	-24.2[e]
CCSD(T)/AVQZ// M06-2X/AVDZ				-25.22	-24.7[e]
CCSD(T)/CBS// M06-2X/AVDZ (1/X^3 :AVTZ/AVQZ)				-25.50	-25.0[e]
Best estimates	-4.03	-3.05; (4.52)	-3.07 ; (3.43)	-25.53 -25.03[k]	-25.0[e,h]

[a] For BrO, the ground electronic state is $\tilde{X}^2\Pi$, and the experimental equilibrium spin-orbit (SO) separation between the $\tilde{X}\ ^2\Pi_{1/2}$ and $\tilde{X}\ ^2\Pi_{3/2}$ states is 975.43 cm^{-1} (or 2.7889 kcal.mol^{-1}) (ref.32). Using this SO splitting, the $\tilde{X}\ ^2\Pi_{3/2}$ SO state of BrO is lower than the unperturbed $\tilde{X}^2\Pi$ state by 1.39 kcal.mol^{-1}.

[b] The first value was computed with M06-2X/AVDZ geometries, while the second value was computed with BD/AVDZ geometries. Note that at BD/AVDZ geometries, the computed spin densities with the AVTZ and AVQZ basis sets suggest that they are closed-shell singlet states, resulting in unreliable relative energies.

[c] The ZPE in the ΔE(0K) calculation of the first value was computed with the M06-2X/AVDZ geometry whereas the ZPE in the ΔE(0K) calculation of the value in brackets was computed with the BD/AVDZ geometry.

[d] Using computed O_2 ($\widetilde{X}^3\Sigma_g^-$) energies and the $\widetilde{X}^3\Sigma_g^-$-$\tilde{a}^1\Delta_g$ separation of 7918.1 cm^{-1} (=22.639 $kcal.mol^{-1}$) from spectroscopic T_e (ref.30).

[e] Using $\Delta ZPE+\Delta E_{298K}^{vib}$ from M06-2X frequency calculations (=0.505 $kcal.mol^{-1}$)

[f] Electronic energies computed with optimized geometries at BD/AVDZ level

[g] Using $\Delta ZPE+\Delta E_{298K}^{vib}$ from BD frequency calculations (=0.372 $kcal.mol^{-1}$)

[h] Electronic energies computed with optimized geometries at M06-2X/AVDZ level

[i] The (Q) contribution was calculated as: BD(TQ)/AVTZ – BD(T)/AVTZ

[j] Assuming additivity in a composite approach: BD(TQ)/CBS = BD(T)/CBS + (Q)

[k] Zero-point corrected value computed by using frequencies obtained at M06-2X/AVDZ level

Table A6 Computed relative energies (kcal.mol^{-1}) of the intermediate, transition state (TS) (ΔE(0K)) for relative energy of TS with zero-point correction), separate products (ΔE^{RX}), and reaction enthalpy at 298 K (ΔH_{298K}^{RX}) with respect to the separate reactants, of channel (2) BrO + $HO_2 \rightarrow$ HBr + O_3 obtained at different levels (all values in the table have been corrected for a spin-orbit correction in BrO) [a].

Level	Intermediate	TS	ΔE(0K)[b]	ΔE^{RX}	ΔH_{298K}^{RX} [c]
M06-2X/AVDZ	-20.81	16.55	15.65	7.09	5.8
BD(T)/AVTZ// M06-2X/AVDZ	-19.57	12.36	11.47	-3.35	-4.7
BD(T)/AVQZ// M06-2X/AVDZ	-20.01	11.17	10.27	-3.71	-5.0
BD(T)/CBS// M06-2X/AVDZ (1/X^3 :AVTZ/AVQZ)	-18.94	10.30	9.40	-3.97	-5.3
BD(TQ)/AVTZ// M06-2X/AVDZ	-18.81	13.89	12.99	-2.38	-3.7
(Q) contribution[d]	0.76	1.52		0.97	
Composite BD(TQ)/CBS[e]// M06-2X/AVDZ	-19.57	11.83	10.93	-3.00	-4.3
Best estimates	-19.57	11.83	10.93	-3.00 -4.32[f]	-4.3

[a] For BrO, the ground electronic state is $\tilde{X}^2\Pi$, and the experimental equilibrium spin-orbit (SO) separation between the $\tilde{X}\ ^2\Pi_{1/2}$ and $\tilde{X}\ ^2\Pi_{3/2}$ states is 975.43 cm^{-1} (or 2.7889 kcal.mol^{-1}) (ref.32). Using this SO splitting, the $\tilde{X}\ ^2\Pi_{3/2}$ SO state of BrO is lower than the unperturbed $\tilde{X}^2\Pi$ state by 1.39 kcal.mol^{-1}

[b] The zero-point energy corrections are computed at M06-2X/AVDZ level.

[c] Using $\Delta ZPE+\Delta E_{298K}^{vib}$ from M06-2X frequency calculations (=-1.33 kcal.mol^{-1}).

[d] The (Q) contribution was calculated as: BD(TQ)/AVTZ – BD(T)/AVTZ

[e] Assuming additivity in a composite approach: BD(TQ)/CBS = BD(T)/CBS + (Q)

[f] Zero-point corrected value computed by using frequencies obtained at M06-2X/AVDZ level

Table A7 Computed relative energies (kcal.mol^{-1}) of the transition state (TS) (ΔE(0K)) for relative energy of TS with zero-point correction), separate products (ΔE^{RX}), and reaction enthalpy at 298 K (ΔH_{298K}^{RX}) with respect to the separate reactants, of channel (3) BrO + HO_2 → OBrO + OH obtained at different levels (all values in the table have been corrected for a spin-orbit correction in BrO) [a] .

Level	TS	ΔE(0K)[b]	ΔE^{RX}	ΔH_{298K}^{RX} [c]
M06-2X/AVDZ	49.63	49.01	31.50	29.9
BD(T)/AVTZ// M06-2X/AVDZ	33.35	32.73	15.55	13.9
BD(T)/AVQZ// M06-2X/AVDZ	33.58	32.96	14.92	13.3
BD(T)/CBS// M06-2X/AVDZ (1/X^3:AVTZ/AVQZ)	33.75	33.13	14.47	12.9
BD(TQ)/AVTZ// M06-2X/AVDZ	35.20	34.58	17.59	16.0
(Q) contribution[d]	1.85		2.04	
BD(TQ)/CBS[e] // M06-2X/AVDZ	35.60	34.98	16.51	14.9
Best estimates	35.60	34.98	16.51, 14.65[f]	14.9

[a] For BrO, the ground electronic state is $\tilde{X}^2\Pi$, and the experimental equilibrium spin-orbit (SO) separation between the $\tilde{X}\ ^2\Pi_{1/2}$ and $\tilde{X}\ ^2\Pi_{3/2}$ states is 975.43 cm^{-1} (or 2.7889 kcal.mol^{-1}) (ref.32). Using this SO splitting, the $\tilde{X}\ ^2\Pi_{3/2}$ SO state of BrO is lower than the unperturbed $\tilde{X}^2\Pi$ state by 1.39 kcal.mol^{-1}. (this correction has been made to all values this table).

[b] The zero-point corrections were computed at M06-2X/AVDZ level.

[c] Using $\Delta ZPE+\Delta E_{298K}^{vib}$ from M06-2X frequency calculations (=-1.614 kcal.mol^{-1}).

[d] The (Q) contribution was calculated as: BD(TQ)/AVTZ – BD(T)/AVTZ

[e] Assuming additivity in a composite approach: BD(TQ)/CBS = BD(T)/CBS + (Q)

[f] Zero-point corrected value computed by using frequencies obtained at M06-2X/AVDZ level.

Table A8 Computed relative energies (kcal.mol^{-1}) of the transition state (TS) (ΔE(0K)) for relative energy of TS with zero-point correction), separate products (ΔE^{RX}), and reaction enthalpy at 298 K ($\Delta H_{298K}{}^{RX}$) with respect to the separate reactants, of channel (4) BrO + HO_2 → BrOO + OH (all values in the table have been corrected for a spin-orbit correction in BrO) [a].

Level	TS	ΔE(0K)[b]	ΔE^{RX}	$\Delta H_{298K}{}^{RX}$ [, c]
M06-2X/AVDZ	42.05	42.44	-3.69	-4.9
BD(T)/AVTZ// M06-2X/AVDZ	34.63	35.02	4.98	3.8
BD(T)/AVQZ// M06-2X/AVDZ	35.59	35.99	6.40	5.2
BD(T)/CBS// M06-2X/AVDZ	36.29	36.69	7.44	6.3
BD(TQ)/AVTZ// M06-2X/AVDZ	35.75	36.15	6.04	4.9
(Q) contribution[d]	1.12		-0.33	
BD(TQ)/CBS[e]// M06-2X/AVDZ	37.41	37.81	7.11	5.9
Best estimates	37.41	37.81	7.11, 5.12[f]	5.9

[a] For BrO, the ground electronic state is $\widetilde{X}^2\Pi$, and the experimental equilibrium spin-orbit (SO) separation between the $\widetilde{X}\ ^2\Pi_{1/2}$ and $\widetilde{X}\ ^2\Pi_{3/2}$ states is 975.43 cm^{-1} (or 2.7889 kcal.mol^{-1}) (ref.32). Using this SO splitting, the $\widetilde{X}\ ^2\Pi_{3/2}$ SO state of BrO is lower than the unperturbed $\widetilde{X}^2\Pi$ state by 1.39 kcal.mol^{-1}.

[b] The zero-point corrections were computed at M06-2X/AVDZ level.

[c] Using $\Delta ZPE+\Delta E_{298K}{}^{vib}$ from M06-2X frequency calculations (=-1.185 kcal.mol^{-1}).

[d] The (Q) contribution was calculated as: BD(TQ)/AVTZ – BD(T)/AVTZ

[e] Assuming additivity in a composite approach: BD(TQ)/CBS = BD(T)/CBS + (Q)

[f] Zero-point corrected value computed by using frequencies obtained at M06-2X/AVDZ level.

Table A9 Computed reaction enthalpies at the highest level in this work (BD(TQ)/CBS + SO(BrO)), reference 16 at CCSD(T)/6-311G** and literature values at various levels of theory (c.f. Table 5.1 in the Supplementary Material) and experimental reaction enthalpies in kcal.mol^{-1} of the five channels (1a,1b,2,3,4) of the BrO + HO_2 reaction.

Channel	Level	ΔH_{298K}	Reference
(1a) $BrO + HO_2 \rightarrow HOBr + O_2$ ($^3\Sigma_g^-$)	Experimental	-45.1	8
	BD(TQ)/CBS + SO(BrO)[a]	-47.5	This work
	CCSD(T)/CBS + SO(BrO)[a]	-47.7	This work
	CCSD(T)/6-311G** + SO(BrO)[a]	-51.4	99
	Best theoretical value from literature	-47.7±1.1	
	Average literature values	-47.5±2.1	
(1b) $BrO + HO_2 \rightarrow HOBr + O_2$ ($\tilde{a}^1\Delta_g$)	Experimental	-25.0±2.1	8,51
	BD(TQ)/CBS + SO(BrO)[a]	-25.0	This work
	CCSD(T)/6-311G** + SO(BrO)[a]	-36.4	99
	Best theoretical value from literature	-25.2±1.5	
	Average literature values	-25.0±2.1	
(2) $BrO + HO_2 \rightarrow HBr + O_3$	Experimental	-7.7	8
	BD(TQ)/CBS + SO(BrO)[a]	-4.3	This work
	CCSD(T)/6-311G** + SO(BrO)[a]	-7.7	99
	Best theoretical value from literature	-4.2(>±0.5)	
	Average literature values	-7.1±3.3	
(3) $BrO + HO_2 \rightarrow OBrO + OH$	BD(TQ)/CBS + SO(BrO)[a]	14.9	This work
	Best theoretical value from literature	17.1±2.0	
	Average literature values	15.3±2.8	
(4) $BrO + HO_2 \rightarrow BrOO + OH$	BD(TQ)/CBS + SO(BrO)[a]	5.9	This work
	Best theoretical value from literature	5.4±2.0	
	Average literature values	2.9±3.5	

[a] For BrO, the ground electronic state is $\tilde{X}^2\Pi$, and the experimental equilibrium spin-orbit (SO) state separation between the $\tilde{X}\ ^2\Pi_{1/2}$ and $\tilde{X}\ ^2\Pi_{3/2}$ states is 975.43 cm^{-1} (or 2.7889 kcal.mol^{-1}) [28].

Using this SO splitting, the $\widetilde{X}\ ^2\Pi_{3/2}$ SO state of BrO is lower than the unperturbed $\widetilde{X}^2\Pi$ state by 1.39 kcal.mol^{-1}.

Table A10 Computed (BD(TQ)/CBS//M06-2X/AVDZ incl. SO correction for BrO) k_{outer} , k_{inner} and $k_{overall}$ values in $cm^3.molecule^{-1}s^{-1}$ of channel (1b) BrO + HO_2 → HOBr + O_2 ($\tilde{a}^1\Delta_g$) at 200 – 400 K. k_{outer}, k_{inner} were calculated from PST and *E*,*J*-TST respectively using VARIFLEX and $k_{overall(i)}$ was calculated using equation (5.1).

T (K)	k_{outer}	k_{inner} [(a)]	$k_{overall(i)}$
200	2.49E-10	7.39E-11	5.70E-11
210	2.51E-10	5.23E-11	4.33E-11
220	2.52E-10	3.83E-11	3.33E-11
230	2.54E-10	2.89E-11	2.60E-11
240	2.55E-10	2.24E-11	2.06E-11
250	2.57E-10	1.78E-11	1.67E-11
260	2.58E-10	1.44E-11	1.37E-11
270	2.59E-10	1.19E-11	1.14E-11
280	2.6E-10	9.98E-12	9.61E-12
298	2.62E-10	7.53E-12	7.32E-12
300	2.63E-10	7.31E-12	7.12E-12
310	2.63E-10	6.37E-12	6.22E-12
320	2.64E-10	5.61E-12	5.50E-12
330	2.65E-10	4.99E-12	4.90E-12
340	2.66E-10	4.48E-12	4.40E-12
350	2.67E-10	4.04E-12	3.98E-12
360	2.67E-10	3.68E-12	3.63E-12
370	2.68E-10	3.37E-12	3.33E-12
380	2.68E-10	3.11E-12	3.07E-12
390	2.69E-10	2.88E-12	2.85E-12
400	2.69E-10	2.68E-12	2.65E-12

(a) The barrier height used in E,J-TST calculations is the zero-point corrected barrier height

Table A11 Computed (BD(TQ)/CBS//M06-2X/AVDZ incl. SO correction for BrO) k_{inner} values calculated with the *E,J*-TST (with VARIFLEX) and TST (with POLYRATE) methods in $cm^3.molecule^{-1}s^{-1}$ for channel (1b) $BrO + HO_2 \rightarrow HOBr + O_2(\tilde{a}^1\Delta_g)$ at 200 – 400 K. [(a)]

T (K)	*E,J*-TST	TST [(b)]
200	7.39E-11	6.65E-11 (7.04E-11)
210	5.23E-11	4.69E-11
220	3.83E-11	3.43E-11
230	2.89E-11	2.59E-11
240	2.24E-11	2.00E-11
250	1.78E-11	1.59E-11
260	1.44E-11	1.28E-11
270	1.19E-11	1.06E-11
280	9.98E-12	8.86E-12
298	7.53E-12	6.67E-12 (6.93E-12)
300	7.31E-12	6.48E-12
310	6.37E-12	5.64E-12
320	5.61E-12	4.96E-12
330	4.99E-12	4.41E-12
340	4.48E-12	3.95E-12
350	4.04E-12	3.57E-12
360	3.68E-12	3.25E-12
370	3.37E-12	2.97E-12
380	3.11E-12	2.74E-12
390	2.88E-12	2.54E-12
400	2.68E-12	2.36E-12 (2.43E-12)

(a) ΔZPE is included in the barrier height (of -3.07 $kcal.mol^{-1}$) used in the VARIFLEX (*E,J*-TST) calculations (column 2) but not in the POLYRATE (TST) calculations (column 3), which use the classical barrier height (-3.05 $kcal.mol^{-1}$).

(b) Values shown in brackets at 200, 298 and 400 K (in column 3) are from conventional TST calculations (with POLYRATE) with a barrier height (-3.07 $kcal.mol^{-1}$) which is -3.05 $kcal.mol^{-1}$ plus the ΔZPE contribution. These results show that the difference between the *E,J*-TST and TST results shown in the table arises from (i) a difference in the barrier height used as well as (ii) the microcanonical treatment of the reactants and TS in the *E,J*-TST method compared to a Boltzmann distribution in the reactants and TS used in the conventional TST method.

Table A12 Computed (BD(TQ)/CBS//M06-2X/AVDZ incl. SO correction for BrO) values of k_{inner} at various VTST levels (TST, CVT and ICVT) with and without CAG correction in $cm^3.molecule^{-1}s^{-1}$ for channel (1b) $BrO + HO_2 \rightarrow HOBr + O_2(\tilde{a}^1\Delta_g)$ at 200 – 400 K, calculated with POLYRATE.

T (K)	TST	TST/CAG	CVT	CVT/CAG	ICVT
200	6.645E-11	7.4903E-12	8.462E-12	8.0651E-12	8.4618E-12
210	4.69E-11	5.8658E-12	6.5949E-12	6.298E-12	6.5947E-12
220	3.4291E-11	4.7138E-12	5.2752E-12	5.0468E-12	5.2751E-12
230	2.585E-11	3.8737E-12	4.316E-12	4.1358E-12	4.3159E-12
240	2.0014E-11	3.246E-12	3.6014E-12	3.4561E-12	3.6013E-12
250	1.5863E-11	2.7669E-12	3.0573E-12	2.938E-12	3.0573E-12
260	1.2834E-11	2.3942E-12	2.6352E-12	2.5355E-12	2.6352E-12
270	1.0575E-11	2.0993E-12	2.3021E-12	2.2175E-12	2.3021E-12
280	8.8565E-12	1.8626E-12	2.0352E-12	1.9625E-12	2.0352E-12
298	6.6681E-12	1.5409E-12	1.6733E-12	1.6164E-12	1.6733E-12
300	6.4773E-12	1.5115E-12	1.6404E-12	1.5848E-12	1.6404E-12
310	5.6408E-12	1.3795E-12	1.4924E-12	1.4431E-12	1.4924E-12
320	4.964E-12	1.2686E-12	1.3682E-12	1.3241E-12	1.3682E-12
330	4.4102E-12	1.1747E-12	1.2632E-12	1.2233E-12	1.2631E-12
340	3.952E-12	1.0944E-12	1.1735E-12	1.1372E-12	1.1735E-12
350	3.5692E-12	1.0253E-12	1.096E-12	9.9334E-13	1.0959E-12
360	3.2465E-12	9.6549E-13	1.0274E-12	9.3369E-13	1.0274E-12
370	2.9722E-12	9.1339E-13	9.6789E-13	8.8174E-13	9.6785E-13
380	2.7374E-12	8.6777E-13	9.1583E-13	8.3627E-13	9.158E-13
390	2.535E-12	8.2762E-13	8.7008E-13	7.9627E-13	8.7005E-13
400	2.3594E-12	7.9214E-13	8.297E-13	7.6092E-13	8.2967E-13

Table A13 Computed (BD(TQ)/CBS//M06-2X/AVDZ incl. SO correction for BrO) values of k_{inner} at TST, CVT and ICVT levels with tunneling correction at the Wigner, ZCT and SCT levels in $cm^3.molecule^{-1}s^{-1}$ for channel (1b) $BrO + HO_2 \rightarrow HOBr + O_2(\tilde{a}^1\Delta_g)$ at 200 – 400 K calculated with POLYRATE.

T (K)	TST/W	TST/ZCT	CVT/ZCT	ICVT/ZCT	TST/SCT	CVT/SCT	ICVT/SCT
200	7.39E-11	7.49E-12	8.07E-12	8.46E-12	7.49E-12	8.07E-12	8.46E-12
210	5.17E-11	5.87E-12	6.30E-12	6.59E-12	5.87E-12	6.30E-12	6.59E-12
220	3.75E-11	4.71E-12	5.05E-12	5.28E-12	4.71E-12	5.05E-12	5.28E-12
230	2.81E-11	3.87E-12	4.14E-12	4.32E-12	3.87E-12	4.14E-12	4.32E-12
240	2.16E-11	3.25E-12	3.46E-12	3.60E-12	3.25E-12	3.46E-12	3.60E-12
250	1.70E-11	2.77E-12	2.94E-12	3.06E-12	2.77E-12	2.94E-12	3.06E-12
260	1.37E-11	2.39E-12	2.54E-12	2.64E-12	2.39E-12	2.54E-12	2.64E-12
270	1.12E-11	2.10E-12	2.22E-12	2.30E-12	2.10E-12	2.22E-12	2.30E-12
280	9.37E-12	1.86E-12	1.96E-12	2.04E-12	1.86E-12	1.96E-12	2.04E-12
298	7.01E-12	1.54E-12	1.62E-12	1.67E-12	1.54E-12	1.62E-12	1.67E-12
300	6.80E-12	1.51E-12	1.58E-12	1.64E-12	1.51E-12	1.58E-12	1.64E-12
310	5.91E-12	1.38E-12	1.44E-12	1.49E-12	1.38E-12	1.44E-12	1.49E-12
320	5.18E-12	1.27E-12	1.32E-12	1.37E-12	1.27E-12	1.32E-12	1.37E-12
330	4.59E-12	1.17E-12	1.22E-12	1.26E-12	1.17E-12	1.22E-12	1.26E-12
340	4.11E-12	1.09E-12	1.14E-12	1.17E-12	1.09E-12	1.14E-12	1.17E-12
350	3.70E-12	1.03E-12	9.93E-13	1.10E-12	1.03E-12	9.93E-13	1.10E-12
360	3.36E-12	9.65E-13	9.34E-13	1.03E-12	9.65E-13	9.34E-13	1.03E-12
370	3.07E-12	9.13E-13	8.82E-13	9.68E-13	9.13E-13	8.82E-13	9.68E-13
380	2.82E-12	8.68E-13	8.36E-13	9.16E-13	8.68E-13	8.36E-13	9.16E-13
390	2.61E-12	8.28E-13	7.96E-13	8.70E-13	8.28E-13	7.96E-13	8.70E-13
400	2.43E-12	7.92E-13	7.61E-13	8.30E-13	7.92E-13	7.61E-13	8.30E-13

Table A14 A summary of values obtained for channel (1b) BrO + HO_2 → HOBr + O_2 ($\tilde{a}^1\Delta_g$) using POLYRATE and employing the BD(TQ)/CBS//M06-2X/AVDZ (incl. SO correction for BrO) IRC.

	BD(TQ)/CBS
$\Delta E_e^{\ddagger}$ [a]	-3.05
$\Delta E_0^{\ddagger}$ [a]	-3.07
$s^*(V_a^G)$	-0.5516
$V_a^G(s^*) - V_a^G(s=0)$	0.8558
$k^{CVT} \approx k^{ICVT}$	Yes
$\kappa^{ZCT}=\kappa^{SCT}=1.0$	Yes
$\kappa^{TST/CAG,200K}$	1.1219E-01
$\kappa^{CVT/CAG,200K}$	9.7397E-01
$k^{TST,200K}$	6.6450E-11
$k^{TST/CAG,200K}$	7.4550E-12
$k^{CVT,200K}$	8.8185E-12
$k^{ICVT/SCT,200K}$	8.8184E-12
$\kappa^{TST/CAG,400K}$	3.3495E-01
$\kappa^{CVT/CAG,400K}$	9.1174E-01
$k^{TST,400K}$	2.3594E-12
$k^{TST/CAG,400K}$	7.9026E-13
$k^{CVT,400K}$	8.3344E-13
$k^{ICVT/SCT,400K}$	8.3342E-13
ω_i/cm^{-1}	228.51i
T/K with $\kappa^{TST/W} \leq 1.2$	200 K – 400 K

[a] Computed classical barrier height, $\Delta E_e^{\ddagger}$ (electronic energy differences at s = 0, including spin-orbit contribution for BrO), and $\Delta E_0^{\ddagger}$ (classical barrier height with zero-point correction, including spin-orbit contribution for BrO) in kcal.mol^{-1}. $s^*(V_a^G)$ is the position of the maximum of the V_a^G curve (denoted as $V_a^G(s^*)$) in Å. Computed rate coefficients, k's, are in cm^{3}molecule^{-1}s^{-1}.

Table A15 Standard state enthalpy of activation ($\Delta H^{\#}$), standard state entropy of activation ($\Delta S^{\#}$) and standard state free energy of activation ($\Delta G^{\#}$) for channel (1b), BrO + HO_2 → HOBr + O_2 ($\tilde{a}^1\Delta_g$) computed at the BD(TQ)/CBS//M06-2X/AVDZ level (incl.SO correction for BrO), at three temperatures 200, 298 and 400 K.

T (K)	$\Delta H^{\#}$ at s= 0Å (kcal.mol^{-1})	$\Delta S^{\#}$ at s= 0 Å (kcal.mol^{-1}K^{-1})	$\Delta G^{\#}$ at s=0 (kcal.mol^{-1})	k_BT/hc^0 with c^0=1 (cm^{3}molecules^{-1}s^{-1})
200	-3.0448	-0.11954	20.863	41.65 x10^{11}
298	-3.0438	-0.11989	32.683	62.06x10^{11}
400	-3.0428	-0.11993	44.929	83.33 x10^{11}

Table A16 Transformations of the standard state enthalpy of activation ($\Delta H^{\#}$), standard state entropy of activation ($\Delta S^{\#}$) and standard state free energy of activation ($\Delta G^{\#}$) values in Table A16 using $\ln k = \ln(k_BT/hc^0) + \Delta S^{\#}/k_B - \Delta H^{\#}/(k_BT)$ (equation 5.3 in text) at 200, 298 and 400 K for the same channel.

T (K)	$-\Delta H^{\#}/k_BT$ at s= 0 Å	$\Delta S^{\#}/k_B$ at s = 0 Å	$-\Delta G^{\#}/k_BT$ at s= 0 Å	(ln (k_BT/hc^0))
200	7.66186069	-60.15934433	-52.49748364	29.06
298	5.14053513	-60.33605095	-55.19551582	29.46
400	3.82839351	-60.35733161	-56.52893810	29.75

Table A17 Relative values of the terms $-\Delta H^{\#}/(k_BT)$, $\Delta S^{\#}/k_B$ and $\ln(k_BT/hc^0)$ at 200, 298 and 400 K taken from Table A17 and taking the value at 400 K as zero in each case. These relative values are plotted against 1000/T in Figure 5.14.

T (K)	$\Delta(-\Delta H^{\#}/k_BT$ at s=0 Å)	$\Delta(\Delta S^{\#}/k_B$ at s= 0 Å)	$\Delta(-\Delta G^{\#}/k_BT$ at s= 0 Å)	Δ(ln (k_BT/hc^0))
200	3.8334671808	+0.197987273	4.03145	-0.69
298	1.3121416219	+0.021280657	1.33342	-0.29
400	0.0000000000	0.0000000000	0.00000	0.000

Table A18 Computed (BD(TQ)/CBS//M06-2X/AVDZ incl. SO correction for BrO) $k_{overall(ii)}$ values obtained from k_{outer} and k_{inner} from equation (6.1) for channel (1b) BrO + HO_2 → HOBr + O_2 ($\tilde{a}^1\Delta_g$) at 200 – 400 K. k_{outer} was obtained from PST calculations with VARIFLEX and k_{inner} was obtained from ICVT/SCT calculations with POLYRATE.

T (K)	k_{outer}	k_{inner}	$k_{overall(ii)}$
200	2.49E-10	8.46E-12	8.18E-12
210	2.51E-10	6.59E-12	6.42E-12
220	2.52E-10	5.28E-12	5.17E-12
230	2.54E-10	4.32E-12	4.25E-12
240	2.55E-10	3.60E-12	3.55E-12
250	2.57E-10	3.06E-12	3.02E-12
260	2.58E-10	2.64E-12	2.61E-12
270	2.59E-10	2.30E-12	2.28E-12
280	2.6E-10	2.04E-12	2.02E-12
298	2.62E-10	1.67E-12	1.66E-12
300	2.63E-10	1.64E-12	1.63E-12
310	2.63E-10	1.49E-12	1.48E-12
320	2.64E-10	1.37E-12	1.36E-12
330	2.65E-10	1.26E-12	1.25E-12
340	2.66E-10	1.17E-12	1.16E-12
350	2.67E-10	1.10E-12	1.10E-12
360	2.67E-10	1.03E-12	1.03E-12
370	2.68E-10	9.68E-13	9.65E-13
380	2.68E-10	9.16E-13	9.13E-13
390	2.69E-10	8.70E-13	8.67E-13
400	2.69E-10	8.30E-13	8.27E-13

Table A19 Comparison of recommended experimentally derived rate coefficients (reference 13) for the BrO + HO2 reaction in the temperature range 200-400 K, with computed values obtained in this work ($cm^3molecule^{-1}s^{-1}$).

T (K)	Experimentally derived (3) k	k^{TST} [a] This work	$k^{ICVT/SCT}$	$k_{overall,(ii)}$ calculated from equation (5.1) this work [b]
200	5.49E-11	6.64E-11	8.46E-12	8.18E-12
220	4.38E-11	3.43E-11	5.28E-12	5.17E-12
240	3.62E-11	2.00E-11	3.60E-12	3.55E-12
260	3.03E-11	1.28E-11	2.64E-12	2.61E-12
280	2.69E-11	8.85E-12	2.04E-12	2.02E-12
298	2.40E-11	6.67E-12	1.67E-12	1.66E-12
300	2.38E-11	6.48E-12	1.64E-12	1.63E-12
320	2.15E-11	4.96E-12	1.37E-12	1.36E-12
340	1.96E-11	3.95E-12	1.17E-12	1.16E-12
360	1.80E-11	3.25E-12	1.03E-12	1.03E-12
380	1.67E-11	2.75E-12	9.16E-13	9.13E-13
400	1.53E-11	2.36E-12	8.30E-13	8.27E-13

(a) See Table 11; TST values for k_{inner} computed with POLYRATE

(b) k_{outer} obtained from PST calculations with VARIFLEX and k_{inner} obtained from ICVT/SCT calculations with POLYRATE (values in column 4)